Technical University
of Munich

Max Planck Institute
for Physics

First generation prototype detectors for the TRISTAN project

Vollständiger Abdruck der von der Fakultät für Physik der Technischen Universität München zur Erlangung des akademischen Grades eines

Doktor der Naturwissenschaften (Dr. rer. nat.)

genehmigten Dissertation von

Tim Benjamin Brunst

aus Karlsruhe.

Vorsitzender:

apl. Prof. Dr. Norbert Kaiser

Prüfer der Dissertation:

1. Prof. Dr. Susanne Mertens
2. Prof. Dr. Stefan Schönert

Die Dissertation wurde am 29.04.2020 bei der Technischen Universität München eingereicht und durch die Fakultät für Physik am 08.07.2020 angenommen.

Document compiled on September 1, 2020.

Abstract

Sterile neutrinos emerge in minimal extensions of the Standard Model of particle physics, which can solve a number of open questions in astroparticle physics and cosmology. If their mass was in the kilo-electron-volt regime, they would be viable dark matter candidates. One way to search for these particles in a laboratory-based experiment is via tritium β-decay, where the additional neutrino mass eigenstate would manifest itself as a kink-like distortion of the spectrum.

The TRISTAN (Tritium Investigations on Sterile to Active Neutrino mixing) group aims at detecting a sterile neutrino signature by measuring the entire tritium β-decay spectrum with an upgraded KATRIN (Karlsruhe Tritium Neutrino) experiment. KATRIN investigates the energetic endpoint of the tritium spectrum to determine the effective mass of the electron anti-neutrino with a sensitivity of 200 meV (90 % C.L.) after an effective data taking time of three years. One of the greatest challenges in operating the system in search for a sterile neutrino is to handle the high signal rates, generated by the strong activity of the KATRIN tritium source. Therefore, a novel multi-pixel silicon drift detector system is being designed, which is able to handle rates up to 100 Mcps and features an excellent energy resolution for electrons of better than 300 eV (FWHM) at 20 keV and an ultra-thin entrance window.

This work has three focuses:

1. the characterization of the first 7-pixel prototype detector with x-rays and electrons,
2. a first search for sterile neutrinos with the prototype detector installed at the Troitsk ν-mass experiment, and
3. a detailed sensitivity study of the final experiment.

First characterization measurements with x-ray lines of ^{55}Fe and ^{241}Am were performed, in which the excellent performance of the entire detector array was verified in terms of energy resolution, noise properties, and calibration linearity. In a next step, mono-energetic electrons from a scanning electron microscope and a rubidium-krypton source were used to develop a semi-empirical model of the detector response to electrons. As the shape of this response function and especially the energy resolution for electrons is strongly influenced by the entrance window thickness, several different entrance window technologies were tested and compared. With an effective dead layer thickness of about 50 nm, the standard technology has shown to be the most reliable option. The Troitsk ν-mass experiment, one of KATRIN's technological predecessors, was instrumented with a TRISTAN prototype detector and searches for sterile neutrinos in a mass range up to 6.6 keV were performed. The novelties of these campaigns are on the one hand an enlarged mass range compared to previous searches at Troitsk ν-mass and on the other hand measurements in both differential and integral mode. As a major result of these investigations, it could be demonstrated, that both methods are prone to largely different systematic uncertainties. Furthermore, analysis strategies were developed, which led to the first upper limits on the sterile neutrino mixing amplitude obtained with a TRISTAN detector of $|U_{\mathrm{e}4}|^2 < 2 \cdot 10^{-2}$ at $m_4 = 3.3\,\mathrm{keV}$ (differential) and $|U_{\mathrm{e}4}|^2 < 7 \cdot 10^{-3}$ at $m_4 = 3.4\,\mathrm{keV}$ (integral), enlarging the previous accessible mass range of Troitsk ν-mass by a factor of three. These measurements depict a key milestone for the TRISTAN project and lay the basis for future searches with more data. Finally, sensitivity studies investigating the impact of detector-related systematic uncertainty on the final KATRIN/TRISTAN sensitivity were performed. It could be shown, that the weaker the energy correlation of an uncertainty, the stronger the impact on the sensitivity. The uncertainty on the measured detector entrance window thickness leads to a degradation of the sensitivity of a factor less than two.

The results of this work contribute significantly to the development of the next generation of prototype detectors and the final detector array with a total of around 3500 pixels. The upgrade of the KATRIN experiment with the final TRISTAN detector system will prospectively take place after the completion of the neutrino mass program.

Zusammenfassung

Sterile Neutrinos treten in minimalen Erweiterungen des Standardmodells der Elementarteilchenphysik auf, die einige offene Fragen in der Astroteilchenphysik und Kosmologie lösen können. Falls ihre Masse im Kiloelectronvolt-Bereich läge, wären sie realistische Kandidaten für Dunkle Materie. Ein Weg, in einem Laborexperiment nach diesen Teilchen zu suchen, ist über den β-Zerfall von Tritium, in dem sich der zusätzliche Masseneigenzustand als knickartige Verzerrung des Spektrums offenbaren würde.

Die Gruppe TRISTAN (Tritium Investigations on Sterile to Active Neutrino mixing) beabsichtigt, die Signatur eines sterilen Neutrinos durch Messung des gesamten β-Zerfallspektrums von Tritium mithilfe eines verbesserten KATRIN- (Karlsruhe Tritium Neutrino) Experiments zu ermitteln. KATRIN untersucht den kinematischen Endpunkt des Tritiumspektrums, um die effektive Masse des Elektron-Antineutrinos mit einer Sensitivität von 200 meV (Konfidenzniveau 90 %) nach einer effektiven Messzeit von drei Jahren zu ermitteln. Eine der größten Herausforderungen beim Betrieb des Systems zur Suche nach einem sterilen Neutrino ist, die hohen Signalraten zu bewältigen, die durch die starke Tritiumquelle von KATRIN erzeugt werden. Daher wird ein neuartiges Multi-Pixel-Siliziumdriftdetektorsystem entwickelt, das Raten von bis zu 100 MHz bewältigt und sich durch eine exzellente Auflösung für Elektronen von besser als 300 eV (FWHM) bei 20 keV und ein ultra dünnes Eintrittsfenster auszeichnet.

Die vorliegende Arbeit hat drei Fokuspunkte:

1. die Charakterisierung des ersten 7-Pixel-Prototypdetektors mit Röntgenstrahlen und Elektronen,
2. ersten Messungen zur Suche nach einem sterilen Neutrino mit dem Prototypdetektor am Troitsk ν-mass Experiment, und
3. eine detaillierte Sensitivitätsstudie des endgültigen Experiments.

Es wurden erste Charakterisierungsmessungen mit Röntgenlinien von ^{55}Fe und ^{241}Am durchgeführt, welche die exzellente Funktionsfähigkeit aller Pixel des Detektors in Hinsicht auf Energieauflösung, elektronisches Rauschen und Kalibrationslinearität

bestätigten. In einem nächsten Schritt wurden mono-energetische Elektronen von einem Rasterelektronenmikroskop und von einer Rubidium-Krypton-Quelle benutzt, um ein semi-empirisches Modell für die Antwortfunktion des Detektors auf Elektronen zu entwickeln. Da die Form der Antwortfunktion und speziell die Energieauflösung für Elektronen stark von der Stärke des Eintrittsfensters beeinflusst wird, wurden mehrere Eintrittsfenstertechnologien getestet und verglichen. Mit einer effektiven Totschichtstärke von ungefähr 50 nm hat sich die Standardtechnologie als die zuverlässigste Option erwiesen. Ein TRISTAN Prototypdetektor wurde am Troitsk ν-mass Experiment, einem von KATRINs technologischen Vorgängern, installiert und es wurde Messungen zur Suche nach sterilen Neutrinos in einem Massebereich bis 6.6 keV durchgeführt. Die Neuheit dieser Kampagnen sind einerseits der im Vergleich zu bisherigen Messungen an Troitsk ν-mass vergrößerte Massebereich und andererseits Messungen sowohl im differentiellen als auch im integralen Modus. Ein wesentliches Ergebnis dieser Untersuchungen ist, dass beide Modi anfällig für weitgehend unterschiedliche systematische Unsicherheiten sind. Weiterhin wurden Analysestrategien entwickelt, was zu ersten mithilfe eines TRISTAN-Detektors bestimmten Obergrenzen auf die Mischungsamplitude steriler Neutrinos führte: $|U_{\mathrm{e}4}|^2 < 2 \cdot 10^{-2}$ bei $m_4 = 3.3\,\mathrm{keV}$ (differentiell) und $|U_{\mathrm{e}4}|^2 < 7 \cdot 10^{-3}$ bei $m_4 = 3.4\,\mathrm{keV}$ (integral). Dabei wurde der für Troitsk ν-mass zugängliche Massenbereich um einen Faktor drei erweitert. Diese Ergebnisse stellen einen wichtigen Meilenstein für das TRISTAN-Projekt dar und bilden die Grundlage für zukünftige Messungen mit größeren Datenmengen. Schließlich wurden Sensitivitätsstudien durchgeführt, um den Einfluss von detektorabhängigen systematischen Unsicherheiten auf die endgültige KATRIN/TRISTAN Sensitivität zu untersuchen. Es konnte gezeigt werden, dass der Einfluss auf die Sensitivität größer ist, wenn die Energiekorrelation der Unsicherheit klein ist. Die Unsicherheit auf die gemessene Stärke des Detektor-Eintrittsfensters führt zu einer Abnahme der Sensitivität um einen Faktor kleiner zwei.

Die Ergebnisse dieser Arbeit tragen maßgebend zur Entwicklung der nächsten Generation von Prototypdetektoren und des endgültigen Detektorsystems mit insgesamt ungefähr 3500 Pixeln bei. Die Aufrüstung des KATRIN-Experiments mit dem endgültigen TRISTAN-Detektorsystem wird voraussichtlich nach Abschluss der Neutrinomassenmessung stattfinden.

Contents

List of Figures

List of Tables

Acronyms

ADC	analog-to-digital converter	27
AGS	Alternating Gradient Synchrotron	4
ALP	axion-like particle	34
API	application programming interface	41
ASIC	application-specific integrated circuit	27
BBN	Big Bang nucleosynthesis	13
BNL	Brookhaven National laboratory	4
CCE	charge collection efficiency	37
CDM	cold dark matter	12
Cesic	carbon-fiber reinforced silicon carbide	31
CMB	cosmic microwave background	8
ComPol	Compton polarimeter	33
CPS	cryogenic pumping section	20
CSA	charge-sensitive preamplifier	40
DAQ	data acquisition	29
DM	dark matter	1
DOF	degrees of freedom	122
DONUT	Direct Observation of Nu Tau	4
DPP	digital pulse processor	27
DPS	differential pumping section	20

EC electron capture . . . 9

ENC equivalent noise charge . . . 47

FBM forward beam monitor . . . 22

FET field-effect transistor . . . 40

FPGA field-programmable gate array . . . 27

FSD final state distribution . . . 118

FWHM full width at half maximum . . . 2

GALLEX Gallium Experiment . . . 11

GERDA Germanium Detector Array . . . 9

GUI graphical user interface . . . 41

HDM hot dark matter . . . 12

HLL Halbleiterlabor of the Max Planck society . . . 28

HOPG highly oriented pyrolytic graphite . . . 82

HV high voltage . . . 99

IAXO International Axion Observatory . . . 34

IBD inverse β-decay . . . 4

Idef-X Imaging Detector Front-end . . . 29

INL integral non-linearity . . . 65

IO inverted ordering . . . 7

JFET junction gate field-effect transistor . . . 30

KARMEN Karlsruhe Rutherford Medium Energy Neutrino . . . 11

KATRIN Karlsruhe Tritium Neutrino . . . 1

KESS KATRIN Electron Scattering in Silicon . . . 67

KIT Karlsruhe Institute of Technology . . . 15

LARA Laser Raman . . . 20

LEP	Large Electron-Positron	4
LSB	least significant bit	65
LSND	Liquid Scintillator Neutrino Detector	11
MAC-E	Magnetic Adiabatic Collimation combined with an Electrostatic filter	16
MC	Monte Carlo	67
MiniBooNE	Mini Booster Neutrino Experiment	11
MOSFET	metal-oxide-semiconductor field-effect transistor	40
MPP	Max Planck Institute for Physics	31
MSW	Mikheev-Smirnov-Wolfenstein	7
MTD	measurement time distribution	160
νMSM	neutrino minimal Standard Model	13
NO	normal ordering	7
P-0	prototype-0	ix
P-1	prototype-1	30
PAE	post-acceleration electrode	26
PDF	probability density function	185
PIN	positive intrinsic negative	21
PMNS	Pontecorvo-Maki-Nakagawa-Sakata	5
ROI	region of interest	10
SAGE	Soviet–American Gallium Experiment	11
SDD	silicon drift detector	2
SDS	spectrometer and detector system	19
SDSS	Sloan Digital Sky Survey	12
SEM	scanning electron microscope	72
SM	Standard Model	1

SMU	source measure unit	45
SNO	Sudbury Neutrino Observatory	6
SRIM	stopping and range of ions in matter	93
SSC	source and spectrum calculation	111
STS	source and transport section	19
TLK	Tritium Laboratory Karlsruhe	15
TMP	turbo molecular pump	20
TRISTAN	Tritium Investigations on Sterile to Active Neutrino mixing	1
TUM	Technical University of Munich	34
USB	Universal Serial Bus	41
WDM	warm dark matter	12
WGTS	windowless gaseous tritium source	1
WIMP	weakly interacting massive particle	12
XMM	x-ray multi-mirror	12

1 Introduction

Over the course of the last century, a great diversity of experiments and theories paved the way to our remarkable understanding of the structure of matter: It was found that all baryonic matter in the universe is made of a few elementary particles, interacting via four fundamental forces [CER20]. The Standard Model (SM) of particle physics is to date the best theory to describe these interactions, comprising three of the fundamental forces and all known elementary particles. However, it does not explain the complete picture of nature. It is believed to omit at least some particles, which constitute to the vast amount of dark matter (DM) in the universe. Especially surprising and thus interesting has been the neutrino sector: Neutrinos are treated as massless in the SM, even though it is known that they have a non-zero mass [Zub12]. Furthermore, they are orders of magnitudes lighter than all other elementary particles. The absolute value of their mass is still unknown, as they are the only particles, which appear with only left-handed helicity.

The existence of so-called sterile neutrinos would elegantly resolve at least some of the above mentioned questions [Adh17]. The term "sterile" refers to the fact that the sterile flavor eigenstate would not participate in any fundamental force.[1] Introducing right-handed partners to the known left-handed neutrinos provides a mechanism, which generates mass and explains the lightness of the latter at the same time. On top, a sterile neutrino in the keV-mass range could account for a large amount of DM and could possibly reconcile recent tensions in cosmological structure observations. To do so, however, they must mix with the active neutrino states, which makes their detection accessible in laboratory-based experiments.

The Tritium Investigations on Sterile to Active Neutrino mixing (TRISTAN) project aims at realizing such a search with the Karlsruhe Tritium Neutrino (KATRIN) experiment. The main goal of KATRIN is to determine the effective electron antineutrino mass [Ang05]. To this end, it precisely measures the kinetic endpoint region of the tritium β-decay spectrum, where the imprint of the neutrino mass is largest. KATRIN excels at a highly luminous windowless gaseous tritium source (WGTS), providing an unprecedented statistical sensitivity of 200 eV (90 % C.L.) after a measurement time of three years. Its operation in search for a sterile neutrino,

---

[1] The mass eigenstate, mostly consisting of the sterile flavor, would interact via gravity.

however, requires to extend the observed spectral region to a wider energy range. The sterile neutrino mass is unconstrained. Its imprint could appear anywhere in the β-spectrum. As a consequence, the electron count rates are increased to $\mathcal{O}(10^8\,\mathrm{cps})$, which cannot be handled by the current KATRIN focal plane detector. In the frame of the TRISTAN project, a novel detector system is thus being developed, in order to upgrade the KATRIN setup and to search for sterile neutrinos in the keV-mass range [Mer15a]. The goal is to reach a sensitivity to the active-to-sterile mixing amplitude at the ppm-level. With this, current laboratory limits could be improved by three orders of magnitude and the parameter space of cosmological interest could possibly be reached.

The main challenge for the TRISTAN detector is to manage the extremely high count rates of $\mathcal{O}(10^8\,\mathrm{cps})$, while maintaining an excellent energy resolution of 300 eV of the full width at half maximum (FWHM) at 20 keV and time stability in the order of years. To test mixing angles of cosmological interest (i.e. $|U_{\mathrm{e}4}|^2 < 10^{-6}$), a precise understanding of the entire tritium spectrum on the ppm-level is required. The final system foresees a 3500-pixel silicon drift detector (SDD) focal plane array. As a first step, a 7-pixel prototype chip was produced and equipped with appropriate read-out systems. This prototype detector is the basis of the experimental work of this thesis. The thesis comprises three main focuses:

1. the characterization of the general performance of the prototype detectors,
2. first measurements in search for sterile neutrinos at the Troitsk ν-mass experiment and the development of the corresponding analysis strategies, and
3. the identification of crucial detector effects and systematic uncertainties for the final experiment.

The thesis is structured as follows: Chapter 2 gives a general introduction to neutrino physics and the particularities of sterile neutrinos. The KATRIN experiment and the TRISTAN project are presented in more detail in chapter 3. The general characterization of the first TRISTAN prototype detector system is discussed in chapter 4. The operation of the prototype system at the Troitsk ν-mass experiment, as well as the analysis of the acquired data is presented in chapter 5. Sensitivity studies with regard to a sterile neutrino search are subject of chapter 6. The work is concluded by a summary and outlook in chapter 7.

2 Neutrino physics

Neutrinos are electrically neutral fermions (spin $\frac{1}{2}$) and appear as the leptonic partners of the electron, muon, and tau in the SM of particle physics. Neutrinos interact only via the weak interaction and gravitation. Their properties have been a vital field of research in the last six decades, which continues growing today.

This chapter gives an introduction to neutrino physics and properties, starting with their postulation and discovery in section 2.1. In section 2.2, neutrino oscillations and their consequence for the neutrino mass is discussed. A summary of neutrino mass measurements is presented in section 2.3. The sterile neutrino, which is of specific interest for the work presented in this thesis, is introduced in section 2.4.

2.1 The discovery of the neutrino

In 1914, J. Chadwick discovered the continuous energy spectrum in single β-decay [Cha14]. At that time, it was assumed to be a two-body decay, which would produce a discrete energy spectrum like in α- or γ-decays. It was vigorously discussed, whether energy conservation might be violated [Bro71]. To not abandon this principle, W. Pauli proposed in his famous letter from 1930 an additional, so far undetected particle [Pau30], which was later named neutrino ν. It should be electrically neutral, have spin $\frac{1}{2}$, and should not travel at the speed of light. In 1934, E. Fermi provided the theoretical basis for continuous β-decay [Fer34]

$$(Z,A) \to (Z+1, A) + \mathrm{e}^- + \bar{\nu}_\mathrm{e} \ , \tag{2.1}$$

with atomic number Z and mass number A of the nucleus, the electron e^- and the electron antineutrino $\bar{\nu}_\mathrm{e}$. Fermi's theory is the precursor to the low-energy limit of the weak interaction and today still valid as such.

In 1956, C. Cowan and F. Reines detected neutrinos for the first time within the project Poltergeist [Cow56]. They used a water target with dissolved cadmium chloride ($\mathrm{CdCl_2}$) between layers of scintillating material, read out by photomultiplier tubes. The setup was placed 11 m from the core of one of the Savannah River Site nuclear fission reactors. Electron antineutrinos coming from the fission process were detected by inverse β-decay (IBD)

$$\bar{\nu}_e + p \rightarrow e^+ + n \ , \tag{2.2}$$

resulting in a prompt and a delayed light signal from positron annihilation and neutron capture, respectively. For this discovery, Reines was awarded with the Nobel Prize in 1995, when Cowan had already died.

Today we know of three neutrino flavor eigenstates. The second flavor, the muon neutrino ν_μ, was detected at the Alternating Gradient Synchrotron (AGS) neutrino experiment at Brookhaven National laboratory (BNL) in 1962 by L. Lederman, M. Schwartz, and J. Steinberger [Dan62]. They demonstrated the different nature of ν_μ emitted in pion decay (compared to ν_e) by observing muon tracks in a spark chamber. All three scientists were awarded with the Nobel Prize in 1988.

After the discovery of the tau lepton in 1975 [Per75], the existence of the corresponding tau neutrino ν_τ was anticipated. It was discovered at the Direct Observation of Nu Tau (DONUT) experiment at Fermilab in 2001 [Kod01] and is assumed to be the last missing particle in the SM. This is because the number of active neutrino species could be infered to be $N_\nu = 2.9840 \pm 0.0082$ from investigations of the Z-decay width at the Large Electron-Positron (LEP) collider [LEP06].[1]

2.2 Neutrino mixing & oscillations

Neutrinos are considered massless in the SM. In order to generate neutrino masses via Yukawa coupling to the standard Higgs field as for all other SM fermions, a neutrino with both positive and negative helicity would be needed (see section 2.3). It was shown, however, by M. Goldhaber at BNL in 1958 that neutrinos appear only with negative and antineutrinos only with positive helicity [Gol58]. This is a consequence of the V-A theory, which predicts maximal parity violation in the weak interaction. Neutrino mass creation via Yukawa coupling is thus not possible in the SM. However, today we know that neutrinos have a small but yet non-zero mass. This is due to the fact that neutrinos oscillate between different flavor eigenstates and points towards a mass creation mechanism beyond the SM.

---

[1] This holds for "light" neutrinos with a mass $m_\nu < 45.6\,\text{GeV}$, less than half the Z-boson mass.

Solar neutrino problem The study of neutrino oscillations was triggered in the 1960s by R. Davis Jr. and J. Bahcall. Bahcall provided theoretical calculations of the ν_e-flux coming from the sun, while Davis designed an experiment to test Bahcall's predictions [Dav64]. The Brookhaven Solar Neutrino Experiment in the Homestake Gold Mine was the first to detect and count solar neutrinos. Davis continued his work until 1994, for which he was awarded with the Nobel Prize in 2002. He found that only one third of the expected neutrinos was detected [Dav68]. This discrepancy was from then on referred to as the solar neutrino problem.

A first step towards the solution of the solar neutrino problem was already taken in 1958 by B. Pontecorvo [Pon58]. He proposed that the existence of a non-zero neutrino mass could allow for $\nu \leftrightarrow \bar{\nu}$ transitions. The modern formalism for leptonic mixing and neutrino oscillations in vacuum was later established by Z. Maki, M. Nakagawa, and S. Sakata [Mak62], as well as by B. Pontecorvo [Pon68]. This formalism predicts the oscillation of solar ν_e into the other two neutrino flavor eigenstates, ν_μ and ν_τ. As the Homestake experiment was sensitive to electron neutrinos only, this could explain the discrepancy between the observed and predicted neutrino flux.

Theory of neutrino oscillations The neutrino flavor eigenstates $|\nu_\alpha\rangle$, where $\alpha \in \{\mathrm{e}, \mu, \tau\}$, are not identical with the mass eigenstates $|\nu_i\rangle$, where $i \in \{1, 2, 3\}$. The two bases can be written as a linear superposition of each other [Zub12]

$$|\nu_\alpha\rangle = \sum_{i=1}^{3} U_{\alpha i} |\nu_i\rangle \qquad \text{or} \qquad |\nu_i\rangle = \sum_{\alpha=\mathrm{e},\mu,\tau} U^*_{\alpha i} |\nu_\alpha\rangle \;, \tag{2.3}$$

using the Pontecorvo-Maki-Nakagawa-Sakata (PMNS) matrix [Tan18]

$$U_{\mathrm{PMNS}} = \begin{pmatrix} U_{\mathrm{e}1} & U_{\mathrm{e}2} & U_{\mathrm{e}3} \\ U_{\mu 1} & U_{\mu 2} & U_{\mu 3} \\ U_{\tau 1} & U_{\tau 2} & U_{\tau 3} \end{pmatrix} \tag{2.4}$$

$$= \begin{pmatrix} c_{12}c_{13} & s_{12}c_{13} & s_{13}e^{-\imath\delta} \\ -s_{12}c_{23} - c_{12}s_{23}s_{13}e^{\imath\delta} & c_{12}c_{23} - s_{12}s_{23}s_{13}e^{\imath\delta} & s_{23}c_{13} \\ s_{12}s_{23} - c_{12}c_{23}s_{13}e^{\imath\delta} & -c_{12}s_{23} - s_{12}c_{23}s_{13}e^{\imath\delta} & c_{23}c_{13} \end{pmatrix} \tag{2.5}$$

with the abbreviations $s_{ij} = \sin\theta_{ij}$ and $c_{ij} = \cos\theta_{ij}$. The mixing angles θ_{12}, θ_{23}, and θ_{13} determine the mixing amplitudes. The parameter δ is a CP violating Dirac phase.[2]

---

[2] If neutrinos are Majorana particles, i.e. their own antiparticles, two additional phases are added.

For simplicity, the phenomenon of neutrino oscillations is introduced on the simpler case of two neutrino flavors

$$\begin{pmatrix} \nu_\alpha \\ \nu_\beta \end{pmatrix} = \begin{pmatrix} \cos\Theta & \sin\Theta \\ -\sin\Theta & \cos\Theta \end{pmatrix} \begin{pmatrix} \nu_i \\ \nu_j \end{pmatrix} \tag{2.6}$$

with a single mixing angle Θ. Considering a neutrino mass eigenstate with the defined mass m_i and energy E, its evolution after traveling the distance L can be written in the ultra-relativistic limit as

$$|\nu_i(L)\rangle = e^{-\imath \frac{m_i^2 L}{2E}} |\nu_i(0)\rangle \quad . \tag{2.7}$$

Considering that mass eigenstates are superpositions of flavor eigenstates (see equation (2.3)), the probability that a neutrino of flavor α will be observed with flavor β is often expressed as

$$P(\alpha \to \beta) = \sin^2(2\Theta)\sin^2\left(1.27 \cdot \Delta m^2 \ [\mathrm{eV}^2] \frac{L \ [\mathrm{km}]}{E \ [\mathrm{GeV}]}\right) \tag{2.8}$$

with the difference of the mass squares $\Delta m^2 = m_j^2 - m_i^2$. Thus, in order to be able to change their flavor as they propagate through space, neutrinos must have different masses ($\Delta m^2 \neq 0$), which means for the three neutrino case that at least two mass states have to be non-zero.

Neutrino oscillation experiments As a first hint for neutrino osicllations, a deficit in the flux of ν_μ produced in the earth's atmosphere was detected at Super-Kamiokande in 1998 [Fuk98]. The flux of neutrinos produced on the opposite side of the earth was reduced compared to the amount coming from the sky directly above the experiment. In 2002, the Sudbury Neutrino Observatory (SNO) collaboration published the first simultaneous measurement of all three neutrino flavors coming from the sun using neutral current reactions in heavy water (D_2O) [Ahm01]. The results showed clear evidence for neutrino oscillations and explained the reduced flux measured by the Homestake experiment. The solar neutrino problem was finally resolved 40 years after its first observation. For this discovery, T. Kajita and A. McDonald, the leaders of Super-Kamiokande and SNO, were awarded with the Nobel Prize in 2015.

Since then, neutrino oscillations have been studied in many different experiments and the values of the mixing angles and mass differences have been determined with high accuracy [Tan18]. The strength of leptonic CP violation δ is planned to be determined in future experiments. The latest values of all oscillation parameters are summarized in table 2.1. However, oscillation experiments are only sensitive to squared mass differences, not to the absolute neutrino mass scale. Furthermore, while the sign

Table 2.1: **Neutrino oscillation parameters.** The values are derived from a global analysis [Est19, NuF18]. Some of the fits yield different results depending on the assumed sign of Δm^2_{31}.

Parameter		**Best fit ±1 σ**	
		NO	**IO**
θ_{12}	[°]	$33.82^{+0.78}_{-0.76}$	
θ_{23}	[°]	$49.6^{+1.2}_{-1.0}$	$49.8^{+1.0}_{-1.1}$
θ_{13}	[°]	8.61(13)	8.65(13)
Δm^2_{21}	$[10^{-5}\,\mathrm{eV}^2]$	$7.39^{+0.21}_{-0.20}$	
Δm^2_{31}	$[10^{-3}\,\mathrm{eV}^2]$	$+2.525^{+0.033}_{-0.031}$	$-2.512^{+0.034}_{-0.032}$
δ	[°]	215^{+40}_{-29}	284^{+27}_{-29}

of Δm^2_{21} is determined by the Mikheev-Smirnov-Wolfenstein (MSW) effect [Wol78, Mik85], the sign of Δm^2_{31} is still unknown. The case, in which $\Delta m^2_{31} > 0$, is called normal ordering (NO). The term inverted ordering (IO) refers to the case $\Delta m^2_{31} < 0$. The absolute mass scale and the mass ordering are two of the fundamental open questions in neutrino physics, both of which are embattled by many scientists and modern experiments.

2.3 The massive neutrino

In the SM, charged fermions gain mass via Yukawa interactions with the Higgs field. In this theory, a Yukawa mass term is added to the SM Lagrangian. Following the notation in [Mer17], this term is given for electrons as

$$\mathcal{L}_{\text{Yukawa}} = -\underbrace{\frac{c_{\mathrm{e}} v}{\sqrt{2}}}_{m_{\mathrm{e}}} \left(\bar{\mathrm{e}}_R \mathrm{e}_L + \bar{\mathrm{e}}_L \mathrm{e}_R\right) \ , \tag{2.9}$$

where c_{e} is the coupling constant, which goes into the electron mass m_{e}. The indexes L and R denote left- and right-handed chirality, respectively. As right-handed neutrinos and left-handed antineutrinos would be necessary for this term, neutrino mass cannot be generated in this way.

Seesaw mechanism Several theories have been developed to introduce neutrino mass to the SM. Most famous is the seesaw mechanism [Moh80, Yan80], in which a mass term [Adh17]

$$\mathcal{L}_{\text{seesaw}} = -\frac{1}{2} \begin{pmatrix} \bar{\nu}_L & \bar{\mathrm{N}}^c_R \end{pmatrix} \begin{pmatrix} m_L & m_D \\ m_D^T & m_R \end{pmatrix} \begin{pmatrix} \nu^c_L \\ \mathrm{N}_R \end{pmatrix} + \text{h.c.} \ , \tag{2.10}$$

is added to the Lagrangian, introducing a right-handed neutrino N_R. The matrix consists of one Dirac mass m_D and two Majorana masses m_L and m_R. The Dirac mass m_D is per definition on the order of the vacuum expectation value of the SM Higgs field

$$m_D = \mathcal{O}\left(|\langle H\rangle|\right) \approx 174\,\mathrm{GeV}\ . \tag{2.11}$$

The eigenstates of the matrix are obtained by diagonalizing the matrix, where two cases are distinguished for $m_L = 0$:[3]

1. **Dirac case:** If $m_R = 0$, both eigenstates equal the Dirac mass m_D. It can be generated via Yukawa interactions, which is the conventional way in the SM. However, an unnatural small coupling constant has to be introduced to explain the lightness of the active neutrino states.

2. **Seesaw (type I):** With the condition $m_R \gg m_D$, the two eigenstates

$$m_1 = \frac{m_D^2}{m_R} \ll m_D \qquad \text{and} \qquad m_2 = m_R\left(1 + \frac{m_D^2}{m_R^2}\right) \approx m_R \tag{2.12}$$

   are found. The name seesaw reflects the fact that the heavier m_R, the lighter m_1. This elegantly explains the lightness of the active neutrino states. At the same time, the eigenstate m_2 becomes very heavy and is in most theories inaccessible for current experiments.

Cosmological limits Most stringent upper limits on the neutrino mass are inferred from cosmological observations, such as the cosmic microwave background (CMB), galaxy surveys, and the Lyman-alpha forest [Goo06]. Massive neutrinos contribute to the cosmological matter density but were relativistic over a long period in the early universe. This means that they were confined to very large gravitational potentials only. Small potentials became washed out, as matter was carried away by the free streaming neutrinos. Consequently, a non-zero neutrino mass suppresses the formation of small-scale structures (galaxies, galaxy groups, etc.) relative to larger ones (superclusters and filaments). The Planck collaboration provides an upper limit on the sum over all neutrino mass eigenstates of [Ade16]

$$m_{\mathrm{tot}} = \sum_{i=1}^{3} m_i < 0.23\,\mathrm{eV}. \tag{2.13}$$

However, these results depend on the underlying cosmological model. Determining the neutrino mass via less model-dependent methods reduces the number of free parameters for cosmological observations, which in turn improves our understanding of structure formation in the universe.

---

[3] The case $m_L \neq 0$ is considered in type II seesaw models [Mer17].

Neutrinoless double β-decay One type of laboratory-based experiments are searches for neutrinoless double β-decay ($0\nu\beta\beta$). Double β-decay refers to the simultaneous decay of two nucleons in an atomic nucleus. The ordinary double β-decay ($2\nu\beta\beta$) is an established process in the SM, in which two electrons are emitted next to their corresponding antineutrinos.[4] For the lepton-number violating $0\nu\beta\beta$ to happen, the neutrino has to be of Majorana nature, i.e. its own antiparticle. The two neutrinos are virtual particles, which annihilate immediately:

$$(Z,A) \rightarrow (Z+2, A) + 2\mathrm{e}^- + 2\bar{\nu}_\mathrm{e} \qquad (2\nu\beta\beta) \; , \tag{2.14}$$

$$(Z,A) \rightarrow (Z+2, A) + 2\mathrm{e}^- \qquad (0\nu\beta\beta) \; . \tag{2.15}$$

As a two-body decay, the summed energy of the electrons thus equals the Q-value of the decay. This would result in a mono-energetic peak at the kinematic endpoint of the corresponding continuous $2\nu\beta\beta$ spectrum, which has not been observed yet. $0\nu\beta\beta$ experiments therefore set lower limits on the half-life of the decay [Zub12]

$$\left(T_{1/2}^{0\nu}\right)^{-1} = G^{0\nu}\,(Q,Z)\,|M_\mathrm{nuc}|^2 \left(\frac{\langle m_{\beta\beta}\rangle}{m_\mathrm{e}}\right)^2 \; , \tag{2.16}$$

where $G^{0\nu}$ is the phase space factor including couplings and M_nuc is the nuclear matrix element. These experiments are thus sensitive to the coherent superposition of neutrino mass eigenstates

$$m_{\beta\beta} = \left| \sum_{i=1}^{3} U_{ei} m_i \right| \; . \tag{2.17}$$

Various double β-decaying elements are investigated, e.g. ^{76}Ge, ^{130}Te or ^{136}Xe. The Germanium Detector Array (GERDA) experiment measured a half-life $T_{1/2}^{0\nu} > 0.9 \cdot 10^{26}\,\mathrm{yr}$, resulting in the current world-leading upper limits $m_{\beta\beta} < 0.07-0.16\,\mathrm{eV}$ [Ago19]. A drawback of this determination of the neutrino mass is that the result is always given in terms of a limit range. This is because the derivation of $m_{\beta\beta}$ depends on the underlying calculation of the nuclear matrix element M_nuc in equation (2.16), which has large theoretical uncertainties. Furthermore, due to complex phases in U_{ei}, $m_{\beta\beta}$ can become very small or even cancel out in the case of NO. An observation would not be possible, even if the process existed.

Direct measurement Laboratory-based experiments, which provide a model-independent determination of the neutrino mass, are precision measurements of the kinematics of β-decays or electron capture (EC). Of specific interest for this

---

[4] Here, double β^--decay is described. Double β^+-decay including positrons does exist as well.

thesis is the β^--decay of tritium (^{3}H). One atom of a tritium molecule (T_2) decays into helium, an electron, and an electron antineutrino:

$$^3\mathrm{H} \rightarrow {}^3\mathrm{He}^+ + \mathrm{e}^- + \bar{\nu}_\mathrm{e} + 18.6\,\mathrm{keV} \ . \tag{2.18}$$

Tritium is well suited for neutrino mass measurements because of its low Q-value of 18.6 keV and short half-life $T_{1/2} = 12.3\,\mathrm{yr}$ [Ott08]. The low Q-value results in a large fraction of events falling into the region of interest (ROI) close to the spectral endpoint, while the short half-life provides a high source luminosity. Furthermore, the simple electronic shell and molecular configuration facilitates theoretical calculations of the decay process. The observable in tritium β-decay is the squared effective electron antineutrino mass

$$m_\beta^2 = m^2\left(\bar{\nu}_e\right) = \sum_{i=1}^{3} \left|U_{ei}\right|^2 m_i^2 \ , \tag{2.19}$$

which is the incoherent sum of neutrino mass eigenstates, where no cancellations are possible. Due to the non-zero effective rest mass of the electron antineutrino, the endpoint of the continuous electron energy spectrum is shifted towards lower energies compared to the theoretical value. More detailed information on this type of measurement is given in section 3.1 on the KATRIN experiment, which holds the world-leading limit on the neutrino mass from a direct measurement $m_\beta < 1.1\,\mathrm{eV}$ [Ake19].

2.4 Neutrinos beyond the Standard Model

As discussed in section 2.3, the existence of a right-handed neutrino N_R would provide a convenient way to give mass to the active neutrinos. However, only left-handed neutrinos are observed in nature. If existent, the right-handed flavor eigenstate would be “sterile” with regard to the weak interaction. Many models introducing one or more sterile neutrinos have been developed [Aba12]. The simplest extension of the SM is the so-called “3+1” scenario with one additional sterile neutrino [Adh17]. In this case, alongside the sterile neutrino flavor eigenstate N, a corresponding sterile neutrino mass eigenstate ν_4 is introduced, resulting in a 4×4 PMNS matrix

$$U_\mathrm{PMNS} = \begin{pmatrix} U_{\mathrm{e}1} & U_{\mathrm{e}2} & U_{\mathrm{e}3} & U_{\mathrm{e}4} \\ U_{\mu 1} & U_{\mu 2} & U_{\mu 3} & U_{\mu 4} \\ U_{\tau 1} & U_{\tau 2} & U_{\tau 3} & U_{\tau 4} \\ U_{\mathrm{s}1} & U_{\mathrm{s}2} & U_{\mathrm{s}3} & U_{\mathrm{s}4} \end{pmatrix} \ . \tag{2.20}$$

The mass eigenstate ν_4 would not be completely sterile, as it is a quantum mechanical superposition of the sterile and active flavors. This makes it experimentally accessible, for instance by observing a distortion in the continuous tritium β-spectrum (see section 3.2.1). A direct detection of a sterile neutrino signature would imply the necessity for an extension of the SM. The mass range of interest covers several orders of magnitude, as the sterile mass is not constrained from particle physics.[5] In the following, three mass scales are presented, each of which has its own scientific motivation.

eV-scale Sterile neutrinos in the eV-mass range have been proposed to solve anomalies, which appeared in short-baseline neutrino oscillation experiments since the early 1990s. The first hint came from the Liquid Scintillator Neutrino Detector (LSND) experiment, where a 3.8 σ excess of $\bar{\nu}_e$ in a $\bar{\nu}_\mu$-beam was found [Agu01]. It could be explained by a light sterile neutrino. The Karlsruhe Rutherford Medium Energy Neutrino (KARMEN) experiment, however, which operated at the same time, did not observe any excess [Eit01]. The LSND result, later reproduced by the Mini Booster Neutrino Experiment (MiniBooNE) [Agu18], puzzles the community to date.

Another anomaly appeared in the Gallium Experiment (GALLEX) [Ham98] and the Soviet–American Gallium Experiment (SAGE) [Abd96], both of which were radio-chemical experiments to measure the solar neutrino flux using IBD in ^{71}Ga. The experiments were calibrated using strong ^{51}Cr and ^{37}Ar ν_e-sources. In the calibration phases, both GALLEX and SAGE measured a decreased rate with a combined significance of 2.8 σ, which again could be explained by a light sterile neutrino.

In 2011, neutrino spectra from nuclear fission reactors for ^{235}U, ^{238}U, ^{239}Pu, and ^{241}Pu were re-evaluated. Together with a new reactor neutrino flux evaluation, the analysis yielded a deficit in the previously measured $\bar{\nu}_e$-rates at 2.5 σ [Men11]. If this deficit is not due to some unknown in reactor physics processes, the existence of an eV-scale sterile neutrino would also resolve this anomaly.

keV-scale A sterile neutrino in the keV-mass range is a candidate for DM. DM was postulated for instance to explain discrepancies in the observed and predicted velocities of the movement of visible matter in a spiral galaxy [Kap22]. Visible matter is of baryonic nature, while DM is a yet unknown form of matter. It would only be affected by gravity or at most also very weak interactions. Today we know that 84.2 % of all matter in our universe consists of DM [Tan18]. A variety of possible DM

---

[5] The term “sterile mass” is casually used for the mass of the fourth neutrino mass eigenstate ν_4.

candidates has been proposed in different theories, e.g. the weakly interacting massive particle (WIMP), axions or primordial black holes. They are usually classified into three types depending on their velocities at the time of their creation [Bau19]: hot dark matter (HDM), cold dark matter (CDM), and the intermediate warm dark matter (WDM). Depending on their creation mechanism, sterile neutrinos in the keV-mass range would belong to the class of either CDM or WDM.

A HDM-only scenario is disfavored, because its effect on structure formation is in contradiction with cosmological observations. Density fluctuations on small scales in the early universe would have been suppressed, as HDM has a large free streaming length [Bau19]. The light neutrino states of the SM contribute to HDM but their masses are too small to explain the total amount of observed DM. Over decades, the most favored type has been CDM, as also small-scale structures like galaxies are reproduced in N-body simulations quite accurately. However, the existence of WDM yields some additional advantages, especially in the context of even smaller structures like dwarf galaxies. Simulations of CDM-only scenarios are not able to exactly reproduce the abundance, properties, and kinematics of dwarf galaxies [Lov12]. Introducing WDM not only affects the formation of dwarf galaxies, but would also explain their inner density profile. Comparing simulations of the Lyman-α forest with spectra from the Sloan Digital Sky Survey (SDSS), limits on the mass $m_4 > 24.4\,\mathrm{keV}$ and mixing amplitude $|U_{\mathrm{e}4}|^2 < 10^{-8} - 10^{-6}$ of sterile neutrino dark matter can be derived [Bau16, Boy19].

A hint for the existence of sterile neutrino DM comes from astrophysical measurements. The x-ray multi-mirror (XMM)-Newton observatory found a mono-energetic x-ray line at 3.5 keV in data from the observation of several galaxy clusters [Bul14, Boy14]. The decay of a hypothetical 7 keV sterile neutrino $\mathrm{N} \rightarrow \nu\gamma$ results in a line at $E_\gamma = \frac{m_\mathrm{N}}{2}$ and would thus explain the observation. However, the result is controversial, as the line could also originate from improper knowledge of all astrophysical lines or considered systematics [Jel15]. Limits on the sterile neutrino mixing amplitude on the order of $|U_{\mathrm{e}4}|^2 < 10^{-8} - 10^{-6}$ are derived from the same observations [Wat12, Boy14].

In 1980, R. Shrock proposed sterile neutrino searches in laboratory nuclear decay experiments [Shr80]. Since then, a wide variety of isotopes (e.g. $^3\mathrm{H}$, $^{35}\mathrm{S}$ or $^{63}\mathrm{Ni}$) and detection techniques (e.g. electric and magnetic spectrometers or implanted Si(Li) detectors) were utilized for the search [Dra15]. In 1985, a distortion in a tritium spectrum, consistent with a 17.1 keV sterile neutrino and mixing probability of 3 %, was observed by J. Simpson [Sim85]. This observation was later ruled out by many other experiments at a high confidence level and the signal was explained by an improper treatment of electron energy losses in the implanted source [Bow95]. An overview of current limits on the sterile neutrino mass and mixing amplitude from

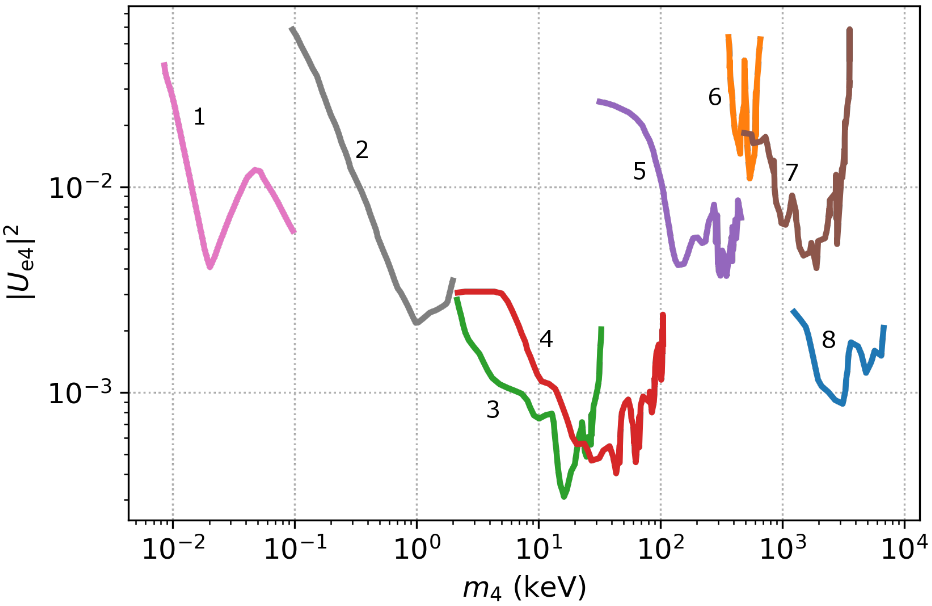

Figure 2.1: **Current sterile neutrino limits from laboratory-based experiments.** These limits are much weaker than limits from cosmological or astrophysical observations, which reach down to $|U_{e4}|^2 < 10^{-8}$. References are: 1 — [Bel14]; 2 — [Abd17]; 3 — [Hol99]; 4 — [Hol00]; 5 — [Sch83]; 6 — [Hin98]; 7 — [Tri03]; 8 — [Deu90]. Adapted from [Abd15, Abd17].

direct measurements is shown in figure 2.1. These limits are orders of magnitudes weaker than the ones from cosmological or astrophysical observations. However, they do not depend on any underlying cosmological or astrophysical models. In section 3.2 will be presented, how the TRISTAN project aims at improving these limits into the parameter space of cosmological interest.

GeV-scale Sterile neutrinos with masses in the GeV-range are predicted in the frame of a neutrino minimal Standard Model (νMSM) to explain the lightness of the active neutrinos through the seesaw mechanism [Asa05]. Furthermore, the existence of such heavy sterile neutrinos would explain the baryon asymmetry in the universe via leptogenesis. To be in agreement with the observed abundances of light elements in the universe, these neutrinos would have decayed before the Big Bang nucleosynthesis (BBN) and could today be produced and searched for only in accelerator experiments [Bez08].

3 The KATRIN experiment & the TRISTAN project

The KATRIN experiment is conducted by the Karlsruhe Institute of Technology (KIT) and is partly hosted by the Tritium Laboratory Karlsruhe (TLK). It investigates the spectral shape around the energetic endpoint of tritium β-decay to determine or constrain the effective mass of the electron antineutrino $\bar{\nu}_e$. It is designed to reach its final sensitivity of 200 meV (90 % C.L.) after an effective data taking time of three years [Ang05]. After the neutrino mass measurement phase, there is a very promising potential to utilize KATRIN to search for the signature of a keV-scale sterile neutrino [Mer15a]. To this end, the experiment has to be upgraded with a novel detector. This endeavor is called the TRISTAN project.

This chapter is divided into two parts, the first of which is a description of KATRIN. It starts with an introduction to the principles of neutrino mass measurements in tritium decay in section 3.1.1. The technical realization of the experiment is described in section 3.1.2.

The second part introduces the TRISTAN project. The imprint of a sterile neutrino on the tritium β-spectrum is illustrated in section 3.2.1, where also the expected sensitivity for an exclusion is presented. The related requirements on the novel detector system are discussed in section 3.2.2. In section 3.2.3, the current status of the TRISTAN project is presented, also specifying the objectives of this work. Section 3.2.4 summarizes other possible applications for the TRISTAN detector.

3.1 The KATRIN experiment

The KATRIN experiment is the next-generation neutrino mass experiment. It is the technological successor of the experiments in Mainz and Troitsk, both of which were able to set an upper limit to the effective electron antineutrino mass (see equation (2.19)) of around $m_\beta < 2\,\mathrm{eV}$ (95 % C.L.) [Ase11, Kra05]. KATRIN aims at improving this limit by one order of magnitude down to 200 meV (90 % C.L.) [Ang05]. If the neutrino had a mass $m_\beta > 350\,\mathrm{meV}$, a $5\,\sigma$ discovery would be possible.

KATRIN started operation with calibration sources in 2016 [Are18] and measurements with tritium in 2018 [Ake20]. In 2019, based on the first neutrino mass measurement campaign, the collaboration was able to improve the previous neutrino mass limit down to $m_\beta < 1.1\,\mathrm{eV}$ (90 % C.L.) [Ake19].

The KATRIN design report [Ang05] is used as general reference for this part of the chapter, if not explicitly stated otherwise.

3.1.1 Measurement principle

KATRIN determines the neutrino mass by precisely investigating the kinematics of tritium decay (see equation (2.18)). According to Fermi's theory [Fer34], the differential β-decay rate can be expressed as

$$\frac{\mathrm{d}\Gamma(E;m_\beta)}{\mathrm{d}E} \propto C \cdot F(Z,E) \cdot (E + m_\mathrm{e}) \cdot p \cdot (E_0 - E) \cdot \sqrt{(E_0 - E)^2 - m_\beta^2}\ , \tag{3.1}$$

where $F(Z,E)$ is the Fermi function [Sim81] and m_β is the effective electron antineutrino mass in equation (2.19). Furthermore, there is the kinetic energy E, momentum p, and mass m_e of the electron. The spectral endpoint energy E_0 is the maximal electron kinetic energy in case $m_\beta = 0$. The constant

$$C = \frac{G_f^2}{2\pi^3 \hbar^7 c^5} \cdot \cos^2\theta_c \cdot |M_\mathrm{nuc}|^2 \tag{3.2}$$

is composed of the Fermi constant G_f, the Cabibbo angle θ_c and the nuclear matrix element M_nuc.

The imprint of the neutrino mass on the tritium spectrum is shown in figure 3.1. The effects of a non-zero neutrino mass becomes large at the spectral endpoint, where the term $(E_0 - E)$ in equation (3.1) vanishes. This results in a reduction of the maximal electron energy, shifting the endpoint towards lower energies, and a local spectral distortion. It should also be noted that actually every mass eigenstate leads to its own shift and distortion. However, the mass differences are too small (see table 2.1) to be resolved with a KATRIN-like experiment. This gives rise to the "effective electron antineutrino mass" m_β, which is the incoherent sum of all neutrino mass eigenstates. Even for resolving this shift, an energy resolution in the order of 1 eV is required, which cannot be achieved by conventional semiconductor particle detectors. Thus, the Magnetic Adiabatic Collimation combined with an Electrostatic filter (MAC-E) principle is applied.

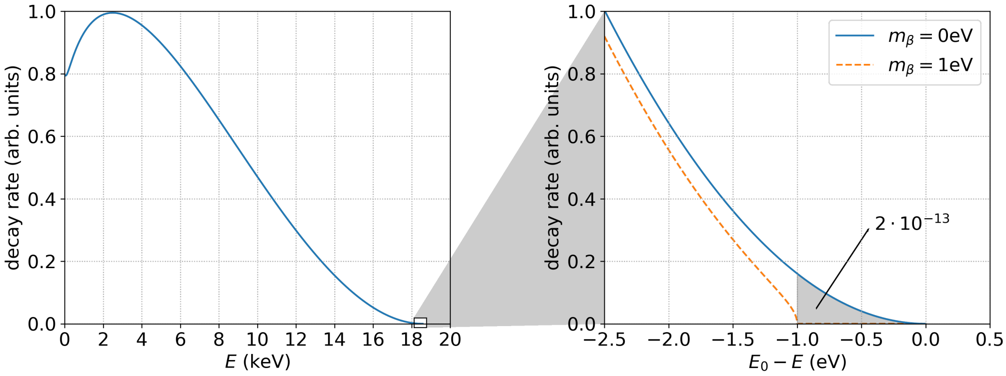

Figure 3.1: **Full tritium β-spectrum and endpoint region.** *Left:* The entire tritium β-spectrum with the endpoint $E_0 = 18.6\,\mathrm{keV}$. *Right:* Zoom at the spectral endpoint region with and without neutrino mass. The straight blue line represents the case, in which $m_\beta = 0\,\mathrm{eV}$. The dashed orange line illustrates the spectral change in case $m_\beta = 1\,\mathrm{eV}$. Into the grey shaded area falls a fraction $2 \cdot 10^{-13}$ of the total decay rate.

The MAC-E principle was generally proposed by P. Kruit in 1983 [Kru83]. Its application for a neutrino mass measurement was proposed by V. Lobeshev in 1985 [Lob85]. Already KATRIN's technological predecessors, the Mainz and Troitsk neutrino experiments, made use of this technology. A scheme of a MAC-E type spectrometer is shown in figure 3.2.

A MAC-E spectrometer acts as a high-pass filter for electrons carrying an energy larger than a certain retarding energy eU, which is defined by the potential U on the spectrometer electrodes. By applying a magnetic field, electrons are adiabatically (i.e. a completely reversible motion) guided through the spectrometer, due to the Lorentz force. Thus, a large fraction of electrons starting from the isotropic decay into the 2π-hemisphere of the spectrometer will be analyzed. This drastically increases the signal rate compared to other technologies, e.g. magnetic spectrometers [Lob85]. However, the spectrometer is only sensitive to the longitudinal momentum component $p_{\|}$ of the electrons' motion, i.e. to the energy component parallel to the magnetic field lines. To overcome this, the magnetic field inside the MAC-E spectrometer is strong at both ends and weak in the center. As the electrons' orbital magnetic moment

$$\mu \approx \frac{E_\perp}{B} = \text{const.} \tag{3.3}$$

is conserved in an adiabatic motion, their transversal momentum component $p_\perp$ is transformed into the longitudinal one, when traveling from the strong into the weak field. The area of the weakest magnetic field B_{min} and highest retarding energy eU is called the analysis plane, i.e. where the electrons' energy is filtered. At this point,

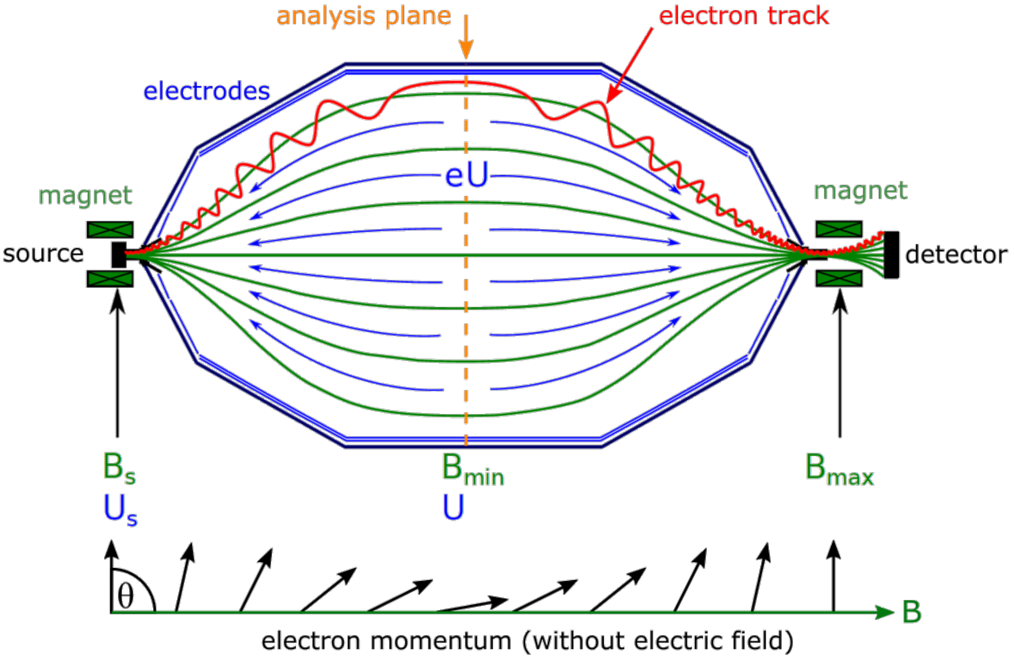

Figure 3.2: **Scheme of a MAC-E type spectrometer.** Superconducting magnets (green) create a magnetic field, which is strong both at the entrance and at the exit of the vacuum tank (black). Electrons (red) coming from the source (on the left) move towards the detector (on the right), spiraling around the magnetic field lines. The black arrows (at the bottom) illustrate the transformation of the electrons' transversal momentum component into the longitudinal one, when traveling from a strong into a weak magnetic field. Additionally, the spectrometer electrodes (blue) form an electric field, which is strongest at the position of the analysis plane (orange). The negatively charged electrons feel a retarding energy eU, so that only electrons with a kinetic energy $E_{\text{kin}} > eU$ are transmitted to the detector. Adapted from [Wan13].

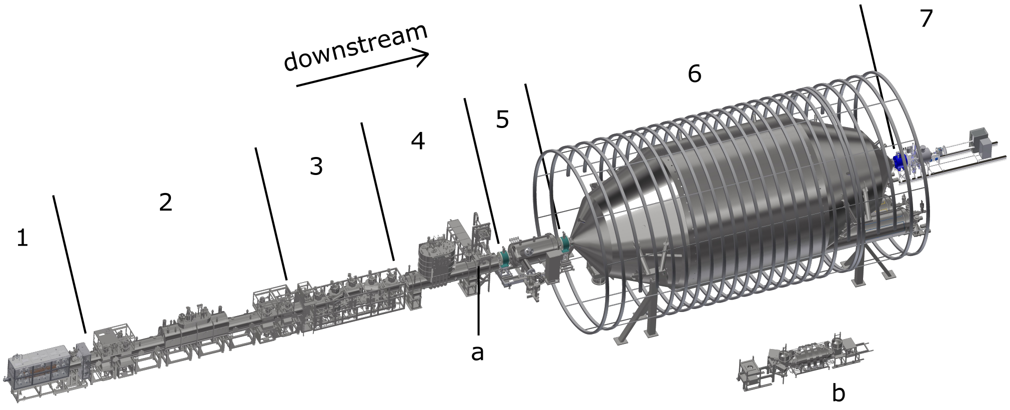

Figure 3.3: **Scheme of the KATRIN beamline.** Components of the beamline are numbered (1 — rear section; 2 — WGTS; 3 — DPS; 4 — CPS; 5 — pre-spectrometer; 6 — main spectrometer; 7: — detector section). Monitor devices are labeled (a — FBM; b — monitor spectrometer). The STS (components 1 – 4) is hosted inside TLK, while the SDS (components 5 – 7) is placed in a separate building. The flight direction of the signal electrons is indicated with "downstream".

a strongly decreased transversal momentum component remains, determining the energy resolution of the spectrometer

$$\Delta E_\perp = E \cdot \frac{B_\mathrm{min}}{B_\mathrm{max}} \; . \tag{3.4}$$

In the case of KATRIN, this results in $\Delta E_\perp = 0.93\,\mathrm{eV}$ at $E = 18.6\,\mathrm{keV}$. By varying the retarding energy eU, an integral tritium spectrum

$$\Gamma(eU; m_\upbeta) = \int_{eU}^{E_0} \frac{\mathrm{d}\Gamma(E; m_\upbeta)}{\mathrm{d}E}\,\mathrm{d}E \tag{3.5}$$

is measured. To do so, the count rate at each retarding energy is measured by a silicon detector, which is positioned at the exit of the spectrometer. A more detailed examination of the differences between integral and differential measurement mode is presented in section 5.1.2.

3.1.2 Experimental setup

A scheme of KATRIN's entire beamline is displayed in figure 3.3. The 70 m long setup is divided into the tritium-containing source and transport section (STS), and the spectrometer and detector system (SDS), which is tritium-free. Its individual parts are described in the following.

Tritium source Besides the MAC-E spectrometer, the WGTS is the second key element of KATRIN. Tritium gas is injected in the middle and streams towards both sides of the tube, while some of the tritium atoms decay. The tube is windowless, as confining the tritium gas behind barriers would lead to a systematic energy loss of the β-electrons. A gaseous source has advantages over a solid one, e.g. spacial homogeneity, simpler (back-)scattering properties, and no charging effects [Lob99]. It is designed to provide an extremely high (10^{11} Bq) and stable (±0.1 %) decay rate. A high activity is required, because the fraction of electrons in the energy ROI is very small (see figure 3.1). A high stability is required to decrease systematic uncertainties in an integral measurement. This is achieved with a closed tritium loop, featuring a controlled injection system. Also the temperature of the 10 m long tube needs to be stabilized at 30 K at the 0.1 % level. The isotopic purity of the tritium gas is $\epsilon_T > 95\,\%$ and continuously monitored with a Laser Raman (LARA) system [Sch13].

Transport section As a consequence of the windowless source tube, the tritium gas has to be prevented with other means from entering the spectrometer section, where any residual tritium would lead to undesired background. Therefore, pumps are installed at both ends of the WGTS. In the transport section, the tritium flow is further reduced by 14 orders of magnitude, while the electrons are carrying towards the SDS. Superconducting magnets maintain a magnetic field not only throughout the transport section but throughout the entire setup. The transport section is divided into two parts: differential pumping section (DPS) and cryogenic pumping section (CPS). In the DPS, mechanical pumping is applied, using turbo molecular pumps (TMPs). The pumped tritium gas is recovered and recycled in a loop system [Pri15]. The walls of the CPS are covered with a 3 K argon frost layer, which acts as a cold trap. To maintain the efficiency, it is regularly regenerated after around 60 days of operation. Both sections are arranged in chicanes to avoid a line of sight for tritium molecules into the SDS.

Spectrometers Two MAC-E-type spectrometers are placed in the KATRIN beamline. A pre-spectrometer creates a first potential barrier to reduce the amount of electrons entering the main spectrometer, lowering the background. The main spectrometer is a tank with a volume of 1240 m^3, in which a vacuum of 10^{-11} mbar is maintained. It has a length of 23.2 m to ensure adiabatic electron motion. Its maximal diameter is 9.8 m to fit the large magnetic flux tube at the position of the analysis plane, where the magnetic field strength is $B_{\mathrm{ana}} = 0.3\,\mathrm{mT}$. The inner surface of the spectrometer tank is covered with wire electrodes to fine-shape the electric field. The tank itself is put at a slightly less negative potential to reduce background from cosmic muons and ambient or intrinsic radioactivity. The pinch magnet at the end of the tank defines the angular acceptance, i.e. the maximal polar angle, under which electrons can start in the source to be seen at the detector. The combination of the pinch magnetic field $B_{\mathrm{max}} = 6\,\mathrm{T}$ together with the source magnetic field $B_{\mathrm{s}} = 3.6\,\mathrm{T}$ results in a polar acceptance angle

$$\theta_{\mathrm{max}} = \arcsin\left(\sqrt{\frac{B_{\mathrm{s}}}{B_{\mathrm{max}}}}\right) \approx 51^{\circ}\ , \tag{3.6}$$

with $\theta \in [0,\pi]$. A system of magnetic air coils around the main spectrometer compensates for the earth magnetic field inside the tank and allows for a precise shaping of the magnetic field.

Detector system The detector is a positive intrinsic negative (PIN) diode on a monolithic silicon wafer. It is divided into 148 pixels, having the same surface area each to equally distribute the count rate. They are arranged in a ring-wise structure to map the radial dependence of the analysis plane electric and magnetic fields. The energy resolution is 1.5 keV (FWHM) at 18.6 keV and the maximal count rate reaches up to tens of kcps [Ams15]. The detector is only used to count incoming electrons in a certain energy ROI as the measured differential spectrum does not carry any information on the neutrino mass. The number of counted electrons N_{e^-} in the energy ROI divided by the acquisition time t_{acq} gives the count rate at the respective retarding energy

$$\Gamma\left(eU\right) = \frac{\left(N_{\mathrm{e}^-}\right)_{\mathrm{ROI}}}{t_{\mathrm{acq}}}\ . \tag{3.7}$$

Rear section The rear section concludes the experiment at the other end of the setup. The rear wall, a gold covered plate, defines the electric ground potential U_{s} relative to the spectrometer high voltage U. Gold is the material of choice, as it has a lower backscattering probability for electrons than stainless steel. With that, systematic uncertainties are reduced, as almost all electrons that are reflected in the spectrometers eventually hit the rear wall. The rear section also contains an electron gun for calibration measurements, positioned behind the gold plate, as well as other diagnostic tools.

Monitoring devices Besides many monitoring devices in and around the KATRIN setup, there are two of specific interest for the TRISTAN project, as they can serve as test facilities. They are highlighted in the following.

The forward beam monitor (FBM) is situated between STS and SDS to monitor the tritium source activity over short time scales [Ell17]. It is a silicon detector, which can be moved in and out of the electron flux tube. As the electron rate at this point has not yet been reduced by one of the spectrometers, the FBM has to handle very high count rates.

The monitor spectrometer is the repurposed MAC-E spectrometer of the Mainz neutrino experiment. It scans over the spectrum of a radioactive $^{83\mathrm{m}}$Kr source. Its K-32 conversion electron line at 17.83 keV has an energy close to the tritium endpoint. Being connected to the high voltage of the main spectrometer electrodes with only a small offset, the long time voltage stability of the latter is monitored [Sle15].

3.2 The TRISTAN project

TRISTAN is a project within the KATRIN collaboration, which explores the experiment's ability to search for a keV-scale sterile neutrino signature. The idea is to utilize KATRIN's strong tritium source to reach sensitivities to a sterile neutrino admixture at the ppm-level by extending the experimental setup with a novel detector and read-out system.

3.2.1 Sterile neutrino signature

As discussed in section 3.1.1, every neutrino mass state leads to a distortion of the β-spectrum. In contrast to the active neutrino masses, however, the mass difference for a keV-scale state is not irresolvable. The sterile neutrino would manifest itself as a kink and a broad distortion in the continuous electron energy spectrum of a β-decay. Figure 3.4 illustrates this effect on the tritium spectrum. The total differential β-spectrum can hence be written as a superposition of the active states with the sterile admixture in a separate term [Adh17]:

$$\frac{\mathrm{d}\Gamma}{\mathrm{d}E} = \underbrace{\cos^2(\theta_\mathrm{s})\frac{\mathrm{d}\Gamma(m_\beta)}{\mathrm{d}E}}_{\text{active}} + \underbrace{\sin^2(\theta_\mathrm{s})\frac{\mathrm{d}\Gamma(m_4)}{\mathrm{d}E}}_{\text{sterile}} \; . \tag{3.8}$$

In this way, only two additional parameters are introduced: m_4 and $\sin^2(\theta_\mathrm{s})$. While the position of the kink depends on the mass of the sterile neutrino m_4, the signal strength of the broad distortion is governed by the active-sterile mixing amplitude $\sin^2(\theta_\mathrm{s}) \approx |U_{\mathrm{e}4}|^2$ (see equation (2.20)). These parameters open up the parameter space for the sterile neutrino search (see figure 2.1).

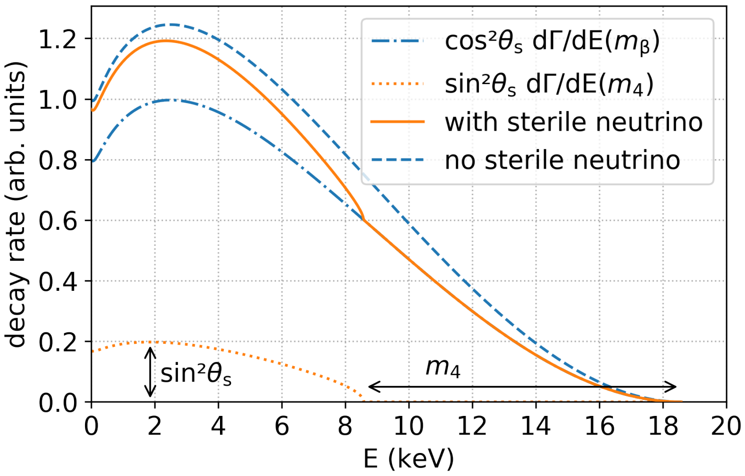

Figure 3.4: **Tritium β-decay spectrum with sterile neutrino admixture.** The spectrum is dominated by the known light neutrino mass states m_β. The admixture of a sterile neutrino is generated for this plot with a mass $m_4 = 10\,\text{keV}$ and an exaggerated large mixing amplitude $\sin^2(\theta_s) = 0.2$.

Using KATRIN for a sterile neutrino search is especially interesting for two reasons: On the one hand, sterile neutrino masses up to the tritium endpoint at 18.6 keV can be explored. On the other hand, the source luminosity of the KATRIN experiment is high enough to achieve unprecedented laboratory limits on the sterile-active mixing angle within a reasonable amount of time. To estimate which part of the sterile neutrino parameter space can be tested, sensitivity studies have been performed for two measurement scenarios:

Phase-0 before the neutrino mass program over several days of measurement time in integral mode with a reduced source activity,

Phase-1 after the neutrino mass program over three years of measurement time in differential mode with full source activity.[1]

Assuming three years of measurement time, KATRIN would be able to exclude the existence of a sterile neutrino down to $|U_{e4}|^2 < 10^{-6}$ in the most sensitive mass region at around 12 keV [Mer15a]. This is a huge improvement with respect to current limits from direct measurements, as illustrated in figure 3.5.

However, as the mass of the sterile neutrino is unknown, its signature could appear anywhere in the spectrum. Thus, the entire spectrum has to be scanned. Measuring with full source activity at low retarding energies leads to an increased signal rate at the detector by several orders of magnitude compared to standard KATRIN

---

[1] See section 5.1.2 for a more detailed examination of the two measurement modes.

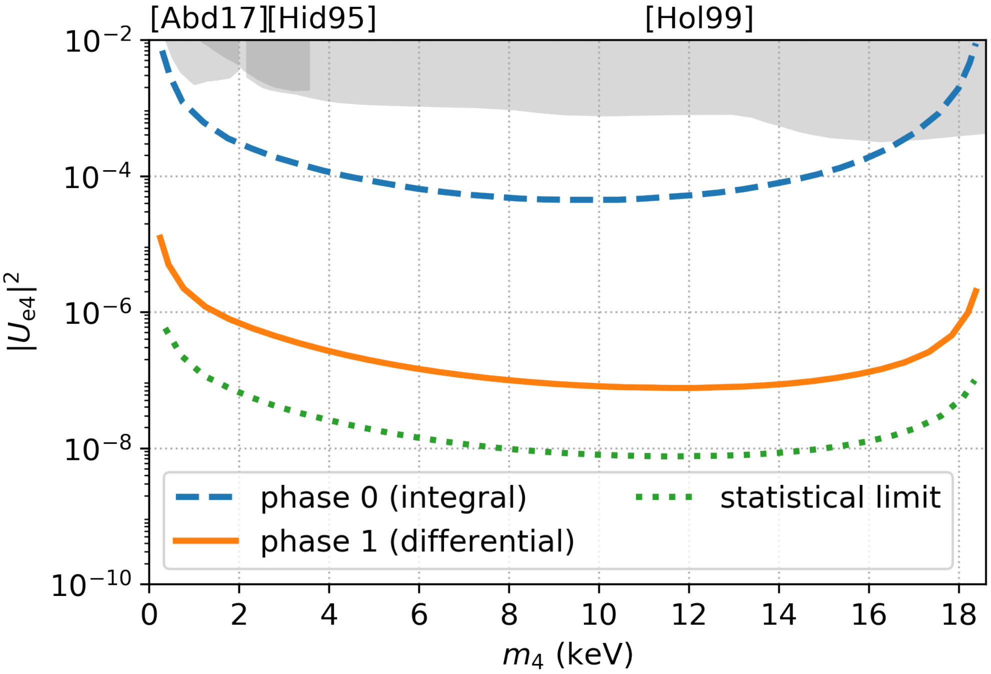

Figure 3.5: **Statistical sensitivity for different stages of TRISTAN.** *Phase-0 (dashed blue)*: This limit could be achieved within seven days of measurement in integral mode at a reduced signal rate of 10^6 cps. This rate reduction is necessary to realize the measurement with the standard KATRIN detector and read-out system. *Phase-1 (solid orange)*: This limit could be achieved within three years of measurement in differential mode at a slightly reduced signal rate of 10^8 cps. An advanced detector system is required to handle these high rates. *Statistical limit (dotted green)*: The statistical limit after three years of measurement with the nominal source activity is given as a reference. Current laboratory-based limits [Hid95, Hol99, Abd17] are depicted by the shaded area. Adapted from [Mer19].

operation. The current KATRIN detector system is not capable of handling such high count rates. Incoming events would constantly pile up and distort the spectrum in a way, that the goal sensitivity to a sterile neutrino admixture could not be reached. Hence, the KATRIN setup has to be upgraded by a new detector and read-out system. The development of this system is the main task of the TRISTAN project.

3.2.2 Detector requirements

To measure a keV-scale sterile neutrino signature at the ppm-level, the corresponding systematic uncertainties have to be on the same order of magnitude. From this fact, a complex optimization problem for the detector design arises, as many variables are interlinked. Resulting requirements on the TRISTAN detector system are discussed in the following. Previously performed investigations [Kor16] and an updated summary [Mer19] serve as general references for this section. Technical realization and functionality of the current detector system (e.g. ASIC, DPP, etc.) are further explained in sections 3.2.3 and 4.1. All mentioned detector effects (e.g. backscattering, charge sharing, etc.) are explained in more detail in section 4.3.1.

Detector geometry From a statistical point of view, the desired ppm-level sensitivity is reached after three years of measurement with the nominal source activity reduced by a factor of 100. This reduction is even necessary to mitigate systematic uncertainty induced by scatterings in the source, which has a strong impact at lower electron energies. As a result, the detector has to deal with a signal rate of about 10^8 cps. To reduce the rate per channel to a manageable level, the idea is to distribute the rate over a large number of pixels $N_\mathrm{px} > 1000$ to arrive at a signal rate smaller than 10^5 cps per channel [Mer19]. The pixels have to be designed and arranged to provide large area coverage, i.e. without dead area between pixels. The choice of a hexagonal pixel shape maintains high statistics and enables vetoing undesired events.

Large pixels with radii $r_\mathrm{px} > 1\,\mathrm{mm}$ are favored, as the probability that electrons hit a boarder between two pixels (i.e. the charge sharing probability) decreases with increasing pixel size. The size of the individual pixels A_px is interlinked with the overall detector size A_det. For a fixed number of pixels

$$N_\mathrm{px} = \mathrm{const.} = \frac{A_\mathrm{px}}{A_\mathrm{det}} = \frac{r^2_\mathrm{px}}{r^2_\mathrm{det}} \ , \tag{3.9}$$

approximating the pixel area with a circle. Here, r_{det} is the detector radius. The detector has to be large enough to cover the entire electron flux

$$\Phi = \text{const.} = A_{\mathrm{det}} \cdot B_{\mathrm{det}} \ . \tag{3.10}$$

In this context, the magnetic field at the position of the detector B_{det} plays an important role: The lower B_{det} is, the larger A_{det} has to be. To minimize the backscattering probability, the magnetic field has to be reasonably low to decrease the incident angle of electrons hitting the detector:

$$\theta_{\mathrm{det}} = \arcsin\left(\sqrt{\frac{B_{\mathrm{det}}}{B_{\mathrm{max}}}}\right) \overset{!}{<} 20° \ . \tag{3.11}$$

A lower detector magnetic field also increases the probability of backscattered electrons to be back-reflected in a higher magnetic field somewhere else in the setup. This decreases the number of undetected electrons, which otherwise would hit the rear wall and get lost. Thus, from this point of view, a large detector is favored.

However, B_{det} also defines the gyroradius

$$r_{\mathrm{L}} = \frac{mv_{\perp}}{eB} \tag{3.12}$$

of the electrons' circular motion in the magnetic field. When an electron is backscattered from the detector and back-reflected in an electric or magnetic field, it shall arrive back at the same pixel of its first impact or an adjacent one, to be registered as backscattered event. For the relation between gyroradius and pixel radius, this implies [Kor16]:

$$\frac{r_{\mathrm{L}}}{r_{\mathrm{px}}} = \frac{mv_{\perp}}{e} \cdot \frac{\pi\sqrt{N_{\mathrm{px}}}}{\Phi} \cdot r_{\mathrm{det}} \overset{!}{<} 1 \ . \tag{3.13}$$

For a constant number of pixels N_{px}, this is the case for small detector radii. Thus, from this point of view, a small detector is favored. Another way of reducing the effect of backscattering (besides further advantages) is the concept of post-accelerating the electrons after having passed the MAC-E spectrometer. A post-acceleration electrode (PAE) is already available in the KATRIN setup as a part of the detector section. It accelerates the electrons up to additional $E_{\mathrm{PAE}} = 10\,\mathrm{keV}$ onto the detector to decrease incident angles and thus the effect of backscattering [Ake19], as well as to decrease energy losses in the detector entrance window. However, the absolute energy resolution decreases with increasing incident energy. For the TRISTAN project, a new post-acceleration energy $E_{\mathrm{PAE}} > 18.6\,\mathrm{keV}$ is envisioned to completely separate pile-up from the tritium spectrum [Des19].

Detector performance An energy resolution $\Delta E < 500\,\mathrm{eV}$ (FWHM) at $20\,\mathrm{keV}$ is necessary to resolve the local characteristic kink-like signature of a sterile neutrino [Mer15a]. With a worse energy resolution, the measurement would rely on the broad impact of a sterile neutrino on the spectral shape, which is much more prone to systematic uncertainty. Moreover, an energy resolution $\Delta E \approx 200\,\mathrm{eV}$ (FWHM) would allow for an analysis method applying a wavelet transform of the β-spectrum [Mer15b], disregarding the overall spectral shape and smooth corrections on it. High resolution for a fast read-out system entails small pixel anode capacitances in the amplification stage to reduce the noise level. A sophisticated SDD design fulfills these requirements on the energy resolution. The detector energy resolution is also improved by a thin entrance window. The entrance window is an only partly sensitive region on the detector surface, where deposited charges are not fully collected. This leads to a statistically distributed energy loss of the electrons. This process washes out the spectrum and results in a systematic uncertainty in the model. The thinner the entrance window, the smaller the uncertainty. Furthermore, a thin entrance window yields a low detection threshold E_{thres}, as very low energetic electrons do not even penetrate into the sensitive volume. A low detection threshold is crucial in order to efficiently veto charge shared events.

Read-out electronics High resolution also demands a low noise contribution from the signal amplifier, usually realized in the form of an application-specific integrated circuit (ASIC). Furthermore, the ASIC has to provide a short signal rise time $t_{\mathrm{rise}} < 50\,\mathrm{ns}$ to allow for pile-up detection and rejection at the high signal rates of the experiment. Another challenge is to keep crosstalk at a low level, given the high read-out channel density. A combination of preamplifier and second, AC-coupled amplification stage helps averaging out non-linearities of the analog-to-digital converter (ADC). Non-linearities in the ADC of the read-out system could mimic a sterile neutrino signature [Dol17]. Using many channels (i.e. many pixels) has the advantage, that the effect of non-linearities is being washed out [Dol17]. However, the number of channels cannot be increased arbitrarily, as cost and complexity of the system should be kept at a manageable level. Further averaging of these non-linearities is supported by digitizing the full signal waveform and filtering the signal amplitude subsequently. High ADC sampling rates $f_{\mathrm{s}} > 100\,\mathrm{MHz}$ and resolution $\sigma_{\mathrm{ADC}} = 14-16\,\mathrm{bit}$ are preferred to reduce the effect of pile-up. High performance is also required from the digital pulse processor (DPP) system, making use of a field-programmable gate array (FPGA). Given the high count rates, fast processing and histogramming of the signals is preferred to keep the data output at a manageable level. In addition, the DPP system has to provide the ability to tag “unclean” events

Table 3.1: **Requirements on the TRISTAN detector system.** The table is segmented into four blocks: 1st — geometrical aspects; 2nd — detector intrinsic features; 3rd — read-out system; 4th — ambient factors.

Feature	Symbol	Requirement
Number of pixels	N_{px}	~ 3500
Detector radius	r_{det}	$\sim 10\,\mathrm{cm}$
Pixel diameter	$2 \cdot r_{\mathrm{px}}$	$\sim 3\,\mathrm{mm}$
Energy resolution	ΔE	$100 - 200\,\mathrm{eV}$
Detection threshold	E_{thres}	$< 1\,\mathrm{keV}$
Dead layer thickness	d_{DL}	$< 100\,\mathrm{nm}$
Sampling rate	f_{s}	$> 100\,\mathrm{MHz}$
ADC resolution	σ_{ADC}	$14 - 16\,\mathrm{bit}$
Time synchronization	σ_t	$< 5\,\mathrm{ns}$
Magnetic field	B_{det}	$\sim 0.7\,\mathrm{T}$
Post acceleration voltage	E_{PAE}	$> 18.6\,\mathrm{keV}$

(backscattering, charge sharing) for offline correction or modeling. This requires a time synchronization $\sigma_t < 5\,\mathrm{ns}$ between read-out channels to correlate simultaneous energy depositions in neighboring pixels.

All resulting requirements on the TRISTAN detector system are summarized in table 3.1.

3.2.3 Status of the TRISTAN project

A staged approach was chosen to address challenges step by step. Several prototype generations are planned with growing numbers of pixels per SDD chip. Some values have already been fixed, others are subject to ongoing investigations. This section gives an overview of the current status of the TRISTAN project, highlighting the objectives of this work. For a more detailed description of SDD technology and the first TRISTAN prototype generation, see section 4.1.

Status before this thesis The first prototype chip generation was produced at the Halbleiterlabor of the Max Planck society (HLL) in 2016.[2] These chips were produced with several pixel sizes and entrance window technologies. As it had already

---

[2] Halbleiterlabor of the Max Planck Society, Otto-Hahn-Ring 6, 81739 München, Germany.

been known that this simpler pixel design will not be used for the final TRISTAN detector, this chip generation was named prototype-0 (P-0). Its purpose was to test the general performance of the SDD design. Several chips were equipped with either of the following front-end preamplifiers:

CUBE The single-channel CUBE ASIC [Bom11] was designed by XGLab in Milan.[3] The same company provided the waveform-digitizing DANTE DPP as a back-end data acquisition (DAQ) system. Both are specifically designed for high count rate spectroscopy applications with SDDs. The system provides an excellent energy resolution of 149 eV (FWHM) at 6 keV with shaping times of only 100 ns. In 2016, no time synchronization between pixels was implemented. A detailed description of CUBE and DANTE is given in section 4.1.2.

Idef-X The Imaging Detector Front-end (Idef-X) ASIC was designed by CEA Paris-Saclay.[4] The signals are processed by a peak-sensing back-end DAQ. Providing 32 channels, the system allows for a time synchronized read-out of all seven pixels. As it was originally developed for space applications and follows different requirements, it reaches a slightly worse energy resolution than the CUBE ASIC of 400 eV (FWHM) at 17 keV [Alt19].

Objectives of this work At the stage of development progress described above, three tasks were covered within this work:

- **Characterization of the general detector performance** In this work, P-0 was characterized with photons and electrons. A comparative study of prototypes with different entrance window technologies was performed. To this end, a model of the observed electron spectrum was developed. All this is subject of discussion in chapter 4.
- **First measurements in search for sterile neutrinos and the development of corresponding analysis strategies** In the frame of this thesis, a first sterile neutrino search with the P-0 detector was performed. To this end, the system was implemented at the Troitsk ν-mass experiment. The instrumentation of Troitsk ν-mass with a TRISTAN P-0 system, measurements in both differential and integral mode, the development of a respective sterile neutrino analysis chain, and the results thereof are presented in chapter 5.
- **Identification of crucial detector effects and systematic uncertainties** Novel detector technologies improve the general detector performance but cannot completely eliminate systematic effects. Studies of the detector response

---

[3] XGLab srl, Bruker Nano Analytics, Via Conte Rosso 23, 20134 Milano, Italy.

[4] Centre CEA de Saclay, 91191 Gif-sur-Yvette cedex, France.

and anticipated detector effects are required to identify systematic uncertainties. The impact of detector-related systematic uncertainty on the sensitivity for a sterile neutrino search, especially related to the entrance window thickness, was investigated and quantified. This is presented in chapter 6.

Ongoing investigations and development In parallel to the three tasks described above, the detector development for TRISTAN has continued and evolved in several other aspects.

A new method of decreasing the entrance window thickness is being investigated. The standard technology to create doped regions at the entrance window is via implantation using an ion beam. A disadvantage of this method is that during the process, dopant atoms diffuse deep into the detector material. This leads to a smeared out doping region and thus a large volume of incomplete charge collection. Epitaxy is a method, in which single layers of silicon are deposited onto the detector surface. By adding other elements to the applied silicon, doping intensity and profile are controlled. The new method is applied at HLL and first test measurements were performed and analyzed [Leb19].

A second prototype generation with state-of-the-art on-chip amplification and optimized pixel diameter of 3 mm is in production. This prototype generation is called prototype-1 (P-1). With an integrated junction gate field-effect transistor (JFET), the first amplification is already realized on the detector chip itself, which greatly reduced the effect of additional capacitances from long traces or bonds, i.e. it reduces the noise [Nic06]. These chips will be available in arrays of 1, 7, 12, 47, and 166 pixels.

To read out these SDD arrays, the 12-channel ETTORE ASIC has been developed by XGLab [Tri18]. ETTORE consists of two amplification stages, which are schematically displayed in figure 3.6. The first stage is a preamplifier, operated in pulsed reset mode. The second stage is an AC-coupled amplifier with a time constant of 15 µs. Preliminary measurements have shown an excellent performance: a rise time of less than 40 ns, no indications for crosstalk, and an energy resolution of 127 eV (FWHM) at 6 keV. ETTORE's performance will be studied in detail together with a 12-pixel P-1 chip at several test stands in Milan.

A next milestone for the TRISTAN project is the "first module" with 166 pixels. It is the first TRISTAN detector system in a three-dimensional geometry, similar to the final setup, i.e. the read-out electronics are completely hidden by the silicon chip, when seen from the direction of incoming electrons. A dummy with insensitive chip and without ASICs is shown in figure 3.7. The chip layout is rectangular to provide scalability and modularity. Furthermore, the routing of electronic traces

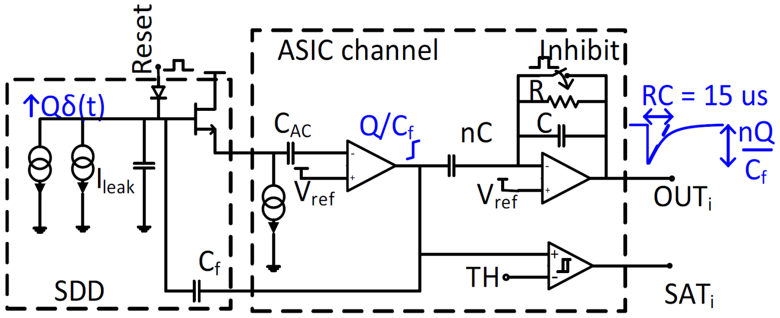

Figure 3.6: **Schematic diagram of one channel of the ETTORE ASIC.** The preamplifier builds a feedback loop with the JFET and the feedback capacitor, both integrated on the SDD chip. When the preamplifier's ramp-like output voltage reaches saturation, the anode charge is reset over a dedicated diode, also integrated on the chip. An inhibit signal is sent to the second stage during the reset. The second AC-coupled amplifier provides an additional gain of $n = 5 - 10$, and an exponential decay with a time constant of 15 µs. A digital comparator is used to transmit the reset signal both to the other channels of the ASIC and to the external electronics, giving the possibility of reseting all ASICs of the system simultaneously. Adapted from [Tri18].

becomes simpler, so that bond connections are required only on two sides of the chip. To each side, an electronics board hosting up to seven ETTORE ASICs will be attached. ETTORE is designed to read out groups of up to 12 pixels, resulting in a total of $12 \times 7 \times 2 = 168$ channels, in order to operate all pixels of one module.

The design of the DAQ system is still ongoing. A DAQ system applicable for the TRISTAN module is being developed at Politecnico di Milano for testing purposes:[5] Three 16-channel analog SFERA ASICs are connected via an FPGA for time synchronization on a 48-channel platform called KERBEROS [Kin20]. An aggregator board, called ATHENA, is being developed, which will combine the data streams of up to four KERBEROS, allowing for a simultaneous read-out of 192 pixels.

A detector array of this size requires a dedicated holding and cooling structure, which is currently developed and built at the Max Planck Institute for Physics (MPP) in Munich.[6] The structure will consist of a carbon-fiber reinforced silicon carbide (Cesic) [Krö02] holder, to which the detector chip will be glued, and a copper arm. Cesic is a ceramic material with the same thermal expansion coefficient as silicon,

---

[5] Dipartimento di Elettronica, Politecnico di Milano, Via Giuseppe Ponzio 34, 20133 Milano, Italy.

[6] Max-Planck-Institut für Physik, Föhringer Ring 6, 80805 München, Germany.

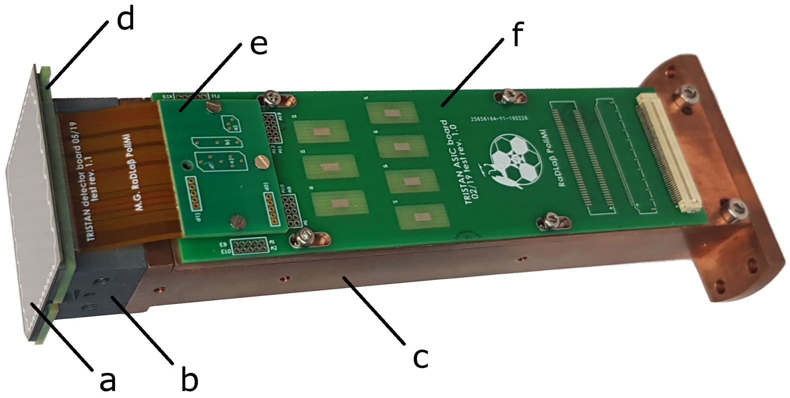

Figure 3.7: **First module dummy.** The silicon chip (a) with 166 pixels is glued onto a Cesic holder (b) mounted on a copper arm (c). The electric connection from chip to detector board (d) is realized with wire bonds. Two flex cables (e) provide the connection to the ASIC board (f). As this is a dummy to test the assembly process, the chip is insensitive and no ASICs are mounted.

which is important to cool the chip without damages. At the same time, it provides a very high thermal conductivity and can easily be produced in any desired shape. The copper arm is thermally connected to the Cesic part and extracts the heat produced by the electronics out of the vacuum. It furthermore carries and cools the ASIC boards. Copper is chosen because of its high thermal conductivity and low cost. An assembly procedure is being established, for which specially designed jigs are foreseen to handle the fragile silicon chip.

The final TRISTAN detector will consist of 21 modules with 166 pixels each, resulting in a total of 3486 pixels. Several DAQ options are under investigation. Both commercial and self-designed systems are being considered. The KATRIN detector vacuum chamber will be replaced by a new chamber, currenty developed at KIT.[7] The full system is planned to be installed in the KATRIN beamline in 2023 or later, after the neutrino mass program has ended.

3.2.4 Other applications for TRISTAN

The development of the sophisticated TRISTAN particle detector system turned out to be interesting not only for a sterile neutrino search. To complete the picture of the TRISTAN project, some other applications are listed below, which are currently investigated.

---

[7] Karlsruher Institut für Technologie, Hermann-von-Helmholtz-Platz 1, 76344 Eggenstein-Leopoldshafen, Germany.

KATRIN's forward beam monitor The forward beam monitor (FBM) is used to monitor the KATRIN source activity over short time scales (minutes) with a precision of better than 0.1 % [Ang05]. It is located at the entrance of the pre-spectrometer in the KATRIN beamline (see figure 3.3), where it sees the full, unfiltered activity of the WGTS. During the first neutrino mass measurement phase, the detector chip was realized as a PIN diode. The performance of the FBM was improved by installing a TRISTAN SDD of the first generation with 0.25 mm pixel diameter [Urb19]. A small diameter is necessary to avoid pile-up effects, given the high electron flux at the FBM's position. Furthermore, the SDD design is ideal to provide a good energy resolution at short DAQ filtering times.

KATRIN's monitor spectrometer The monitor spectrometer is the upgraded spectrometer of the Mainz Neutrino Mass Experiment. It was repurposed to continuously monitor the long term (weeks) voltage stability of the KATRIN main spectrometer. To this end, it scans over a well-defined, sharp electron line of a solid $^{83\mathrm{m}}$Kr source (see section 4.4.3), close to the tritium endpoint energy. The monitor spectrometer is located in a building next to the KATRIN spectrometer hall (see figure 3.3) and directly coupled to the retarding voltage of the main spectrometer. Its performance will be improved by exchanging the current detector by the "first module" of the TRISTAN detector. With its 166 pixels, the spacial distribution of the source activity will be resolved. For the TRISTAN project, the monitor spectrometer is a good test-bench for deploying the first module with a P-1 chip in a realistic experimental environment.

Polarimetry with ComPol Compton polarimeter (ComPol) is a space mission, which aims at measuring the polarization of the black hole binary system Cygnus X-1. By measuring the polarization, insights in emission mechanisms are anticipated, which produce the low energetic part of the measured radiation spectrum. This again gives insights to the composition of objects of this kind. As a space application, strong constraints on sensitive detector area and weight exist. The TRISTAN detector is a promising candidate for the project, as it provides many pixels with low mass and good spacial resolution. Furthermore, a low energy range is accessible due to its low detection threshold, while its good energy resolution enables a sophisticated event selection. A first field test with a helium-filled balloon called "COCOTE-TRISTAN/TJB" was already performed in 2016.[8] Sensitivity studies for future missions are being performed [Mei19].

---

[8] The abbreviations stand for *Compact Compton telescope* and *TRISTAN joue au ballon*.

Axion search with IAXO The International Axion Observatory (IAXO) is a helioscope experiment, which aims at detecting axions and axion-like particles (ALPs) originating from the sun [Sem14]. The axion is a hypothetical particle, which was proposed in 1977 to solve the strong CP problem [Pec77]. As a massive but weakly interacting particle, it would also contribute to DM. If existent, the solar axion would be converted into detectable photons in the presence of the strong magnetic field inside a helioscope. As a rare event search, IAXO requires a setup providing a very low radioactive background. TRISTAN detectors are currently being tested on their intrinsic radioactivity in underground laboratories at the Technical University of Munich (TUM).[9]

---

[9] Technische Universität München, Arcisstraße 21, 80333 München, Germany.

4 Characterization of the first TRISTAN prototype detectors

In this chapter, the characterization of the first TRISTAN prototype detector generation is presented. In section 4.1, the components of the setup and their functionality are explained. The general characterization with standard x-ray and γ-sources is presented in section 4.2. In section 4.3, studies of the detector response to electrons are presented. Also in this section, a model for the detector response is developed, which will be used throughout the following chapters.

4.1 TRISTAN prototype-0 detector system

In this section, the functionality of the TRISTAN prototype-0 (P-0) detector system is explained, starting with the silicon detector chips in section 4.1.1. The readout electronics, namely the CUBE ASIC and the DANTE DPP, are discussed in section 4.1.2.

4.1.1 7-pixel detector chips

The underlying technology for the TRISTAN detector development is the silicon drift detector (SDD), a special type of semiconductor detector. Semiconductor detectors are widely used in spectroscopy and as particle trackers or detectors [Kno10]. They reach much higher energy resolutions and lower thresholds than older technologies (e.g. ionization chamber). When radiation penetrates an ionization detector, free charge carriers are produced, i.e. electron-hole pairs. The radiation energy E is linearly proportional to the amount of free charges.

$$N = \frac{E}{E_{\text{pair}}} = \frac{Q}{e} \,, \tag{4.1}$$

with the electron-hole pair production energy E_{pair}, the produced total charge Q, and the elementary charge e. The energy of the ionizing radiation E is determined by measuring the produced charge Q.

The advantage of semiconductor detectors is their narrow band gap between conductive and valence band, resulting in a low required energy to produce electron-hole pairs E_{pair} compared to other materials. Most commonly used semiconductor materials are

$$\text{silicon } (E_{\text{pair}} = 3.6\,\text{eV}) \text{ and} \tag{4.2}$$

$$\text{germanium } (E_{\text{pair}} = 2.9\,\text{eV}) \ . \tag{4.3}$$

Silicon detectors are cheap, robust and flexible but cannot be thicker than a few millimeters. This is due to the high silicon melting point at 1414 °C and the associated impurities in the crystal.[1] Germanium detectors are produced with a thickness in the order of centimeters and can therefore be used as total absorption detectors for radiation with energies up to the MeV-range. However, they must be cryogenically operated, due to their small energy band gap at high temperatures [Var67].

To operate a semiconductor detector, the bulk material has to be depleted, i.e. no thermally excited free charge carriers must exist inside the bulk, as they would completely deluge the radiation signal. Depletion is achieved by implanting a p-n junction close to the entrance window, to which a voltage U_{bias} is applied. Increasing U_{bias} in reverse bias mode, as illustrated in figure 4.1, the bulk gets depleted and an electric field is generated. As a result, free electrons are drifted towards the anode contact, while holes are drifted towards the cathode.

When energy is deposited inside the bulk, free charge carriers are created in an extended charge cloud, as opposed to a point-like deposition. This is especially relevant, when investigating border effects (e.g. borders between pixels or the detector surface) and for the best achievable energy resolution. Unavoidable fluctuations in the size of the charge cloud and the number of created charge carriers are the limiting factor for semiconductor detectors in terms of energy resolution. However, the number of created charge carriers does not follow a purely statistical random process, as the ionization of an atom depends on its discrete electron shells. The process was first quantified by U. Fano [Fan47], introducing the Fano factor

$$F = \frac{\sigma^2}{\mu} \ , \tag{4.4}$$

with the observed variance σ^2 and the mean μ of a random process. For a Poisson distribution, the Fano factor is defined as $F = 1$, while in a semiconductor material $F < 1$, resulting in a better energy resolution compared to a purely statistical process. The Fano factor is a material and temperature dependent quantity, which can be measured, e.g. for silicon at room temperature $F = 0.115$ [Ali80]. The

---

[1] Si(Li) detectors can be produced and operated with thicknesses in the order of centimeters.

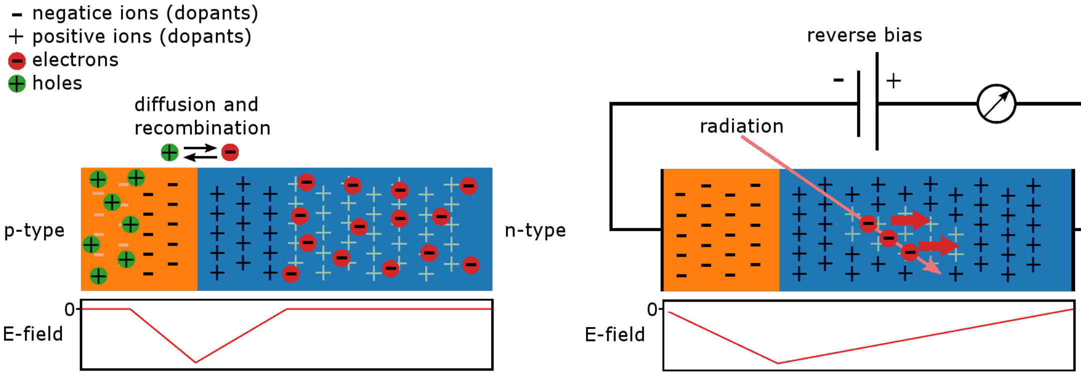

Figure 4.1: **Scheme of a p-n junction in a semiconductor detector.** *Left:* At the transition of p- and n-type material, free electrons and holes diffuse into the oppositely doped region and recombine. The remaining ionized dopants in the depletion region create an electric field, counteracting the movement of free charges. *Right:* By increasing a voltage in reverse bias mode, the depletion region spreads until the electric field covers the entire bulk material. When ionizing radiation penetrates the detector, free electrons are created and drift towards the anode, unable to recombine. This creates a measureable current pulse proportional to the energy of the incident radiation. Adapted from [Alt19].

limiting noise component for semiconductor detectors is expressed by the Fano limit [Lec95]

$$\sigma_{\text{Fano}} = \sqrt{F \cdot E \cdot E_{\text{pair}}} \ . \tag{4.5}$$

The silicon drift detector (SDD) is based on a design by E. Gatti [Gat84] and brings advantages over conventional semiconductor detectors. In contrast to for instance PIN diodes, SDDs have a very small anode relative to the sensitive volume. This leads to a reduced read-out capacitance and thus a reduced noise level. To maintain full and complete charge collection in the bulk, ring contacts are implanted on the read-out side surface of the chip, surrounding the anode in their center. By applying decreasing negative potentials from the outside to the inside rings, free electrons drift towards the anode from all sides, providing a high charge collection efficiency (CCE) over the entire bulk material. The CCE indicates how many of the created charge carriers reach the anode, i.e. how much of the deposited energy is detected. A geometry of an SDD pixel and its electric potential is shown in figure 4.2. By implanting drift rings directly on a monolithic silicon wafer, the separation into pixels is accomplished only by the electric fields. Thus, the SDD design allows to create detector arrays without dead area between pixel.

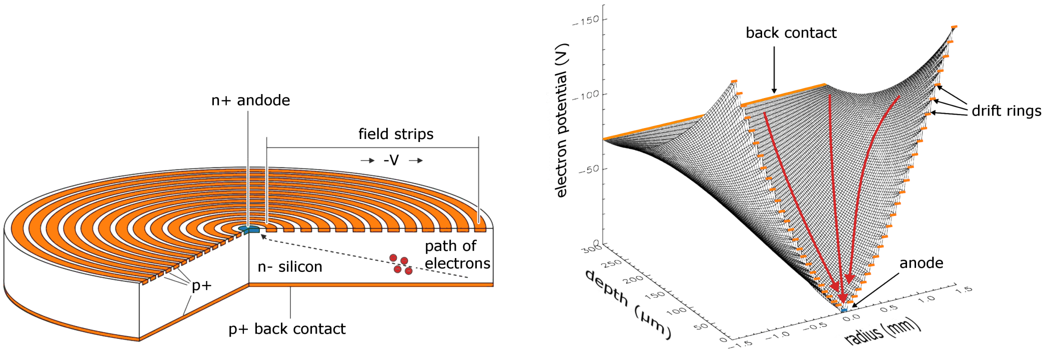

(a) SDD pixel geometry. (b) SDD pixel potential.

Figure 4.2: **Scheme of an SDD and its electric potential.** (a) Geometry of one pixel of an SDD. The anode (blue) is surrounded by drift rings (orange). (b) Calculated potential over one pixel of an SDD. A bias voltage (here $U_{\mathrm{bias}} = -70\,\mathrm{V}$) is applied to the back contact (orange line). The drift rings (orange dots) are set on decreasing negative potentials from larger to smaller radii. Electrons (red arrows) drift to the anode (blue dot), which is located at the point of lowest potential. Both adapted from [Lec01].

The TRISTAN P-0 detector chips consist of seven hexagonally shaped pixels with an anode capacitance of only 110 fF. A hexagonal pixel shape has been chosen, as round pixels cannot be arranged in a grid without gaps. With hexagonal pixels, this problem is bypassed, while at the same time the electric field configuration approaches the ideal circular geometry better than with for instance a quadratic shape. The chips were produced with several pixel diameters (0.25, 0.5, 1, and 2 mm) to validate the expected charge sharing, backscattering, and in particular noise behaviors. Additionally, four different doping profiles were applied at the entrance window with the intention to increase the CCE in the region close to the surface. The chip thickness is 450 µm.

A 2 mm pixel diameter version with twelve drift rings is shown in figure 4.3. A pixel arrangement has been chosen, in which one pixel is surrounded by six other pixels in a gapless fashion. Voltage dividers are integrated onto the chip to supply the drift rings. The application of bond wires with small diameters of 14 µm reduces additional capacitances. The entire array is surrounded by a guard ring, which prevents charges from leaving the sensitive volume. The outer six pixels can be used as a veto for the so-called “golden pixel” in the middle. Additionally, two temperature diodes were implanted on the chip, one of which is connected and operational, one as a backup.

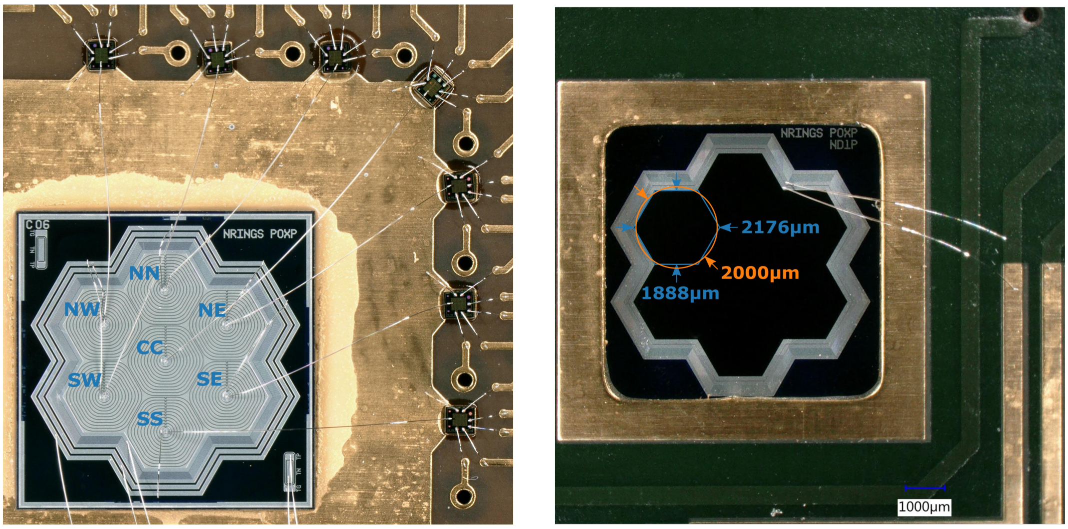

(a) Front side. (b) Back side.

Figure 4.3: **Front and back side of the TRISTAN P-0.** (a) The signal read-out electronics are placed on the front side of the detector. The anode of each pixel is surrounded by twelve drift rings. Each anode is connected to a CUBE ASIC via a bond wire. The other bonds supply the voltage of the inner- and outermost drift rings, and the temperature diode, which is visible in the lower right corner of the chip. The names of the outer pixels (blue letters) are based on the compass directions with arbitrary orientation. The central pixel is called “CC”. (b) The entrance window is on the back side of the detector. No ring structure is visible, as the entire surface is covered by the cathode. Both the cathode and the guard ring voltages are supplied via bond wires. The dimensions of one hexagonal pixel and the equivalent 2 mm circle are shown in blue and orange, respectively.

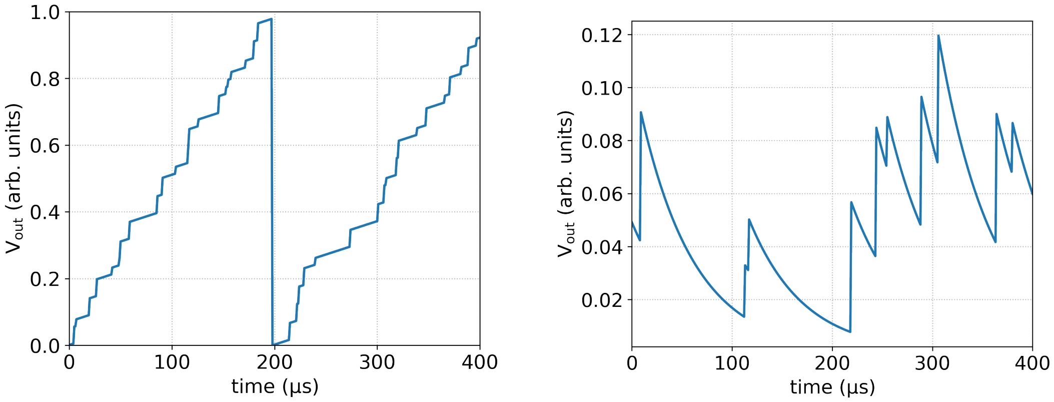

(a) Pulsed reset.

(b) Continuous reset.

Figure 4.4: **Waveforms in pulsed and continuous reset mode.** (a) The leakage current continuously charges the feedback capacitor, leading to an increasing ramp. A signal from an incident particle manifests itself as a steep step in the ramp. The reset is triggered when the ramp reaches a saturation threshold. (b) The feedback capacitor is continuously discharged over a resistor in a way that leakage current cannot accumulate. Signals from incident particles lead to a short pulse, which is slowly reset with a characteristic time constant defined by the resistor.

4.1.2 CUBE ASIC & DANTE DPP

The energy depositions in the silicon chip are amplified and processed using a chain of read-out components. For the investigations in this thesis, CUBE and DANTE have been chosen as front- and back-end read-out.

CUBE is a single-channel charge-sensitive preamplifier (CSA) based on a metal-oxide-semiconductor field-effect transistor (MOSFET) [Bom11]. Each pixel anode of P-0 is directly connected to the input of a CUBE ASIC via a wire bond (see figure 4.3(a)). CUBE features a field-effect transistor (FET) with very high transconductance, specifically designed to read out SDDs without integrated FET. The combination of its excellent noise performance with the small P-0 anode capacitance promises good energy resolution, even when operating the system at high signal rates $\mathcal{O}$(kcps). CUBE is operated in pulsed reset mode: Signal and leakage current lead to an accumulation of charge on the feedback capacitor. When the latter is saturated, the charge is reset by a transistor, leading to the characteristic ramp of the pulsed reset, shown in figure 4.4(a). The influence of leakage current is minimized by operating the SDD at low temperatures.

The CUBE preamplifiers are powered by an 8-channel bias board. It generates and filters all supply voltages from an external input. All voltages are manually adjustable at potentiometers on the board. Furthermore, it manages the simultaneous reset of all connected CUBEs and provides an inhibit signal during the reset. Optionally, the reset can be triggered from an external signal. The output signals of the CUBEs are buffered and amplified on the board. This is necessary to send the analog signals via coaxial cables to the DPP.

The DANTE DPP is used to digitize the entire waveform and to filter the signals in two steps. It features an ADC with a sampling frequency of 125 MHz and a resolution of 16 bit. Thereafter, two trapezoidal filters are applied on the digital waveform for event triggering and pulse shaping, respectively. This is realized in a FPGA. DANTE is linked with a PC either via Universal Serial Bus (USB) or Ethernet connection. Several settings (e.g. amplification gain, filtering times, and thresholds) are adjustable using a graphical user interface (GUI) or application programming interface (API). Besides debugging modes, the data is acquired in waveform mode, list mode or spectrum mode:

- In **waveform mode**, the entire digitized waveform is saved. This acquisition mode provides most information on the signals (e.g. signal rise times). However, it cannot be acquired continuously and vast disk space is needed.
- In **list mode**, the filtered energy in terms of an ADC bin amplitude is saved for each event next to its time stamp. Since 2017, an 8-channel version of DANTE is available, which allows to read out all seven pixels of P-0 synchronized in time.
- In **spectrum mode**, only one histogram of the ADC bin amplitudes is saved per acquisition. Time information is lost but this mode requires least disk space and allows for quick performance checks.

The interplay of DANTE's two trapezoidal filters has to be understood to correctly interpret the results of the following investigations. A trapezoidal filter in general acts as a frequency filter to determine the signal amplitude independent of noise. Its working principle is illustrated in figure 4.5. It is characterized by two quantities: shaping time and gap time. Both are quantized by the sampling frequency of the ADC, i.e. 8 ns in DANTE. The digitized waveform is averaged over a given time interval, called shaping time t_{shape}. The optimal length of the shaping time is dictated by the noise contributions and the signal rate. The same averaging is performed for a second time window, separated from the first one by the gap time t_{gap} (see figure 4.5(a)). To guarantee a faultless energy reconstruction, the gap time has to cover at least the signal rise time. The output of a trapezoidal filter is the difference of the averaged amplitudes of both shaping time windows. It is continuously calculated,

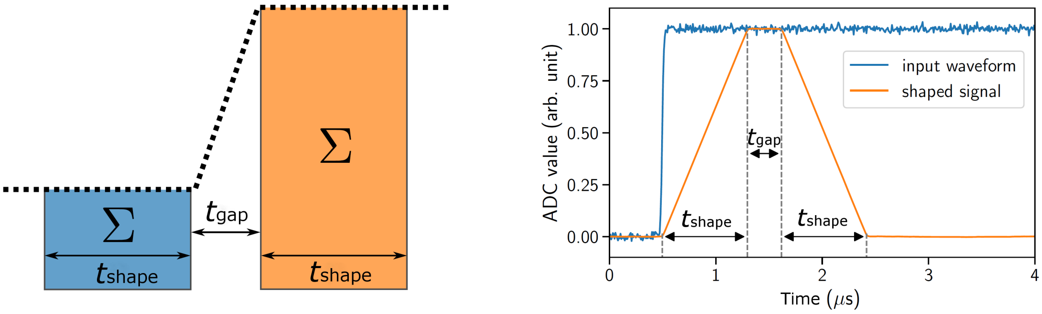

(a) Scheme of shaping and gap time. (b) Waveform with resulting trapezoid.

Figure 4.5: **Working principle of a trapezoidal filter.** (a) The black dots represent the signal waveform, sampled with the ADC frequency. The averaged samples in the orange time window get subtracted from those in the blue one. Both windows have the length of one shaping time t_{shape}. The gap time t_{gap} has to be at least as long as the signal rise time, to not distort the trapezoidal shape. (b) An exemplary waveform (blue) with the resulting trapezoidal shape (orange) after filtering. Adapted from [Des19].

while both windows move along the waveform, always separated by t_{gap}. The name "trapezoidal filter" originates from the shape of its output, when a signal is encountered (see figure 4.5(b)). The height of the trapezoid represents the measured energy and the width is determined by both shaping and gap time. Due to the averaging over the shaping time, noise influences are mitigated.

In DANTE, the fast filter with short shaping times detects events exceeding a set threshold. Only those are passed to the energy filter with longer shaping times for a proper energy determination. This provides precise energy reconstruction even at high signal rates.

4.2 General performance with photons

The goal of the measurements described in this section is to characterize the general performance of P-0 using standard x-ray and γ-sources. Based on these measurements, a routine has been established, which newly received detectors have to pass before further usage.

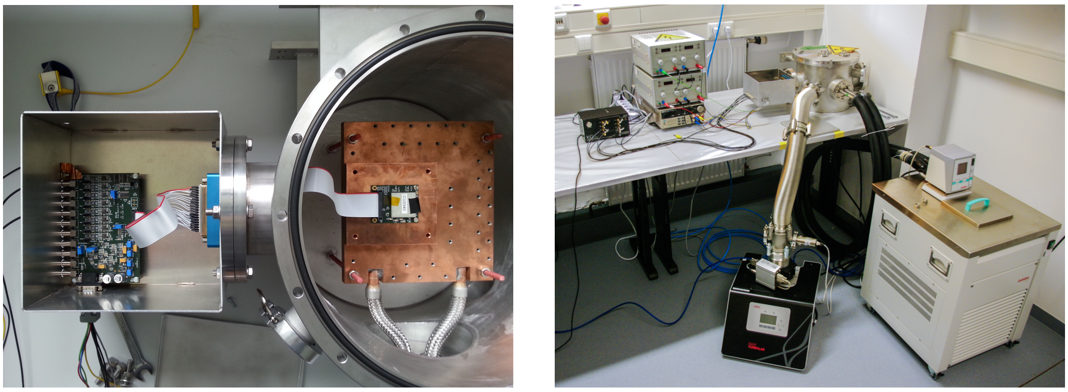

(a) Detector and bias board.

(b) Ambient devices.

Figure 4.6: **TRISTAN test stand at MPP.** (a) Vacuum chamber with detector and cooled copper plate. The aluminum cover over the ASICs protects the bond wires and facilitates handling the detectors. The signals are transmitted to the bias board via a feedthrough in a vacuum flange. The bias board shares the ground potential with the box and the vacuum vessel. (b) The DANTE box is connected to a PC via USB. A low voltage power supply is used to provide the operation voltage of the bias board, while two low-noise power supplies are used to provide the high voltages for the SDD. Pressures of around 10^{-7} mbar and temperatures of $-30\,°\mathrm{C}$ are provided by vacuum pump and chiller, respectively.

Experimental setup The detectors are installed inside a vacuum chamber onto a copper holder, thermally coupled to a cooling plate. The plate is cooled with cooling fluid based on silicone and provided from an external chiller. The measurements have to be performed in vacuum to prevent humidity in the air to freeze on the detector surface, when it is cooled to temperatures below 0 °C. A vacuum of around 10^{-7} mbar is reached with a combination of diaphragm pump and TMP. The electrical connection to the detector is realized with a D-Sub vacuum feedthrough on a flange. The interior of the vacuum chamber is displayed in figure 4.6(a).

The bias board is mounted in a metal box, attached to the vacuum chamber. Hence, board, box, and chamber share the same ground potential. To guarantee a good electrical connection, a broad ground connection between board and box is necessary, as opposed to a thin cable. All detector voltages are supplied by low-noise power supplies to the bias board. The output channels of the bias board are directly connected to the DANTE input ports. For measurements, in which the temperature diode was not used, its cable was removed, as it has shown to pick up noise. Instead,

Table 4.1: **X-ray and γ-lines of ^{55}Fe and ^{241}Am.** Listed are the weighted averages of all sublines [Chu99].

Isotope	Origin	Energy (keV)	Intensity (%)
^{55}Fe	Mn-K$_{\alpha}$	5.895	25.400
	Mn-K$_{\beta}$	6.490	2.991
^{241}Am	Np-L$_{l}$	11.871	0.660
	Np-L$_{\alpha}$	13.927	10.670
	Np-L$_{\eta}$	15.861	0.153
	Np-L$_{\beta}$	17.457	11.904
	Np-L$_{\gamma}$	21.037	2.920
	α	26.345	2.400
	α	59.541	35.900

the displayed temperature at the cooling device serves as a temperature monitor, even though it is expected to be a bit colder than the actual detector temperature. The setup of ambient devices is shown in figure 4.6(b).

Radioactive standard sources Iron (^{55}Fe) and americium (^{241}Am) radioactive sources were used for characterization and calibration. Both sources provide x-ray and γ-lines in the keV-region of interest for TRISTAN, considering the endpoint of the tritium spectrum at 18.6 keV plus at least the same post acceleration energy. A summary of all relevant lines of the two sources is given in table 4.1.

^{55}Fe The radioactive isotope iron-55 is most often produced by irradiation of iron with neutrons. It decays to manganese-55 (^{55}Mn) via EC with a half-life $T_{1/2} = 2.73\,\text{yr}$ [Chu99]. As a closed source, the emitted 5.19 keV Auger electrons are stopped by a thin shield over its surface. It also features x-rays with 5.9 keV and 6.5 keV, which easily penetrate the shield. These lines are interesting, as they lie only 0.6 keV apart. Whether they are well separated or not allows to estimate the detector resolution already by eye.

^{241}Am Americium-241 is bred as a side product in nuclear power plants. It decays to neptunium-237 (^{237}Np) via α-decay with a half-life $T_{1/2} = 432.2\,\text{yr}$ [Chu99]. The emitted α-particles are stopped in a shield. X-ray and γ-lines lie in the energy range of 11.9 – 26.3 keV. A more remote line lies at 59.5 keV. However, its actual intensity is reduced, when measured with the 450 µm thick TRISTAN detector, as high energetic photons penetrate the silicon bulk without interacting.

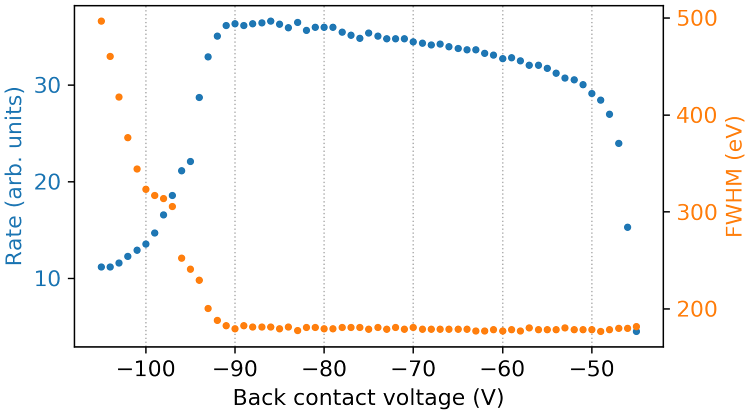

Figure 4.7: **Back contact voltage scan.** An ^{55}Fe source was measured with the 2 mm pixel diameter detector SC-2. Rate and resolution are shown for a back contact voltage scan from −105 to −45 V. A plateau with CCE > 80 % reaches from −90 to −50 V. At both sides of the plateau, the detector performance decreases due to improper depletion. The optimum is $V_{\mathrm{bc}} = -88\,\mathrm{V}$.

Optimal supply voltages Four supply voltages for the P-0 chip are adjustable on the bias board: back contact V_{bc}, back frame V_{bf}, inner drift ring V_{r1}, and outer drift ring V_{rx}. If not set to their optimal values, the detector performance might be degraded, e.g. in terms of CCE. Thus, the voltages were decoupled from the bias board and supplied individually by a source measure unit (SMU). Like this, each voltage was scanned over a certain range, while the resolution and input count rates were monitored during a measurement of ^{55}Fe.

The largest impact on the detector performance is apparent, when the back contact voltage V_{bc} is changed. The dependence of resolution and count rate on V_{bc} is shown in figure 4.7. A plateau with a high CCE above 80 % is apparent between −50 and −90 V, normalized to the optimal value at −88 V. For $|V_{\mathrm{bc}}| < 50\,\mathrm{V}$, the detector chip is not fully depleted. For $|V_{\mathrm{bc}}| > 90\,\mathrm{V}$, the electric field lines get shifted towards the read-out side. Consequently, signal electrons get lost between the drift rings. Furthermore, the potential difference between back contact and back frame must not be larger than 10 V. Only minor impact on the detector performance is observed, when other supply voltages are scanned. As the doping profile affects the depletion characteristics, one detector of each available entrance window technology was tested. All show a similar behavior. A set of optimal voltages is identified for the 2 mm pixel diameter detectors. These are listed in table 4.2, next to recommended values for 1 mm pixel diameter detectors for comparison.

Table 4.2: **Supply voltages for P-0.** The optimal voltages for a 2 mm pixel diameter chip were identified. They are applicable for all entrance window technologies. Recommended values for 1 mm pixel diameter chips are given as a reference. The difference in the ring voltages originates from the different number of drift rings per pixel.

Name	Symbol	Supply voltage (V) 1 mm	Supply voltage (V) 2 mm
Back contact	V_{bc}	−100	−88
Back frame	V_{bf}	−110	−93
Inner drift ring	V_{r1}	−20	−20
Outer drift ring	V_{rx}	−60	−110
Drift rings	N_{rings}	6	12

Temperature dependence The performance of the P-0 detector system is studied in terms of achievable resolution to explore its limits and to check, whether it meets the project's requirements. As the operating temperature influences the performance of semiconductor detectors, an ^{55}Fe source was measured at stabilized temperatures ranging from 25 down to −50 °C.

The temperature diode voltage was read out at several temperatures using a voltmeter. For silicon, a linear decrease over temperature $\frac{\mathrm{d}U}{\mathrm{d}T} = -2.7\,\mathrm{mV/°C}$ is expected. The resulting calibration curve is shown in figure 4.8(a). It shows a linear behavior in the temperature range of −35 to 20 °C. The slope is −8.83(1) mV/°C, which is in agreement with an amplification factor in the range 3 − 4. At each temperature, the 6 keV line is fit with a Gaussian function to determine the temperature dependent detector resolution. Below −30 °C, no significant improvement of the resolution is observed. Above 0 °C, the resolution deteriorates exponentially. It is concluded that the detectors have to be cooled at least to −30 °C during operation to achieve optimal performance.

The measurement at −30 °C was repeated and analyzed in more detail. Before the measurement, special attention was given to a proper grounding of all components. Especially important was a broad connection from the bias board ground contact to the bias board box to effectively minimize noise on the waveform. The shaping time of the trapezoidal energy filter was set to $t_{\mathrm{shape}} = 1\,\mu\mathrm{s}$. A fit to the two spectral lines of ^{55}Fe at −30 °C is shown in figure 4.9. The main peaks are well approximated by Gaussian distributions. However, both peaks show small tails towards lower

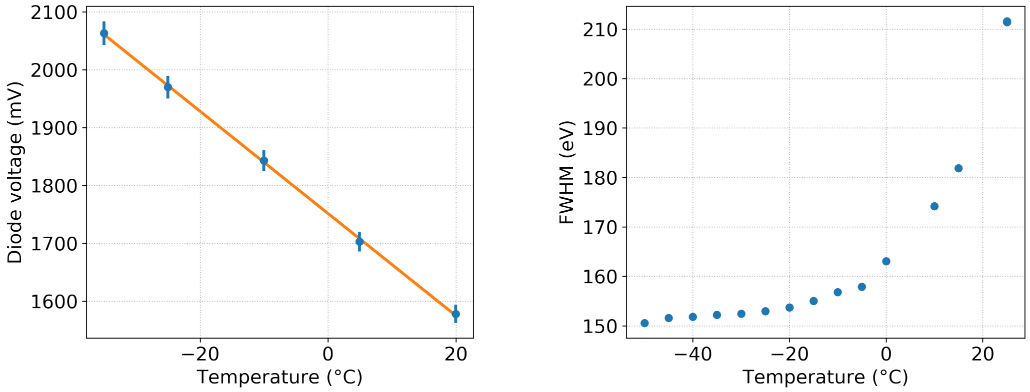

(a) Calibration curve of the temperature diode. (b) Temperature dependent resolution.

Figure 4.8: **Temperature dependence of P-0.** (a) The temperature diode shows a linear calibration curve with a slope of −8.83(1) mV/°C. The uncertainty on the voltage measurement is estimated to be 1 %. (b) The achievable resolution is approximately flat below −30 °C and rises exponentially for higher temperatures.

energies. Even though photons in this energy range interact point-like via absorption, the charge cloud extends into the insensitive area. Therefore, a phenomenological function [Egg04] was used to fit each peak.

An energy resolution of 139 eV (FWHM) was achieved at 5.9 keV. The Fano limit for semiconductor detectors at this energy is $\Delta E_{\text{Fano}} = 119\,\text{eV}$ (FWHM). With this, the chips are well suited for the purpose of the TRISTAN project.

Noise properties The energy resolution is most often expressed as full width at half maximum (FWHM)

$$\Delta E = 2.3548 \cdot \sigma \ , \tag{4.6}$$

where σ indicates the width of a Gaussian distribution. The best achievable energy resolution of a detector is not only a feature of the silicon chip, but also of the read-out electronics. While the number of created charge carriers in the chip (Fano noise) is energy dependent, the electronics noise is given by capacitance and temperature of the chip, as well as amplification and filter properties of the read-out chain. Especially the properties of the energy filter that acts as a frequency filter play an important role. To characterize the noise in the read-out system independent of the measured energy, the resolution is translated into an equivalent noise charge (ENC). The ENC states the number of electrons created in the detector, which yields a signal equally intense as the noise, i.e. a signal-to-noise ratio of one.

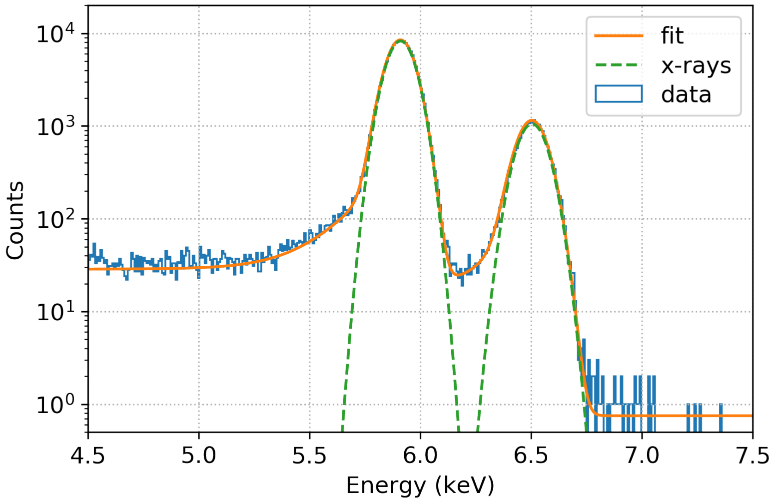

Figure 4.9: **Energy spectrum of ^{55}Fe with spectral fit.** The spectrum of ^{55}Fe (blue) was recorded with a P-0 detector at −30 °C. The two lines are clearly separated. Two phenomenological functions [Egg04] similar to a hypermet were used for the fit (orange). The Gaussian parts of the two lines are indicated in green. Adapted from [Mer19].

Depending on environmental influences (e.g. external noise sources, temperature, etc.) the ENC can be minimized by optimizing the energy filter shaping time t_{shape}. Hereby, three noise components with different dependencies are distinguished [Spi05]:

- **Current noise** increases with t_{shape}. For long shaping times, the increase of charge due to leakage current in a shaping time window cannot be approximated as zero. The filter starts to "see" the leakage current.

- **Voltage noise** decreases with t_{shape} and increases with capacitance C. For short shaping times, small noise fluctuations (i.e. high frequencies) lead to a degradation of the energy resolution. The longer t_{shape} is, the more the fluctuations are averaged out.

- **1/f-noise** is independent of t_{shape} but increases with capacitance C. Its characteristic 1/f-behavior is only relevant below the so-called corner frequency. This is usually at much larger shaping times, where the noise is dominated by the current noise. For the frequency range of interest for TRISTAN, the 1/f-noise is equivalent to white noise, i.e. constant over all frequencies.

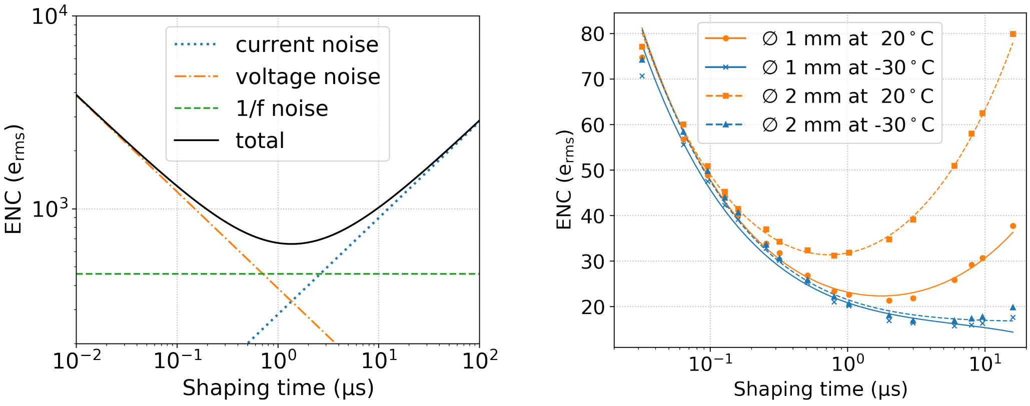

(a) Theoretical noise contributions.

(b) Measured noise curve.

Figure 4.10: **Theoretical and measured noise curves.** (a) The three noise contributions in equation (4.7) add up to the total noise level. (b) The measured ENC as a function of energy filter shaping time. The performance of the 1 mm (straight line) and 2 mm (dashed line) pixel diameter detector is compared at room temperature (orange) and −30 °C (blue). The contribution of current noise is increased at room temperature, especially for the larger detector. At −30 °C, the current noise is reduced to a negligible level, such that the performance of detectors is equal. Adapted from [Mer19].

As shown in figure 4.10(a), these components add up to the total ENC, which can consequently be expressed as

$$\mathrm{ENC}^2\left(t_{\text{shape}}\right) = \underbrace{F_i \cdot i^2 \cdot t_{\text{shape}}}_{\text{current}} + \underbrace{F_u \cdot u^2 \cdot \frac{C}{t_{\text{shape}}}}_{\text{voltage}} + \underbrace{F_f \cdot A_f \cdot C^2}_{1/\text{f}}\,, \tag{4.7}$$

with the noise current i, the noise voltage u, the noise coefficient for 1/f-noise A_f, and the noise factors of the trapezoidal filter for each contribution F_i, F_u, and F_f. For a more detailed explanation of all components see [Spi05]. In equation (4.7) it becomes clear that in general, the noise improves with decreasing capacitance. This is noteworthy, as the small anode capacitance is a specific feature of the SDD technology.

A noise curve, i.e. a scan of the resolution over the shaping time, was measured for P-0 systems with both 1 and 2 mm pixel diameter at room temperature and −30 °C. From the measured Gaussian resolution σ, the ENC is determined by quadratically subtracting the Fano limit σ_{Fano} and dividing by the pair production energy E_{pair} [Spi05]:

$$\text{ENC} = \frac{\sqrt{\sigma^2 - \sigma_{\text{Fano}}^2}}{E_{\text{pair}}} \tag{4.8}$$

The resulting noise curves are displayed in figure 4.10(b). At room temperature, the degradation of resolution at long shaping times is more pronounced for the 2 mm pixel diameter detector, as the current noise contribution increases with pixel size. At −30 °C, the same resolution was achieved with both the 1 and 2 mm pixel diameter detector. Consequently, the temperature dependent leakage current is suppressed to a negligible level for both pixel sizes. This demonstrates that the performance of chips with large pixel sizes is recovered when cooled. As the planned pixel diameter for the final detector is 3 mm, this is an important result for TRISTAN. Even for shaping times $t_{\text{shape}} < 1\,\mu\text{s}$, the ENC is still well below $20\,\text{e}_{\text{rms}}$. As TRISTAN will operate at high rates in the order of 10^5 cps per pixel, a good performance at short shaping times is crucial.

Pixel homogeneity The noise curve is compared between different pixels of one chip to study the homogeneity of the pixels. Pixels inhomogeneity could result from inhomogeneities in the doping of the silicon wafer, from the different lengths of the wire bonds, or from the different components within the CUBEs. Thus, the same measurement and analysis procedure as described in the previous paragraph was applied to each pixel individually. The resulting noise curves are shown in figure 4.11. The average deviation over all shaping times and pixels is 1.79 %. Slight deviations from the average are visible for pixel NW at short shaping times and for pixel CC at long shaping times. In general, the chip shows an ideal homogeneity. Small differences are irrelevant, as every pixel will be calibrated individually in the final setup.

Calibration linearity Linearity of the calibration funtion is an important feature for TRISTAN, as any energy scale distortion, which cannot be corrected for with a smooth calibration function, will degrade the experiment's sensitivity [Dol17]. An ^{241}Am spectrum was measured. All major peaks are fit to obtain the respective position in terms of ADC channels. The theoretical energy of each peak is plot over these ADC channels in figure 4.12. The data is fit with a linear calibration function and shows a deviation from linearity of less than 0.1 % for all data points. This result demonstrates an excellent linearity over the entire energy range of interest for TRISTAN.

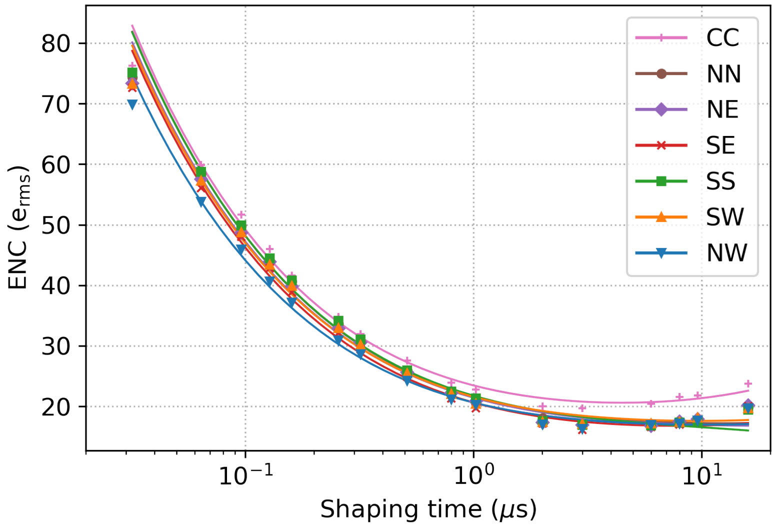

Figure 4.11: **Noise curve for all pixels of P-0.** The pixels are labeled according to figure 4.3(a).

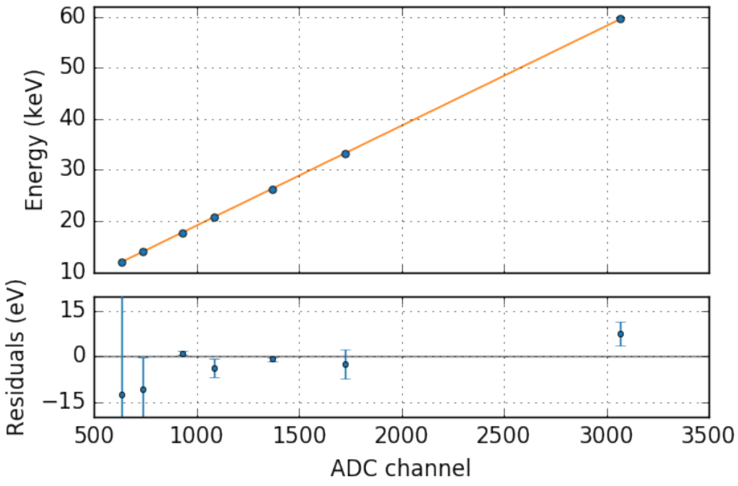

Figure 4.12: **Linear calibration curve using ^{241}Am.** The blue dots indicate the position of the photon peaks in the ^{241}Am spectrum (see table 4.1). The error bars are only visible in the resudial plot and contain the uncertainty of the line positions and the fit uncertainty. Adapted from [Mer19].

Long term stability KATRIN's measurement periods are limited by the tritium capacity of the cold trap in the CPS and last for about 60 days. The TRISTAN detector system will continuously operate during this period. The time stability of the detector performance is crucial for the sterile neutrino search, as any unknown drift or fluctuation would distort the spectrum and induce systematic uncertainty.

To study the long term performance already with the P-0 system, an ^{241}Am source was measured over the course 135 h. The detector was influenced by the temperature in the laboratory, as the chiller was not activated during the measurement. Analyzed are the position in terms of ADC channels and the resolution of the peaks at 12 and 60 keV, evaluated after approximately every 2.5 h.

The result for the 12 keV line is illustrated in figure 4.13. The observed relative drift in peak position is 0.034 % over the course of the acquisition. Even though this is negligibly small, the evolution contradicts the hypothesis of no drift. Additionally, a day time dependent variation is apparent. The temperature was not monitored but the position follows the temperature in the laboratory to a certain degree. The observed relative drift in resolution is 0.177 % and in good agreement with a no drift hypothesis with a p-value of 53.5 %. The 60 keV line shows a similar behavior with an average peak position in ADC channel 3928 and an average resolution of 455 eV.

Regarding the final system, this means that the temperature has to be stabilized and monitored to avoid drifts and thus spectral distortions. This holds not only for the silicon chip, but also for the read-out electronics outside the vacuum chamber, which might also be affected by temperature fluctuations. In a second measurement with stabilized temperature, the drift in peak position was found to be below 0.01 % extrapolated to 135 h. Radiation damages in the silicon material can potentially arise for longer exposure or higher count rates and degrade the detector's performance. This is unlikely for electron energies in the keV-range, but has not yet been checked thoroughly.

Detection threshold The detection threshold indicates the minimal energy an event can have to be recognized as such by the detector. It denotes the border between real events and noise fluctuations. A low detection threshold is necessary to correct for effects like backscattering and charge sharing, which would otherwise distort the spectral shape. In the P-0 system, the threshold is set on the fast filter in terms of ADC channels. However, the threshold is not a sharp cut at a certain energy: The combination of fast filter and energy filter leads to a smooth transition over several ADC channels: If the fast filter detects an excess on the

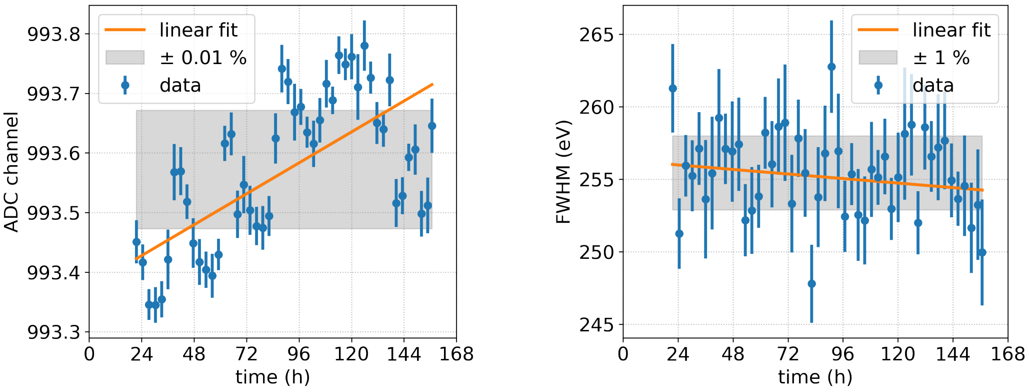

(a) Peak position.

(b) Resolution.

Figure 4.13: **Peak position and resolution during a long term measurement.** An ^{241}Am source was measured over the course of 135 h. Both plots show the respective feature for the L_{α}-line at 14 keV. (a) The peak position follows a day-night variation of the laboratory temperature. A drift towards higher positions is apparent. The grey band shows a 0.01 % deviation of the average value. (b) The relative drift in resolution is 0.177 % and in good agreement with a no drift hypothesis within uncertainty. As the detector was not cooled, the best achievable resolution for this energy is not reached. The grey band shows a 1 % deviation of the average value.

waveform larger than the threshold, the event is passed to the energy filter. Due to noise fluctuations, it happens that the energy filter reconstructs an energy, which is smaller than the actual threshold. Vice versa, it happens that the signal is not passed to the energy filter, event though the more precise energy filter would have reconstructed an event above threshold. The larger the signal amplitudes, the wider the transition.

4.3 Response to electrons

As the final TRISTAN detector will measure electrons, the characteristics of a measurement of these particles are studied. As charged particles, electrons behave differently in the silicon detector than neutral photons. Relevant effects and their features are explained in section 4.3.1. An attempt to model the resulting electron spectrum is presented in section 4.3.2.

4.3.1 Detector effects

A detector is a complex system, composed of many individual components, each of them influencing the result in their own characteristic way. To measure a tritium spectrum at the ppm-level, these features need to be understood in detail. Some of them are specifically important for measurements with charged particles like in KATRIN with electrons. They partly affect the same regions in an energy spectrum and are thus difficult to disentangle. This is true for a mono-energetic source and even more for a continuous spectrum. In the following, relevant detector effects are described, as they will be referred to throughout the thesis.

4.3.1.1 Effects in the silicon chip

The effects presented in this section concern energy losses in the silicon wafer. Each of them are random processes, which makes it impossible to correctly reconstruct the energy of single events. Only by means of statistics, the initial spectrum can be recovered, if all effects are known to a sufficient degree. The impact of some of these effects on a measurement of a mono-energetic electron source is visualized in figure 4.14. The mono-energetic input is transformed to a broad energy spectrum with a peak at the initial energy and distributions towards both higher and especially lower energies.

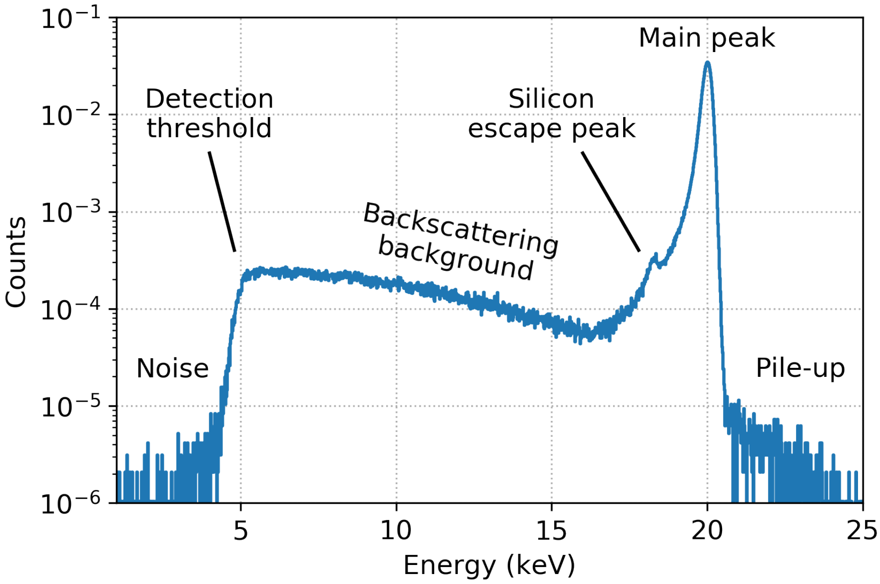

Figure 4.14: **Exemplary electron spectrum.** The spectrum was measured with 20 keV mono-energetic electrons from an electron microscope (see section 4.4.2). It is normalized to the total amount of measured events. The mono-energetic electrons are redistributed to higher and especially lower energies. The most dominant detector effects are labeled. Note the logarithmic y-axis.

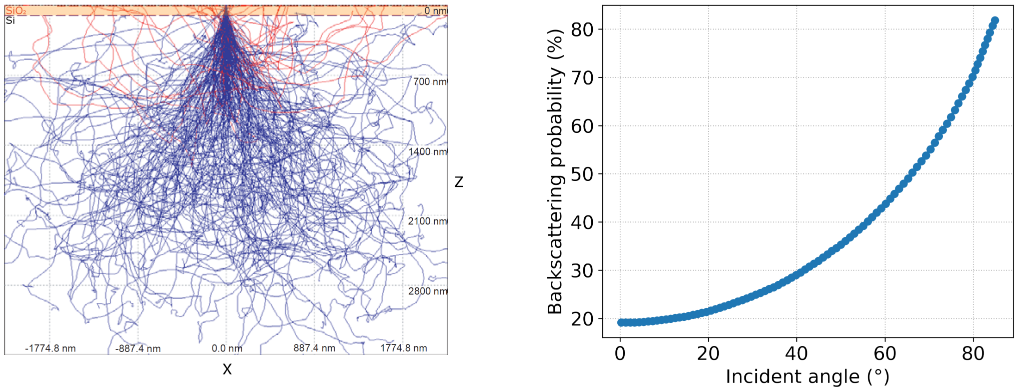

(a) Electron paths inside silicon.

(b) Backscattering probability.

Figure 4.15: **Backscattering characteristics.** (a) Simulated paths of 20 keV mono-energetic electrons in silicon to a depth $z = 3.5\,\mu\text{m}$ are shown. In this simulation [Arm04], a 100 nm thick SiO_2 layer was added on top of the material. The red trajectories represent backscattered events, i.e. electrons that scatter in a way that they leave the detector through the entrance window with some remaining energy. Adapted from [Arm04]. (b) The backscattering probability strongly increases with larger incident angles. Electrons were simulated using KESS with fixed incident energy $E_{\text{in}} = 25\,\text{keV}$. Adapted from [Ren11].

Backscattering While traveling though the silicon material, elastic and inelastic scatterings lead to a change of the movement direction of the electrons. The angular change in each scattering is a random process, so that the trajectories of many electrons are spatially fanned out, as visualized in figure 4.15(a). Some electrons undergo an angular change in a way that they again leave the silicon material though the entrance window. Others do not even enter the sensitive volume but scatter under an angle larger than 90° directly on the detector surface or in the insensitive SiO_2 layer. These electrons are labeled backscattered.

The effect on the spectrum is a redistribution of events towards lower energies, as a part of the initial energy remains undetected, when the electrons leave the detector. This feature is labeled as backscattering background in figure 4.14 and much more pronounced for electrons compared to photons. The backscattering probability strongly depends on the electrons' angle of incidence α_{in} relative to the detector surface. While the fraction of backscattered electrons with perpendicular incidence ($\alpha_{\text{in}} = 0°$) is about 18 %, it is increased to above 50 % at $\alpha_{\text{in}} > 65°$, as shown in figure 4.15(b). The backscattering slightly decreases with increasing energy, as the electron penetrate deeper into the bulk.

Regarding the characterization of the P-0 system with electron, the incident angles of the used electron sources have to be considered. The effect of backscattering can be mitigated by using electron sources with a small expansion or by placing the source further away from the detector to reduce the incident angle. However, this is only possible with strong sources, as the count rate usually gets reduced by both means.

Charge sharing Charge sharing appears, when an electron hits the detector at or close to the border between two or more pixels. Due to the extension of the charge cloud, the charges are split and each part is drifted to the anode of the respective pixel. This results in a pulse in both pixels with a summed energy, which equals the initial energy of the particle. In the case of the P-0 chips, this can even happen at the intersection of three pixels but the probability is negligibly small [Alt19].

Charge sharing depends on the electric field configuration inside the detector material. In the case of P-0, the electric field configuration, shown in figure 4.16, is such that the divergence of the electric field occurs deep inside the material. No difference in the charge sharing properties between electrons and photons is measurable [Alt19]. However, the effect is energy dependent, as high energetic particles create a larger initial charge cloud [Mat02]. It further depends on the pixel size. The effect of charge sharing is smaller for large pixel sizes, due to the increased ratio of pixel area to border.

The effect on the spectral shape is an increase of events especially in the energy region below the main peak, as illustrated in figure 4.17(a). If correctly tagged, events that underwent charge sharing can be reconstructed by summing the energies measured in both pixels. However, a certain amount of energy always gets lost and the energy resolution of the recovered peak is deteriorated by a factor of $\sqrt{2}$ [Alt19]. Therefore, charge sharing events are usually removed by applying a multiplicity cut, i.e. coincident events that triggered in two or more pixels (multiplicity ≥ 2) within a defined time window are not considered. The time window is optimized to effectively removing charge sharing, while not removing too many random coincidences. The resolution for coincidence in time is given by the sampling frequency of the ADC, which is 8 ns in the case of P-0.

However, not all charge sharing events are correctly tagged due to shared energy fractions, which fall below the detection threshold. The energy of charge sharing events is in the least cases shared 1:1, due to the spatial Gaussian distribution of the charge cloud. Most often, the largest fraction is deposited in pixel A, while pixel B receives only a small rest. When the amplitude of the shared energy registered in

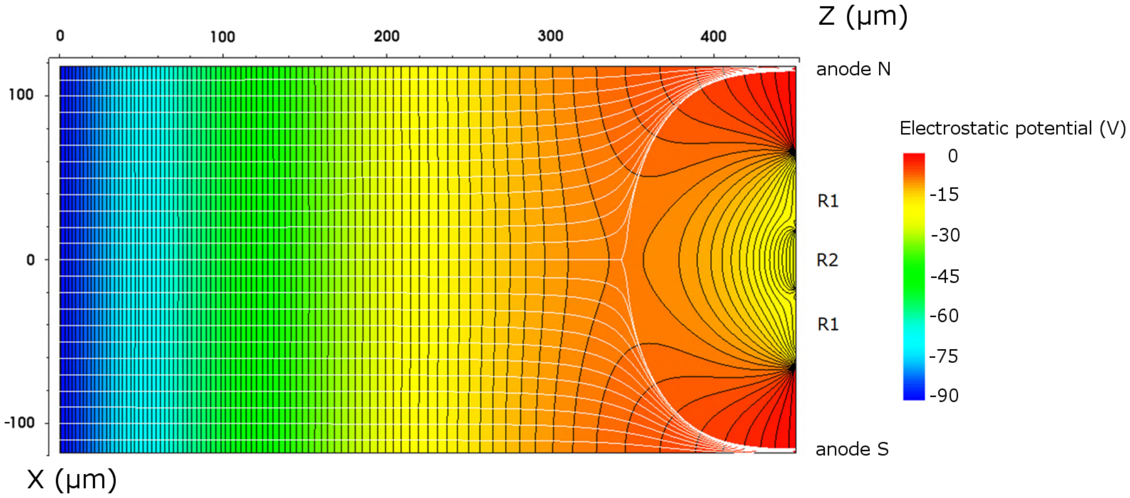

Figure 4.16: **Simulated electrostatic potential inside a TRISTAN detector.** The entrance window is at $z = 0\,\mu\text{m}$. The border between two pixels is situated at $x = 0\,\mu\text{m}$. Their anodes, respectively labeled with "anode N" and "anode S", are placed on the front side of the chip ($z = 450\,\mu\text{m}$). "R1" and "R2" denote drift rings. The pixel diameter of the simulated chip is $250\,\mu\text{m}$. The strength of the electrostatic potential is color coded from 0 V in red to -90 V in blue. The black lines denote equipotentials. The simulated trajectories of signal electrons (white) diverge only at a depth $z \approx 300\,\mu\text{m}$. (Courtesy of P. Lechner, internal meeting on May 22, 2019.)

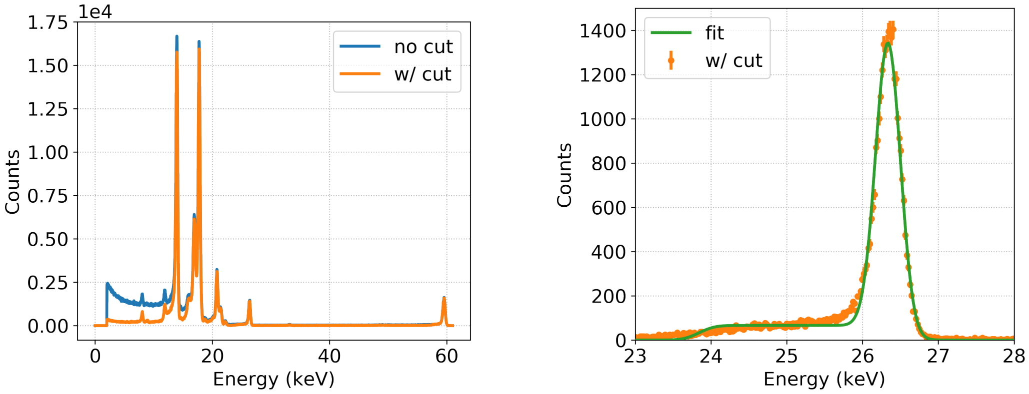

(a) Multiplicity cut.

(b) Undetected charge sharing.

Figure 4.17: **Effect of charge sharing on the spectral shape.** (a) An ^{241}Am source was measured with a 250 µm pixel diameter P-0 chip. The smaller the pixel diameter, the stronger the effect of charge sharing. A multiplicity cut removes all events, which triggered simultaneously in two or more pixels. Adapted from [Urb19]. (b) The ^{241}Am line at 26 keV after the multiplicity cut. Undetected charge sharing creates a plateau at the low energy shoulder of the main peak, which was modeled and fit with an empirical model [Alt19].

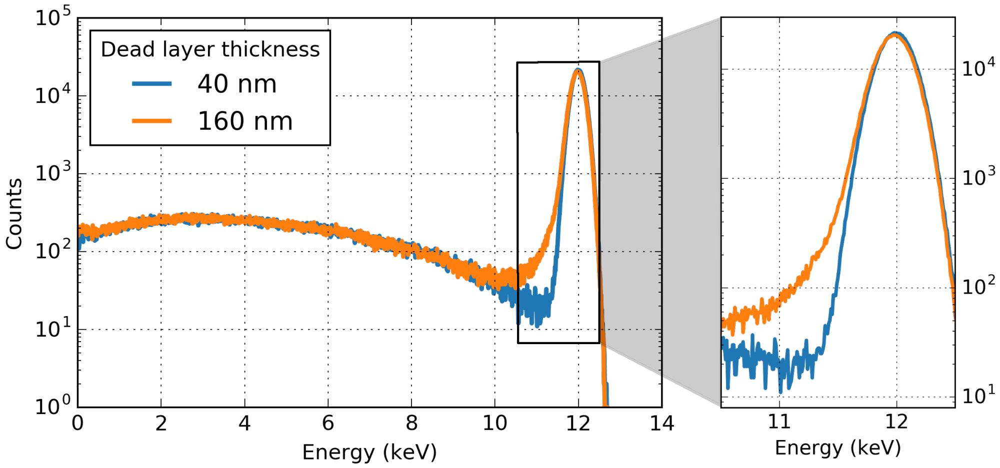

Figure 4.18: **Incomplete charge collection at the entrance window.** The spectra were simulated with KESS, assuming a dead layer model for the CCE (see section 4.4.1) and a detector resolution of 150 eV (FWHM) over the entire energy range. The dead layer leads to a low energy tail and shifts the main peak towards lower energies.

pixel B lies below the set threshold, only pixel A triggers on the event but measures an energy reduced by the fraction deposited in pixel B. In the spectrum, this results in a plateau towards lower energies next to the main peak with the length of the energy threshold, as displayed in figure 4.17(b).

Further mitigation might be possible by applying a cut on the signal rise time. As charge sharing occurs at the border between pixels, the charge cloud takes longer to drift to the anode. While drifting, the charge cloud diffuses internally, i.e. it gets larger. Consequently, events hitting the chip far away from an anode appear with an increased signal rise time. Controversial results were obtained in first investigations of this behavior, which requires more investigation. For more details on charge sharing studies with a P-0 equipped with an Idef-X ASIC see reference [Alt19].

Entrance window The entrance window of every semiconductor detector is covered with a region of incomplete charge collection. Charge deposited in this region has a probability of less than 100 % to contribute to the measured signal, i.e. the measured energy is underestimated. The effect on the spectral shape is the appearance of a low energy tail next to the main peak and a shift of the latter towards lower energies. The effect is much more pronounced for charged particles than for photons, as illustrated in figure 4.18 for electrons.

In the case of P-0, the region of incomplete charge collection is made of two components. The entrance window surface of the P-0 chips is covered with a 10 nm thick silicon oxide (SiO_2) layer. As SiO_2 is an insulator, only high energetic secondary electrons created in this region are able to reach the sensitive volume. This layer is unavoidable, as it grows as soon as the silicon chip is exposed to ambient air. To avoid inhomogeneities over the entrance window surface, its growth is controlled during the production of the chips.

The second contribution results from the depth of the doping profile at the entrance window. As it reaches several tens of nanometers into the bulk, the electric field does not expand with full strength to the surface of the detector. Electron-hole pairs created in this region diffuse through the material until they either enter a region with a stronger electric field and drift to the anode or recombine eventually. If they recombine, they do not contribute to the measured charge signal, i.e. deposited energy gets lost. Different doping profiles were applied to the P-0 chips, resulting in different shapes of the electric field. Both the doping profile and the electric field can be calculated [Har97] but the resulting CCE is still difficult to predict and requires dedicated measurements. Additionally, a new method involving epitaxial growth of the doping layer is currently being investigated in order to decrease the entrance window thickness [Leb19].

Several attempts have been made to model the entrance window effect. As charged particles, the energy loss per distance $\frac{\mathrm{d}E}{\mathrm{d}x}$ of electrons in matter is described by the Bethe formula [Bet53]. However, this approach has some disadvantages: According to simulations [Ren11], electrons with 18 keV interact in average only 3.8 times over the distance of 100 nm in silicon. As a result, the energy loss in such a thin layer is basically random. When calculating the energy loss using the Bethe formula, a straight trajectory with constant $\frac{\mathrm{d}E}{\mathrm{d}x}$ is assumed, leading to an underestimation of the energy loss.[2] Thus, the best approach so far to determine entrance window properties is the comparison with simulations, assuming a region of incomplete charge collection on the detector surface. Two models for the CCE and dedicated investigations of the entrance window of P-0 are presented in section 4.4.

Silicon escape peak An escape peak is generated by the following sequence of events: A shell electron of an atom in the detector material is ionized by incident radiation. Any ionizing radiation is capable of doing so. The resulting hole is filled by an electron from an outer shell, emitting a photon with the energy difference between the two shells ΔE. This happens on all shells and transitions but the most

---

[2] The integral over the lost energy is not evaluated, as the energy loss in thin layers is negligible.

prominent is K_α. In many cases, the photon gets reabsorbed inside the detector. However, it sometimes escapes without interacting and carries away a fraction of the incident energy, which remains undetected.

For mono-energetic incident radiation, this results in a second peak, shifted to lower energies, e.g. for silicon by $\Delta E_{K_\alpha} = E_{\text{esc}} = 1.74\,\text{keV}$ [Tho01]. This feature is visible in figure 4.14. Escape peaks from other shells are concealed by the backscattering background. The amplitude of the escape peak depends on several properties, such as type and energy of the incident radiation, the ionization probability of the detector material, but also on the individual detector geometry. Thus, it has to be determined for every detector individually, in order to be included in a model of the measured spectrum.

In the case of a tritium measurement, i.e. a continuous incident spectrum, an entire second tritium spectrum is composed by the superposition of escape peaks at all energies. It has the same shape as the usual tritium spectrum, but smaller amplitude and endpoint energy. With regard to a sterile neutrino search in tritium decay, the signature is very similar to a sterile neutrino with a mass of $m_4 = E_{\text{esc}}$ (see figure 3.4).

4.3.1.2 Effects in the read-out electronics

The effects presented in this section concern rate and energy misconstruction, induced by features in the read-out chain. For detailed investigations with the DANTE DPP see reference [Des19].

For the following discussion, it is important to note that in radioactive decays, events are independent from each other and randomly distributed in time. Thus, the probability of observing n events in a given time window Δt follows a Poisson distribution [NAS19]

$$P\left(n; \Delta t, \Gamma\right) = \frac{\left(\Delta t \cdot \Gamma\right)^n}{n!} \cdot \mathrm{e}^{-(\Delta t \cdot \Gamma)} \,, \tag{4.9}$$

with a constant signal rate Γ. Figure 4.19(a) shows the resulting distribution of times between consecutive events

$$f\left(\Delta t, \Gamma\right) = \Gamma \cdot \mathrm{e}^{-(\Delta t \cdot \Gamma)} \,. \tag{4.10}$$

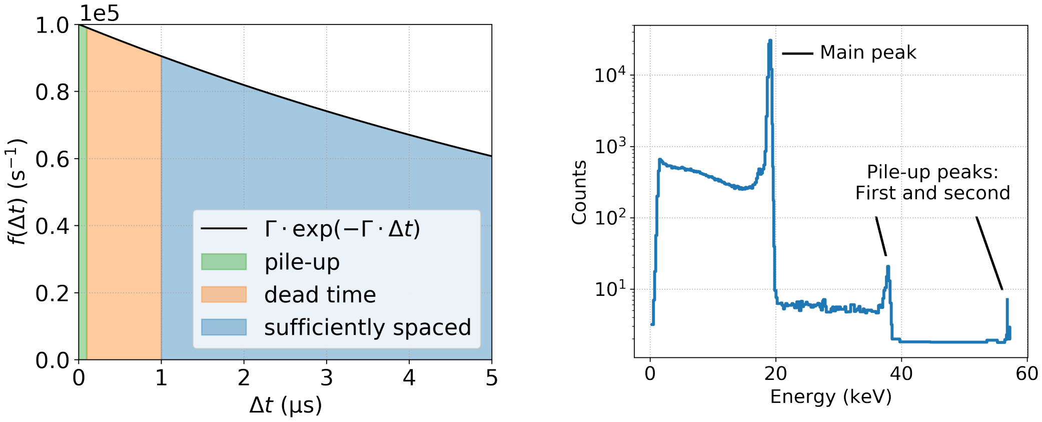

(a) Distribution of times between events.

(b) Spectrum with pile-up.

Figure 4.19: **Timing effects in the read-out.** (a) It is assumed that an event hits the detector at $t = t_0$. If a second event arrives within the "pile-up" window (green), both events pile up and appear as a single event in the detector. If the second event arrives within the "dead time" window (orange), it cannot be processed, as the DAQ requires a certain time to read out the first event. During this time, the detector is insensitive to other incoming events. If the second event arrives within the "sufficiently spaced" window (blue), both events are sufficiently spaced in time and are normally read out by the DAQ. Realistic values were chosen for a measurement with the P-0 system: signal rate $\Gamma = 10^5$ cps, pile-up resolution $\Delta t < \tau = 100\,\text{ns}$, dead time $t_\text{dead} = 1\,\mu\text{s}$. Adapted from [Des19]. (b) The plot shows a spectrum of mono-energetic electrons with an incident energy of 19 keV. The count rate is high enough, that consecutive events pile up and appear as a single event in the DAQ, leading to pile-up peaks at twice and even three times the incident energy.

Dead time Dead time refers to a certain time during an acquisition, in which the DAQ is not sensitive to measuring incoming events. A short dead time is crucial for TRISTAN, as the expected rate in the final system is extremely high. With increasing dead time, more data gets lost and at some point, the detector is insensitive during the entire acquisition. Especially in the integral measurement mode, a dead time correction is crucial: The higher the rate, the more events fall into the dead time window, which leads to a rate dependent distortion of the integral spectrum.

In P-0, dead time is induced by two features: The first contribution results from the operation in pulsed reset mode. Completely emptying the feedback capacitor from accumulated charge takes a few hundred nanoseconds. During this reset time, the CUBE ASICs are inhibited with a voltage signal. After the reset, the inhibit signal is turned off and the CUBEs instantly become sensitive. This sudden increase in voltage leads to an overshoot on the waveform. To not trigger on this overshoot, the DAQ provides an additional software time window, in which no signals are analyzed after a reset. This so-called recovery time t_{rec} is slightly longer than the inhibit signal on the ASICs. Every time a reset happens, this recovery time adds to the total dead time of the acquisition.

The second dead time contribution comes from the fact, that the DAQ system requires a certain time to analyze an incoming event. According to equation (4.10), it happens that events fall into this time interval (see figure 4.19(a)). If this is the case, the output shapes of the trapezoidal energy filter overlap in a way that a proper energy reconstruction becomes impossible and both events are rejected. Thus, this dead time contribution is determined by the trapezoidal energy filter shaping time t_{shape} and gap time t_{gap}. The total dead time of the P-0 system is given as

$$t_{\mathrm{dead}} = N_{\mathrm{reset}} \cdot t_{\mathrm{rec}} + N_{\mathrm{event}} \cdot (t_{\mathrm{shape}} + t_{\mathrm{gap}}) \ . \tag{4.11}$$

Deviations are possible due to the applied pile-up rejection algorithm. Additional dead time may result from noise events triggering the read-out, if the threshold value is set too low. The incident rate Γ_{in} is calculated from the measured one Γ_{meas} using

$$\Gamma_{\mathrm{in}} \approx \Gamma_{\mathrm{meas}} \cdot \mathrm{e}^{2 \cdot \Gamma_{\mathrm{meas}} \cdot t_{\mathrm{dead}}} \ . \tag{4.12}$$

This equation would be exact, if the rate in the exponent was Γ_{in}.

Pile-up According to equation (4.10), consecutive events even happen in time windows, which are smaller than the minimal time resolution τ of the DAQ system (see figure 4.19(a)). If this is the case, both events are indistinguishable and appear as a single event. For a mono-energetic input, this leads to a second peak at twice the incident energy and a stretched out backscattering background over the entire energy range. At very high rates, this can even lead to a second or more pile-up peaks.

In the case of the P-0 system, the minimal time resolution τ is determined by the DANTE trapezoidal fast filter dead time. However, means are implemented in the DANTE DPP to mitigate pile-up of two different kinds:

$\Delta t > \tau$ The first kind is pile-up with a Δt larger than the fast filter dead time τ but smaller than the energy filter dead time. It thus appears as two distinct events for the fast filter. In the subsequent energy filter with longer shaping and gap time, however, the events would overlap in a way that the energy is faulty reconstructed. Therefore, both events are rejected at the level of the fast filter. Both of them still contribute to the dead time, which, however, can be shorter than $2 \cdot (t_{\text{shape}} + t_{\text{gap}})$, due to the overlap.

$\Delta t < \tau$ The second kind is pile-up with a Δt smaller than τ, which is not even detected by the fast filter. Therefore, the signal rise time on the waveform is evaluated, on which DANTE provides the option to set an upper limit. If the events happen with a Δt larger than this limit, i.e. they appear as a single event with an unusual long signal rise time, they are rejected. One would expect that this feature also influences charge sharing: The rise time of typical signals in P-0 are on the order of 50 ns, whereas charge sharing signals show rise times up to 150 ns. Consequently, a rise time limit in the range of 50 – 150 ns should lower the amount of detected charge sharing events. However, this assumption was not validated so far and needs further investigation.

If the time difference between two events is smaller than the signal rise time, they cannot be distinguished by any means and appear as one event with high energy (see figure 4.19(b)).

ADC non-linearities ADCs are used to digitize analog signals, usually voltages. This happens with a certain resolution, determined by the number of bits. The number of bits indicates how often the dynamic range can be divided by two, until the smallest achievable distance between actual voltage and ADC quantization is reached. This distance remains as a quantization error, usually expressed in terms of the least significant bit (LSB), the last quantization step. Due to imperfections in the components of the internal architecture of an ADC (e.g. capacitors, comparators, etc.), this quantization error is not constant over the entire input voltage range, as shown in figure 4.20(a). This behavior is quantified by the integral non-linearity (INL). The INL is characterized using a well-known signal (e.g. a sinusoidal wave with a certain frequency f_{in}) given as an input signal to the ADC. By histogramming and

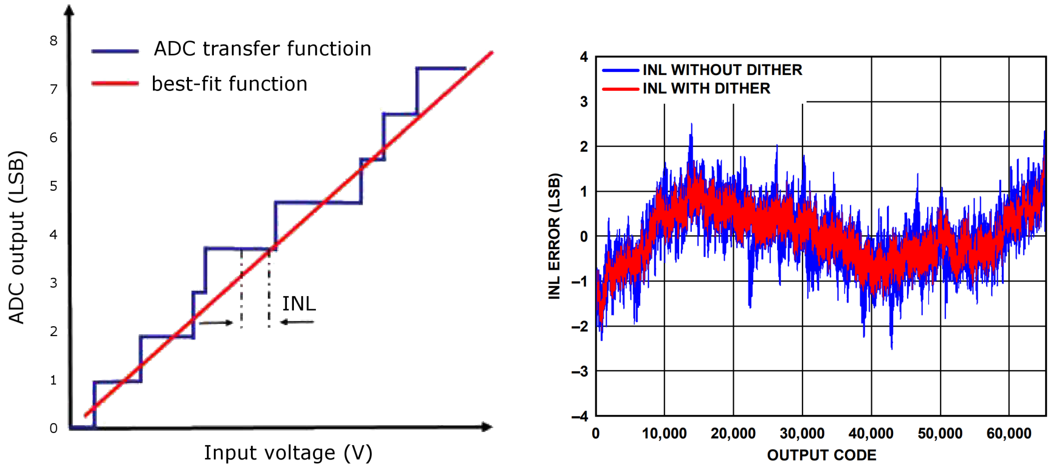

(a) Scheme of an ADC transfer function.

(b) ADC non-linearities in DANTE.

Figure 4.20: **ADC integral non-linearity.** (a) The transfer function translates an input voltage into quantized ADC bits. The ADC output increases by one LSB for each step. The step width is not constant over the voltage range, due to imperfections of internal components of the ADC. The deviation between the transfer and best-fit function is the integral non-linearity (INL). (b) INL of AD9265 BCPZ-125 [Ana19] over its 65 536 (16 bit) output bins at an input frequency $f_{\text{in}} = 9.7\,\text{MHz}$. Here, a dither was applied to smoothen the INL.

normalizing the counts in each ADC output bin, the respective INL is determined. This is exemplarily shown in figure 4.20(b) for the ADC “AD9265 BCPZ-125” [Ana19], which is used in DANTE.

ADC non-linearities lead to errors in the energy determination and thus to distortions in the shape of the measured spectrum. It was found that these distortions drastically affect the sensitivity to a sterile neutrino signature [Dol17]. Several means were identified to recover the sensitivity by averaging or smearing out the INL:

1. **Pixelated detector** The final TRISTAN detector is planned to consist of almost 3500 pixels, each of them equipped with an own ADC. As the INL of each ADC is slightly different, the effect of the total INLs averages out and is drastically reduced.

2. **Waveform digitization** By digitizing the entire waveform (opposed to digitizing only the output of the trapezoidal filter), the quantization is sensitive to the baseline of each signal. Consequently, different ADC outputs are used to measure the same energy. As each ADC output has a different INL, the effect of the total INL again average out.

3. **Post-acceleration** Post-accelerating the electrons from tritium decay leads to a higher energy and thus to a steeper signal rise on the waveform. With a steeper slope, the signals cover more ADC output bins, such that the trapezoidal filter averages the INLs over a wider range and the total effect gets smeared out.

Dedicated studies of the effect of INLs on a sterile neutrino search are documented in reference [Dol17]. However, these studies are based on hypothetical INLs, modeled in sophisticated simulations. The effect of realistic INLs like in DANTE is currently under investigation.

4.3.2 Detector response model

All of the detector effects mentioned in the previous section affect the shape of the measured energy spectrum. In order to search for a sterile neutrino signature, which is a spectral shape distortion, a model is needed to describe the response of the detector to electrons. In the most general case, a response gives the probability for an electron to change its energy, direction of motion, and/or position. For a detector, this means the probability of an event to be detected with an energy E, given a certain initial energy E_{in}. The detector response summarizes the probabilities for all initial energies.

The conventional way to determine a detector response is to find an empirical analytic function, which fits mono-energetic spectra of all E_{in}. *Analytic* functions are fast to use, compared to for instance a Monte Carlo (MC) simulation with a large amount of data, which may take a considerable amount of time. The advantage of *empirical* functions is their flexibility to adopt to any shape if only enough free parameters are introduced. This at the same time is a disadvantage, as empirical functions easily become degenerate, when too many free parameters are used. Furthermore, empirical functions are not based on a real physical background, i.e. their parameters are not predictable. As soon as the experimental setup changes in some way, they have to be determined again.

The terms of the P-0 response function are initialized using a MC simulation. A simulation package was developed by the KATRIN collaboration to simulate the energy loss and trajectory of electrons in silicon, called KATRIN Electron Scattering in Silicon (KESS) [Ren11]. Great emphasis was put on the behavior of electrons with energies in the keV-range, which was found to be insufficiently treated in other simulation packages, e.g. Geant4. KESS is based on first principles: In scatterings of electrons with silicon atoms, doubly differential inelastic cross sections are used to describe the energy loss of the electrons. Elastic differential cross sections are used to describe their angular deflections. Furthermore, the creation of knock-on and Auger electrons during ionization or excitation and the subsequent rearrangement of the shell are considered.

KESS is used to generate mono-energetic electron spectra at several energies. A simulated spectrum at 18 keV is shown in figure 4.21. The figure also shows the fit of a response function to the simulated data. The model is based on a response for photons [Egg04] and was adapted to fit electron spectra with the following form [Alt19]:

$$f_{\mathrm{det}}(E;\mu,\sigma,n_0,n_1,n_2,n_3,\beta_1,\beta_2,a,b) = \underbrace{n_0\cdot \mathrm{e}^{-\left(\frac{\mu-E}{\sqrt{2}\sigma}\right)^2}}_{\text{Gaussian}} \tag{4.13}$$

$$+\sum_{i=1}^{2}\underbrace{n_0\cdot n_i\cdot \mathrm{e}^{-\frac{\mu-E}{\beta_i}}\cdot\left(1-\mathrm{erf}\left[-\frac{\mu-E}{\sqrt{2}\sigma}+\frac{\sigma}{\sqrt{2}\beta_i}\right]\right)}_{\text{Dead layer}} \tag{4.14}$$

$$\underbrace{+\,\mathrm{Re}\left[n_0\cdot n_3\cdot\left(\frac{E-a}{\mu}\right)^b\cdot\left(1-\frac{E}{\mu}\right)^c\right]\cdot\Theta(\mu-E)}_{\text{Backscattering}}\ . \tag{4.15}$$

It consists of a Gaussian term (equation (4.13)), which is usually used to fit the main peak. Depending on the individual spectrum, one or two dead layer tails (equation (4.14)) are used to describe the main peak's low energy shoulder. They are called dead layer tails, as the entrance window effect has shown to be most significant in this region (see figure 4.18). The simulated spectrum in figure 4.21 is fit with only one dead layer tail. As will be shown in section 5.2.3, a second term is added to better fit spectra of actual electron measurements. The backscattering background (equation (4.15)) describes the energy distribution over a wide range until the detection threshold. Selecting the real part Re prevents this term from becoming imaginary during the fit. The Heaviside step function Θ prevents it from becoming negative for $E > \mu$. The response function consists in total of ten free parameters, where

μ is the mean of the Gaussian function (usually $\mu \approx E_{\mathrm{in}}$),

σ is the width of the Gaussian function and the dead layer tails,

n_0 is the overall normalization,

n_i with $i \in \{1,2\}$ are the normalizations of the two dead layer tails relative to n_0,

n_3 is the normalization of the backscattering background relative to n_0,

β_i with $i \in \{1,2\}$ are the slopes of the low energetic half of the dead layer tails,

a is the detection threshold cutoff,

b is the curvature of the backscattering background at its low energy end, and

c is the curvature of the backscattering background at its high energy end.

If necessary, the silicon escape peak is described by one additional Gaussian function with position $\mu - E_{\text{esc}}$ and amplitude n_4:

$$f_{\text{esc}}(E; \mu, \sigma, n_0, n_4) = n_0 \cdot n_4 \cdot \mathrm{e}^{-\left(\frac{\mu - E_{\text{esc}} - E}{\sqrt{2}\sigma}\right)^2} \quad . \tag{4.16}$$

This model is used throughout this thesis to determine the detector response whenever necessary. Its parameters are thereby referred to as ψ. The model has shown to be flexible enough to approximate both simulated and measured electron spectra of any initial energy and provides a satisfying fit results in all applications.

4.4 Entrance window investigations

As described in section 4.3.1.1, the entrance window of the P-0 chips is covered by an insensitive SiO_2 layer and a subsequent region of incomplete charge collection. The thickness of the SiO_2 layer is known to be 10 nm, determined via ellipsometry. This is possible, as SiO_2 has different optical properties than the bulk made of pure silicon.

The properties of the region of incomplete charge collection are more difficult to determine. Although doping profile and electric field are known, the CCE cannot be easily inferred from this information. In this section, chips with different doping profiles and thus different CCEs are compared to make relative statements on their performance and to identify the best technology for TRISTAN. The entrance window technologies applied to the P-0 chips are listed in table 4.3.

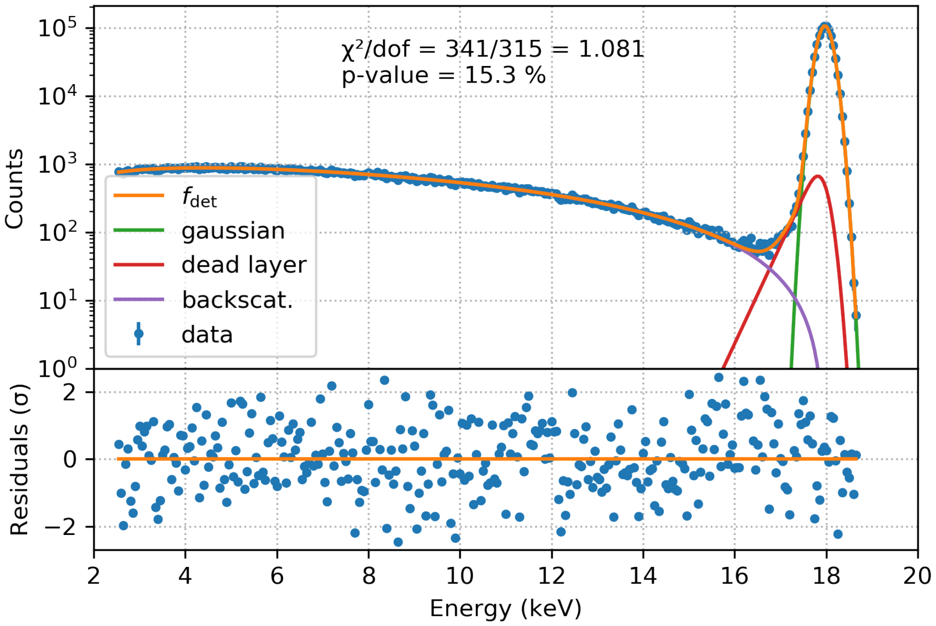

Figure 4.21: **Simulated spectrum and empirical response model.** The plot shows a fit of the empirical model in equations (4.13) to (4.15) to a mono-energetic response at 18 keV simulated using KESS. The ROI begins above the detection threshold at 2.5 keV. Only one dead layer tail and no silicon escape peak is assumed.

Table 4.3: **P-0 entrance window technologies.** The label $x \in 1{,}2$ is a consecutive number for the various chips with the same entrance window technology. "Counter implantation" refers to an additional doping with donors at higher energies to counteract the effect of the acceptors in deeper regions. A reduced dose of acceptors reduces the doping strength to begin with. These technologies were applied with the goal of improving the CCE with regard to the standard implantation.

Doping profile	Abbreviation
Standard implantation	S0-x
Standard dose with counter implantation	SC-x
Reduced dose implantation	R0-x
Reduced dose with counter implantation	RC-x

4.4.1 Entrance window models

The effect of the entrance window on the spectral shape is a spectral distortion at the low energy shoulder of the main peak and a shift of the latter towards lower energies. The strength of the effect can thus be quantified by measuring one or both features. However, both distortion and shift depend on the initial electron energy E_{in}. To describe the entrance window effect independently of E_{in} but as a characteristic feature of the individual detector, a model is required, which only depends on intrinsic parameters of the chip. A straightforward approach is to express the CCE as a function of depth z inside the detector. In a next step, KESS simulations are performed, tracking each energy deposition over the thickness of the detector, on which the CCE function is applied. With that, the measured peak position shift in eV can be translated to a characteristic depth d of the CCE in terms of nm. There are many functions to think of in order to describe a z-dependent CCE. Two of them are presented in the following.

Dead layer model The simplest model is a completely insensitive layer on the detector surface, which is called “dead layer”. The CCE is a step function

$$\mathrm{CCE}\,(z) = \begin{cases} 0 & \text{for } z \leq d \\ 1 & \text{for } z > d \end{cases} \tag{4.17}$$

and is characterized by only one parameter: the depth of the insensitive area d. It is simple and fast to apply. However, this model fails in reproducing all spectral details [Wal13], which is expected, as a step-like efficiency increase in a physical process is unlikely.

Partial event model A more sophisticated description of the entrance window CCE is given by a partial event model [Lec98, Pop00]. The name originates from the fact, that a certain part of the charge could is detected, while some other part is lost. One possible way to parameterize the corresponding CCE is [Leb19]

$$\mathrm{CCE}\,(z) = \begin{cases} 0 & \text{for } z < s \\ \frac{1}{2} \cdot \left[1 + \mathrm{erf}\left(\frac{z-d}{\sqrt{2s^2}}\right)\right] & \text{for } s \leq z \leq d\,. \end{cases} \tag{4.18}$$

The model is described by two parameters, where d determines the thickness of a dead layer on the detector surface and s describes the increase in CCE below this layer. Compared to the dead layer model, the characteristic depth d in a partial event model is smaller, as the CCE builds up only in deeper regions.

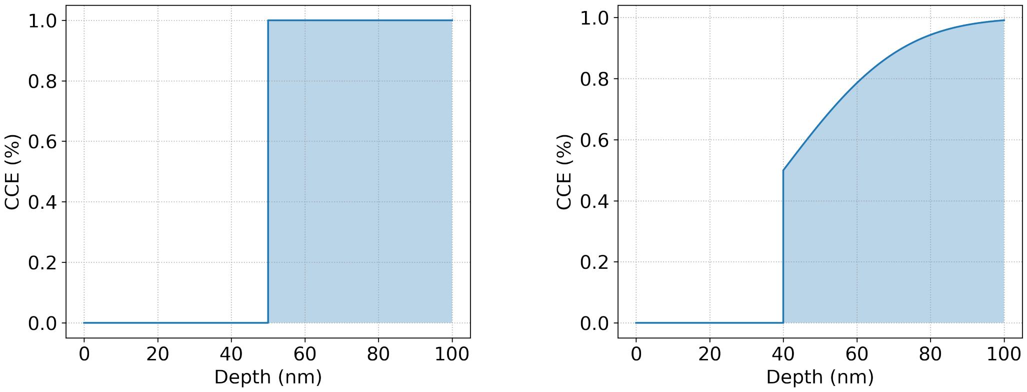

(a) Dead layer model.

(b) Partial event model.

Figure 4.22: **Entrance window models.** (a) The dead layer is a completely insensitive region on the detector surface. Below a certain depth d, the CCE is immediately maximal (here $d = 50\,\mathrm{nm}$). (b) In a partial event model, the CCE below the dead layer (here $d = 40\,\mathrm{nm}$) increases with depth, depending on a second parameter s (here $s \approx 25\,\mathrm{nm}$). The integral (blue shaded regions) are the same under both curves.

4.4.2 Measurements with a scanning electron microscope

In order to measure the peak position shift δ induced by energy loss in the entrance window, a mono-energetic source is required, providing a mono-energetic peak. As the effect is stronger for charged particles, electrons are preferred over photons.[3] Such a source, available for TRISTAN, is the scanning electron microscope (SEM) “JSM-IT300” from Jeol, located at HLL.[4] Measurements with P-0 detectors at the SEM and the analysis of the aquired data are documented in reference [Sie19]. The underlying ideas and concepts, as well as the results of these investigations are summarized in the following.

4.4.2.1 Experimental setup & electron microscope

Electron microscopes are generally used to visualize structures, which are too small to be resolved optically. As electrons are massive particles, they are described by a de Broglie wavelength

$$\lambda = \frac{h}{p} \tag{4.19}$$

---

[3] The effect is even stronger with heavier particles (see appendix A).

[4] JEOL (Germany) GmbH, Gute Änger 30, 85356 Freising, Germany.

with momentum p and Planck's constant h. The de Broglie wavelength can be orders of magnitudes smaller than the wavelength of optical photons. Thus, smaller structures are resolvable. Analogous to glass lenses in an optical light microscope, electron optical lenses are formed by a shaped magnetic field in order to focus the electron beam onto the sample.

A SEM works in a way that the image area is repeatedly scanned with an electron beam of a size in the order of 10 nm. The electrons are emitted from a tungsten spiral heated to around 2000 °C and accelerated in an electric field. The heat of the tungsten spiral determines the intensity of the electron beam, while the electric field strength provides electron energies in the range of $0.3 - 30$ keV. The electron beam scans over the sample, focused by a fast changing magnetic field. The backscattered electrons are analyzed by detectors situated next to the sample desk inside a vacuum chamber. As different surfaces have different absorption and thus different backscattering properties, an image of the sample based on the intensity of the backscattered electrons is reconstructed.

Figure 4.23(a) shows a picture of a P-0 detector inside the SEM vacuum chamber at HLL. A dedicated holder was designed to adjust the detector on the sample desk. The read-out electronics are placed outside vacuum and are not visible on the picture. A feedthrough was welded into a flange of the microscope vacuum chamber to provide the electrical connection between detector and read-out. Figure 4.23(b) shows a picture of a P-0 chip, taken with the SEM.

Prior to the electron measurements, a calibration was performed using an ^{241}Am source, mounted in a holder above the detector. It should also be noted, that the non-conductive SiO_2 layer on the entrance window surface gets charged up, when it is exposed to the electron beam over a longer time. As a consequence, incident electrons feel a repulsive potential δ_{charge}, which decreases the measured energy as a function of time. To mitigate this effect, the detector should not be illuminated with high intensity of the electron beam over a longer period. High intensity is required to produce a SEM picture, which helps positioning the detector in the vacuum chamber. For an electron measurement, the beam intensity has to be greatly reduced to not saturate the read-out. Further mitigation is possible by changing the position of the incident beam on the chip surface from time to time.

4.4.2.2 Bremsstrahlung method

The precision of the SEM's electron beam energy is very high (< 1 eV), while its accuracy is only about 2 % of the set value. Thus, the beam energy is calibrated using its Bremsstrahlung spectrum. To this end, a 6 µm thick aluminum foil was

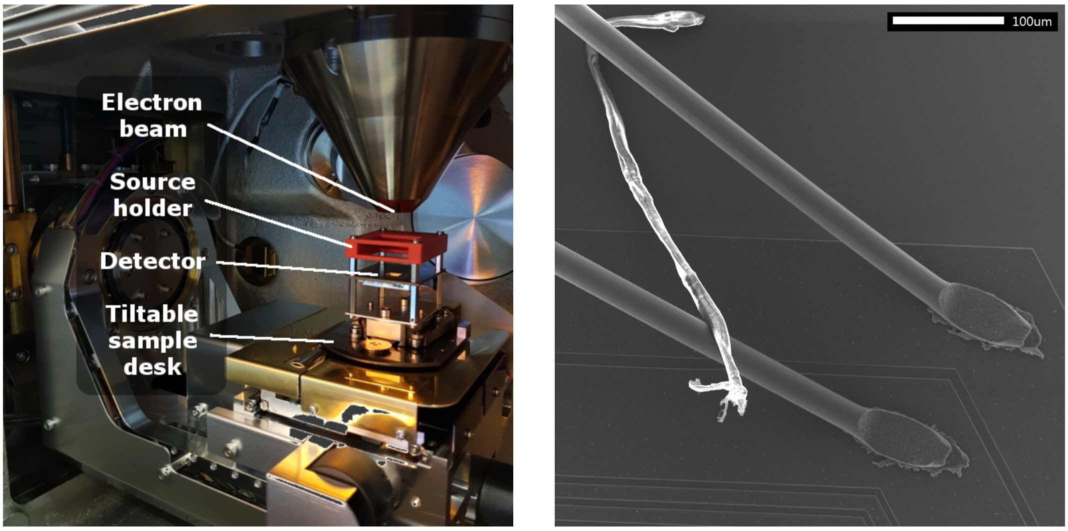

(a) P-0 inside the SEM vacuum chamber. (b) SEM picture of P-0 backside bonds.

Figure 4.23: **Electron microscope vacuum chamber and P-0 backside bonds.** (a) The detector entrance window is facing upwards and is centered below the exit of the electron beam of the SEM. The red structure is a plastic holder to mount calibration sources. Both detector and holder are installed on a 5-axis movable sample desk, allowing to change the incident angle of the electron beam relative to the detector surface. (b) Picture of the back frame and back contact bonds of P-0, taken with the SEM. A hair was found between the two bonds, which was removed before starting the entrance window measurements.

inserted into the beam line. Inside the aluminum material, electrons are stopped creating Bremsstrahlung. The Bremsstrahlung spectrum was measured with the P-0 detector, where the spectral endpoint E_0 determines the absolute energy of the electron beam. The peak shift induced by the entrance window is determined by comparing E_0 with the main peak position μ in an electron spectrum, measured after having removed the aluminum foil. This way, the measurement is decoupled from inaccuracies of the electron beam energy. It was checked that the set electron beam energy is reproduced after opening and closing the vacuum chamber to remove the aluminum foil.

For the Bremsstrahlung measurement, the beam energy was set to 18 keV. Although the entrance window effect is stronger for lower energies, 18 keV were necessary to achieve a reasonable count rate with the given thickness of the aluminum foil. Lower energies can be chosen with thinner foils, which were however not available for the experiment. With a count rate for Bremsstrahlung photons of around 166 cps, the acquisition was performed over 12 h, to gain a reasonable amount of data in the spectral endpoint region. Only events in the central pixel are analyzed. Figure 4.24(a) shows a fit to the obtained Bremsstrahlung spectrum, using Kramer's law up to the second order [Fer71]

$$f(E) = A \cdot \frac{E_0 - E}{E} + B \cdot \frac{E_0 - E}{E^2} \ , \tag{4.20}$$

where A and B are normalization factors. The fit yields an endpoint position $E_0 = 17.757(7)\,\mathrm{keV}$.

For the electron measurement, the aluminum foil was removed from the beam line. Apart from that, the experimental setup remained unchanged. The electron spectrum, acquired within a measurement time of 30 min, is fit using the empirical model for electrons in equations (4.13) to (4.15). An additional Gaussian function was added to fit the escape peak according to equation (4.16). The result is shown in figure 4.24(b). The fit yields a peak position $\mu = 17.648(1)\,\mathrm{keV}$, resulting in an energy shift $\delta = E_0 - \mu = 99(7)\,\mathrm{eV}$. Considering all possible influences, the peak shift consists of the following constituents:

$$\delta = \delta_{\mathrm{window}} + \delta_{\mathrm{bias}} + \delta_{\mathrm{source}} \ , \tag{4.21}$$

where δ_{window} is the shift due to energy losses in the entrance window, $\delta_{\mathrm{bias}} = 88\,\mathrm{eV}$ is the shift due to the bias voltage, and δ_{source} a potential influence of the source. After subtracting $\delta_{\mathrm{bias}} = 88\,\mathrm{eV}$, the measured shift remains affected by possible influences of the source:

$$E_0 - \mu = 11(7)\,\mathrm{eV} = \delta_{\mathrm{window}} + \delta_{\mathrm{source}} \ . \tag{4.22}$$

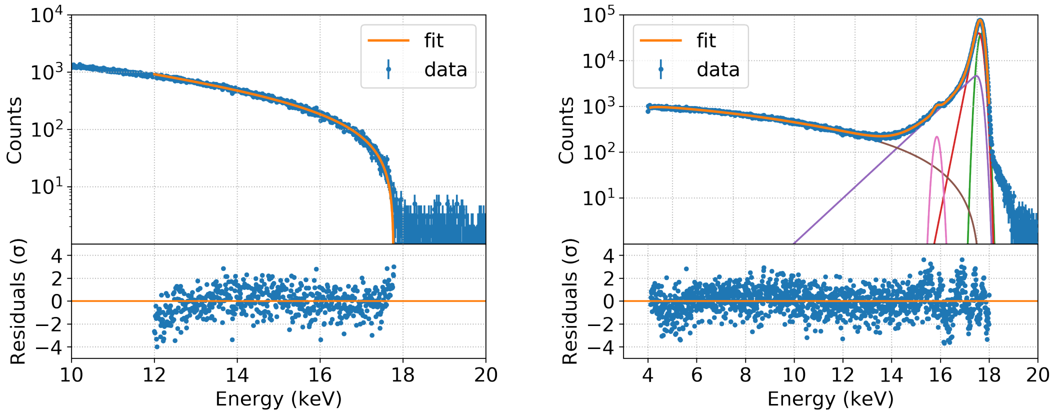

(a) Fit to the Bremsstrahlung spectrum.

(b) Fit to the SEM electron spectrum.

Figure 4.24: **Analysis of the Bremsstrahlung method.** Measured events are displayed in blue, the fit is shown in orange. The residuals of the fit are given in units of the statistical uncertainty σ. (a) The endpoint of the Bremsstrahlung spectrum is determined by a fit using Kramer's law in equation (4.20). (b) The electron spectrum is fit with the empirical model in equations (4.13) to (4.16). The individual subfunctions of are shown in different colors. Both adapted from [Sie19].

Furthermore, it is not clear, how the aluminum foil influences the electric field between the exit of the electron beam tube (0 V) and the detector entrance window (−88 V). The Bremsstrahlung method is thus not reliable enough to determine properties of the entrance window. Additionally, it is limited for technical reasons: Even with a barely tolerable high current at the tungsten spiral, the count rate of Bremsstrahlung photons on the detector is low, which requires measurement times of 12 h. As a consequence, only one entrance window technology was investigated, namely the standard implantation. Further measurements at different energies would also enable to establish a more sophisticated entrance window model, based on more than one parameter.

4.4.2.3 Tilted beam method

To eliminate possible influences of the source and to compare the different entrance window technologies among each other, the tilted beam method was applied [Joh90]. The principle is visualized in figure 4.25, using a dead layer model. By tilting the beam direction relative to the detector surface by a given angle α, the distance, which

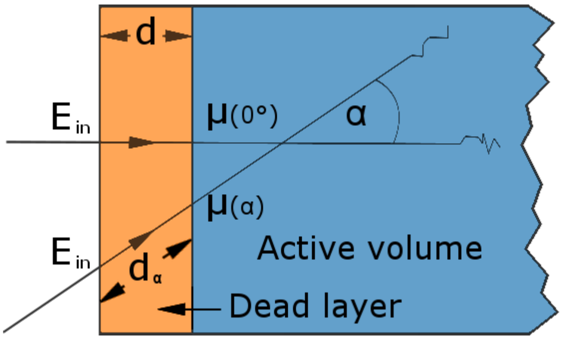

Figure 4.25: **Scheme of the tilted beam method.** A dead layer model is assumed with an insensitive region (orange) of thickness d. The sensitive volume is shown in blue. A measurement of electrons with initial energy E_{in} yields a peak position at μ_0 for perpendicular incidence and at μ_α for a beam, tilted by an angle α relative to the detector surface. Adapted from [Joh90].

electrons travel through the dead layer d effectively increases with α to d_α.[5] From geometrical considerations, the respective peak shift is derived as

$$\delta_\alpha + \delta_{\mathrm{bias}} + \delta_{\mathrm{source}} = E_{\mathrm{in}} - \mu\left(\alpha\right) = \frac{\mathrm{d}E}{\mathrm{d}x} \cdot \underbrace{d \cdot \frac{1}{\cos\alpha}}_{d_\alpha} \,, \tag{4.23}$$

where $\frac{\mathrm{d}E}{\mathrm{d}x}$ is the electrons' stopping power in silicon and δ_α is the influence of the entrance window, now with a certain incident angle α. All three δ_α, δ_{bias}, and the dependence on the absolute calibration of the electron beam energy E_{in} are eliminated by comparing δ_α with shift at perpendicular incidence $\alpha = 0°$:

$$\mu\left(0°\right) - \mu\left(\alpha\right) = \frac{\mathrm{d}E}{\mathrm{d}x} \cdot d \cdot \left(\frac{1}{\cos\left(\alpha\right)} - 1\right) \,. \tag{4.24}$$

4.4.2.4 Comparison of entrance window doping profiles

The tilted beam method is applied to directly compare the different entrance window technologies applied to the various P-0 chips. Using detector S0-1 (see table 4.3), the peak position difference $\Delta E_\alpha = \mu\left(0°\right) - \mu\left(\alpha\right)$ was measured at several angles for $E_{\mathrm{in}} = 14\,\mathrm{keV}$. The cosine dependence in equation (4.24) results in a strong increase of the effect at large angles. The maximal angle was $\alpha = 60°$, as also the backscattering probability rapidly increases with larger angles (see figure 4.15(b)).

---

[5] As in this case the electron beam is fixed and the detector is movable, the expression "tilted detector method" would be more appropriate.

The application of equation (4.24) requires the knowledge of the stopping power $\frac{\mathrm{d}E}{\mathrm{d}x}$. As explained in section 4.3.1.1, however, simulations yield more accurate results than a calculation using $\frac{\mathrm{d}E}{\mathrm{d}x}$. Therefore, KESS simulations were performed to translate this result to an entrance window thickness in terms of nm. Assuming a simple dead layer (see equation (4.17)) with various thicknesses d, the peak shifts δ_α were simulated with the same angles α and incident energy E_{in} as in the measurement. A linearly increasing detector resolution was implemented according to the ^{241}Am calibration measurement. The peaks in the simulated spectra are fit in the same manner as the measured ones. A linear behavior between peak shift and dead layer thickness is found (see figure 4.26(a)). The cosine in equation (4.24) leads to the functional relation shown in figure 4.26(b). For all dead layer thicknesses a χ^2-value is calculated, quantifying the agreement between simulated and measured result. The minimum is found at

$$d^{\mathrm{S0-1}} = 94(7)\,\mathrm{nm}\ , \tag{4.25}$$

which can thus be interpreted as the thickness of the entrance window, according to the applied dead layer model. No additional calibration of the electron gun is required, which makes this method much easier applicable and faster to perform than the Bremsstrahlung method. It should be mentioned, that both methods rely on the accuracy of simulations with KESS. The result also confirms, that the energy-dependent peak position difference ΔE_α can be related to an energy-independent property of the detector. This property of the detector can be used as an input to model the detector response using either simulations or an analytic model.

A second detector with standard implantation technology, S0-2, was measured under the exact same conditions. Its effective dead layer thickness is found to be

$$d^{\mathrm{S0-2}} = 52(7)\,\mathrm{nm}\ . \tag{4.26}$$

Due to its thinner entrance window, detector S0-2 is used as a reference to compare with other entrance window technologies. The reason for the larger effective dead layer thickness of S0-1 could not be determined. A fully functional detector with reduced dose and counter implantation (RC-x) was not available at the time of the measurements. SC-2 shows an effective dead layer thickness of only

$$d^{\mathrm{SC-2}} = 6(7)\,\mathrm{nm} \tag{4.27}$$

but a 20 % worse resolution due to 5 times higher leakage current. Even by cooling the detector to −30° the resolution cannot be recovered to the same level as with detector S0-2. Consequently, an entrance window with standard dose and counter implantation is not suited for the TRISTAN detector. Investigations with detector

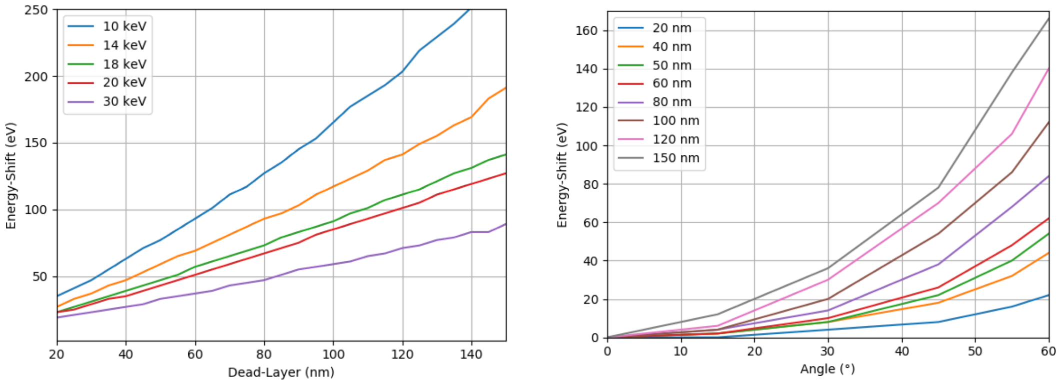

(a) Peak shift over dead layer thickness.

(b) Energy difference over incident angle.

Figure 4.26: **Simulations of the entrance window effect.** The curves were determined using KESS. (a) The graph shows the peak shift δ of the main peak in an electron spectrum over the thickness of a dead layer on the detector entrance window surface relative to the incident energy E_{in}. (b) This graph shows the peak position difference ΔE in a measurement with tilted detector at an incident angle α compared to perpendicular incidence ($\alpha = 0°$) for an initial energy $E_{\mathrm{in}} = 14\,\mathrm{keV}$. Both adapted from [Sie19].

R0-2 yield an effective dead layer thickness of

$$d^{\mathrm{R0-2}} = 46(6)\,\mathrm{nm}\ , \tag{4.28}$$

which is compatible with the result of S0-2 within uncertainty. The same is true for the measured energy resolution. However, the implantation technology with a reduced dose has not been tested as much as the standard implantation, which is more reliable. Thus, the standard implantation technology is the baseline for the TRISTAN detector. A summary of all investigated detectors is given in table 4.4.

4.4.2.5 Conclusion

The SEM is a useful tool to investigate features of the detector, as it provides a narrow and stable, mono-energetic electron beam. It was used to study the impact of different entrance window technologies on the performance of the P-0 detectors. A counter implantation results in an extremely thin effective dead layer but the energy resolution of this detector suffers from an increased leakage current. An implantation with a reduced dose brings no major advantage over the standard implantation. Based on these observations, the well-tested standard technology was identified

Table 4.4: **Effective dead layer thicknesses of P-0 detectors.** The entrance window thicknesses d are listed for all detectors investigated at the SEM. The values are based on simulations with KESS. At the time of the measurements, no fully functional detector with reduced dose and counter implantation (RC-x) was available.

Detector	d (nm)
S0-1	94(7)
S0-2	52(7)
SC-2	6(7)
R0-2	46(6)

as the best suited technology for the TRISTAN detector to date. In the future, measurements at different energies are foreseen, to establish a more sophisticated model for the CCE in the entrance window.

4.4.3 Measurements with a ^{83}Rb/$^{83\mathrm{m}}$Kr source

Another source of mono-energetic electrons, used to study the detector response and in particular the entrance window of the P-0 detectors, is a ^{83}Rb/$^{83\mathrm{m}}$Kr source. This section summarizes investigations [Leb19] of this source with P-0 detectors.

4.4.3.1 Experimental setup & ^{83}Rb/$^{83\mathrm{m}}$Kr source

Rubidium-83 (^{83}Rb) is produced by exposing a gaseous krypton target to a proton beam for around 12 h [Sen18]. It decays via pure EC to krypton-83m ($^{83\mathrm{m}}$Kr) with a half-life $T_{1/2} = 86.2\,\mathrm{d}$, emitting two x-rays at 12.6 keV and 14.1 keV, respectively [McC15]. $^{83\mathrm{m}}$Kr is the second excited state of ^{83}Kr with an excitation energy of 41.6 keV. It deexcites via a cascade of two γ-transitions with the energies 32.2 keV and 9.4 keV. These transitions also provide a large number of conversion electrons. Neglecting recoil energies of γ- and electron emission, the energy of a conversion electron E_n emitted from an atomic shell n is given by

$$E_n = E_\gamma - B_n \;, \tag{4.29}$$

with the energy of the emitted photon E_γ and the electron binding energy B_n of the respective shell. The K-shell has the highest binding energy $B_\mathrm{K} = 14.4\,\mathrm{keV}$, which results in a conversion electron line at $E_\text{K-32} = 17.8\,\mathrm{keV}$ for the 32.2 keV γ-transition.

Table 4.5: **X-ray, γ- and conversion electron lines of ^{83}Rb and $^{83\mathrm{m}}$Kr.** Listed are the weighted averages of all sublines [Chu99, Vén18]. The M and N conversion electron lines of the same transition lie so closely together that they are treated as a single peak.

(a) photons

Isotope	Origin	Energy (keV)	Intensity (%)
^{83}**Rb**	Kr-K$_\alpha$	12.633	51.000
	Kr-K$_\beta$	14.126	7.744
$^{83\mathrm{m}}$**Kr**	ϵ	9.396	9.396
	ϵ	32.147	32.147

(b) electrons

Isotope	Origin	Energy (keV)	Intensity (%)
$^{83\mathrm{m}}$**Kr**	L-9.4	7.516	79.970
	M,N-9.4	9.152	14.184
	K-32	17.824	24.800
	L-32	30.446	63.660
	M,N-32	31.950	11.443

Conversion electrons from the K-shell do not exist for the 9.4 keV γ-transition, as $E_\gamma < B_\mathrm{K}$. The conversion electron lines originating from the shells L, M and N exist for both γ-transitions. The M and N lines lie so closely together, that they are treated as a one. Additional lines arise from further x-ray transitions with lower energies and the emission of Auger electrons, filling vacancies in the electronic shell. However, they are of minor interest for the following investigations, as the respective peaks lie in a low energetic continuum, polluted by fluorescence lines of surrounding materials, mostly iron and copper. A summary of all relevant photon and conversion electron lines emitted in the decay and deexcitation cascades of ^{83}Rb and $^{83\mathrm{m}}$Kr is given in table 4.5. For the sake of simplicity, only the term $^{83\mathrm{m}}$Kr source is used to refer to the products of the combined decay cascades of both ^{83}Rb and $^{83\mathrm{m}}$Kr.

Due to its conversion electron line at 17.83 keV, which is only by about 760 eV lower than the tritium endpoint, $^{83\mathrm{m}}$Kr has been frequently applied in many tritium neutrino experiments for calibration purposes [Rob91, Pic92, Sto95, Lob02]. Such $^{83\mathrm{m}}$Kr sources are produced at the U-120M cyclotron of the Nuclear Physics Institute of the Czech Academy of Sciences.[6] At the KATRIN experiment, calibration phases are regularly performed, in which $^{83\mathrm{m}}$Kr is injected in gaseous form into the WGTS. $^{83\mathrm{m}}$Kr also exists in the form of solid sources, which are applied in the KATRIN monitor spectrometer [Erh14, Sle15]. For the TRISTAN project, $^{83\mathrm{m}}$Kr sources are of specific interest for the following reasons:

- The conversion electron lines appear in first approximation as discrete, mono-energetic peaks in the spectrum.

---

[6] Nuclear Physics Institute, Czech Academy of Sciences, Hlavní 130, Řež, 250 68 Czech Republic.

- The measured spectrum contains both photon and electron lines, which enables an in-situ calibration (photons) and the physics measurement (electrons) at the same time.
- Several lines of both photons and electrons lie in the ROI for KATRIN, i.e. in the low keV range.

For the entrance window investigations, evaporated sources are used as they can be easily installed inside the TRISTAN test stand vacuum chamber. They are produced by evaporating ^{83}Rb in vacuum, where it is deposited as a mono-atomic layer on a graphite carrier substrate. As the layer thickness is in the order of single atoms, the emitted conversion electrons do not have to pass through a thick layer of ^{83}Rb, where they would deposit parts of their energy from the deexcitation. As soon as a ^{83}Rb atom decays into $^{83\mathrm{m}}$Kr, it becomes gaseous at room temperature. Only conversion electrons emitted by krypton atoms, which stick to the surface of the substrate and decay there reach the detector. The ratio of these atoms to atoms, which are pumped out of the vacuum chamber before they decay is described by the retention factor, which depends on the carrier substrate. Sources for TRISTAN were produced using two different materials as carrier substrates, namely rigid graphite and highly oriented pyrolytic graphite (HOPG). HOPG is assumed to have better backscattering properties, as the individual graphite crystallites are well aligned with each other.

Unlike the x-ray and γ-sources introduced in section 4.2, the $^{83\mathrm{m}}$Kr sources do not have a cover on their surface, as this would lead to an energy loss of the emitted electrons. As also air would stop the electrons, the sources need to be operated in vacuum. The pressure in the vacuum chamber was below $5 \cdot 10^{-5}$ mbar in all measurements. Figure 4.27 shows a copper holder specifically designed to install a $^{83\mathrm{m}}$Kr source in the TRISTAN test stand vacuum chamber. The good thermal conductivity of copper enabled stabilizing the detector and source temperature to 15°. The holder is tiltable up to an angle of 60° around an axis, aligned with the center of the detector chip. It has to be noted, that due to the expansion of the source, the maximal incident angle of conversion electrons in the detector is 38°, even without tilting the holder. In measurements of the entrance window properties, this will lead to a slight overestimation of its thickness.

4.4.3.2 Comparison of calibrations with ^{241}Am & $^{83\mathrm{m}}$Kr

Prior to the $^{83\mathrm{m}}$Kr measurement, a calibration using an ^{241}Am source was performed. It serves as a cross check of the calibration determined using the photon lines in the $^{83\mathrm{m}}$Kr spectrum. The ^{241}Am peaks were approximated with Gaussian functions,

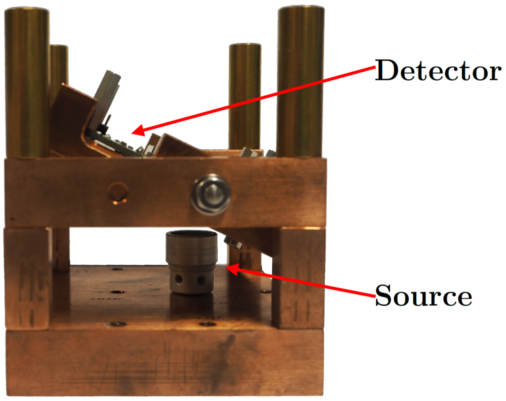

Figure 4.27: **Copper holder for the $^{83\mathrm{m}}$Kr source.** The detector is mounted on a tiltable stage. The entrance window faces downwards to the source. Due to the high thermal conductivity of copper, the holder provides the possibility to stabilize the temperature of both the detector and the source. Adapted from [Leb19].

yielding a linear calibration function $E = m \cdot x + c$ with

$$m = 5.1649(6)\,\frac{\mathrm{eV}}{\mathrm{ADC\,bin}}\ , \tag{4.30}$$

$$c = 479(5)\,\mathrm{eV}\ . \tag{4.31}$$

All measurements with $^{83\mathrm{m}}$Kr were performed over 48 h. A typical spectrum of $^{83\mathrm{m}}$Kr with perpendicular incidence is shown in figure 4.28.

The energy calibration is performed with the Kr-K$_\alpha$ and Kr-K$_\beta$ lines, which are approximated by the combination of a Gaussian, a linear, and a step function:

$$\begin{aligned} f_{\mathrm{det}}(E; \mu, \sigma, A_{\mathrm{G}}, A_{\mathrm{S}}, m, c) = {} & A_{\mathrm{G}} \cdot \mathrm{e}^{-\frac{(E-\mu)^2}{2\sigma^2}} \\ & + m \cdot E + c \\ & + A_{\mathrm{S}} \cdot \left[1 - \mathrm{erf}\left(\frac{E - E_0}{\sqrt{2\sigma^2}}\right)\right]\ . \end{aligned} \tag{4.32}$$

The linear function accounts for the backscattering background, originating from lines at higher energies. The step function is necessary to model the small tail originating from energy losses in the entrance window. The parameters of the linear calibration function are

$$m = 5.1649(3)\,\frac{\mathrm{eV}}{\mathrm{ADC\,bin}}\ , \tag{4.33}$$

$$c = 479(3)\,\mathrm{eV}\ , \tag{4.34}$$

which shows an excellent agreement with the calibration using the ^{241}Am source.

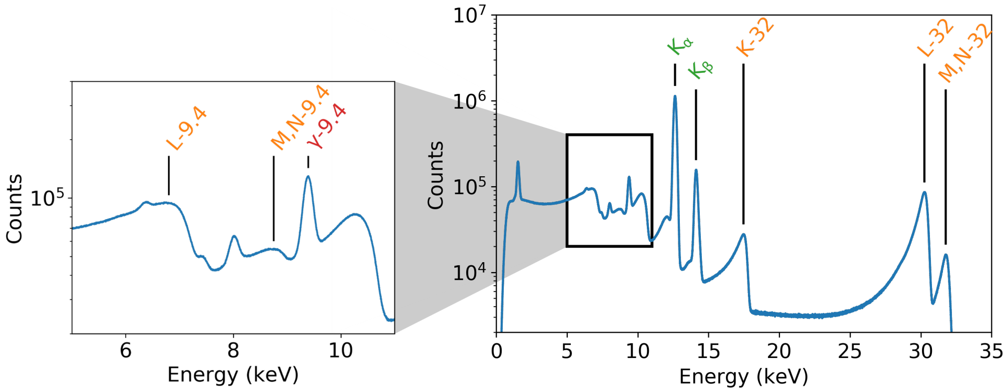

Figure 4.28: **Measured spectrum of the ^{83}Rb/$^{83\mathrm{m}}$Kr source.** The relevant lines for this thesis (see table 4.5) are labeled in colors: X-ray lines in green, γ-lines in red, and conversion electron lines in orange.

4.4.3.3 Comparison of entrance window doping profiles

The tilted beam method was applied to eliminate the impact of the source carrier substrate on the peak position. Measurements with a standard entrance window detector (S0-1) and a reduced dose entrance window detector (R0-2) were performed at two tilting angles, $\alpha = 0°$ and $60°$. The electron lines are fit using the empirical model in equations (4.13) and (4.14). The backscattering background (see equation (4.15)) is replaced by the step function in equation (4.32) and a constant background c. Each subline of the L-32 and M,N-32 peak is fit individually, fixing their relative intensities and positions.

The measured peak position differences $\Delta E_{60°}$ are displayed in figure 4.29 for both detectors, S0-1 and R0-2. As expected, $\Delta E_{60°}$ decreases for higher incident energies, as high-energetic electrons are less affected by the entrance window. Consistently with the measurements at the SEM (see section 4.4.2), detector S0-1 shows a significantly larger effective dead layer thickness than R0-2. However, the absolute value of the effective dead layer of S0-1, derived with the SEM (94(7) nm) and the $^{83\mathrm{m}}$Kr source (146(8) nm), are not in a very good agreement. This difference is attributed to a malfunctioning of S0-1. It is the detector, which was used for most applications in the TRISTAN group and could have suffered from damage in the time period between the measurement at the SEM and the measurement with $^{83\mathrm{m}}$Kr. The investigation should thus be repeated with the second prototype of this entrance window technology, namely detector S0-2.

For detector R0-2, the values of the derived effective dead layer thickness are in good agreement for the SEM (52(7) nm) and $^{83\mathrm{m}}$Kr (48(5) nm) measurements. The slightly larger peak position differences and resulting effective dead layer thickness

Table 4.6: **Effective dead layer thicknesses from SEM and $^{83\mathrm{m}}$Kr.** The effective dead layer thicknesses d obtained from measurements at the SEM and with $^{83\mathrm{m}}$Kr are listed for both investigated detectors. The values obtained from simulations with Geant4 are also listed.

Detector	Source	Simulation	d (nm)
S0-1	SEM	KESS	94(7)
	$^{83\mathrm{m}}$Kr	KESS	146(8)
		Geant4	210(2)
R0-2	SEM	KESS	46(6)
	$^{83\mathrm{m}}$Kr	KESS	48(5)
		Geant4	70(2)

obtained from the $^{83\mathrm{m}}$Kr measurements could result from a broader initial angular distribution due to the expansion of this source and its spacial activity distribution on the graphite carrier. Both is not a priori adjustable in the KESS framework and subject of ongoing investigations. The results of both methods are listed in table table 4.6 for both detectors.

Dependence on simulation codes The results stated above rely on simulations to interpret a peak position shift in terms of eV as an effective dead layer thickness in terms of nm. All values quoted are based on KESS simulations. To test the validity of these results, Geant4 simulations were performed using the same geometry and input values as for KESS. The obtained effective dead layer thicknesses are given in table 4.6. The large discrepancy to the values obtained with KESS must result from the underlying libraries and processes in both simulations. It was found that the Geant4 libraries contain outdated values at least for the transition energies of the x-ray lines Kr-K_α and Kr-K_β. As a result, the peaks in the spectrum are not aligned when comparing both simulations. Furthermore, histograms of the deposited energy in thin layers in the order of tens of nm show very different shapes. Detailed investigations of accounted effects in both simulation packages are required to evaluate their precision with regard to simulating electrons with low energies and energy depositions in thin layers.

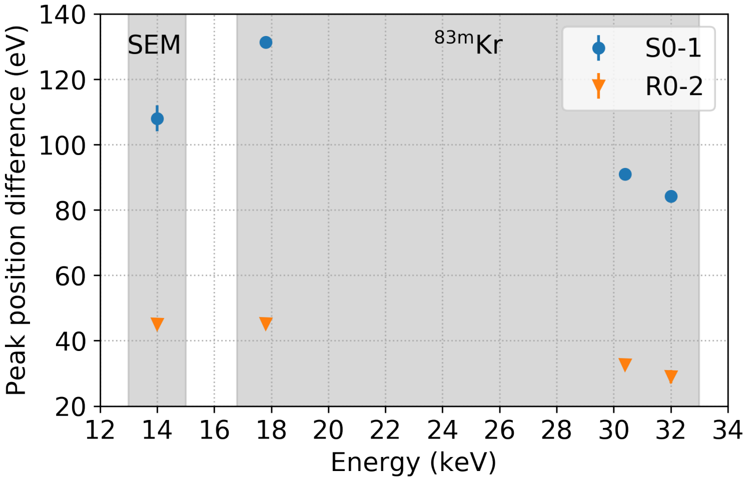

Figure 4.29: **Peak position differences in SEM and ^{83m}Kr measurements.** The peak position difference between $\alpha = 0°$ and $60°$ is shown as a function of incident energy for the measurements at the SEM and with ^{83m}Kr. Almost all error bars are too small to be visible.

4.4.3.4 Conclusion

The ^{83m}Kr source is a useful tool to investigate features of the detector, as it provides both mono-energetic photon and electron lines over the ROI of TRISTAN. It was used to cross check the result of the entrance window investigations performed with the SEM. The derived effective dead layer thickness for R0-1 is in good agreement with the results obtained with the SEM (see section 4.4.2). The effective dead layer thickness of S0-1 was found to be significantly larger than the one for R0-1, which is consistent with the observations with the SEM. The exact value of the effective dead layer thickness of S0-1, however, does not agree well with the SEM result. This difference could possibly arise due to a degradation of detector S0-1 between the two measurements or an undetermined difference between the two used methods. The interpretation of the measured energy shift as effective dead layer was found to depend on the underlying simulation. KESS and Geant4 lead to different effective dead layer thicknesses by about $30-40\,\%$.

To resolve last ambiguities, the ^{83m}Kr measurement is planned to be repeated with a second standard implantation entrance window prototype detector. The exact influence of the distributions of both the initial angle and spacial activity of the source is subject of ongoing investigation. An influence of the used carrier substrate was observed, which makes a relative measurement necessary, based on the described tilted beam method, in order to extract information on the entrance window properties.

5 Sterile neutrino search with a TRISTAN detector at the Troitsk ν-mass experiment

The topics of this chapter are measurement campaigns with a TRISTAN detector at the Troitsk ν-mass experiment. This includes the instrumentation of Troitsk ν-mass with a P-0 system, as well as measurements in two different measurement modes, differential and integral, and the analysis of thereby acquired data. The goal of these investigations is to demonstrate the feasibility of a sterile neutrino search as planned in the upgrade of the KATRIN experiment with the final TRISTAN detector and readout system. The results of this work were published in [Bru19].

In section 5.1, setup and features of the Troitsk ν-mass experiment are introduced. The campaign in differential mode is presented in section 5.2, while the integral campaign is topic of section 5.3. The results of both campaigns are compared with existing limits in section 5.4. The chapter is summarized in section 5.5.

5.1 The Troitsk ν-mass experiment

The Troitsk ν-mass experiment [Abd15] is conducted by the Institute for Nuclear Research of the Russian Academy of Sciences.[1] As a technological predecessor of KATRIN, it was designed to analyze the electron spectral shape in the endpoint region of tritium β-decay in order to measure the effective electron antineutrino mass m_β or to set upper limits. It was commissioned in 1985 and continued the neutrino mass measurement phase until 2005, resulting in a world best upper limit $m_\beta < 2.05\,\mathrm{eV}$ (95 % C.L.) [Ase11] at that time.[2] The data were later reevaluated to search for the admixture of a sterile neutrino with a mass in the range

---

[1] INR RAS, Prospekt 60-letiya Oktyabrya 7a, Moscow 117312, Russian Federation.

[2] A comparable result was reached by the Mainz neutrino experiment [Kra05].

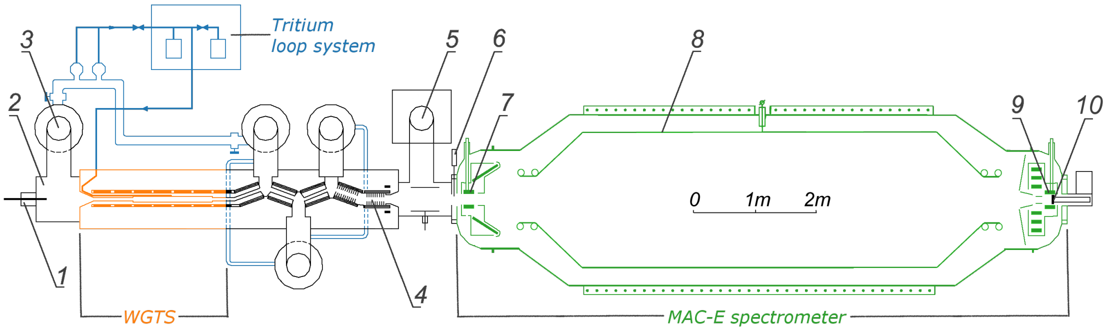

Figure 5.1: **Scheme of the Troitsk ν-mass experiment.**Bblue: tritium loop system; orange: WGTS; green: MAC-E spectrometer; 1 — electron gun; 2 — stainless steel tank; 3 — diffusion pumps; 4 — argon cryo-pump; 5 — Ti-pump; 6 — fast shutter; 7 — pinch magnet; 8 — spectrometer electrode; 9 — detector magnet; 10 — detector. Adapted from [Abd15].

of 2 – 100 eV [Bel13]. In 2015, the setup was upgraded with a larger spectrometer to expand the search to the low keV-range [Abd15]. First results were published in 2017 [Abd17], excluding a sterile neutrino admixture with $m_4 = 1\,\text{keV}$ at $|U_{e4}|^2 < 3 \cdot 10^{-3}$ (95 % C.L.).

5.1.1 Experimental setup

A scheme of the entire Troitsk ν-mass experiment is displayed in figure 5.1. Its experimental setup is very similar to KATRIN's (see section 3.1.2), comprising the two main components WGTS and MAC-E spectrometer. As both components are smaller compared to their equivalents in KATRIN, the activity of the Troitsk ν-mass WGTS is lower by a factor of about ten and the achievable resolution of the spectrometer is worse by a factor of 1.6 ($\Delta E_\perp = 1.5\,\text{eV}$). Other noticeable differences are the following:

- The gas, which is injected into the source section, consists to a large fraction of non-tritiated molecules, namely H_2, hydrogen-deuterium (HD), and D_2. The most abundant tritiated molecule is deuterium-tritium (DT). The gas also contains small admixtures of hydrogen-tritium (HT) and T_2, as well as traces of residual air (N_2 and O_2). The total amount of tritium atoms is not known a priori.

- The tritium loop system is not designed to maintain stable pressure and decay rate in the WGTS. The tritium gas decays and is pumped out, leading to a decrease of the count rate at the detector over the course of a measurement.

The source is periodically refilled, as soon as the count rate at the detector is considered to be too low. A measurement campaign is hence divided into several “fills”.

- The WGTS is not closed by a golden rear wall but the magnetic field lines diverge into a stainless steel tank. The ground potential relative to the spectrometer high voltage is determined by the combined potential of this tank and the source tube.

- The magnetic field inside the WGTS is 0.6 T and rises up to 3.6 T at both of its ends. This field configuration creates a magnetic trap, which confines electrons with initial polar angles $\theta > 24.1°$ to the WGTS. This is intended to prevent electrons, which stem from tritium atoms sticking to the walls of the source tube, to enter the spectrometer. Some electrons escape this trap and reach the spectrometer after inelastic scattering and a large angular change. These electrons can be understood as an additional measured spectrum with redistributed electron energies towards lower values. This mechanism is called “trapping effect” (see section 5.2.3.2).

- The pinch magnet is located at the entrance of the main spectrometer (not at its exit) with a magnetic field of 7.2 T. This results in an acceptance angle $\theta_{\mathrm{max}} = 16.8°$. The detector magnet provides a magnetic field of 2.2 T.

- The detector is a single channel PIN diode with a diameter of 25 mm [Abd15]. Its sensitive area is limited by a copper collimator with a diameter of 17 mm in front of the silicon chip. The detector surface is covered with a thin gold layer, resulting in a detection threshold of 4 keV. The signal is amplified analogously and analyzed with a shaping time of 1 µs. Only afterwards, the signal gets digitized by a 12 bit ADC. The DAQ allows for count rates up to 30 kHz with a constant dead time of 7.2 µs, limiting the ability for a sterile neutrino search at high count rates and thus the accessible mass range. The 30 cm long detector section is separated via a valve from the main spectrometer, which enables to remove the entire detector system, without having to vent the spectrometer volume. Mounted on a movable holder, the detector can be moved further into the detector magnet once the valve has been opened.

Electron sources Additionally to β-electrons from tritium decay, two other electron sources are available in Troitsk ν-mass. It should be noted, that the respective creation mechanisms are different and thus lead to different responses, i.e. spectral shapes, when measured with the detector (see section 5.2.3.1).

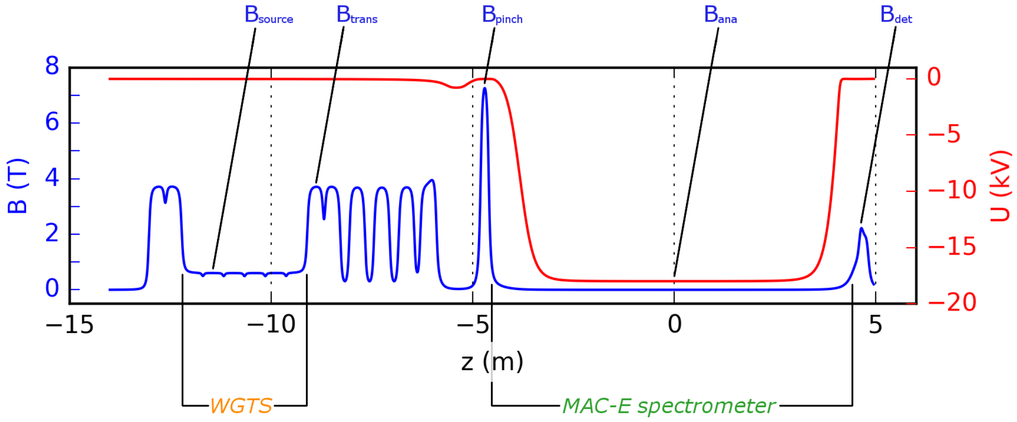

Figure 5.2: **Magnetic and electrostatic fields in Troitsk ν-mass.** The graph shows the field configuration with nominal magnet currents and a retarding potential $U = -18\,\mathrm{kV}$. The z-axis follows the orientation in figure 5.1. The values of the labeled magnetic fields are given in table 5.1.

Table 5.1: **Magnetic fields in Troitsk ν-mass.** The table lists the labeled fields in figure 5.2 from the source towards the detector.

Position	Symbol	Magnetic field (T)
Source tube	B_{source}	0.6
Transport section	B_{trans}	3.6
Pinch magnet	B_{pinch}	7.3
Analysis plane	B_{ana}	$6 \cdot 10^{-4}$
Detector magnet	B_{det}	2.2

An electron gun is installed at the rear end of the setup, providing mono-energetic electrons with a resolution $\sigma_{\text{egun}} < 1\,\text{eV}$ [Abd15]. This is achieved by illuminating a gold cathode, which is set to a negative potential U_{egun}, with an ultraviolet deuterium lamp. The emitted photo-electrons escape the gold surface with an energy $E = eU_{\text{egun}}$. The magnetic air coil system around the spectrometer (usually compensating for the earth magnetic field) is tuned to focus the electron beam onto the detector, where its diameter is about 1 mm. The electron gun is mostly used to measure the gas density in the WGTS (see section 5.3.3).

Another source of mono-energetic electrons is the spectrometer electrode. Electrons are constantly created through impact ionization of positive ions hitting the electrode, which is on a negative potential U_{spec}. When the magnetic field inside the spectrometer is turned off, these electrons are not constrained to the magnetic field lines by the Lorentz force but propagate freely. Some reach the detector, which is on ground potential. Thus, the electrons carry exactly the energy $E = eU_{\text{spec}}$ with a resolution $\sigma_{\text{spec}} < 1\,\text{eV}$, when they hit the detector. As the electrons propagate freely, the count rate is only around 0.1 cps. It is increased to a few tens of cps by turning on the detector magnet: In this configuration, its magnetic field lines point at the spectrometer electrode on one side; on the other side, they are focused onto the detector.

5.1.2 TRISTAN in Troitsk

In 2017, a joint initiative between the TRISTAN group and the Troitsk ν-mass collaboration was started. The idea of this initiative was to integrate a TRISTAN detector system in the Troitsk ν-mass beam line. This approach has the following advantages for both groups:

- The sensitivity of the Troitsk ν-mass sterile neutrino program is limited by systematic uncertainty related to the detector, namely events under detection threshold and electronics dead time [Abd17]. By using the novel TRISTAN detector system, Troitsk ν-mass overcomes its dominant sources of systematic uncertainty.

- The Troitsk ν-mass setup depicts an ideal test stand for the TRISTAN detector, as it is the only KATRIN-like experiment in operation, which is capable of a keV-scale sterile neutrino search using tritium β-decay. The TRISTAN prototype detectors can there be tested in an experimental environment similar to the final application in KATRIN.

Three measurement campaigns with a TRISTAN detector at Troitsk ν-mass were performed so far. Thereby, two different measurement modes were explored:

1. In **differential mode**, the spectrometer retarding energy eU is set to a low value, such that electrons of a wide energy range pass the spectrometer. The energy of the electrons is measured with the detector, which thus determines the resolution of the observed differential spectrum. The latter is defined as the number of counts per energy bin as a function of electron energy E. A sterile neutrino search in this mode has not been performed before, as the excellent energy resolution of the TRISTAN detector system enables to do so for the first time. A measurement campaign in differential mode took place in May and June 2017 over three days with a 1 mm pixel diameter P-0 chip equipped with an Idef-X ASIC. In a proof-of-concept study [Alt19], it was shown that the search for a sterile neutrino signature with Troitsk ν-mass upgraded by a TRISTAN detector is generally possible. A second, extended measurement campaign in differential mode took place in November 2017 over two weeks with the P-0 chip equipped with CUBE ASICs as presented in section 4.1. Measurement, analysis and results of this campaign are presented in section 5.2.

2. In **integral mode**, the spectrometer retarding potential U is scanned over a range of several kV. At each measurement point, only electrons with energies $E > eU$ pass the spectrometer.[3] Their number is determined by integrating over all counts in the differential spectrum measured by the detector. The individual shape of the energy spectrum is in the first instance irrelevant for the analysis. By dividing the number of observed events by the acquisition time, the count rate is determined. The count rate as a function of retarding energy eU yields the integral tritium spectrum. The integral mode is primarily applied in neutrino mass measurements (see section 3.1.1) and thus represents the standard measurement mode of Troitsk ν-mass and KATRIN. A measurement campaign in integral mode with the same TRISTAN P-0 system as in the preceding differential campaign took place in April 2018 over three weeks. Measurement, analysis and results of this campaign are subject of section 5.3.

Low energy structure In the data of both campaigns presented in this work, an undesired structure is observed. It is referred to as the “bump” and appears in differential spectra as a peak on top of the backscattering background, shifted from the set retarding energy by

$$eU - \mu_{\mathrm{bump}} \approx 5\,\mathrm{keV}\ . \tag{5.1}$$

---

[3] Disregarding the work function of for instance the source tube.

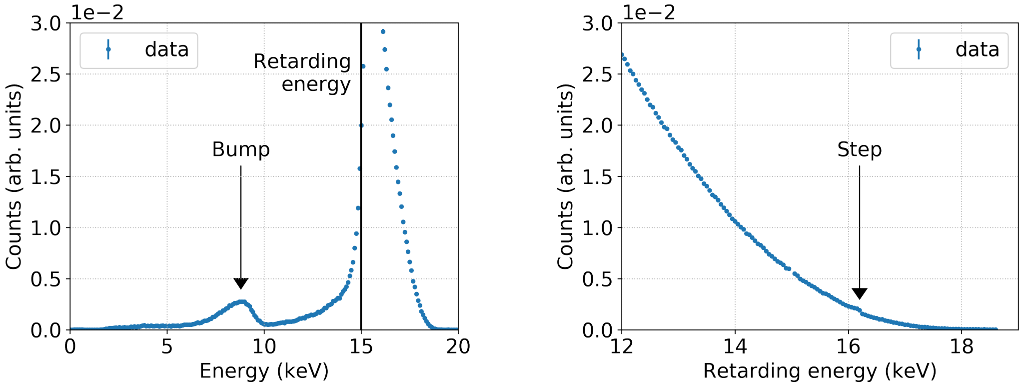

(a) Bump in a differential spectrum.

(b) Bump in an integral spectrum.

Figure 5.3: **Appearance of the bump.** Both plots show a tritium measurement normalized to the total number of counts and acquired during the integral campaign in April 2018. (a) The bump appears around 5.5 keV below the retarding energy in a differential spectrum. (b) In an integral spectrum, the bump leads to a step at around 16 keV, as it appears only in measurements with lower retarding energies.

In integral spectra, the structure appears as a step at a retarding energy $eU \approx 16\,\mathrm{keV}$: The bump only appears in measurements with lower retarding energies, contributing to the count rate in the corresponding range. Examples of measured spectra, both differential and integral, are displayed in figure 5.3.

The origin of the bump is not entirely understood. Negative ions in the residual gas in the spectrometer tank [Sch14] are excluded by a simulation using the stopping and range of ions in matter (SRIM) 2013 package [Zie04, Zie19]: In the simulation, hydrogen atoms with a kinetic energy $E_{\mathrm{in}} = 13\,\mathrm{keV}$ impinge on a silicon detector. Assuming a dead layer model with a thickness of 60 nm, the hydrogen peak does indeed appear at $13 - 5 = 8\,\mathrm{keV}$ in the differential spectrum. However, its width is much larger than the width of the bump observed in the tritium measurements. Another hypothesis relates the bump to a Penning trap in the rear part of the spectrometer, which builds up due to a temporarily increased pressure.

The bump distorts the measured spectral shape, concealing the signal of a possible sterile neutrino admixture. Therefore, all measurements of the differential campaign, in which the bump appears, are excluded from the analysis. In the integral campaign, the bump appears in all retarding energy scans. The bump is thus subtracted from the data and a corresponding systematic uncertainty is introduced (see section 5.3.4.2).

5.2 Differential campaign

The campaign presented in this section took place in November 2017 and is the first sterile neutrino search with the P-0 system as presented in section 4.1. Section 5.2.1 gives an overview of the performed measurements. The thereby acquired data are processed and selected in order to perform a sterile neutrino search, all of which is described in section 5.2.2. Influences of the experimental setup on the measured response are evaluated in section 5.2.3. The sterile neutrino search itself is presented in section 5.2.4.

5.2.1 Measurements in differential mode

The standard Troitsk ν-mass detector is installed on a long rod and cooled by liquid nitrogen. The detector is not easily exchangeable, so that a new holding structure was designed for the TRISTAN prototype. Figure 5.4(a) shows this holder inside a test box, where it was tested prior to its installation in the Troitsk ν-mass setup. The detector was mounted on a plastic plate and connected to a feedthrough in a vacuum flange via a flat cable. The two rods, to which the plate was attached, were rigid and the position of the detector inside the setup was hence fixed. After the standard Troitsk ν-mass detector had been removed from the detector section, the P-0 system was installed with an ^{241}Am source attached to the two rods in front of the detector chip. A calibration measurement with photons was performed, while the shutter to the spectrometer was still closed. To remove the ^{241}Am source, the detector section had to be re-opened. The ambient devices of the setup at the detector section in their final configuration are shown in figure 5.4(b).

The subsequent measurements are divided into two parts. In the first part, tritium was injected into the source section. The current of the magnets was slowly increased, providing a field at the detector position of approximately 0.2 T. The shutter to the source and transport section was opened and β-electron measurements were performed at different retarding energies in the range of $1-16$ keV with rates of about $3-900$ cps. Each of these measurements is referred to as one “run”. Almost every second run was performed at a retarding energy of 13 keV. On the basis of these repetitive so-called “monitor points”, changes in the experimental conditions can be easily identified. Common to all runs are the (standard) settings in table 5.2.

The tritium measurements were interrupted twice: The first time, a measurement of the background was performed with closed shutter to the transport section (run 2). The second time, a magnet quenched due to insufficient liquid helium supply during

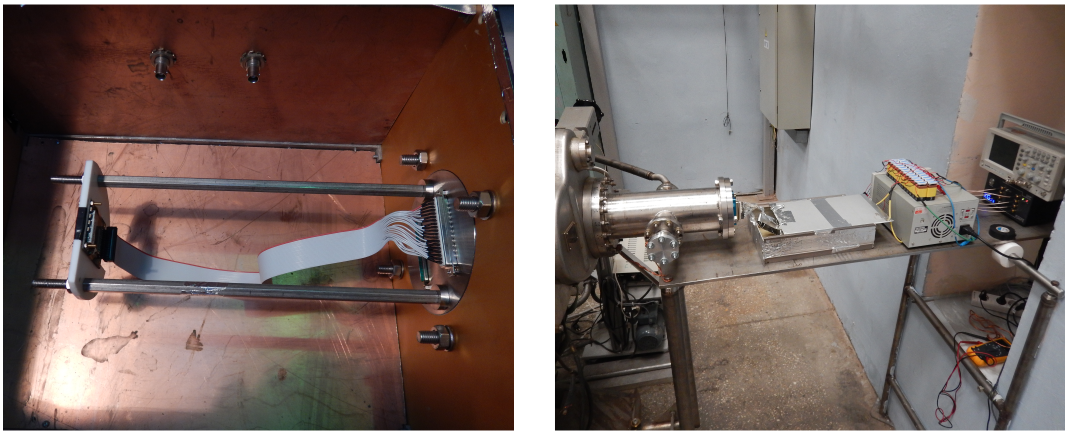

(a) Detector holding structure. (b) Ambient devices.

Figure 5.4: **Setup of the differential campaign.** (a) The picture shows the 30 cm long detector holder in a copper test box before its installation in the Troitsk ν-mass beam line. The detector board was screwed onto a plastic plate, which was attached to two metal rods. Those were mounted on a vacuum flange, which fit to the Troitsk ν-mass detector section. The flat cable electrically connected the detector board to a vacuum feedthrough in the flange. The holder was designed to align the silicon chip at the symmetry axis of the beam tube. The BNC connectors in the background wall had been necessary in the previous campaign with the Idef-X system. (b) The detector was installed at the detector section. The spectrometer is just outside the left frame of the picture. Aluminum tape was applied to the cables to shield them from external noise influences. The bias board was put into a conductive metal box. This box shared its ground potential with the table and the detector tube via a copper cable. Batteries were used to provide a stable high voltage to the detector chip. The bias board was powered with a low voltage power supply. The DANTE box is visible on the right below an oscilloscope, which was used for debugging purposes.

Table 5.2: **Standard measurement settings of the differential campaign.** The nominal magnetic field configuration especially refers to 150 A at the pinch and the detector magnets. The detection threshold in channel 125 is equivalent to about 2.5 keV.

Parameter	Setting
Detector chip	S0-1
Magnetic field configuration	nominal
Energy filter shaping time	0.8 µs
Detection threshold	in channel 125
DANTE firmware version	218.2113.3115

run 17 and had to be restarted. Meanwhile, electrode measurements were performed and a second detector chip was tested (runs 18 and 19). All runs of this first part of the measurement campaign are listed in table 5.3.

The second part of the differential campaign are response measurements, for which the tritium gas was removed from the source section. Electron gun measurements were performed with acceleration energies in the range of 13 – 19 keV (runs 31 – 44). At each energy, the air coil system was tuned to achieve a high rate in the central pixel of the detector chip. Electrode measurements were performed with and without magnetic field (runs 45 – 60). During run 56, episodes with temporarily increased spectrometer pressure led to bursts in the count rate. For the last run, the ^{241}Am source was re-installed to the detector holder and a second calibration measurement was performed with closed shutter (run 61). All runs of this second part of the campaign are listed in table 5.4.

5.2.2 Data quality & corrections

The acquired data is processed and controlled for systematic effects. Corrections are performed and the data is selected with regard to performing a sterile neutrino search.

Calibration Both in the beginning and at the end of the campaign, calibration measurements with an ^{241}Am source were performed. The difference in rates results from the changed alignment of source and detector chip after re-installing the source on the detector holder. The same calibration procedure (see section 4.2) is applied for both measurements but different calibration parameters are obtained, listed in table 5.5. The slopes of the linear calibration function of the two measurements

Table 5.3: **Measurements of the differential campaign (1).** Run 0 is a calibration measurement. Run 2 is a background measurement with closed shutter to the transport section. After a magnet quench (run 17), the magnets had to be restarted. Electrode measurements were performed meanwhile (runs 18 and 19). All measurements were performed with standard settings (see table 5.2), if not stated otherwise: B — bump appearance; 1 — magnets turned off; 2 — magnet quench and source refill; 3 — ramp of magnets; 4 — chip R0-1; 5 — new battery pack.

Date	Run	Source	HV (kV)	Counts ($\cdot 10^3$)	Rate (cps)	Comments
Nov 25	0	^{241}Am	0	37	13.16	1
25	1	tritium	13	541	110.2	
25	2	bknd	13	0	0.0001	
25	3	tritium	12	559	168.3	
25	4	tritium	12.5	623	117.1	
25	5	tritium	13	556	94.0	
25	6	tritium	13.5	566	79.2	
Nov 26	7	tritium	13	558	94.1	
26	8	tritium	14	570	46.8	
26	9	tritium	13	562	79.2	B
26	10	tritium	14.5	488	24.9	
26	10.1	tritium	14.5	6	20.8	
26	11	tritium	14.5	109	19.7	
26	12	tritium	13	315	50.2	B
26	13	tritium	16	60	3.6	
26	14	tritium	13	335	33.0	B
Nov 27	15	tritium	15.5	96	4.6	
27	16	tritium	13	150	23.4	B
27	17	tritium	15	7	3.9	2
27	18	electrode	13	1	0.4	3
27	19	electrode	13	0	0.0003	3, 4
27	20	tritium	15	337	19.0	
27	21	tritium	13	2525	63.2	B
Nov 28	22	tritium	12.5	597	59.5	B
28	23	tritium	12	456	69.0	B, 5
28	24	tritium	11	386	100.0	B
28	25	tritium	9	806	199.3	
28	26	tritium	7	932	352.0	
28	27	tritium	5	2556	575.5	
28	28	tritium	3	3117	877.7	
28	29	tritium	1	3941	888.0	
28	30	tritium	13	1061	24.8	B

Table 5.4: **Measurements of the differential campaign (2).** The column I_{det} states the current of the detector magnet. In therewith labeled measurements, all other magnets were turned off. No entry means nominal currents. B — bump appearance; 1 — rate increase due to pressure excess in the spectrometer.

Date	Run	Source	HV (kV)	Counts ($\cdot 10^3$)	Rate (cps)	I_{det} (A)	Comments
Nov 29	31	e-gun	19	31	52.8		
29	32	e-gun	18	411	733.3		
29	33	e-gun	17	611	665.5		
29	34	e-gun	16	264	449.9		
29	35	e-gun	15	170	210.7		
29	36	e-gun	15	1069	716.3		
29	37	e-gun	13	304	638.6		
29	38	e-gun	14	251	763.6		
29	39	e-gun	16	357	784.3		
29	40	e-gun	13	227	307.8		
29	41	e-gun	14	215	364.2		
29	42	e-gun	16	89	70.5		
29	43	e-gun	13	62	26.7		B
29	44	e-gun	14	244	142.5		
29	45	electrode	13	245	16.0	50	
Nov 30	46	electrode	15	265	16.4	50	
30	47	electrode	14	222	16.2	50	
30	48	electrode	13	244	42.9	150	
30	49	electrode	19	249	46.9	150	
30	50	electrode	18	110	42.6	150	
30	51	electrode	16	138	44.6	150	
30	52	electrode	16	103	53.1	150	
30	53	electrode	15	99	47.0	150	
30	54	electrode	14	104	44.6	150	
30	55	electrode	17	101	46.3	150	
30	56	electrode	13	-	-	0	1
Dec 01	56.1	electrode	13	1	0.9	0	
01	57	electrode	13	26.65	0.7	0	
01	58	electrode	13	2	0.5	0	
01	59	electrode	13	30	0.5	0	
Dec 02	60	electrode	20	20	0.8	0	
02	61	^{241}Am	0	36	18.7	0	

Table 5.5: **^{241}Am calibration in the differential campaign.** Two calibration measurements were performed with ^{241}Am, which yield different calibration parameters for the linear calibration function $E = m \cdot \mathrm{ADC\,channel} + c$.

Run	Slope m (keV/ADC channel)	Offset c (keV)
0	$1.060(6) \cdot 10^{-2}$	$-1.3(1)$
61	$1.057(6) \cdot 10^{-2}$	$-1.5(1)$

match within uncertainty. The different offsets lead to a change of the peak positions of 25 ADC channels, which corresponds to about 265 eV. Furthermore, a calibration drift over the entire campaign is observed with a maximal deviation of 70 eV. This is illustrated in figure 5.5(a) using the calibration parameters obtained in run 61. These ^{241}Am calibrations are thus not used in the analysis. Instead, electron measurements are calibrated as explained in the following.

The calibration of electrode measurements is illustrated in figure 5.5(b). A fit of a Gaussian function to a narrow region around the main peak position of each measured energy is performed. The obtained values are fit linearly to yield the calibration curve. Electron gun measurements are treated analogously.

The calibration of tritium data is performed for every run individually. Two calibration points are extracted:

1. The first calibration point is the so-called “high voltage (HV) cut”, the turning point in a tritium spectrum at the position of the respective retarding energy [Alt19]. In order to determine its position, the first derivative of the measured spectrum is calculated, in which the turning point appears as a peak. The derivative and the subsequent fit of a Gaussian function to the peak are shown in figure 5.6(a). The uncertainty on the position of the HV cut is in the order of 1 % for all tritium measurements.

2. The second calibration point is the endpoint of the tritium spectrum $E_0 \approx 18.575\,\mathrm{keV}$ [Ott08, Mye15]. In order to determine its position, the Kurie plot [Kur36]

$$K\,(\mathrm{ADC\,channel}) = \sqrt{\frac{N\,(\mathrm{ADC\,channel})}{F \cdot p^2}} \tag{5.2}$$

   is generated, where N is the number of counts per ADC channel, F is the Fermi function, and p is the momentum of the electron. The Kurie plot has been developed in 1936 to transform a β-spectrum to a linear shape. This facilitates

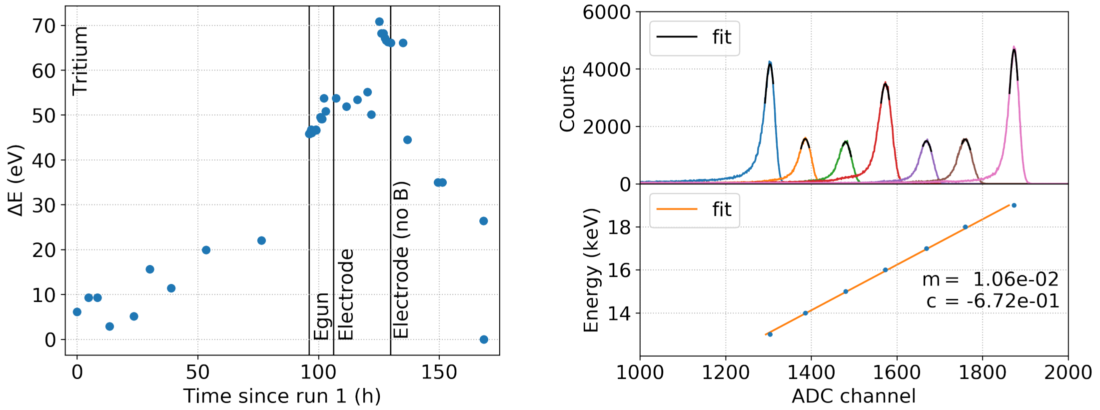

(a) Calibration drift.

(b) Electrode calibration.

Figure 5.5: **Calibration with ^{241}Am and electrode electrons.** (a) The plot shows the deviation ΔE from the set voltage to its measured value for all runs of the differential campaign using the calibration of the ^{241}Am measurement run 61. The error bars are too small to be visible. The maximal deviation is 70 eV. (b) *Top:* Each color shows an electrode measurement at a different spectrometer voltage. Each peak is fit with a Gaussian function to determine its position. *Bottom:* The resulting calibration function is linear, error bars are not visible.

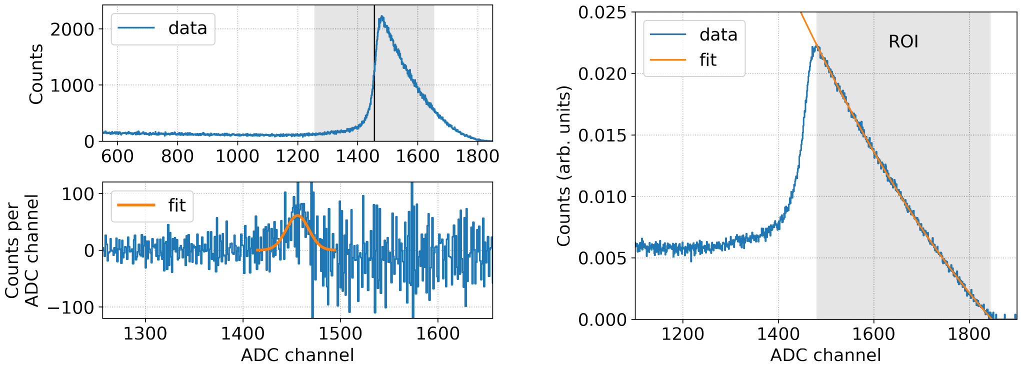

(a) Fit of the HV cut. (b) Fit of the spectral endpoint.

Figure 5.6: **Calibration of tritium measurements.** (a) *Top:* An exemplary tritium spectrum (blue) with a retarding energy $eU = 14.5\,\mathrm{keV}$. The HV cut is marked with a black line. *Bottom:* The derivative of the data in the shaded area is enlarged. The turning point of the HV cut becomes a peak, which is fit with a Gaussian function (orange). (b) The Kurie plot is fit with a second degree polynomial in the ROI (grey). The intersection with the x-axis determines the spectral endpoint position.

a fit of the endpoint and hence the measurement of a neutrino mass without the application of modern computers. An exemplary Kurie plot of run 10 is shown in figure 5.6(b). The displayed spectrum does not have a linear shape due to the experimental response, which is not taken into account. Instead, a second degree polynomial is used to determine the spectral endpoint position.

A calibration based on only two points requires perfect linearity of the detector's calibration function, which has been demonstrated for P-0 in section 4.2. The applied calibration method may still be prone to systematic uncertainty. Therefore, the energy scale is parameterized in the fit to the tritium spectrum (see section 5.2.4.3). The calibration can potentially be improved by directly correcting for detector effects (e.g. entrance window) and accounting for uncertainty of input parameters (e.g. theoretical tritium endpoint).

Resolution The energy resolution for photons is determined in both ^{241}Am measurements: The 14 keV line is fit with a Gaussian function and its width is translated into a FWHM, resulting in

$$\begin{aligned} &277(4)\,\mathrm{eV} \quad (\mathrm{run}\,0),\\ &307(5)\,\mathrm{eV} \quad (\mathrm{run}\,61). \end{aligned}$$

These values are larger compared to the measured resolution in the laboratory at MPP. This is presumably caused by additional noise source in the Troitsk ν-mass experimental hall, which might also explain the deviation between the two runs and the drift of the calibration. The energy resolution for electrons is estimated from the electrode measurements by measuring the FWHM of the peaks directly. Values between

$$\begin{aligned} &306\,\text{eV} \quad \text{at } 13\,\text{keV (run 48)},\\ &402\,\text{eV} \quad \text{at } 18\,\text{keV (run 50)} \end{aligned}$$

are obtained. The resolution for electrons is larger than the resolution for photons, which is expected due to the entrance window effect. It surprises, however, that the 19 keV measurement (run 49) yields the best energy resolution $\Delta E = 285\,\text{eV}$ of all electrode measurements. Also this is probably connected to the unstable experimental setup. In any case, the measured energy resolution is sufficient to perform a first sterile neutrino search with the P-0 system.[4]

Adiabaticity Non-adiabatic effects can arise for electrons with high surplus energies $E_\text{surp} = E - eU$ over the retarding energy eU. In a neutrino mass measurement, the minimal retarding energy is hundreds of eV below the tritium endpoint E_0, the maximal electron energy. Neutrino mass experiments are designed in a way that full adiabatic transport is guaranteed in this energy region. For a sterile neutrino search, however, the retarding energy is lowered several keV below E_0 to access a broader sterile neutrino mass range, leading to higher surplus energies. Electrons with larger E_surp are less decelerated by the retarding potential and traverse the spectrometer with higher velocities. Here, the magnetic field gradient ΔB is crucial: If an electron traverses a large ΔB with a high velocity, its orbital magnetic moment μ is not conserved any longer (see section 3.1.1). This leads to chaotic changes of the electrons' polar angle θ and to an incomplete transformation of the transversal energy component $E_\perp$ into the longitudinal $E_\|$. As a result, electrons that started with an energy, which would have been high enough to pass the spectrometer $E_\text{in} > eU$ get reflected nonetheless, due to their persistent $E_\perp$. This leads to a decreased count rate at high surplus energies, i.e. at low retarding energies. The effect also has a radial dependence: At a large radial distance from the spectrometer's symmetry axis, the magnetic field lines are bent more strongly. Non-adiabatic effects are enhanced for electrons traversing the spectrometer in these regions.

Radius and surplus energy, at which non-adiabatic effects occur, can be both measured and simulated. However, for the geometry in the differential campaign, none of such had been performed at the time of the measurements. 14 keV is the lowest

---

[4] The resolution for electrons in the pilot sterile neutrino search was $\Delta E \approx 440\,\text{eV}$ [Alt19].

retarding energy, at which adiabatic motion is guaranteed for the standard Troitsk ν-mass configuration [Abd17] (larger detector in a stronger magnetic field). It was estimated for P-0, that adiabatic transport is expected even at 13 keV, as both a smaller detector radius and a weaker magnetic field at the detector position decrease the risk of non-adiabatic electron transport.[5] Almost every second run is a monitor point with a retarding energy of 13 keV. By stacking the data of these runs, the statistical uncertainty is largely decreased. The 13 keV retarding energy data is thus most suited to perform a sterile neutrino search.

Bump The runs in which the bump appears are accordingly labeled in tables 5.3 and 5.4. Its amplitude increases over the course of the campaign, as shown in figure 5.7(a). If the bump originated from a Penning trap, its amplitude would relate to an increasing pressure. The pressure in the WGTS shows no relation to the bump's appearance, as can be seen in figure 5.7(b). A potential relation to the pressure in the spectrometer cannot be checked, as the corresponding pressure sensor was at its lower sensitivity of 10^{-9} mbar throughout the campaign. As the bump causes a spectral distortion, it might conceal a possible sterile neutrino signature and has to be removed from the data, which is possible in several ways:

- **Energy cut** The ROI is constrained to the energy region above the bump, i.e. $E > 9\,\text{keV}$ for the differential spectrum with $eU = 13\,\text{keV}$. By doing so, a significant fraction of the backscattering background is removed, which, however, constitutes a valuable mean to control the detector response (see section 5.2.4.3).

- **Bump subtraction** The bump is parameterized with an appropriate function, which is then subtracted from the data. The approach, however, neglects the backscattering background of the bump itself or introduces large systematic uncertainty (see section 5.3.4.2). If the bump had also appeared in the background run 2, its shape could have been used to subtract the bump in tritium measurements.

- **Data exclusion** Data, in which the bump appears are excluded from the sterile neutrino analysis. The remaining runs with a retarding energy of 13 keV are runs 1, 5, and 7. This approach decreases the amount of data by a factor of four and hence increases the statistical uncertainty by a factor of two. Nevertheless, the 13 keV runs remain the data set with the smallest statistical uncertainty. This way is chosen to remove the bump from the data.

---

[5] This estimation was later validated (see section 5.3.2).

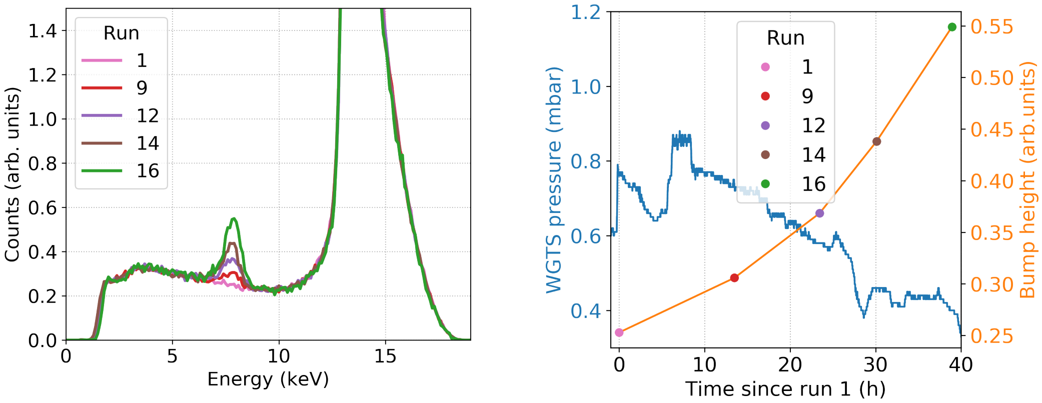

(a) Bump in different runs. (b) WGTS pressure and bump height.

Figure 5.7: **Evolution of the bump.** (a) The bump height increases with the number of runs, while its position remains. The retarding energy is 13 keV in all runs. (b) The pressure in the WGTS (blue) decreases over time, as gas gets pumped out steadily. On the contrary, the amplitude of the bump shows an exponential increase over time. The same runs are shown as in (a).

Charge sharing In some acquisitions, the time stamps of pixel NW are not synchronous to those of the six other pixels but shifted by several hours. This feature originates from the internal signal structure of the DANTE DPP: DANTE consists of a total of eight identical electronics boards, each of which constitutes one read-out channel. Seven of them are used for the P-0 detector, where pixel NW is connected to the last board in the signal chain of the time reset after an acquisition. During the differential campaign, this board sometimes skipped the reset signal, causing the time stamp shift. This malfunction has later been corrected in a DANTE firmware update. For what concerns the data of the differential campaign, however, the affected time stamps need to be corrected, in order to account for charge sharing. This is done in the following steps:

1. The time of the previous acquisition is subtracted from all time stamps of pixel NW. A residual shift of up to several milliseconds remains, as the last (first) event of the previous (subsequent) measurement does not exactly coincide with the end (start) of the acquisition.

2. The time stamps of pixel NW are simultaneously shifted in steps of 8 ns, scanning over the range of several milliseconds. At each step, the number of multiplicity-2 events in pixel NW with adjacent pixels is determined. The

> number of random coincidences is approximately constant. Only if the correct time stamp offset of pixel NW is found, an increase of multiplicity-2 events is observed, due to real charge sharing.

With increasing acquisition time, i.e. increasing number of time stamps, this correction approach gets computationally expensive. Fortunately, in run 1 only the first three time stamps are affected and thus removed. All other time stamps are synchronous with those of the other pixels, yielding the expected amount of multiplicity-2 events. Runs 5 and 7 are not affected by the time stamp shift at all.

Charge sharing events are then removed by a multiplicity cut (see section 4.3.1.1). Figure 5.8(a) shows a scatter plot of charge sharing events and random coincidences. The latter (if not piled up) do not distort the shape of the measured spectrum and are useful data which shall not be removed. Thus, the coincidence time window $\Delta t_{\mathrm{coinc}}$ is determined, for which the amount of residual charge sharing events (Type II error) is small, while a least amount of random coincidences is removed (Type I error). The number of multiplicity-2 events is calculated for coincidence time windows in the range of $8-280\,\mathrm{ns}$. The result is illustrated in figure 5.8(b). This is the case for $\Delta t_{\mathrm{coinc}} = 136\,\mathrm{ns}$, which is chosen as the optimal coincidence time window to perform the multiplicity cut.

5.2.3 Response to electrons

The response to electrons and its importance in measuring a continuous spectrum were introduced in section 4.3.2. As tritium electrons are generated in the WGTS, the response is affected not only by the detector: On the electrons' trajectory from the WGTS to the detector, they undergo scatterings on tritium molecules, as well as reflections and angular changes in electric and magnetic fields. Thus, the response of the entire system has to be accounted for, which is done in separate parts. For each part, the response is expressed in the form of a response matrix, where the rows represent the initial energy and the columns represent the measured energy. These matrices can easily be multiplied with each other. The resulting total response matrix is then convolved with the tritium model spectrum to obtain the expected spectrum at the detector. The individual response matrices are determined via both measurements and simulations, as described in the following.

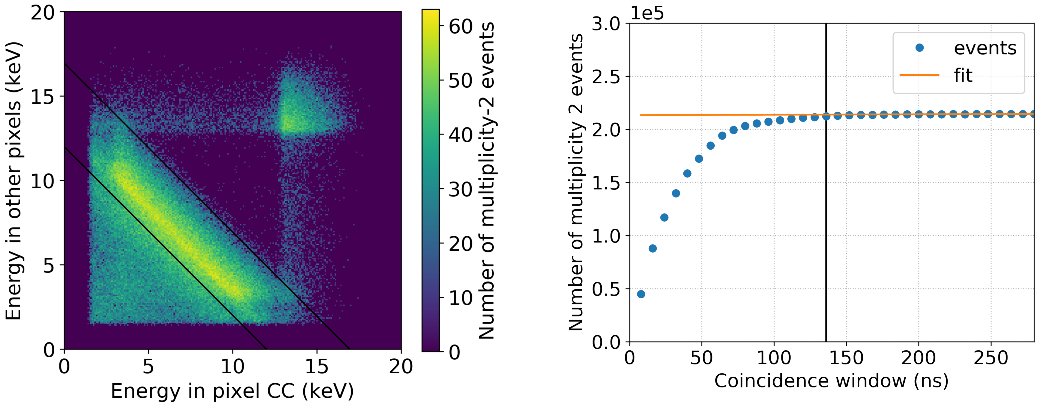

(a) Scatter plot of coincident events.

(b) Coincidence time window scan.

Figure 5.8: **Multiplicity analysis in the differential campaign.** (a) The scatter plot shows tritium data with $eU = 13\,\mathrm{keV}$ (run 21). Each entry represents a multiplicity-2 event, triggered simultaneously in pixel CC and any adjacent pixel. The area in between the two black lines mostly consists of real charge sharing events. The horizontal line at 13 keV on the y-axis and the vertical line at 13 keV on the x-axis, as well as the triangle at 13 keV on the angle bisector mostly consist of random coincidences. (b) The number of detected multiplicity-2 events in run 1 as a function of coincidence time window $\Delta t_{\mathrm{coinc}}$. The points above 200 ns are fit with a linear function (orange). The difference between the data (blue) and the fit is larger than 1 % for windows $\Delta t_{\mathrm{coinc}} < 136\,\mathrm{ns}$ (black line). Consequently, events which trigger two pixels within a coincidence time window of 136 ns are removed from the data.

5.2.3.1 Detector response

The detector response is a major component to model the shape of the differential tritium spectrum. The general shape of the response of the P-0 detectors to mono-energetic electrons has been established in section 4.3.2. It is given by the empirical model in equations (4.13) to (4.15). A method has been developed to determine the detector response accounting for the entire continuous tritium spectrum:

1. Mono-energetic electrons are measured at several initial energies in the ROI. The measured spectral shape at each energy is fit with the empirical model. These steps have already been performed in section 4.3.2.

2. In order to model the entire continuous tritium spectrum, the obtained responses are interpolated for all possible energies. To this end, an energy dependence for each of the parameters of the empirical model is introduced. This reduces the number of free parameters to one, namely the mean of the Gaussian function $\mu \approx E_{\mathrm{in}}$.

3. The empirical model is evaluated for each incident energy bin of the given measured tritium spectrum. Combining the resulting individual responses in the form of a matrix yields the detector response matrix D.

Sliced tritium spectrum As described above, the first ingredients for the detector response are mono-energetic electron measurements at several initial energies. These can principally be obtained from any electron source available in Troitsk ν-mass. As the response is meant to reproduce the behavior of β-electrons, an approach is tested, in which the response is generated based on actual tritium measurements. Several tritium measurements are performed at different retarding energies eU. The tritium measurements of the differential campaign were performed in the range $eU = 12-16\,\mathrm{keV}$ in steps of $500\,\mathrm{eV}$, as shown in figure 5.9(a). A quasi mono-energetic response is generated by subtracting a spectrum with eU_i from the one with eU_{i+1}. Examples are displayed in figure 5.9(b). Casually said, the continuous tritium spectrum is sliced into quasi mono-energetic responses by the MAC-E spectrometer. Quasi mono-energetic means, that the residual width of the retarding energy step is not negligible, leading to a deviation from mono-energetic responses. This is especially noticeable for high retarding energies. The resolution of the quasi mono-energetic spectra can be improved by decreasing the step size between retarding energies. However, the smaller the step size, the smaller the amount of data, which remains and does not get subtracted. Furthermore, at high retarding energies $eU > 15\,\mathrm{keV}$, the count rate is only in the order of a few cps. This results in large statistical

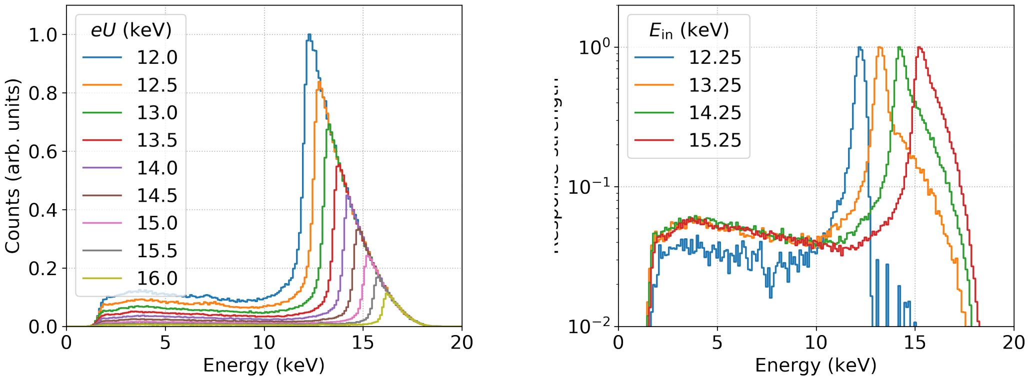

(a) Retarding energy steps.

(b) Subtracted tritium spectra.

Figure 5.9: **Detector response from tritium measurements.** (a) The tritium spectra are normalized, such that the shape above the respective retarding energies align. The step size between retarding energies is 500 eV. (b) The detector response is determined by subtracting the tritium spectra with adjacent retarding energies. For clarity, not all responses are shown. Especially for high energies, the subtracted spectra show a strong deviation from mono-energetic responses.

uncertainties, even with acquisition times of several hours. This approach is thus not feasible to determine the detector response at the Troitsk ν-mass experiment.[6]

Electron gun The electron gun at the rear section of the setup provides mono-energetic electrons with adjustable energy and a resolution $\sigma_{\text{egun}} < 1\,\text{eV}$ (see section 5.1.1). However, measuring different initial energies is not trivial: The air coil system needs to be adjusted at each setting in order to focus the electron beam onto the detector. Furthermore, the beam spot is in principle circular with a radius smaller than 1 mm but extends into an non-circular shape in the low magnetic field at the detector position. The detector chip does not get homogeneously illuminated, such that a different spectral shape is measured in each pixel and no multiplicity cut can be performed. Moreover, the angular distribution of electrons from the gun is narrower then the angular distribution of β-electrons: Electrons are accelerated in forward direction by the potential of the gun, whereas tritium electrons are emitted isotropically. The electron gun is hence not suited to determine the detector response.

---

[6] It might be possible with the high activity tritium source of KATRIN.

Spectrometer electrode Electrons emitted from the spectrometer electrode illuminate the entire detector chip homogeneously and have a broader angular distribution than electrons from the electron gun [Alt19]. However, the measurement of these electrons requires to change the magnetic field configuration in the spectrometer, affecting the measured response. For instance, the fraction of backscattered electrons, which are back-reflected onto the detector is increased, as the magnetic field lines connect the detector with the spectrometer electrode. Furthermore, the response of the spectrometer electrode does not include effects in the source and transport section, as the electrons are generated only in the spectrometer. Nevertheless, they are considered to be most suited of all sources to determine the detector response.

The electrode measurement at each spectrometer voltage U is fit with the empirical model in equations (4.13) to (4.15).[7] Figure 5.10 shows an exemplary fit to the measurement with $eU = 15\,\mathrm{keV}$ (run 53). Two dead layer tails are applied, yielding a better fit result. The silicon escape peak (see equation (4.16)) is not visible in any electrode measurement and is thus not included in the model. The energy threshold is fixed to $E_{\mathrm{thres}} = a = 2\,\mathrm{keV}$. To interpolate the response for any given binning, a linear dependence on μ is introduced for the parameters σ, n_1, n_2, n_3, β_1, β_2, b, and c. To this end, a linear function is fit to all obtained fit values of each function parameter, e.g.

$$\beta_2\left(\mu\right) = m_{\beta_2} \cdot \mu + c_{\beta_2} \tag{5.3}$$

with slope m_{β_2} and offset c_{β_2}. An exception is made for the two remaining parameters:

n_0 is the overall normalization and cannot be inferred from electrode measurements. Each response is hence initially normalized to a maximal height of one.

n_3 is the normalization of the backscattering background relative to n_0. As it seems to be uncorrelated with μ, it is described by a constant factor c_{n_3}.

This procedure yields a total of 15 free parameters m_σ, c_σ, m_{n_1}, c_{n_1}, m_{n_2}, c_{n_2}, m_{β_1}, c_{β_1}, m_{β_2}, c_{β_2}, m_b, c_b, m_c, c_c, and c_{n_3}, which are in the following referred to as ϕ. The response can now be calculated for every initial electron energy $E_{\mathrm{in}} \approx \mu$.

The normalization is corrected for the amount of backscattered electrons, which do not get back-reflected but traverse the setup in opposite direction and get lost in the rear section.[8] The probability to lose electrons in this manner can be expressed as:

$$P_{\mathrm{loss}}\left(E_{\mathrm{in}}\right) = P_{\mathrm{bs}}\left(E_{\mathrm{in}}\right) \cdot P_{eU}\left(E_{\mathrm{bs}} > eU\right) \cdot P_\theta\left(\theta > 9.6°\right) \ . \tag{5.4}$$

---

[7] The parameters of the empirical model have been called ψ.

[8] A similar investigation was performed by the Troitsk ν-mass group [Gri16].

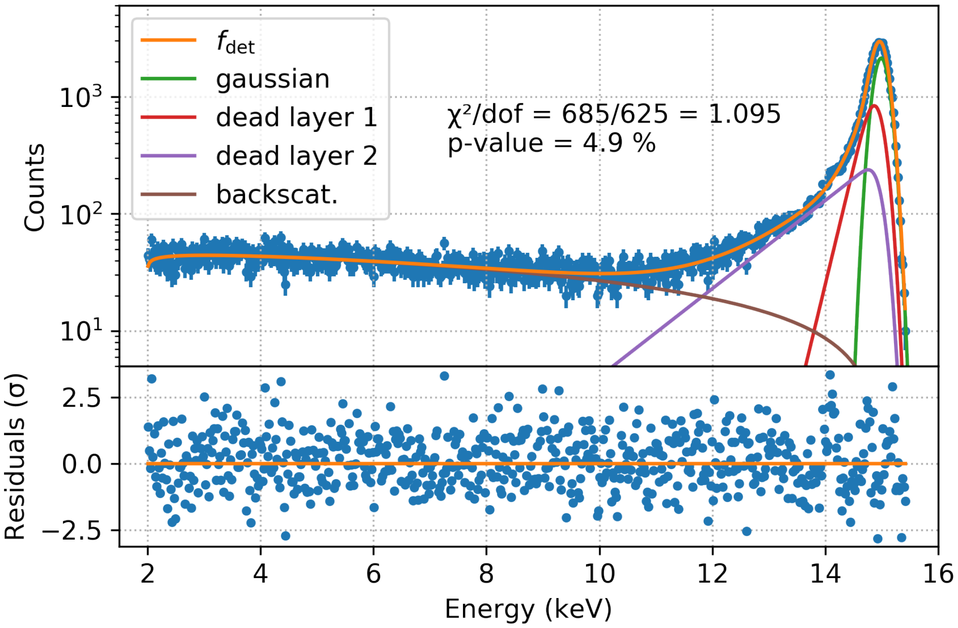

Figure 5.10: **Response parameterization in Troitsk ν-mass.** The plot shows an electrode measurement at 15 keV (blue). The data is fit with the empirical model, including the dead layer tails and no silicon escape peak. The residuals are normalized to the statistical uncertainty and show no noticeable pattern.

P_{bs} is the probability for electrons to backscatter on the silicon chip as a function of incident energy E_{in}, averaged over their angular distribution. P_{bs} is simulated using KESS.

P_{eU} is the transmission probability for backscattered electrons in the spectrometer. The energy distribution of backscattered electrons is obtained from the same simulation as before. P_{eU} is obtained as the fraction of backscattered electrons with $E_{\mathrm{bs}} > eU$.

P_{θ} is the probability for backscattered electrons to pass the pinch magnet. The angular distribution is also obtained from KESS. Electrons with polar angles $\theta > \arcsin\left(\sqrt{\frac{B_{\mathrm{det}}}{B_{\mathrm{pinch}}}}\right) = 9.6°$ are able to pass the pinch magnet.

A simulation is performed for incident energies of 13, 16, and 19 keV. A linear fit yields

$$P_{\mathrm{loss}}\left(E_{\mathrm{in}}\right) = 1 - \left(5.72 \cdot 10^{-7} \cdot E_{\mathrm{in}}\ [\mathrm{eV}] - 7.432 \cdot 10^{-3}\right)\ , \tag{5.5}$$

which changes the normalization by 1.5 % at 13 keV and up to 1.8 % at 18.6 keV. Multiplied by this term, the response is evaluated for each energy of the given binning. The generated responses are combined in the detector response matrix D, displayed in figure 5.11(a).

5.2.3.2 Response of source & transport section

A software package based on C++ was specially developed for keV-scale sterile neutrino searches in KATRIN-like experiments [Lok18]. It accounts for the energy loss through scattering in the WGTS, as well as for MAC-E spectrometer transmission properties. Following the name of the source and spectrum calculation (SSC) package for KATRIN [Gro15], it is called “SSC-sterile”.[9] Dividing the gas column in the source section into virtual slices, the response of the WGTS is initialized by a MC simulation for each slice. The probabilities for electrons to have a particular energy and direction at the exit of the source are put in a binned format. Effects like multiple transits of electrons through the WGTS due to reflections at magnetic mirrors, as well as the transmission of electrons trough the spectrometer are propagated by repeated matrix multiplications. The consecutive multiplication of all involved responses yields the response matrix R_{SSC}, illustrated in figure 5.12(a). It combines almost all effects in the source and transport section. There are however two exceptions, which are presented in the following.

---

[9] Even though both packages have nothing in common.

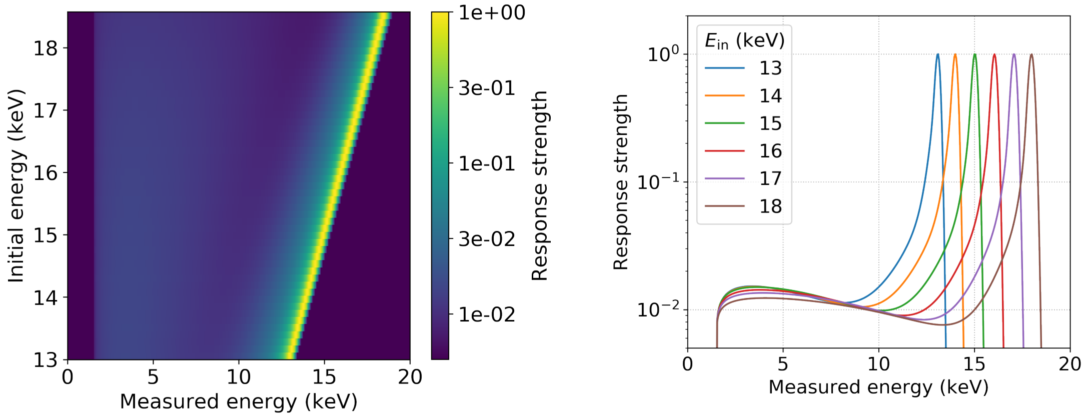

(a) Detector response matrix.

(b) Response functions at several energies.

Figure 5.11: **Detector response from electrode measurements.** (a) The detector response matrix includes all detector effects. It is meant to be convolved with the tritium β-decay model, which describes the spectrum above the retarding energy $eU = 13\,\text{keV}$ (y-axis). After the convolution, the model is able to describe the entire measured differential tritium spectrum above the detection threshold $E_{\text{thres}} = 2\,\text{keV}$. (b) Each row in the response matrix yields a mono-energetic response function based on the empirical model. The response resembles the electron spectrum obtained from an electrode measurement at the corresponding initial energy.

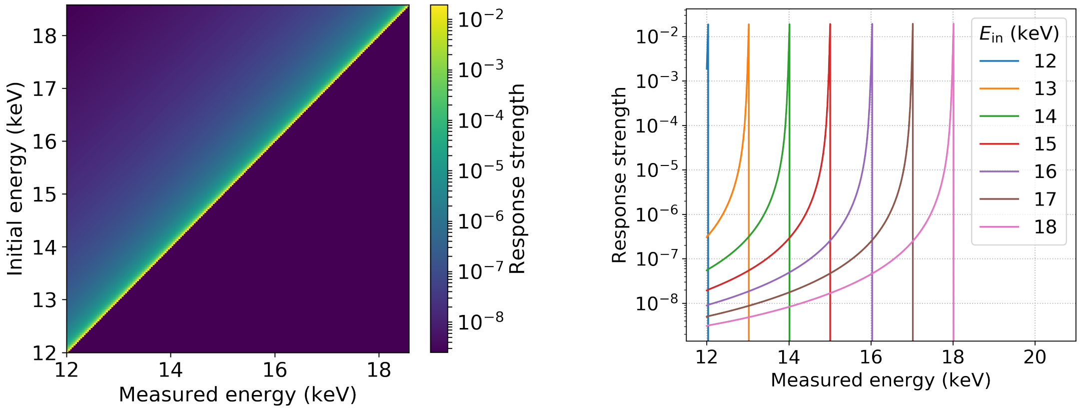

(a) SSC-sterile response matrix.

(b) Response functions at several energies.

Figure 5.12: **SSC-sterile response for source and transport section.** To account for the response of the source and transport section, the SSC-sterile response matrix in (a) is convolved with the tritium β-decay model. Its limit at low energies is the retarding energy, here 12 keV. No electrons with lower energies are transmitted through the spectrometer. Its limit at high energies is the tritium decay endpoint. No electrons with higher energies are created in the source. Its shape at integer initial energy values (horizontal rows) is displayed in (b). Most electrons maintain their initial energy (main peak). Some electrons lose energy by scattering in the source and are shifted towards lower energies.

Trapping effect Electrons with large initial polar angles

$$\theta > \arcsin\left(\sqrt{\frac{B_{\text{source}}}{B_{\text{trans}}}}\right) = 24.1° \tag{5.6}$$

get magnetically reflected at both ends of the WGTS and are confined to the source by the trapping effect (see section 5.1.1). Depending on the evolution of their polar angle, these electrons have three potential destinations, which are illustrated in figure 5.13. Most of them remain trapped in the source and lose energy in scatterings until they get absorbed on the walls of the source tube. Some scatter in a way, that their decreased polar angle allows them to escape the trap in either direction. If those electrons escape towards the rear end, they are guided onto the stainless steel tank and get absorbed. If they escape towards the spectrometer with polar angles

$$\theta > \arcsin\left(\sqrt{\frac{B_{\text{source}}}{B_{\text{pinch}}}}\right) = 16.8° \ , \tag{5.7}$$

they are reflected at the pinch magnetic field. In this case, they most likely do not scatter again, due to the low gas density in the source. Consequently, they arrive at the rear section with unchanged polar angle and also get absorbed in the stainless steel tank. Only if electrons get to polar angles $\theta < 16.8°$ in one scattering, they pass also the pinch magnet and proceed to the spectrometer. This requires a large angular change

$$\Delta\theta > 24.1° - 16.8° = 7.3° \ . \tag{5.8}$$

Electrons, which eventually reach the spectrometer are in the following referred to as “passed events”.

Simulating angular changes with sufficiently high precision for a large amount of events requires a great computational effort and is not yet manageable with SSC-sterile. The trapping effect was first investigated for neutrino mass measurements at Troitsk ν-mass using dedicated MC simulations [Ase11], which focused on the tritium endpoint region. For this work, an enhanced MC simulation is performed to extend the analysis to energies in the keV-range.[10] It includes the following steps:

1. Generate an electron in the volume of the source.
2. Draw random propagation length according to its mean free path.
3. Check whether it could have left the source in either direction.

---

[10] Procedure and results of this simulation are described in an internal tech note from Jan 12th 2017.

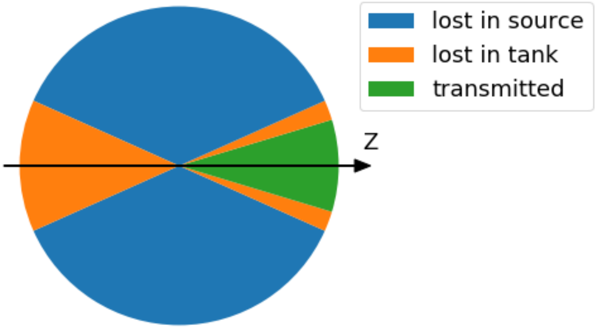

Figure 5.13: **Polar angles of trapped electrons.** The diagram shows possible destinations of trapped electrons in the Troitsk ν-mass WGTS, depending on their polar angle θ relative to the symmetry axis z of the setup. If the polar angle of an electron stays above 24.1° (blue area), it eventually gets absorbed on the walls of the source tube. Once the electron scatters to an angle in the orange regions, it gets absorbed in the stainless steel tank. Only of it undergoes an angular change $\Delta\theta > 7.3°$ and ends up with a polar angle in the green region, the electron proceeds to the spectrometer.

4. If yes, tag the event accordingly and start from step 1. If not, model the collision and continue with step 5.
5. Repeat from step 2 until the electron energy falls below a set limit.

The simulation depends on two approximations: Firstly, electrons scatter at most once during a traverse through the WGTS. This approximation is valid for the low gas density of the Troitsk ν-mass tritium source. Secondly, electrons are equally likely to scatter over the entire length of the WGTS. This is not true, as their longitudinal velocity decreases in higher magnetic fields, in which they consequently spend more time. This effect has however shown to be negligible in a cross check using a detailed simulation including accurate tracking and field calculations with less events.

Electrons with initial energies $E_\mathrm{in} = 12$, 14, 16, and 18 keV were simulated. Figure 5.14(a) shows a histogram of the simulated energy loss of electrons eventually leaving the source into the direction of the spectrometer. For all initial energies, the simulation yields a flat distribution in energy loss over at least 4 keV. For each E_in, a constant trapping factor

$$C_\mathrm{trap}\left(E_\mathrm{in}\right) = \frac{\bar{n}\left(E_\mathrm{in}\right)}{N\left(E_\mathrm{in}\right) \cdot h} \tag{5.9}$$

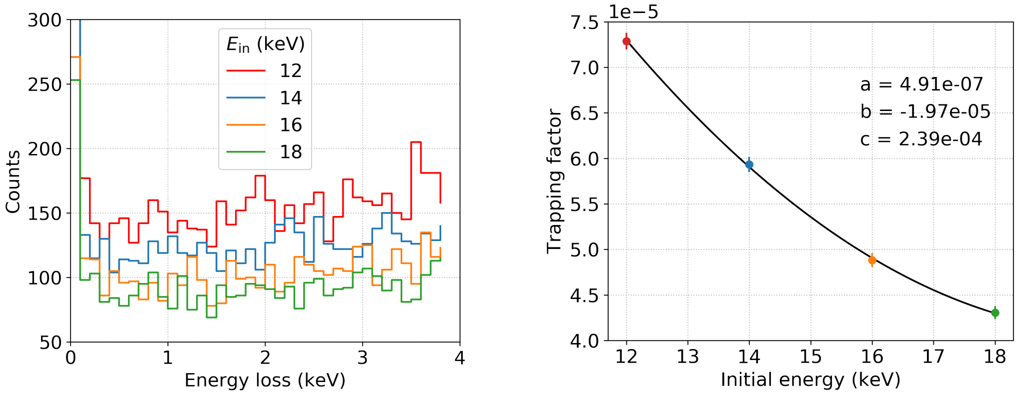

(a) Distribution of energy losses.

(b) Energy dependent trapping factor.

Figure 5.14: **Results of the trapping simulation.** (a) The energy loss distribution is flat over the simulated range of 4 keV and is thus approximated by a constant factor C_{trap}. (b) The factor depends on the electrons' initial energy E_{in}. The trapping factor is normalized to the total number of passed events and a bin width of 100 eV. The behavior is approximated by the second degree polynomial $p(E_{\text{in}}) = aE_{\text{in}}^2 + bE_{\text{in}} + c$.

is extracted, where $\bar{n}$ are the histogram counts averaged over the energy loss range, N is the total number of passed events, and h is the energy loss bin width. These factors are shown in figure 5.14(b) over their respective initial energy, interpolated with a second degree polynomial. The first bin accounts for an energy loss smaller than 100 eV, which is smaller than the energy resolution of the detector. This bin is thus neglected. The trapping factor states the number of additional electrons arriving at the detector for a given initial energy. Its magnitude depends on the ratio of inelastic σ_{inel} to quasi-elastic σ_{elas} cross sections and their respective energy dependency:

$$C_{\text{trap}} \propto \frac{\sigma_{\text{inel}}}{\sigma_{\text{elas}}} \ . \tag{5.10}$$

The trapping effect is small with factors in the order of 10^{-5} for a 100 eV energy interval. Nevertheless, its influence on the spectral shape has to be accounted for, as it gets large when integrated over several keV.

To easily combine the response of the trapping effect with R_{SSC}, the trapping factor is evaluated for the same initial energy binning and expressed in a trapping response matrix R_{trap}, shown in figure 5.15(a). The total source and transport response matrix is obtained as

$$R\left(qU; E_{\text{in}}\right) = R_{\text{SSC}}\left(qU; E_{\text{in}}\right) \cdot R_{\text{trap}}\left(E_{\text{in}}\right) \ . \tag{5.11}$$

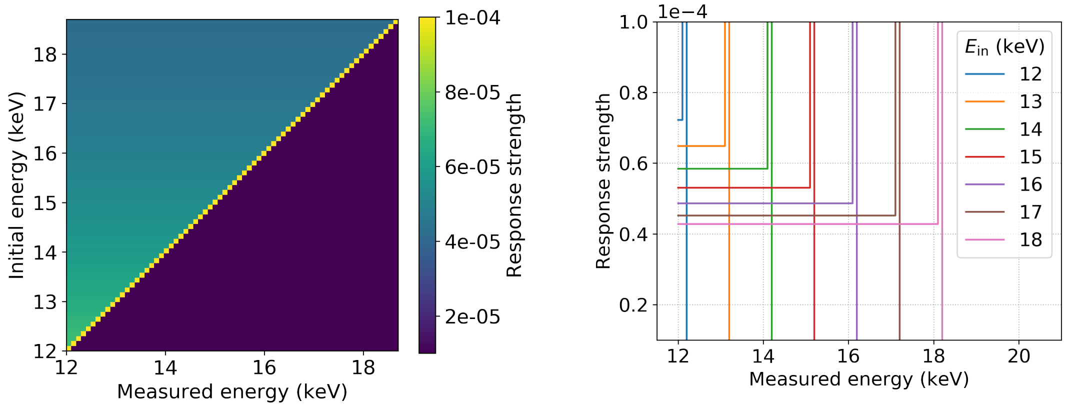

(a) Trapping effect response matrix.

(b) Response functions at several energies.

Figure 5.15: **Trapping effect response.** The trapping response matrix in (a) is multiplied with the one from SSC-sterile. The constant trapping factors become visible in its shape at integer energies, displayed in (b). The constant becomes larger for smaller energies according to the second degree polynomial in figure 5.14(b). The main peak height is 1 for each initial energy, as electrons from the trapping effect are treated as additional events, slightly changing the normalization.

5.2.4 Differential sterile neutrino search

As elaborated in section 5.2.2, the data, which are analyzed in search for a sterile neutrino admixture, consist of runs 1, 5, and 7. After performing calibration and multiplicity cut, the counts in the central pixel are stacked. Stacking means that the counts in each bin i of the energy calibration are summed over all three runs. The final spectrum consists of a total of about 1.43 million events. The sterile neutrino search is conducted with the goal of developing and testing analysis strategies with regard to the differential mode, rather than pushing the exclusion limit to a new level. The obtained results are valuable information for the TRISTAN project to draw conclusions for future measurement campaigns either at Troitsk ν-mass or at the KATRIN experiment.

5.2.4.1 Differential model

The model of the differential tritium spectrum

$$\begin{aligned}\frac{\mathrm{d}\Gamma(E;m_\beta)}{\mathrm{d}E} &= S(E,E_0)\cdot F(Z,E)\cdot(E+m_\mathrm{e})\cdot p\\ &\cdot\sum_i P_i\cdot(E_0-E-E_i)\cdot\sqrt{(E_0-E-E_i)^2-m_\beta^2}\end{aligned} \tag{5.12}$$

is based on the model introduced in section 3.1.1. The constant C in equation (3.1) is irrelevant, as the model is normalized in the fit to the data. Apart from that, the model contains two modifications:

- **Small term corrections** The term S includes the following small term corrections [Wil91]: screening of the β-electron by the orbital electron of the tritium atom; the effect of the β-electron moving into a recoiled electric field; nuclear ^{3}He, weak magnetism, and V-A interference recoils; exchange between the β-electron and an orbital electron; the convolution of the lepton and nucleonic wavefunctions through the nuclear volume; the effect of the finite nuclear size on the solution of the Dirac equation for the β-electron; radiative corrections. These corrections have been calculated in order to measure the neutrino mass with a KATRIN-like experiment. They have a negligible effect on the investigations presented in this thesis, as they only affect the spectrum above 16.6 keV with a relative strength of $\leq 0.1\,\%$. Nevertheless, they have already been implemented for future searches with a larger amount of data.

- **Final state distribution** After the decay of a tritium atom, the daughter molecule remains in an excited state E_i with the probability P_i. Both can be calculated from first principle [Sae00]. The corresponding final state distribution (FSD) is shown in figure 5.16(a). This calculation is, however, not straightforward and has so far only been done for the tritium endpoint region to be used in neutrino mass measurements. A simplified method was developed [Sch19a], which enables to estimate the FSD for a wider electron energy range to be used in a keV-scale sterile neutrino search. The model predicts the ground state distribution to move towards lower excitation energies E_i for decreasing initial electron energies E_{in}, as shown in figure 5.16(b). At the same time, the width of the distribution decreases, while the corresponding probabilities increase. The model depends on the following simplifications:

    1. The ground state distribution is approximated by a Gaussian distribution.

    2. The molecule is assumed to be a harmonic oscillator with a small anharmonic term. The width of the distribution is then described by the zero-point motion of the oscillator.

    3. Possible emission angles of the β-electron are constrained to either 0° or 180° with equal probability.

    4. Interactions between the electron and the daughter molecule are neglected.

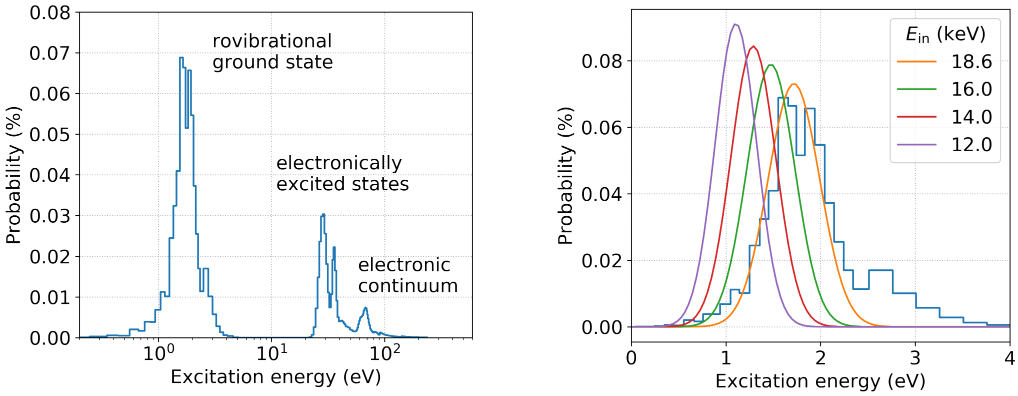

(a) Three parts of the FSD.

(b) Shift of the ground state.

Figure 5.16: **Final state distribution.** (a) Final state distribution for T_2 at the spectral endpoint $E_0 = 18.6\,\text{keV}$ [Sae00]. The states can be separated into three parts: the ground state, centered around 1.7 eV; electronically exited states in the range of 22 – 55 eV; electronic continuum above 55 eV. (b) The ground state distribution (blue) is approximated with a Gaussian function (orange), which shifts towards lower excitation energies with decreasing electron energy.

These simplifications are valid in the electron energy range of 6 – 18.6 keV. For lower initial energies, negative excitation energies are predicted, which are nonphysical. The description of the FSD at this energy range requires a more accurate model or the calculation from first principle.

The model in equation (5.12) is convolved with the response matrices of the source and transport section R, and of the detector D:

$$f_{\text{diff.model}}(E; N, E_0, E', \phi, B) = N \cdot \left[\frac{\mathrm{d}\Gamma(E; E_0)}{\mathrm{d}E} \times \Big(R\,(eU, E') \cdot D(E'; \phi) \Big) \right] + B \,, \quad (5.13)$$

where N is a normalization factor, B is a constant background, and $E' = m_{E'} \cdot E + c_{E'}$ is the energy scale of the response matrices. The latter is decoupled from the calibration of the data to account for the observed calibration shift (see figure 5.5(a)).

5.2.4.2 Treatment of systematic uncertainty

The largest systematic uncertainty in the differential measurement mode arises from the detector parameterization.[11] The electrons from the spectrometer electrode have different incident angles to the detector and back-reflection properties than β-electrons from tritium decay. A deviation in the responses is therefore expected but difficult to quantify, as β-electrons only appear in a continuous spectrum. To still account for this uncertainty, all energy dependent model parameters ϕ are free in the fit. This way, other systematic effects are considered automatically, as will be shown in the following.

Events below the detection threshold make up one major systematic uncertainty in the standard Troitsk ν-mass sterile neutrino search. This is because the search is performed in integral mode, i.e. a measurement of the count rate. Their number (or rate) can only be modeled with large uncertainty. In differential mode, however, events below the threshold do not carry much information about a sterile neutrino admixture. If these events were detectable, they would contribute to the backscattering background, which is used to evaluate the performance of the detector response model. The detectable part of the backscattering background is already enough to do so.

In Troitsk ν-mass or any KATRIN-like experiment, the backscattering effect refers not only to backscattering at the detector but also to back-reflection at electric and magnetic fields (see table 5.1). Backscattered events can hit the detector several times, each time depositing only small fractions of their initial energy. Both backscattering and back-reflection are accounted for by the backscattering background of the empirical model. As described in section 5.2.3.1, this treatment requires the electrons from the electrode to have the same backscattering and back-reflection properties as β-electrons. However, due to the different magnetic field configurations during the respective measurements, they have not. By treating the parameters of the backscattering background as free parameters in the fit to the tritium spectrum, systematic uncertainty is introduced to account for this deviation of responses.

The entrance window effect is treated likewise. Its influence is mainly modeled by the two dead layer tails, whose parameters are free in the fit to the tritium spectrum. This not only accounts for the entrance window effect but also for charge sharing: Due to the choice of the 136 ns long coincidence window, the multiplicity cut removes more than 99 % of detected charge sharing events (see section 5.2.2). However, due to events below the detection threshold, a certain amount remains undetected. These remaining electrons form a plateau below each imagined mono-energetic line in the

---

[11] The cross check is subject of chapter 6.

continuous tritium spectrum (see section 4.3.1.1). The dead layer tails are used to model exactly this part of the spectrum. By leaving their parameters free in the fit to the tritium spectrum, the plateau is absorbed in the tails and the remaining charge sharing effect is accounted for by the introduced uncertainty. Moreover, the plateau's amplitude rises as a smooth function of energy [Alt19]. It has been shown that smooth functions barely affect the sterile neutrino sensitivity [Mer15a]. The effect of charge sharing thus requires no further consideration.

Dead time is the second major systematic in the standard Troitsk ν-mass sterile neutrino search. Also dead time, however, is an issue especially in integral mode: The higher the rate, the higher the dead time during an acquisition. Measuring at different retarding energies means measuring at different rates and thus with different dead times. This leads to a distortion of the integral spectrum. In differential mode, however, the measurement is performed at only one retarding energy. As β-decay is a statistical process, electrons of all energies have the same probability to fall into the dead time window, i.e. all bins in the differential spectrum are affected likewise. The dead time effect is absorbed by a free normalization factor in the fit and is thus not further considered.

The probability for two events to pile up is derived as the integral of equation (4.10) over the time interval $[0,\tau]$ (see section 4.3.1.2). The minimal time resolution of DANTE DPP is about $\tau = 100\,\mathrm{ns}$. With the highest count rate $\Gamma_{\mathrm{run\,1}} = 110.2\,\mathrm{cps}$, this results in

$$P_{\text{pile-up}} = \int_0^\tau f\left(\Delta t, \Gamma\right) \mathrm{d}\Delta t \approx 0.1\,\% \ . \tag{5.14}$$

Moreover, events with energies above the tritium endpoint show no structure, which would point towards pile-up. The number of events in this region is in accordance with background. The effect of pile-up is thus neglected. The background count rate is 0.1 mcps at a retarding energy of 13 keV. Compared to an average count rate of 94 cps in the tritium data, the background is at the 0.1 % level and hence negligible.

5.2.4.3 Fit & exclusion limit

The search for a sterile neutrino signature is performed via a $\Delta\chi^2$-test: The model in equation (5.13) does not include a sterile neutrino admixture and is thus referred to as "null-hypothesis" $H_0(m_4 = 0, |U_{\mathrm{e}4}|^2 = 0)$. The data is fit with this model and the goodness of fit is expressed as $\chi^2(H_0)$, which determines the baseline for the search. At each point in a two-dimensional grid in the sterile neutrino parameter space, an admixture with the corresponding parameters m_4 and $|U_{\mathrm{e}4}|^2$ is added in the model.

This model is referred to as "alternative hypothesis" $H_1(m_4, |U_{e4}|^2)$. Its goodness $\chi^2(H_1)$ is compared to the result of the null-hypothesis:

$$\Delta\chi^2 = \chi^2(H_1) - \chi^2(H_0) = \begin{cases} \leq Q\,(1-\alpha) & \text{not reject} \\ > Q\,(1-\alpha) & \text{reject} \end{cases} . \tag{5.15}$$

The alternative hypothesis, i.e. a sterile neutrino admixture with corresponding m_4 and $|U_{e4}|^2$, is either rejected or not rejected, depending on the designated significance level α. The quantile Q of a χ^2-distribution with two degrees of freedom (DOF) (m_4, $|U_{e4}|^2$), which corresponds to the 95 % C.L. interval of the normal distribution, is given as $Q(1-0.05) = 5.991$.[12] This approach requires H_0 to yield the best goodness of fit (smallest χ^2-value) and the obtained parameters $\hat{\phi}$ to yield a physically valid detector response. The entire procedure is explained in more detail in the following.

Fit of the null-hypothesis The χ^2-fit function has the form

$$\chi^2(N,E_0,E',\phi,B) = \sum_E \frac{\Big(y(E) - f_{\text{diff.model}}(E; N,E_0,E',\phi,B)\Big)^2}{\sigma^2_{y(E)}} , \tag{5.16}$$

with the Poissonian statistical uncertainty $\sigma_{y(E)} = \sqrt{y(E)}$ of the data. The sum evaluates the function over energy bins in the range of 2 − 18.6 keV, in which the model is valid. For bins with few counts (rule of thumb: $n < 100$), a Poissonian likelihood function should rather be used [Cow98]. Out of 331 bins, however, for eight bins $n < 100$ and only for one $n < 10$, so that the inaccuracy is tolerable and a correction is omitted. The resulting 20 free parameters are

N, the overall normalization,

E_0, the tritium spectral endpoint,

E', i.e. $m_{E'}$ and $c_{E'}$, the energy calibration of the response matrices,

ϕ, the 15 parameters of the detector response, and

B, the constant background.

Usually in Troitsk ν-mass or KATRIN, the endpoint is not constrained by a pull term. In the presented analysis, however, a fit without the pull term results in an endpoint value, which deviates by −87 eV from expectation. Such a large deviation is

---

[12] Limits from the KATRIN collaboration are often given at 90 % C.L., corresponding to $Q = 4.605$.

not physical and originates from inaccurate modeling of the spectrum. The endpoint is thus constrained with a Gaussian pull term

$$\chi^2_{\mathrm{pull}}(E_0) = \frac{(E_0 - 18\,575\,\mathrm{eV})^2}{(4\,\mathrm{eV})^2} \tag{5.17}$$

to the expected value of around 18 575 eV with an uncertainty of 4 eV. Considering a Q-value for tritium β-decay of 18 592 eV [Mye15], as well as molecular tritium decay and experimental effects (e.g. work function of the WGTS and spectrometer) [Ott08], the chosen value and uncertainty are justified. The pull term prevents the large deviation but at the same time leads to a degradation of the goodness of fit.

The result of the fit is shown in figure 5.17. The pull term leads to a fitted endpoint value of $E_0 = 18\,574.0(25)\,\mathrm{eV}$. The normalization $N = 0.9916(9)$ is initialized to be one and shows no unexpected behavior. The constant background $B = 0.41(81)$ is in accordance with zero. Due to numerical problems in the fit, the robust Nelder-Mead algorithm [Nel65] is chosen. The usage of a different fitting algorithm (e.g. BFGS [Bro70, Fle70, Gol70, Sha70]) yields non-physical detector response functions with negative counts in some region of the spectrum. The Nelder-Mead algorithm, however, does not produce a covariance matrix of the fit parameters and thus no uncertainties on the fitted parameter values. Instead, the above given uncertainties are determined via bootstrapping: The data is randomly fluctuated 10^4 times, according to a Poissonian distribution of counts in each bin. For each sample, the fit is repeated and the obtained values are put into histograms, shown in figure 5.18. The parameter uncertainty is determined as the width of a Gaussian function, fit to the respective histogram.

The correlation matrix is obtained from the same 10^4 randomly fluctuated MC data sets by calculating the sample covariance of all sample parameters. The pairs of slope m_ϕ and offset c_ϕ of a fitted parameter ϕ are as expected anti-correlated. They are used to retrieve the parameters ψ and their respective correlations. They are displayed in figure 5.19, together with the other parameters: normalization N, endpoint E_0, energy calibration E', and background B.

The χ^2-value of the fit is 364. With 331 energy bins and 20 free parameters, this results in $331 - 20 = 311$ DOF and a reduced χ^2 of

$$\chi^2_{\mathrm{red}} = \frac{\chi^2}{\mathrm{DOF}} = 1.172\ . \tag{5.18}$$

The corresponding p-value is 2.0 %. This means that the observed or a larger difference between model and data would occur in 2 % of many repeated measurements, given the null-hypothesis was true. For the purpose of this investigation, the model describes

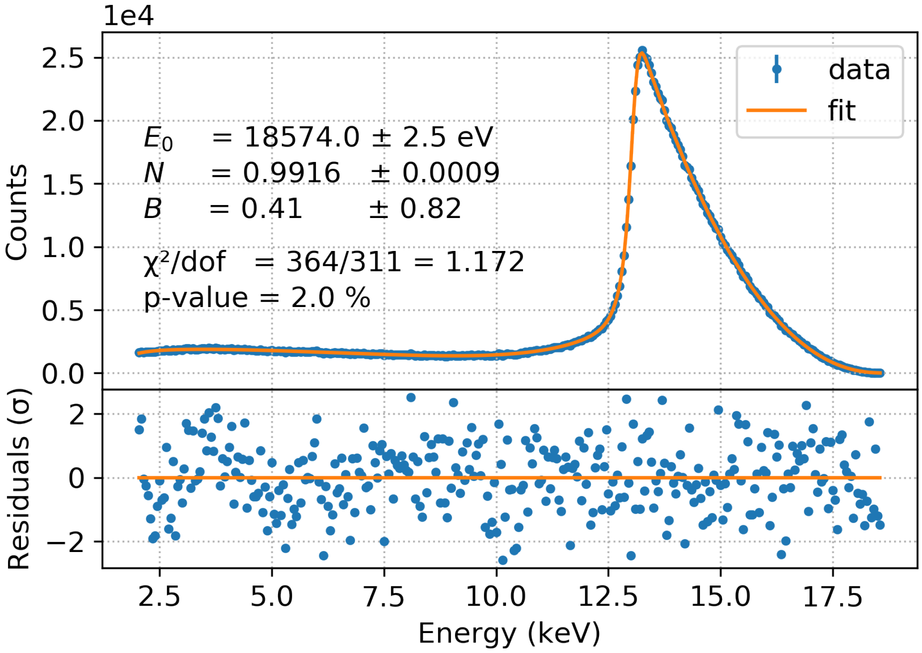

Figure 5.17: **Fit to the data of the differential campaign.** The data (blue) are three combined runs with a retarding energy of 13 keV. The statistical error bars are too small to be visible. The model (orange) includes a theoretical β-decay spectrum with additional corrections and the response of the system. The residuals (bottom) are normalized to the statistical uncertainty. Adapted from [Bru19].

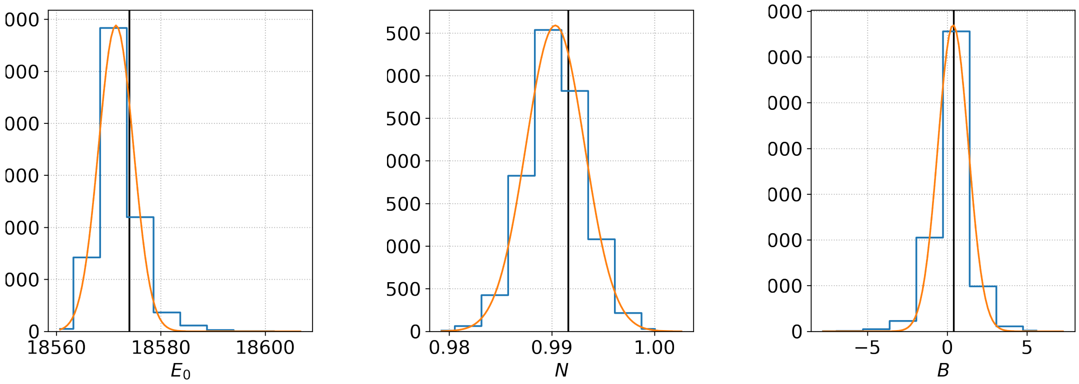

(a) Endpoint.

(b) Normalization.

(c) Background.

Figure 5.18: **Differential fit uncertainties from bootstrapping.** The data set is randomized 10^4 times and all samples are fit in the same way with the model in equation (5.13). The resulting values of (a) endpoint, (b) normalization, and (c) background are put in a histogram. Their distributions are approximated by a Gaussian function. The width σ of this function yields the respective parameter uncertainty. The black vertical line indicates the obtained value from the fit to the actual measured data.

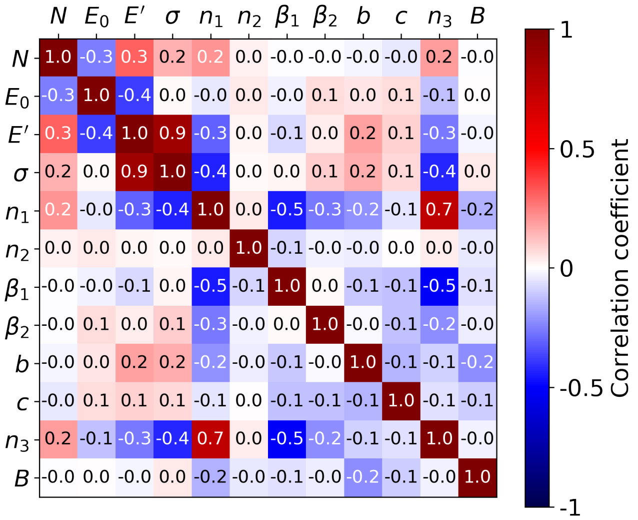

	N	E_0	E'	σ	n_1	n_2	β_1	β_2	b	c	n_3	B
N	1.0	-0.3	0.3	0.2	0.2	0.0	-0.0	-0.0	-0.0	-0.0	0.2	-0.0
E_0	-0.3	1.0	-0.4	0.0	-0.0	0.0	-0.0	0.1	0.0	0.1	-0.1	0.0
E'	0.3	-0.4	1.0	0.9	-0.3	0.0	-0.1	0.0	0.2	0.1	-0.3	-0.0
σ	0.2	0.0	0.9	1.0	-0.4	0.0	0.0	0.1	0.2	0.1	-0.4	0.0
n_1	0.2	-0.0	-0.3	-0.4	1.0	0.0	-0.5	-0.3	-0.2	-0.1	0.7	-0.2
n_2	0.0	0.0	0.0	0.0	0.0	1.0	-0.1	-0.0	-0.0	0.0	0.0	-0.0
β_1	-0.0	-0.0	-0.1	0.0	-0.5	-0.1	1.0	0.0	-0.1	-0.1	-0.5	-0.1
β_2	-0.0	0.1	0.0	0.1	-0.3	-0.0	0.0	1.0	-0.0	-0.1	-0.2	-0.0
b	-0.0	0.0	0.2	0.2	-0.2	-0.0	-0.1	-0.0	1.0	-0.1	-0.1	-0.2
c	-0.0	0.1	0.1	0.1	-0.1	0.0	-0.1	-0.1	-0.1	1.0	-0.1	-0.1
n_3	0.2	-0.1	-0.3	-0.4	0.7	0.0	-0.5	-0.2	-0.1	-0.1	1.0	-0.0
B	-0.0	0.0	-0.0	0.0	-0.2	-0.0	-0.1	-0.0	-0.2	-0.1	-0.0	1.0

Figure 5.19: **Correlations of the fit parameters in the differential campaign.** The parameters ψ (i.e. σ, n_1, …) are retrieved using the fitted parameters ϕ (i.e. m_σ, c_σ, m_{n_1}, …). The latter are anti-correlated in pairs of slope m_ϕ and offset c_ϕ.

the data in an acceptable way, even when punished by the pull term on the endpoint. A small residual pattern is apparent at around 3 keV but it is not statistically significant and thus not further considered. In this regard, the null-hypothesis can be used as the baseline for the sterile neutrino search.

Null-hypothesis check In a next step, the response function parameters obtained from the tritium fit $\hat{\phi}$ need to be validated. The parameters are valid, if they reproduce the shape of the spectrometer electrode data. To this end, the empirical model (see equations (4.13) to (4.15)) is evaluated using the parameters from the tritium fit $\hat{\phi}$ and compared to its shape using the parameters from the fit to the spectrometer electrode data ϕ. Both resulting spectra are shown in figure 5.20. The response obtained from the tritium fit slightly deviates from the response of the electrode measurements. Especially the normalization of the backscattering background shows a growing deviation with increasing initial energy. This most likely results from the fact that the backscattering behavior of electrode and β-electrons is different. The deviation is potentially mitigated by fitting a slope also to the linear energy dependence of n_3 and treating m_{n_3} as a free parameter in the null-hypothesis fit. In general, however, the parameters $\hat{\phi}$ lead to a physically valid reproduction of the electrode electron spectra.

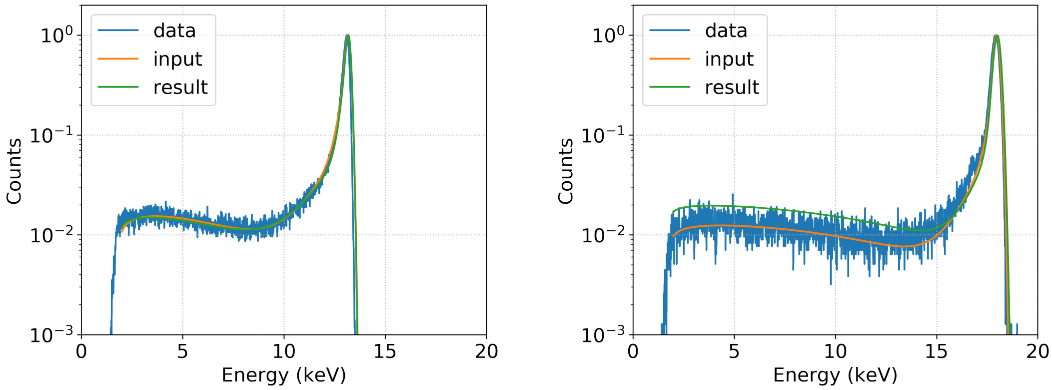

(a) Response at 13 keV.

(b) Response at 18 keV.

Figure 5.20: **Detector response from both electrode and tritium fit.** The electrode electron spectrum (blue) is shown for exemplary initial energies of (a) 13 keV and (b) 18 keV. Superimposed is the empirical model with the parameters ϕ, obtained from the fit to this data (orange), and with the parameters $\hat{\phi}$, obtained from the null-hypothesis fit (green). Especially the normalization of the backscattering background shows a deviation at high initial energies.

A comparison of the linear energy dependence of the parameters ϕ and $\hat{\phi}$ is shown in figure 5.21(a). A smaller value of $\hat{\beta}_2$ means a steeper slope of the second dead layer tail. The fact that β_2 (and also β_1) decreases with energy means, that the effect of the entrance window decreases with energy, reproducing the expected behavior (see section 4.3.1.1). The deviation between β_2 and $\hat{\beta}_2$ is always $< 15\,\%$. The detector resolution $\hat{\Delta E}$ shows a larger gradient than in the electrode measurements. Given this behavior, not only the absolute but also the relative energy resolution would degrade with increasing energy. This is not the expected physical behavior and may be caused by a feature of the empirical model: Larger values of ΔE compensate for a change in another parameter (e.g. n_1), due to the correlation between the two. In any case, the tendency of the linear energy dependence is reproduced for all parameters of the empirical model. Also in this regard, the null-hypothesis can be used as the baseline for the sterile neutrino search.

Sensitivity and exclusion Before calculating an exclusion based on the measured data, the expected sensitivity is determined. A sensitivity curve is calculated by the following steps:

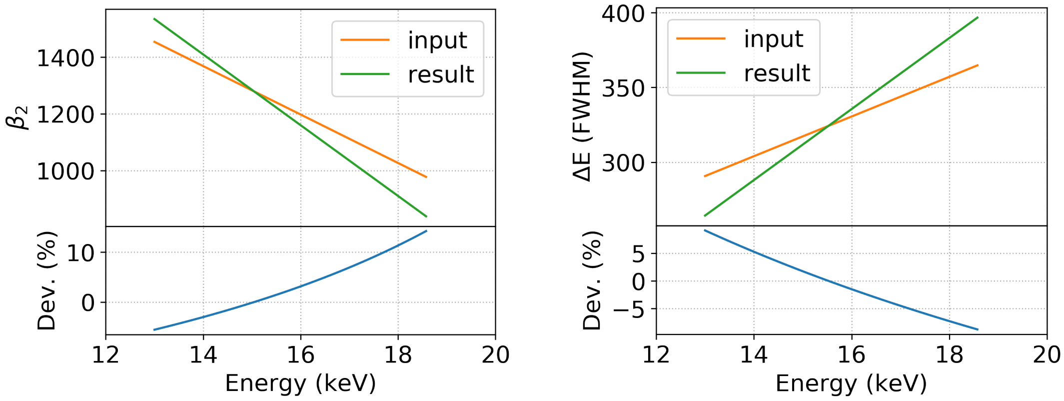

(a) Slope of the second dead layer tail.

(b) Energy resolution.

Figure 5.21: **Response energy dependence before and after the fit.** Exemplary, the linear energy dependence of (a) β_2 and (b) σ (expressed as FWHM) obtained from the electrode measurement (orange) is compared to the energy dependence obtained in the fit to tritium data (green). The lower plot (blue) shows the respective deviation in percent.

1. An artificial, unfluctuated data set is generated [Cow11], which is nothing but the model in equation (5.13), normalized to the amount of collected data. This model does not include a sterile neutrino.

2. The MC data set is fit with a model including a sterile neutrino admixture of a given combination of m_4 and $|U_{\mathrm{e}4}|^2$. To maintain numerical stability during the fit, pull terms towards the parameters $\hat{\phi}$ with a large uncertainty size of each parameter value are added to the χ^2-function:

$$\chi^2_{\mathrm{stab}} = \chi^2(N,E_0,E',\phi,B) + \chi^2_{\mathrm{pull}}(E_0) + \sum_{i=1}^{15} \frac{\left(\phi_i - \hat{\phi}_i\right)^2}{\hat{\phi}_i^2} \ . \tag{5.19}$$

3. Such a fit is performed for many points of a grid in the (m_4, $|U_{\mathrm{e}4}|^2$)-parameter space. At each point, the goodness of fit is calculated and compared to the null-hypothesis according to equation (5.15).

4. The points in the parameter space, at which $\Delta\chi^2 = Q$ are interpolated using matplotlib's pyplot.contour (version 2.1.2).

The resulting sensitivity curve is shown in figure 5.22 as dashed orange line. It indicates the exclusion, which can be expected given the amount of collected data and systematic uncertainty. A large deviation between exclusion and sensitivity would point towards an error in the analysis. The explored mass range is determined by the retarding energy applied in the measurement:

$$E_0 - eU = 5.6\,\mathrm{keV}\ . \tag{5.20}$$

The best sensitivity is reached at $m_4 = 3-4\,\mathrm{keV}$. For smaller and higher masses, the sensitivity is degraded. Low masses correspond to a spectral area close to the tritium endpoint, in which the count rate is low and the statistical uncertainty is large. High masses correspond to a spectral area close to the retarding energy. The spectral fit approach is particularly sensitive to the broad spectral distortion induced by the sterile neutrino admixture (opposed to the wavelet approach, which is sensitive to the kink). If the kink is located close to the retarding energy ($m_4 \approx E_0 - eU$), the spectral distortion is strongest outside of the ROI and the sensitivity is degraded.

The above described process is repeated 13 times with a statistically fluctuated MC data set. The only difference to the procedure before is that in step 1, the counts in the bins are randomized according to a Poissonian distribution. This results in 13 different sample sensitivity curves, which are indicated in figure 5.22 in greyscale: The darker a point in the (m_4, $|U_{\mathrm{e4}}|^2$)-parameter space, the more often it is excluded in the 13 sample sensitivity curves. The black area is excluded in all samples, while the white area is excluded in none of them. The comparison of this result to the sensitivity of the artificial data set (dashed orange) illustrates how statistical fluctuations impact the sensitivity. If the model describes the measured data precise enough, the latter can be interpreted as one of many possible statistical fluctuations of the former.

To calculate the exclusion curve, the above described process is performed on the actual measured data: Step 1 is skipped and the MC data set is replaced with the measured data. For 17 out of 10×10 points in the (m_4, $|U_{\mathrm{e4}}|^2$)-parameter space, a better goodness of fit is obtained than for the null-hypothesis. However, this is mostly the case for small mixing angles and small or large masses. In this regions, the sensitivity is low and the differences may result from statistical fluctuations. Even the difference between $\chi^2(H_0)$ and the best goodness $\chi^2_{\mathrm{best}} = 362$ ($m_4 = 5.0\,\mathrm{keV}$, $|U_{\mathrm{e4}}|^2 = 4.1 \cdot 10^{-2}$) is not statistically significant. The null-hypothesis thus remains the baseline for the sterile neutrino exclusion. The resulting exclusion curve is shown in figure 5.22 as a solid orange line. Given the measured data, the parameter space for a sterile neutrino admixture above this line is excluded at 95 % C.L. The best exclusion is

$$|U_{\mathrm{e4}}|^2 < 2 \cdot 10^{-2} \quad \text{at} \quad m_4 = 3.3\,\mathrm{keV}\ . \tag{5.21}$$

The exclusion curve is well aligned with the expected sensitivity. In a mass range of $m_4 \approx 0.8-2.5\,\mathrm{keV}$, the exclusion slightly exceeds the sensitivity, which is possible due to statistical fluctuations. For masses $m_4 > 3.5\,\mathrm{keV}$, the exclusion does not

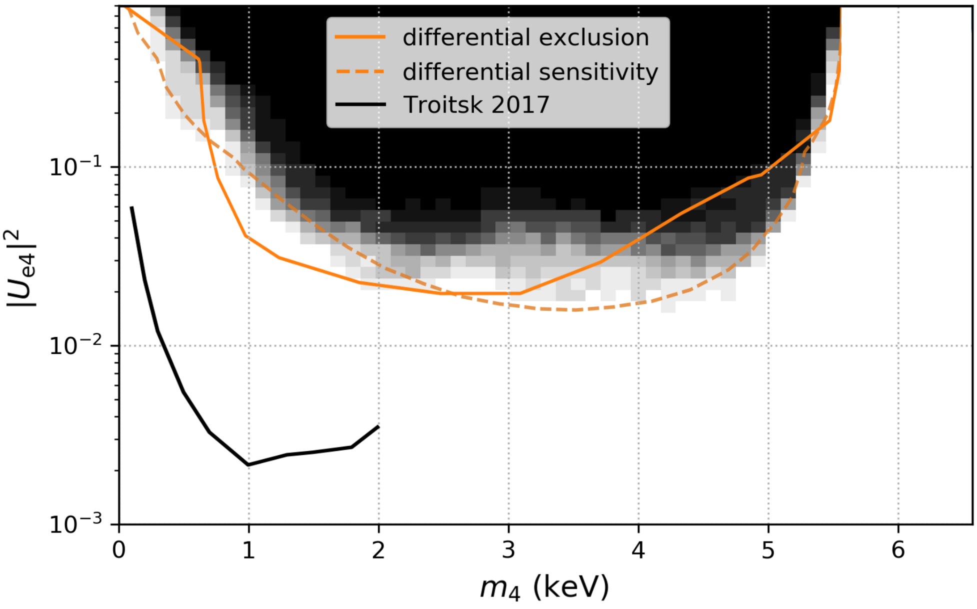

Figure 5.22: **Differential sensitivity and exclusion.** The dashed orange line indicates the statistical and systematic sensitivity, based on a non-fluctuated MC data set. The black parameter space is excluded by all 13 sensitivity curves with fluctuated MC data. The lighter the point, the less often it is excluded. The white area is never excluded. The straight orange line is the exclusion curve of the differential campaign. The black curve shows the latest result of the Troitsk ν-mass collaboration [Abd17] (integral measurement). The confidence level is 95 % for all curves.

quite reach the sensitivity, as small χ^2-values are obtained for relatively large sterile neutrino admixtures. This behavior has already been observed in earlier investigations with different data and was attributed to the many free parameters of the model, allowing for a compensation of the sterile neutrino signal [Alt19].

5.3 Integral campaign

In integral mode, the retarding energy is scanned over a range of several keV. At each setting, events that reach the detector are counted, i.e. all events that pass the retarding energy are integrated, yielding one measurement point in the spectrum. The campaign presented in this section took place in April 2018 and is the first sterile neutrino search with the P-0 system in integral mode. Section 5.3.1 gives a summary of the performed measurements. Corrections on both the differential and integral spectra are performed, which is described in section 5.3.2. In section 5.3.3, the experimental response is determined. The sterile neutrino search in integral mode is presented in section 5.3.4.

5.3.1 Measurements in integral mode

For the integral campaign, the detector holder was upgraded by a movable rod, shown in figure 5.23(a). This enabled to insert the detector further into the detector magnet. The magnetic field at this new position was around 1 T. As in the differential campaign, the P-0 system was tested in the copper box prior to its installation at the Troitsk ν-mass detector section (see figure 5.4(a)). The setup at the detector section in its final configuration is shown in figure 5.23(b). To perform automated measurements, the DANTE DPP was integrated into the Troitsk ν-mass DAQ system. This new software configuration was tested using electrons from the spectrometer electrode and from the electron gun. Furthermore, the (standard) settings in table 5.6 were established.

Table 5.7 gives an overview of the performed measurements. The tritium measurements are divided into five fills of the WGTS with new tritiated gas (see section 5.1.1). Each fill consists of several scans of the retarding energy range, so-called “sets”. With the automated DAQ system, the spectrometer voltage was changed according to a pre-arranged list. At each setting, DANTE automatically initiated an acquisition over 30 s. A usual set contains 132 measurement points at different retarding energies and 21 monitor points at 15 keV. To minimize the systematic impact of the steadily decreasing activity during a fill, the scans were performed in alternating directions in a range of 18.6 – 12 keV and vice versa. The voltage histories of two exemplary sets

Table 5.6: **Standard measurement settings of the integral campaign.** The nominal magnetic field configuration especially refers to 150 A at the pinch and the detector magnets. The detection threshold in channel 150 is equivalent to about 3 keV. The used DANTE firmware version 219.242.3412 was the first to feature the parameter “pile-up threshold”, which was set to 1 in the beginning and changed to 75 after fill 3 set 2.

Parameter	Setting
Detector chip	S0-1
Magnetic field configuration	nominal
Energy filter shaping time	2.016 µs
Detection threshold	in channel 150
DANTE firmware version	219.242.3412
Pile-up threshold	1, 75

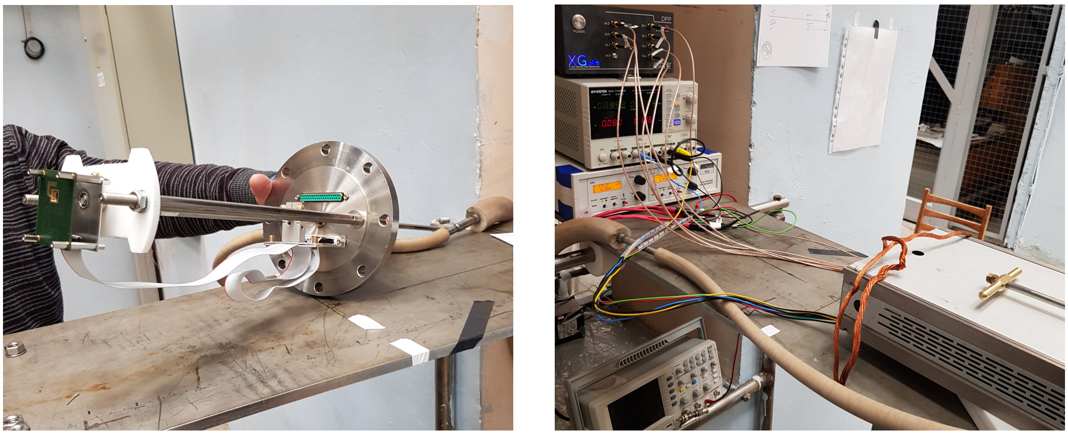

(a) Movable detector holding structure.

(b) Ambient devices.

Figure 5.23: **Setup of the integral campaign.** (a) The detector holding structure had been upgraded with a metal plate, which provided the ground potential also to the detector board. The plate was mounted on a movable rod, which enabled using a handle from outside vacuum to insert the detector another 20 cm into the detector magnet. This required a longer flat cable connection between detector board and vacuum flange. (b) The handle, which was used to move the detector, is visible on the right. Below the handle is the bias board box, which was attached to the table with a thicker copper cable, providing a better electrical connection to share the ground potential. The batteries were replaced by an ultra-stable high voltage power supply.

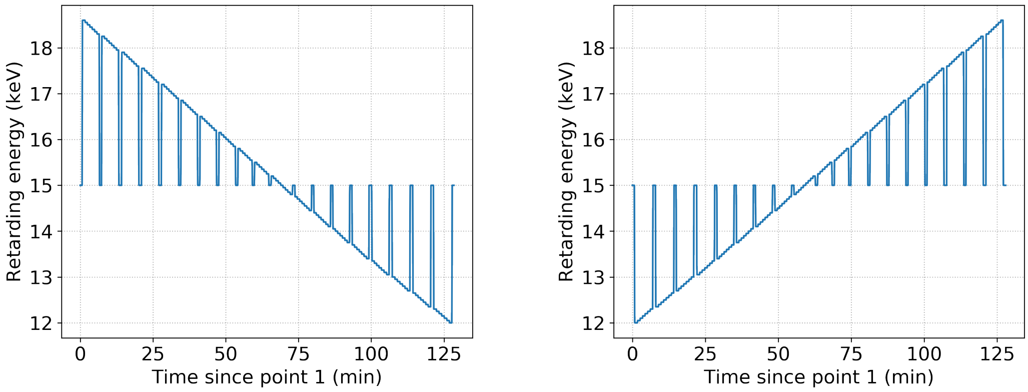

(a) HV during fill 3 set 5.

(b) HV during fill 3 set 6.

Figure 5.24: **Voltage history in integral mode.** Every set starts and ends with a monitor point, measured at a retarding energy of 15 keV. (a) Set 5 of fill 3 is a downwards scan: After the first monitor point, the retarding energy is decreased in steps of 50 eV in the range of 18.6 – 12 keV. Each retarding energy is kept for about 30 s and every fifth measurement is another monitor point at 15 keV. (b) Set 6 of fill 3 is an upward scan, in which the retarding energy is increased.

are shown in figure 5.24. Including the time to stabilize the spectrometer voltage, the duration of a usual set adds up to 128 min. After the first two sets of fill 3, the pile-up threshold in the DANTE DPP was set to 75. This is half of the set detection threshold in ADC channels, which is the recommended value according to the manufacturer, XGLab. A power failure in the entire building occurred during fill 3, which led to an outage of the cryogenic helium cooling of the magnets, which consequently quenched. Maintenance work was done on 23rd of April and the system was restarted on April 24. At the end of the campaign, additional test were performed to understand the origin of the bump.

The term “column density” refers to the gas density of the tritium source, integrated over the length d of the cylindrical WGTS tube:

$$\int \rho\left(z\right) \mathrm{d}z = \rho d \left[\mathrm{cm}^{-2}\right] \ . \tag{5.22}$$

Over the course of a fill, gas was pumped out, such that ρd was decreasing. Different densities lead to different scattering probabilities of the electrons on gas molecules, which changes the experimental response of the source section. The column density was thus determined at least once per fill in four sets with the electron gun. The electron gun voltage was fixed to $U_{\mathrm{egun}} = 19\,\mathrm{kV}$ and the spectrometer voltage was scanned over the range 18.50 – 19.01 keV. The count rate at each setting was

Table 5.7: **Measurements of the integral campaign.** The measurement campaign is divided into five fills. After the tritium measurements of fill 3, the magnets quenched due to a power failure. The measurements were interrupted for one day. Besides measurements with tritium, the column density was regularly determined using the electron gun. Adiabaticity measurements were performed, as well as acquisitions of only background events. All measurements were performed with standard settings (see table 5.6), if not stated otherwise: P — wrong pile-up threshold; 1 — empty source; 2 — fast shutter closed.

Date	Type	Source	# sets	Comments
Apr 16 – 18	Fill 1	tritium	16	P
Apr 17	Column density	e-gun	4	P
Apr 18	Column density	e-gun	4	P
Apr 18 – 19	Fill 2	tritium	9	P
Apr 19	Column density	e-gun	4	P
Apr 19 – 22	Fill 3	tritium	38	
Apr 20	Column density	e-gun	4	
Apr 24	Background	bknd	2	1, 2
Apr 24	Background	bknd	2	1
Apr 24	Adiabaticity	e-gun	7	1
Apr 24	Adiabaticity	bknd	3	1
Apr 24 – 25	Fill 4	tritium	8	
Apr 25	Column density	e-gun	4	
Apr 25 – 26	Fill 5	tritium	10	
Apr 26	Column density	e-gun	4	
Apr 26	Adiabaticity	e-gun	2	1
Apr 26	Adiabaticity	bknd	2	1
Apr 26	Background	bknd	6	1

determined in an acquisition over 20 s. At a retarding energy slightly below −19 keV, no β-electrons reach the detector: Only electrons from the electron gun, which do not lose any energy, contribute to the count rate. At lower retarding energies, the count rate increases, as also electrons that lose energy by scattering in the source pass the spectrometer. The ratio of rates at the two retarding energies depends on the column density ρd. The evaluation of the ρd measurements is explained in section 5.3.3.

Adiabaticity measurements were performed with empty WGTS. Like in the column density measurement, the electron gun was fixed to −19 kV but the retarding energy was scanned to much lower values (i.e. 12 keV), such that electrons from the gun reach higher surplus energies. In each step, the air coil system was tuned in order to focus the electron beam onto the detector. The count rate was determined in acquisitions over 10 s. Non-adiabatic effects are investigated in section 5.3.2.

Once a stainless steel vessel (e.g. the WGTS tube) is exposed to tritium gas, some tritium atoms penetrate its walls and bond to the metal lattice [Hir84]. These atoms are not removed by pumping and therefore the vessel remains contaminated. Due to influences as the work function of the WGTS tube or a changed FSD, β-electrons from this residual tritium lead to a background with a different spectral shape compared to the one from gaseous tritium. To correct for this, the background was measured twice during the differential campaign. One additional background measurement was performed with closed shutter between transport section and spectrometer. The analysis of these measurement is presented in section 5.3.2.2.

5.3.2 Data quality & corrections

Fills 1 and 2 were performed with a pile-up threshold setting of one. After changing it to 75, the count rate increased by a factor of 1.5. It is assumed that too many events had falsely been rejected in all acquisitions before. Fills 4 and 5 consist of much less sets than fill 3, which furthermore features both background and adiabaticity measurements. The analysis thus focuses on the data of fill 3 to begin with. The following sets of fill 3 are considered flawed and are thus rejected: Sets 1 and 2 were performed with the wrong pile-up threshold setting. The new software configuration (DANTE DPP integrated into Troitsk ν-mass DAQ) broke during the acquisition of sets 11 and 19, which contain only 64 and 9 points, respectively. During set 32, the voltage did not change automatically but got stuck at 12 keV for about 20 min. The power failure occurred during set 38 after only 40 measurement points. An overview of the remaining tritium measurements is given in table 5.8.

Table 5.8: **Tritium measurements of fill 3 of the integral campaign.** The second column states the time after the start of set 3. The column "direction" refers to the direction of the retarding energy scanning. The count rate refers to the first 15 keV monitor point and events in the central pixel excluding noise events. The bump appeared in all sets at retarding energies below around 16 keV.

Date	Time (h:min)	Set	Source	Direction	Rate (cps)
Apr 19	0:00	3	tritium	down	2668
19	2:36	4	tritium	down	2593
19	5:06	5	tritium	down	2510
19	7:15	6	tritium	up	2399
Apr 20	9:23	7	tritium	down	2369
20	11:31	8	tritium	up	2261
20	13:39	9	tritium	down	2252
20	15:47	10	tritium	up	2124
Apr 20	21:57	12	tritium	down	1799
20	24:05	13	tritium	down	1776
20	26:14	14	tritium	up	1675
20	28:38	15	tritium	down	1661
20	30:45	16	tritium	up	1633
20	32:53	17	tritium	down	1591
20	35:00	18	tritium	up	1502
Apr 21	37:50	20	tritium	down	1485
21	39:57	21	tritium	up	1423
21	42:48	22	tritium	down	1390
21	44:55	23	tritium	up	1352
21	47:10	24	tritium	down	1337
21	49:06	25	tritium	up	1286
21	51:34	26	tritium	down	1246
Apr 22	53:57	27	tritium	down	1248
22	56:05	28	tritium	up	1198
22	58:11	29	tritium	down	1195
22	60:18	30	tritium	up	1142
22	62:33	31	tritium	down	1138
22	67:38	33	tritium	down	1124
22	69:45	34	tritium	up	1039
22	71:52	35	tritium	down	1021
22	73:59	36	tritium	up	951
22	76:05	37	tritium	down	956

Table 5.9: **Calibration measurements of fill 3 of the integral campaign.** The second column states the time after the start of set 3. The count rate is given for the central pixel excluding noise events. For column density measurements, the count rate refers to the point with $eU = 18.5\,\text{keV}$, for all measurements to the first acquisition at $eU = 15\,\text{keV}$. B — bump appearance.

Date	Time (h:min)	Set	Source	Rate (cps)	Comments
Column density					
Apr 20	18:18	1	e-gun	880	
20	18:39	2	e-gun	863	
20	19:01	3	e-gun	843	
20	19:22	4	e-gun	856	
Background					
Apr 24	111:47	1	bknd	22	
24	115:26	2	bknd	26	B
Adiabaticity					
Apr 24	114:48	1	e-gun	433	B
24	116:04	2	e-gun	424	B
24	116:21	3	e-gun	416	B
24	116:36	4	e-gun	405	B
24	116:52	5	e-gun	406	B
Apr 24	117:36	1	bknd	11	B
24	117:51	2	bknd	14	B
24	118:12	3	bknd	13	B

In sets 6 and 7 of the adiabaticity measurements, the first three points were not saved. An overview of the analyzed non-tritium measurements is given in table 5.9.

As in the differential campaign, the acquired data is processed and controlled for systematic effects. In integral mode, however, this is done in two steps:

1. At each retarding energy point, a differential spectrum is acquired, which is treated individually. This is only possible due to the excellent energy resolution of the P-0 detectors.

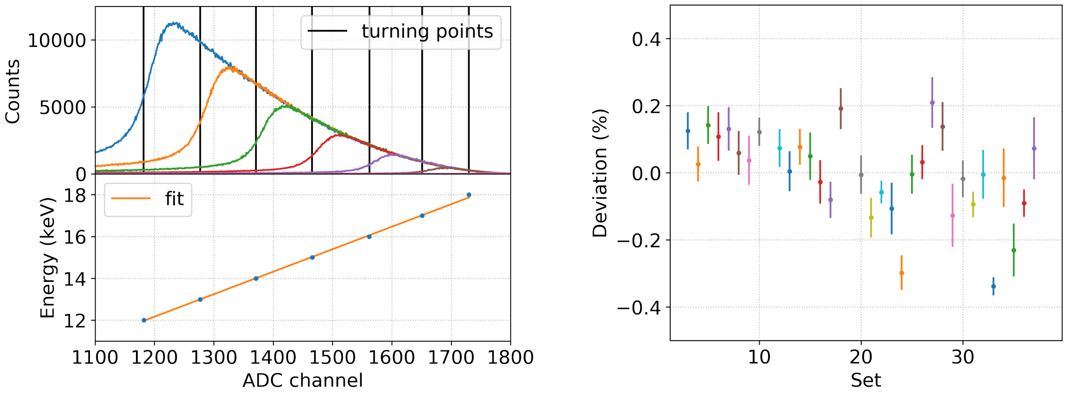

(a) Tritium calibration.

(b) Monitor point stability.

Figure 5.25: **Calibration in integral mode.** The plots are based on the data of fill 3. (a) *Top:* Each color shows a tritium measurement at a different retarding energy between 12 and 18 keV. The calibration is performed on the turning points of the HV cuts. *Bottom:* The resulting calibration curve is linear. (b) The calibration is applied to all monitor points and the deviation to the mean is calculated.

2. After that, the counts of each measured point are integrated and the corresponding count rate is calculated. The second step of treatment is performed on the generated integral spectrum.

Calibration The corrections on the differential spectrum require an energy calibration. Just for this correction, the spectra of all points at each retarding energy in fill 3 are stacked to increase the amount of data. That means that there is only one spectrum per retarding energy. The turning point of the HV cut is determined for each of these spectra. The calibration curve is determined by a linear fit to all of the turning points, as shown in figure 5.25(a). The result is cross checked: For each set, the spectra of all 15 keV monitor points are stacked and their turning points are determined. The calibration is applied on the turning points and compared to their average. The result is shown in figure 5.25(b). The deviation is smaller than 0.4 % for all sets. After set 15, a larger spread of the deviation is apparent, which, however, shows no systematic pattern. The calibration is thus considered sufficiently precise to be applied to all measurements of fill 3.

Resolution On the one hand, the sterile neutrino search is performed on the integral spectrum, whose energy resolution is determined by the spectrometer. On the other hand, a good energy resolution of the detector is still beneficial, as it facilitates

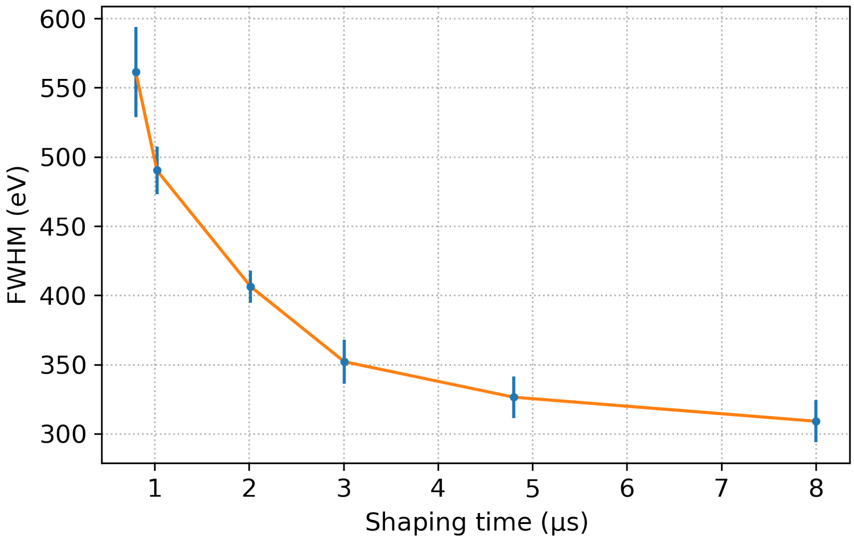

Figure 5.26: **Integral campaign noise curve.** With a shaping time of 2 µs, the measured energy resolution $\Delta E = 406(12)$ eV (FWHM) at 18 keV. The orange line is drawn to guide the eye.

and improves corrections on the differential spectrum. Figure 5.26 shows a noise curve, determined using the electron gun. The chosen shaping time of 2 µs leads to a FWHM of

$$406(12)\,\text{eV at } 18\,\text{keV} .$$

This result is comparable with the energy resolution of the differential campaign (402 eV at 18 keV) within uncertainty. The performance of the P-0 system and the noise influences in the Troitsk ν-mass experiment remain unchanged.

Adiabaticity The rate at each adiabaticity measurement point is calculated, subtracting background events. The rate is averaged over three adiabaticity measurements, as three background measurements were performed. Figure 5.27(a) shows the resulting rates over surplus energies up to $E_{\text{sur}} = 7$ keV. The average rate $\Gamma_{\text{egun}} \approx 398.7(8)$ cps is determined by a fit of a constant in an energy region, in which the rate is not decreased: Measurement points with a surplus energy $E_{\text{sur}} < 300$ eV are rejected due to energy loss in excited states [Sae00]. Measurement points with $E_{\text{sur}} \geq 6$ keV show a decreased rate with a deviation from the constant of more than $2\,\sigma$. This is an indication for non-adiabatic transport.

The measurement results are cross checked with simulations using the KASSIOPEIA framework [Fur17]. It was developed by the KATRIN collaboration to perform large-scale MC simulations of the entire KATRIN experiment. Electromagnetic fields

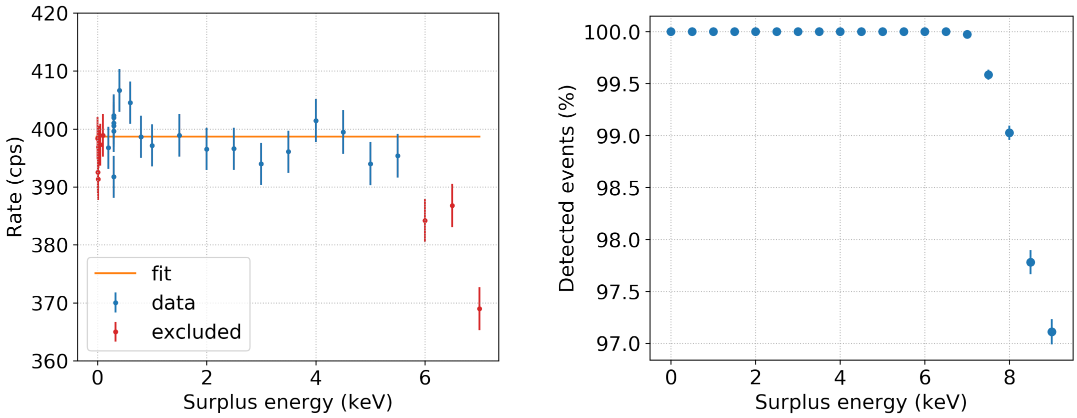

(a) Adiabaticity measurement.

(b) Adiabaticity simulation.

Figure 5.27: **Adiabaticity measurement and simulation.** (a) The electron gun energy was fixed at 19 keV. The blue data points are fit to determine the count rate. (b) KASSIOPEIA simulation with $E_{\mathrm{in}} = 14\,\mathrm{keV}$. Non-adiabatic transport is observed for $E_{\mathrm{sur}} \geq 7\,\mathrm{keV}$.

are calculated for a given geometry of HV electrode and magnetic coils, through which particles are tracked in small steps. Adjusting the geometry, any KATRIN-like experiment can be simulated. A total of 10^5 electrons are generated in the WGTS. To account for the radial dependence of non-adiabatic effects, the electrons are generated at the maximal radius from the symmetry axis, at which they still hit the detector. The detector is positioned in a magnetic field of 1 T, resembling the configuration of the integral campaign. The relative amount of detected events is calculated for a fixed electron energy $E_{\mathrm{egun}} = 14\,\mathrm{keV}$ and surplus energies of up to 9 keV. The result is shown in figure 5.27(b). The number of detected events decreases for surplus energies $E_{\mathrm{sur}} \geq 7\,\mathrm{keV}$ as a result of non-adiabatic transport.

The measurement points with a minimal retarding energy $eU = 12\,\mathrm{keV}$ in the integral campaign correspond to $E_{\mathrm{sur}} = 18.6 - 12 = 6.6\,\mathrm{keV}$. This energy is just at the border of incidence of non-adiabatic effects: According to the measurement, the rate is decreased by about 1 %, while the simulation yields adiabatic motion. The entire retarding energy range is thus considered in the sterile neutrino analysis.

Charge sharing The multiplicity cut is performed with a coincidence time window $\Delta t_{\mathrm{coinc}} = 200\,\mathrm{ns}$, which is determined analogously to the differential campaign (see section 5.2.2).

5.3.2.1 Corrections on the differential spectrum

Bump The bump appears in integral spectra as a step at a retarding energy $eU \approx 16\,\mathrm{keV}$ (see figure 5.3(b)). It appears in all tritium sets in fill 3, such that one cannot focus on data without the bump (like in the differential campaign). The effect can be circumvented by analyzing the integral spectrum only above 16 keV. However, this would restrict the accessible mass range of the sterile neutrino search to $m_4 < E_0 - 16\,\mathrm{keV} \approx 2.6\,\mathrm{keV}$. Consequently, the idea of treating the bump is to subtract the additional counts from the differential spectrum and to introduce appropriate systematic uncertainty. Several approaches are tested to subtract the bump:

- **Sliding cut** The differential spectrum is cut at an energy E_{cut}, which is larger than the peak position of the bump. Only the high energetic part is integrated to yield the corresponding data point in the integral spectrum. As the bump position moves with the retarding energy, also E_{cut} must be movable. Hence the name of the approach: “sliding cut”. However, at each retarding energy, a different fraction of the backscattering background is cut. The corresponding correction is not trivial: It would introduce systematic uncertainty, comparable to events below threshold, which is the largest uncertainty in the standard Troitsk ν-mass sterile neutrino search. The approach is thus not further pursued.

- **Parameterization** The bump's shape is approximated and fit with a Gaussian function, which is then subtracted from the data. However, the bump itself has a backscattering background, which is not accounted for by this approach. In order to remove also the backscattering background, the bump has to be parameterized with a more sophisticated function, e.g. the empirical model for mono-energetic electrons (see equations (4.13) to (4.15)). The fit of this function to the bump in a tritium spectrum suffers from large uncertainty, as the backscattering background of the bump is largely overlain by the backscattering background of the β-electrons. The approach is thus not further pursued.

- **Background subtraction** The idea of this approach is to subtract the shape of the bump as it appears in background measurements from tritium measurements. In a background measurement, the peak of the residual tritium is cut, as shown in figure 5.28(a). Only the bump remains, which can then be subtracted from the tritium data.[13] With this, it is also accounted for the bump's backscattering background. The bump of the background measurement does not appear at the exact same position and with the same amplitude as in a tritium measurement with the corresponding retarding energy. Both parameters are thus fit: The

---

[13] The residual tritium background is corrected for separately on the integral spectrum.

deviation of the resulting tritium spectrum from a constant c is minimized in the energy region of interest with the bump's main peak. The goodness of fit is expressed in a χ^2-value of the form

$$\chi^2 = \sum_i \frac{(c - m_i)^2}{\sigma_i^2} , \tag{5.23}$$

where i runs over the bins in the region of interest, m_i are the counts of the resulting spectrum, and σ_i are their propagated uncertainties. The constant c is determined by averaging over all counts m_i. This procedure is illustrated in figure 5.28(b). As the bump does not appear at all retarding energies, the integral spectrum is divided into three regions:

1. At retarding energies $eU < 15.5\,\mathrm{keV}$, the bump appears in both tritium and background measurements. The bump in the background spectrum is subtracted from each tritium measurement with the corresponding retarding energy.
2. At retarding energies $15.5\,\mathrm{keV} < eU < 16.2\,\mathrm{keV}$, the bump appears in the tritium measurement, but not in the background spectrum with the same eU. The described procedure is executed with several bump background spectra with $eU < 15.5\,\mathrm{keV}$. The background spectrum, resulting in the lowest χ^2-value, is subtracted from the tritium measurement.
3. At retarding energies $eU > 16.2\,\mathrm{keV}$, the bump appears neither in tritium, nor in background measurements. No correction is necessary.

The bump is subtracted from all measurements and corresponding systematic uncertainty is introduced in section 5.3.4.2. At this point, it should already be mentioned that, due to a residual pattern in the fit of the null-hypothesis, only set 3 of fill 3 is used for the sterile neutrino search in integral mode (see section 5.3.4.4). Most of the examples and figures are thus generated based on the data of this set.

Detection threshold The fraction of events below detection threshold is a retarding energy dependent quantity. Every retarding energy dependent effect on an integral spectrum has to be corrected for. The threshold according to the set value in the DANTE DPP is about 2.5 keV. However, a correction using this value yields a distorted integral spectrum. The differential spectrum has a kink at around 4 keV. At lower energies, the backscattering background is strongly decreased. Furthermore, a KESS simulation shows a flat continuation of the backscattering background at the count level of 4 keV. Hence, a value of 4.1 keV is chosen to correct for events below detection threshold: A region of the measured tritium spectrum above 4.1 keV but below the main peak of the bump is averaged. The bump is already subtracted

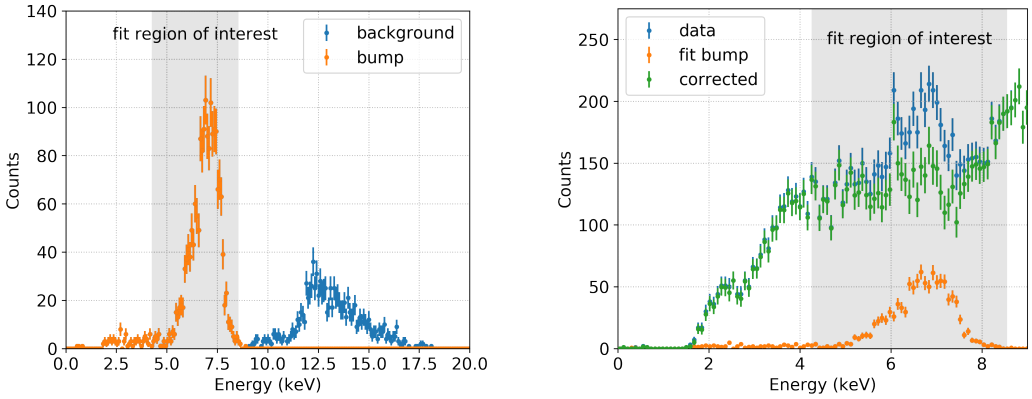

(a) Cut of residual tritium.

(b) Bump subtraction.

Figure 5.28: **Subtraction of the bump.** Both plots are based on the data of fill 3 set 3 at a retarding energy of 12 keV. (a) All bins in the background spectrum (blue) above the bump are set to zero to remove events from residual tritium. The region in which the remaining bump (orange) is fit to the data is shadowed. (b) However, as the bump has a backscattering background at energies below the ROI, the entire bump (orange) is subtracted from the tritium data (blue). Adapted from [Bru19].

at this stage, but the subtraction results in larger uncertainties in the region of the bump's main peak. All bins below 4.1 keV are then set to the averaged value n_{ave}, i.e. n_{ave} is extrapolated as the level of measured counts towards lower energies. The procedure is illustrated in figure 5.29(a).

Figure 5.29(b) shows the amount of added events as a function of retarding energy eU. Added events make up between 4 % at 12 keV and 1 % at around 17.5 keV. At higher eU, energy bins in the region of extrapolation contain only a few counts. This leads to large statistical uncertainty in this region.

5.3.2.2 Corrections on the integral spectrum

Dead time The lower the retarding energy, the higher the rate at the detector, and thus the more DAQ dead time. This makes dead time a retarding energy dependent effect, which needs to be corrected for. The dead time of each acquisition is calculated according to equation (4.11). Additional dead time is introduced by the multiplicity cut:

$$t_{\mathrm{dead}}^{\mathrm{multi}} = 6 \cdot 2 \cdot \Delta t_{\mathrm{coinc}} \ , \tag{5.24}$$

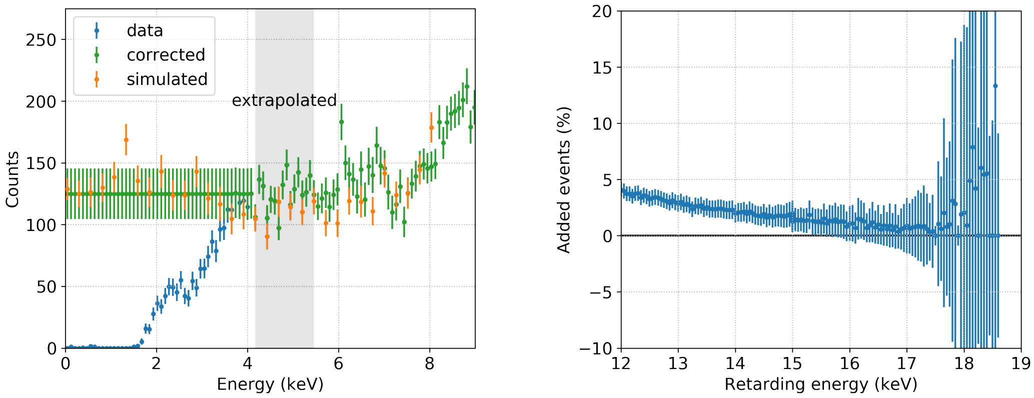

(a) Added events and simulation.

(b) Retarding energy dependency.

Figure 5.29: **Correction of events below detection threshold.** Both plots are based on the data of fill 3 set 3. (a) The retarding energy is 12 keV. The average number of data counts (blue) in the shaded region is extrapolated towards lower energies (green). The orange points show the result of a KESS simulation without detection threshold. Adapted from [Bru19]. (b) The amount of added events relative to all events in the spectrum drops as a function of the retarding energy until 17 keV. At higher retarding energies, very few counts are in the region of extrapolation and the statistical uncertainty becomes large.

where the factor 6 is the number of pixels surrounding CC. The factor 2 results from the fact, that the multiplicity cut removes events happening Δt_{coinc} before and after the event in CC. For each point in the integral spectrum, the measured rate is multiplied by a correction factor, calculated according to equation (4.12).

Rate decrease and fluctuation Over the course of a fill, tritium decays and gas is pumped out, such that the source activity decreases. This leads to a distortion of the integral spectrum: Later acquired points in a scan over the retarding energy range have lower rates relatively compared to earlier acquired points. In a first step to counteract this effect, most scans were performed in alternating direction through the eU-range: Downward scan means 18.6 – 12 keV, upward scan refers to 12 – 18.6 keV. A second correction step is based on the 15 keV monitor points: In the standard Troitsk ν-mass analysis, sets in which the rates of the corresponding monitor points fluctuate more than 10 % are rejected from the analysis [Ase11]. This is not the case in any set of fill 3. The monitor points are furthermore used to calculate time dependent rate correction factors. Their rates are fit over time using an exponential function

$$A \cdot \mathrm{e}^{-\lambda t} \ , \tag{5.25}$$

with a normalization factor A and the decay rate λ. This is done in three blocks:

$$\text{sets } 3-10, \qquad \text{sets } 12-21, \qquad \text{and sets } 22-37. \tag{5.26}$$

The blocks are separated by steps in the rate decrease, shown in figure 5.30(a). The correction factors are calculated as

$$f_{\mathrm{j}}^{\mathrm{b}} = \Gamma_0^{\mathrm{b}} \cdot \mathrm{e}^{\lambda^{\mathrm{b}} \cdot t_j} \ , \tag{5.27}$$

where subscript j indicates the respective set and superscript b indicates the respective block. The correction factors of each block are normalized to the rate of the first monitor point Γ_0, respectively. The rate of every set is multiplied with the corresponding correction factor. Figure 5.30(b) illustrates the rate correction of set 3.

Background A differential spectrum of the residual tritium background at $eU = 12\,\text{keV}$ is shown in figure 5.28(a). An integral background spectrum is generated as follows: In all points of both background measurements in fill 3, bins at $E < eU - 2\,\text{keV}$ are set to zero. This is done to cut the bump. Acquisitions without bump appearance are included as well, to treat all measurements in the same manner. The remaining counts in each point are integrated, yielding one integral spectrum

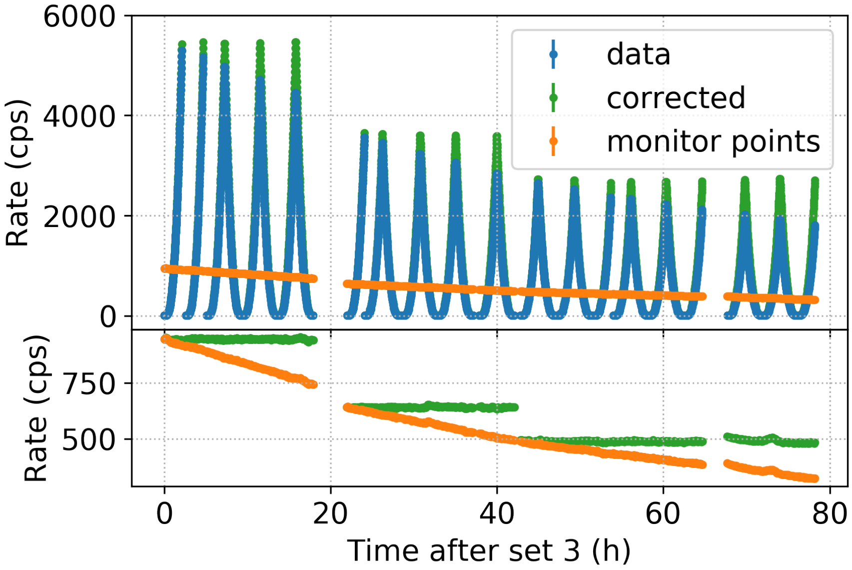

(a) Rate correction of fill 3.

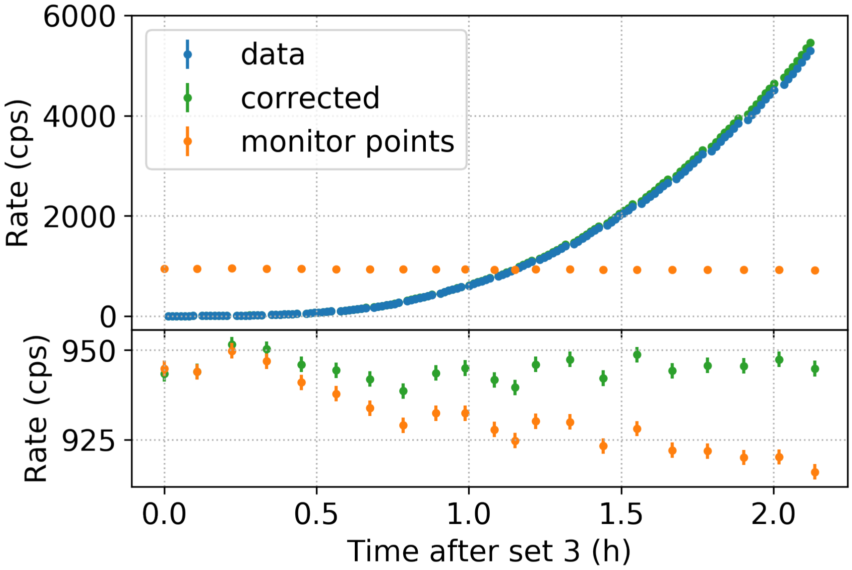

(b) Rate correction of set 3.

Figure 5.30: **Rate decrease correction.** (a) Fill 3 is divided into three blocks. *Top:* All measured points of all sets in fill 3 (blue). The 15 keV monitor points are shown in orange. *Bottom:* Each block of monitor points is fit individually with an exponential function. The rate decrease is corrected (green) with correction factors determined from the fit. (b) A zoom on set 3.

for each background measurement. The count rate is constant over time and for $eU = 12\,\mathrm{keV}$ in the order of 30 cps. Corresponding dead time is thus neglected. A correction of the rate decrease is not necessary, as the residual tritium background is constant. The two integral background spectra are averaged and the result is subtracted from every tritium set.

5.3.3 Column density & response determination

As in the differential campaign, the experimental response is included via response matrices. The response of the detector is used to model the shape of the measured differential tritium spectrum and is thus only relevant in differential mode. In integral mode, all counts of the differential spectrum are integrated and its shape is irrelevant for the sterile neutrino search. The response of source and transport section is again determined using SSC-sterile. One input parameter for SSC-sterile is the column density, which decreased over the course of fill 3. Therefore, a source and transport section response matrix $(R_{\mathrm{SSC}})_s$ is generated for each set s. Four column density measurements were performed with the electron gun during fill 3. Their results are extrapolated to determine the column density for each set.

Figure 5.31(a) shows the rates of an exemplary column density measurement with the electron gun at $E_{\mathrm{egun}} = 19\,\mathrm{keV}$. At small surplus energies $E_{\mathrm{sur}} < 10\,\mathrm{eV}$ ($eU > 18.99\,\mathrm{keV}$), the count rate is low: Electrons, which lose energy through scatterings in the WGTS, cannot pass the spectrometer. A plateau expands up to about $E_{\mathrm{sur}} = 10\,\mathrm{eV}$, which originates from non-scattered electrons. If they had scattered, they would have lost at least this energy in an excitation or ionization process of a molecule in the source. At higher surplus energies $E_{\mathrm{sur}} > 100\,\mathrm{eV}$, the count rate increases to a constant level, as almost all emitted electrons reach the detector. This region is called saturated. The column density is inferred from the ratio of rates between the plateau Γ_{plat} and the saturated region Γ_{sat} [Ang05]:

$$\rho d \sigma_{\mathrm{inel}} = -\log\left(\frac{\Gamma_{\mathrm{plat}}}{\Gamma_{\mathrm{sat}}}\right) , \tag{5.28}$$

where $\sigma_{\mathrm{inel}} = 3.456 \cdot 10^{-18}\,\mathrm{cm}^2$ is the total inelastic scattering cross section of electrons on tritium [Ase00].[14] The quantity $\rho d \sigma_{\mathrm{inel}}$ has no unit. To obtain Γ_{plat}, the rates of eight measurements on the plateau are averaged. To obtain Γ_{sat}, the rates of six measurements at $E_{\mathrm{sur}} = 500\,\mathrm{eV}$ ($eU = 18.5\,\mathrm{keV}$) are averaged. The retarding energy $eU = 18.5\,\mathrm{keV}$ is smaller than the tritium endpoint $E_0 \approx 18.6\,\mathrm{keV}$, such that also β-electrons reach the detector. Their rate, however, is negligibly small with 0.04 cps ($< 0.01\,\%$).

---

[14] The term column density is casually used for both quantities ρd and $\rho d \sigma_{\mathrm{inel}}$.

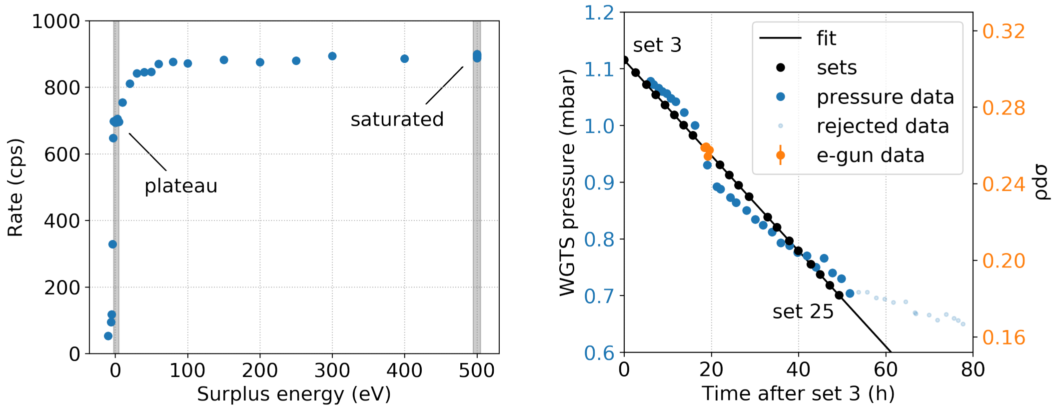

(a) Electron gun measurement.

(b) Relation to WGTS pressure.

Figure 5.31: **Column density determination.** (a) The column density is determined as the ratio of the count rate at the plateau to the saturated region. (b) The pressure in the WGTS (blue) is monitored about every 2 h. The electron gun measurements (orange) were performed within about 1 h. Both data is fit with a linear function (black), which corresponds to both y-axes (blue and orange). The black dots indicate the mean time of sets 3 – 25 in fill 3. The deviation of the fit from later pressure monitor points (light blue) gets large, such that sets later than set 25 are excluded from the analysis.

Table 5.10: **Column density in the integral campaign.** The pressure in the WGTS p_{WGTS} at the time of the individual sets is interpolated from the pressure monitor points. The corresponding column density $\rho d\sigma_{\mathrm{inel}}$ is extrapolated from electron gun measurements. The standard deviation of a Gaussian fit to the histogram of 10^4 correlated random fluctuations of the linear function yields the uncertainties.

Set	p_{WGTS} (mbar)	$\rho d\sigma_{\mathrm{inel}}$	Set	p_{WGTS} (mbar)	$\rho d\sigma_{\mathrm{inel}}$
3	1.115	0.30(6)	14	0.895	0.24(3)
4	1.093	0.30(5)	15	0.874	0.23(3)
5	1.072	0.29(5)	17	0.839	0.22(3)
6	1.054	0.29(4)	18	0.821	0.22(3)
7	1.036	0.28(4)	20	0.797	0.21(3)
8	1.018	0.28(4)	21	0.779	0.21(4)
9	1.000	0.27(3)	22	0.755	0.20(4)
10	0.982	0.27(3)	23	0.737	0.19(4)
12	0.931	0.25(3)	24	0.718	0.19(4)
13	0.913	0.25(3)	25	0.701	0.18(4)

With this procedure, the column density during the four electron gun measurements is determined. To determine the column density during the individual tritium sets, a relation to the pressure in the WGTS p_{WGTS} is established, which is monitored about every 2 h. Both the column density and the WGTS pressure are fit with a linear function, shown in figure 5.31(b). The deviation from this function gets large for sets later than set 25. The proximity in time of the electron gun measurements, however, does not allow approximating a more accurate function (e.g. an exponential decrease). The corresponding sets (26 − 37) are thus excluded from the sterile neutrino search. The resulting values for $\rho d\sigma_{\mathrm{inel}}$ of all remaining sets are listed in table 5.10.

Other input values for the response calculation with SSC-sterile are the source magnetic field $B_{\mathrm{source}} = 0.6\,\mathrm{T}$, the pinch magnetic field $B_{\mathrm{pinch}} = 7.3\,\mathrm{T}$, and the magnetic field in the analysis plane $B_{\mathrm{ana}} = 6 \cdot 10^{-4}\,\mathrm{T}$. The correction of the trapping effect is applied as in the differential campaign (see section 5.2.3.2). The response matrix R_{trap} is independent of the column density. The set dependent total response matrices of source and transport section $R_s\,(eU; E)$ are obtained in a matrix multiplication according to equation (5.11).

5.3.4 Integral sterile neutrino search

As explained in section 5.3.2.1, the sterile neutrino search is performed on the data of fill 3 set 3 only. The incomplete subtraction of the bump leads to a residual pattern, which is enhanced when combining the data of more sets. The final spectrum consists of a total of about 5.28 million events. However, the following description of analysis methods is generalized for a given number of sets. An individual set is referred to as set s. This enables the combination of data from several acquisitions in future campaigns at the Troitsk ν-mass experiment. A corresponding analysis framework has been established in Python.

5.3.4.1 Integral model

The model of the integral tritium spectrum is based on the model derived for the differential campaign (see equation (5.12)). It contains small term corrections and an energy dependent final state distribution. The model is convolved with a response matrix R_s and integrated from the respective retarding energy eU to the tritium endpoint E_0, resulting in an integral tritium decay model for each set i:

$$\Big(f_{\mathrm{int.model}}(eU; N, E_0, B)\Big)_s = N \cdot \int_{eU}^{E_0} \left[\frac{\mathrm{d}\Gamma(E,E_0)}{\mathrm{d}E} \times R_s(eU,E)\right] \mathrm{d}E + B \ . \tag{5.29}$$

5.3.4.2 Covariance matrix method

Uncertainties are propagated with the covariance matrix method whenever possible. A covariance matrix M contains the covariance between elements of a given parameter set, for instance the parameters $\vec{\omega}$ of a linear fit function:

$$\vec{\omega} = \begin{pmatrix} m \\ c \end{pmatrix} , \qquad M_{\vec{\omega}} = \begin{pmatrix} \sigma^2_{m,m} & \sigma^2_{m,c} \\ \sigma^2_{c,m} & \sigma^2_{c,c} \end{pmatrix} . \tag{5.30}$$

The diagonal elements of the covariance matrix, $\sigma^2_{m,m}$ and $\sigma^2_{c,c}$, are the variances (the squared standard deviations) of the parameters slope m and offset c, respectively. The off-diagonal elements of M are the covariance of m and c, where $\sigma^2_{m,c} = \sigma^2_{c,m}$. Hence, covariance matrices are square matrices, which are always symmetric and positive semi-definite. The covariance can be translated into a correlation coefficient. Slope and offset are usually negatively correlated: If m increases, c decreases and vice versa.

In this work, covariance matrices are used to account for correlated uncertainties in integral tritium spectra. If the spectrum f is expressed as a vector (like $\vec{\omega}$ in equation (5.30)) the corresponding covariance matrix M contains

- uncorrelated uncertainties of each retarding energy bin on its diagonal and
- bin-to-bin correlated uncertainties as off-diagonal elements.

Uncorrelated uncertainties are for example statistical uncertainties in a counting experiment: The counts (or rates) at each retarding energy are independent of those of any other retarding energy. Systematic effects, however, can affect several measurements similarly and thus several retarding energy bins simultaneously. The correlation is expressed in the respective covariance.

Specifically, covariance matrices are used to account for correlated uncertainties in the χ^2-fit of the integral spectrum. Given a model f, which depends on parameters $\vec{\theta}$, the usual χ^2-function

$$\chi^2(\vec{\theta}) = \sum_j \frac{\left(y_j - f_j(\vec{\theta})\right)^2}{\sigma^2_{y_j}} \ , \tag{5.31}$$

does only account for the standard deviations σ_{y_j} of the data points y_j. Correlated uncertainties are neglected. Using the covariance matrix method, the χ^2-function is expressed in matrix notation as

$$\chi^2(\vec{\theta}) = \left(y - f(\vec{\theta})\right)^T M^{-1} \left(y - f(\vec{\theta})\right) \ . \tag{5.32}$$

The covariance matrix M accounts for both uncorrelated (diagonal) and correlated (off-diagonal) uncertainties. Advantages of this method are, that covariance matrices are easily calculable and combined to a total matrix

$$M_{\text{tot}} = M_1 + M_2 + \dots \tag{5.33}$$

by adding the matrices of individual, uncorrelated effects. To calculate the covariance matrix for a systematic effect M_{sys}, the MultiSim method is applied [Sch19b].[15] The procedure contains the following steps [Fra13]:

1. Considering the correction of a systematic effect depends on the parameters $\vec{\omega}$, these parameters are randomly varied multiple times according to their correlations. An example: A systematic effect is corrected by multiplying the tritium decay model f with a linear function. Then, a large number $N = \mathcal{O}(10^4)$ of random parameters m and c is generated according to a

---

[15] The name is an abbreviation for *multiple simulations*.

multivariate distribution determined by $M_{\vec{\omega}}$. A large N is necessary, as the generated covariance matrix M_{sys} is an estimator for the true covariance matrix, to which M_{sys} converges for $N \to \infty$.

2. For all N variations of $\vec{\omega}$, an integral tritium spectrum is generated. This means in the example, that a linear correction function is calculated for each $(m,\, c)$-parameter set. Each function is then multiplied by the tritium decay model f. This results in N tritium model spectra $\vec{f} \equiv \mathbf{f}$, each including a different realization of the correction.
3. The covariance matrix M_{sys} is calculated using Python's numpy.cov, which makes use of the sample covariance

$$M_{\text{sys}} = \frac{1}{N-1} \sum_{i=1}^{N} \left(\mathbf{f}_i - \bar{\mathbf{f}}\right) \left(\mathbf{f}_i - \bar{\mathbf{f}}\right)^T \qquad \text{with} \qquad \bar{\mathbf{f}} = \frac{1}{N} \sum_{i=1}^{N} \mathbf{f}_i \ . \tag{5.34}$$

Two additional features connected to covariance matrices are used in this work. One is the application of fractional covariance matrices, which are defined by [Sch19b]

$$M_{jk} = \left(M_{\text{frac}}\right)_{jk} \cdot \bar{f}_j \cdot \bar{f}_k \ . \tag{5.35}$$

This enables to use the same covariance matrix on models with different normalizations but other conditions being equal. An example: The covariance matrix for a systematic effect M_{s3} was generated using the data of set 3. This included the rather time consuming generation of N realizations of the corresponding correction. Now, the effect shall be considered in set 25, which comprises less data than set 3. To avoid performing another N corrections, the fractional covariance matrix $(M_{\text{frac}})_{\text{s3}}$ is calculated. In order to apply the covariance matrix in the fit, $(M_{\text{frac}})_{\text{s3}}$ is renormalized to the amount of data in set 25 according to equation (5.35). This utilization of fractional covariance matrices is not entirely correct, as systematic effects may depend on the count rate. However, this inaccuracy is negligible for the purpose of the presented investigations. In the following, a fractional covariance matrix is only used, when explicitly mentioned.

The second feature is the application of so-called “shape-only” covariance matrices. When generating a covariance matrix M based on given data, e.g. set 3, an uncertainty of a parameter can lead to an overall normalization uncertainty in the corresponding covariance matrix, apart from a shape-only effect. The normalization, however, is a free parameter in the fit. To not account for this uncertainty twice, all normalization uncertainties are eliminated by the shape-only covariance matrix $M_{\text{shape-only}}$. It is calculated as follows:

1. A large number N' of random integral spectra f is generated, accounting for bin-to-bin correlations given by the covariance matrix M.

2. Each sample f is normalized with the ratio of the total expected number of counts in all spectra to the total number of counts in f:

$$f_{\text{shape-only}} = f \cdot \frac{\sum_j \bar{f}_j}{\sum_j f_j} \,. \tag{5.36}$$

3. The shape-only covariance matrix $M_{\text{shape-only}}$ is calculated according to equation (5.34), but using $\mathbf{f}_{\text{shape-only}}$ instead of $\mathbf{f}$.

In the following, every generated matrix is transferred into its shape-only equivalent before use.

Bump subtraction The amplitude of the bump in background measurements has been fit to the bump in tritium measurements (see figure 5.28). To account for the uncertainty of the fit, a covariance matrix is calculated. To this end, the $1\,\sigma$ uncertainty of the amplitude fit value is determined. This is shown for an exemplary retarding energy of 15 keV in figure 5.32(a). The amplitude is varied 10^4 times. Each time, bump subtraction and subsequent integration of counts is executed. This is done for every point in a set s, resulting in 10^4 integral sample spectra $\mathbf{y}_s$, from which a bump amplitude covariance matrix $(M_{\text{amp}})_s$ is calculated. As the bump's shape differs from acquisition to acquisition, an individual covariance matrix is generated for each set s in fill 3, instead of using a fractional matrix. The matrix consists of diagonal elements only, as the bump subtraction is performed at each measurement point individually. Correlation between bumps at different measurement points does not exist.

The bump's amplitude is correlated to its position, as both are fit simultaneously. This would actually require to generate random values for both parameters simultaneously, drawn from a multivariate distribution with two dimensions. However, the bump's position depends on the quantization of ADC channels, such that the bump spectrum can only be shifted in discrete steps of the channel. The $1\,\sigma$ uncertainty on the bump's position is smaller than one channel. This holds for every measurement point. Nevertheless, the position of the bump is varied 10^4 times within plus or minus one channel. A bump position covariance matrix $(M_{\text{pos}})_s$ is generated as described above. This matrix contains much smaller entries than the bump amplitude covariance matrix, as the corresponding uncertainty is much smaller. Figure 5.32(b) shows the combined matrix $(M_{\text{bump}})_{\text{s3}} = (M_{\text{amp}})_{\text{s3}} + (M_{\text{pos}})_{\text{s3}}$ for both the shift and the position of the bump for set 3.

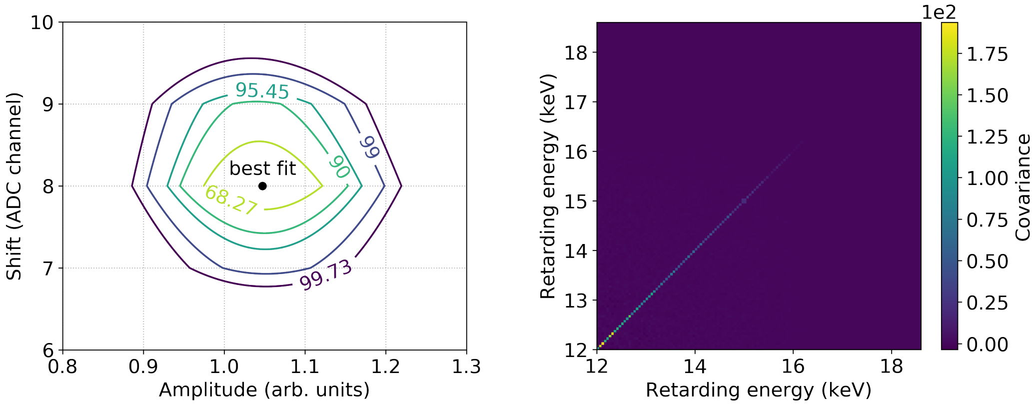

(a) Correlation of bump fit parameters.

(b) Bump covariance matrix.

Figure 5.32: **Systematic uncertainty of the bump subtraction.** All plots are generated based on the data of fill 3 set 3. (a) The uncertainty regions for different confidence levels (C.L.) in the two-dimensional parameter space of a bump fit at $eU = 15\,\mathrm{keV}$. The 1 σ uncertainty (68.27 % C.L.) of the shift is smaller than one ADC channel. The parameters are varied within their uncertainty to generate the covariance matrices for the amplitude and the shift of the bump. As the bump is individually subtracted at each measurement point, both matrices show no bin-to-bin correlations. The combined covariance matrix is shown in (b).

Detection threshold For the correction of events below detection threshold, a constant number of counts in the differential spectrum has been added for energies below 4.1 keV. In this energy region, the simulation that was used to cross check the correction shows a potential deviation from a constant (see figure 5.29(a)). A systematic uncertainty is introduced for this deviation in the form of a threshold covariance matrix $(M_{\text{thres}})_s$. To this end, a quadratic term

$$q\,(E) = a \cdot (E - b)^2 \tag{5.37}$$

is added to the correction, which describes the counts in the energy range below the detection threshold. Its origin is placed at half the detection threshold $b = 0.5 \cdot 4.1 = 2.05\,\text{keV}$. Its amplitude a is randomly varied according to a uniform distribution in a range, which resembles the deviation observed in the simulated data. Figure 5.33(a) shows the correction function with a maximal amplitude of the quadratic term. Each random value is used to generate a realization of the events below threshold correction for all points in an integral spectrum. In total, 10^4 sample spectra $\mathbf{y}_s$ with different corrections are generated, from which the covariance matrix is calculated. The covariance matrix for set 3 is shown in figure 5.33(b). In contrast to the covariance matrix of the bump subtraction, it includes bin-to-bin correlations, as one amplitude of the quadratic term is used for all points in a set. The covariance is largest at low retarding energies, for which also the count rate (i.e. the amount of data) is highest. The relative uncertainty is actually largest at high retarding energies, representing the behavior shown in figure 5.29(b). An individual covariance matrix is generated for each set, as the spectral shape in the region of extrapolation partly depends on the precedent bump subtraction.

Trapping effect The retarding energy dependent trapping factors have been fit with a second degree polynomial $p(E_{\text{in}})$ (see figure 5.14(b)). To account for the uncertainty of the fit, a trapping covariance matrix M_{trap} is generated. Correlated uncertainties of the polynomial's parameters are obtained from the fit. Random values for the parameters are drawn 10^4 times within their correlated $1\,\sigma$ uncertainties. For each set of parameters, a trapping response matrix is generated, which is subsequently applied on the tritium decay model according to equation (5.29). The normalization of the model is thereby arbitrary. All resulting sample spectra $\mathbf{f}_s$ are used to calculate M_{trap}. This covariance matrix is based on the tritium decay model and not on actual measured data. The only feature which changes from set to set is its normalization. Thus, the fractional matrix $M_{\text{trap,frac}}$ is calculated, shown in figure 5.34(a).

The trapping correction depends on the ratio of inelastic to quasi-elastic cross sections (see equation (5.10)), both of which are given as an input to the trapping simulation. The quasi-elastic cross section σ_{elas} is given without uncertainty [Tra83,

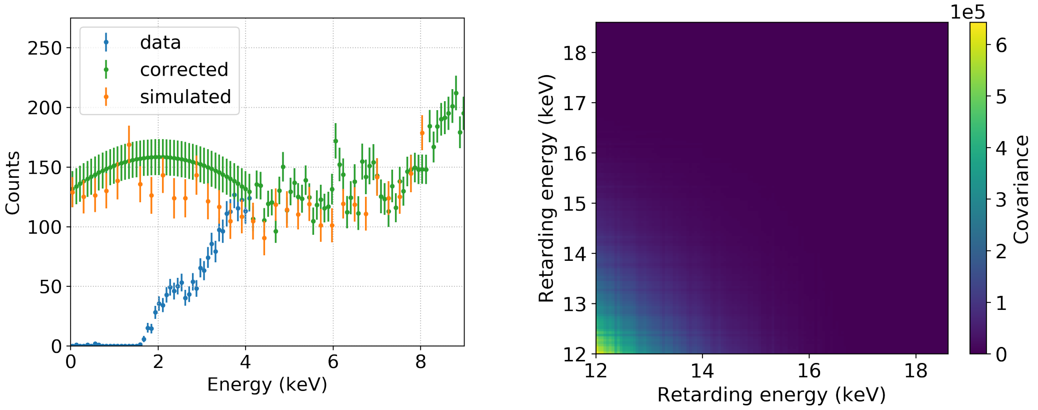

(a) Correction with maximal quadratic term.
(b) Threshold covariance matrix.

Figure 5.33: **Systematic uncertainty of the threshold correction.** (a) The plot shows the same data as figure 5.29(a) but with a maximal amplitude of the quadratic term. The amplitude is varied within this range to generate the covariance matrices for the correction of events below detection threshold, e.g. (b) for fill 3 set 3.

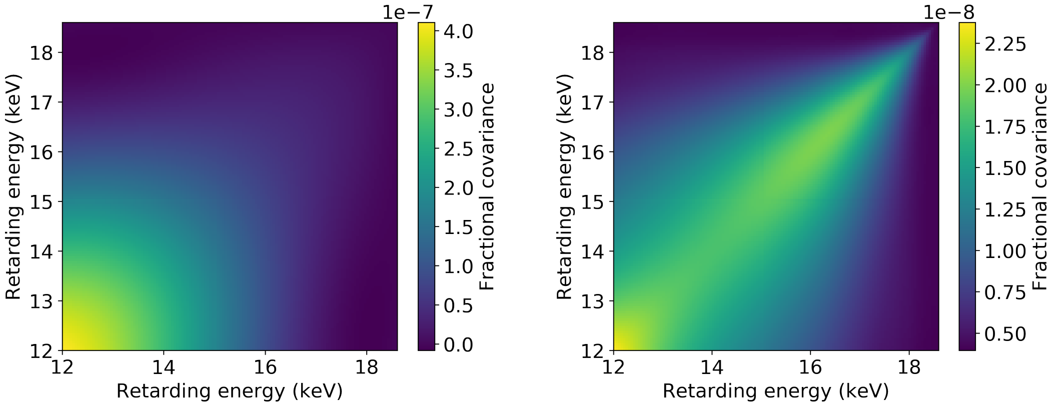

(a) Trapping covariance matrix.
(b) Cross section covariance matrix.

Figure 5.34: **Systematic uncertainty of the trapping correction.** Both plots show the respective fractional covariance matrix. (a) The trapping covariance matrix is generated by varying the parameters of the polynomial function, which is used to fit the retarding energy dependent trapping factors. (b) The cross section covariance matrix is obtained by repeating the trapping simulation with extremal values for σ_{inel}.

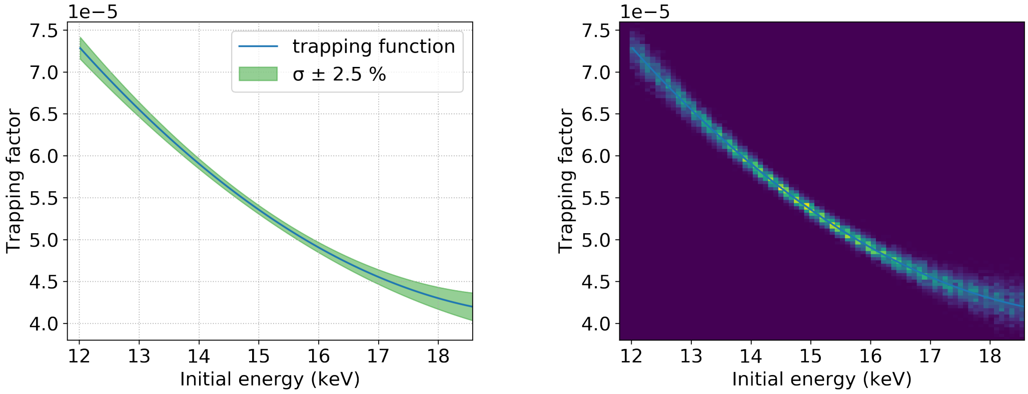

(a) Uncertainty band of the trapping function.

(b) Random number generation.

Figure 5.35: **Treatment of uncertainty in the trapping simulation.** (a) The trapping simulation is repeated with extremal input values of $\sigma_{\mathrm{inel}} \pm 2.5\,\%$. The resulting uncertainty band (green) around the original trapping function (blue) is interpreted as $1\,\sigma$ of a Gaussian distribution. (b) Random numbers are generated according to the Gaussian distribution, which are used to calculate a covariance matrix for the uncertainty on σ_{inel}.

Liu87], while the uncertainty on the inelastic cross section σ_{inel} is about $2\,\%$ [Ase00]. The trapping simulation is repeated with different inputs: once with $\sigma_{\mathrm{inel}} - 2.5\,\%$ and once with $\sigma_{\mathrm{inel}} + 2.5\,\%$. The analysis of the simulated data is performed in the same manner as described in section 5.2.3.2, yielding two extremal trapping functions: $p(E_{\mathrm{in}}; \sigma_{\mathrm{inel}} - 2.5\,\%)$ and $p(E_{\mathrm{in}}; \sigma_{\mathrm{inel}} + 2.5\,\%)$. The difference between the two is interpreted as the standard deviation of a Gaussian distribution, from which 10^4 random sample functions $\mathbf{f}_s$ are drawn. This procedure is illustrated in figure 5.35. The trapping correction is applied and a cross section covariance matrix is generated as described above. Its fractional matrix $M_{\mathrm{crsec,frac}}$ is shown in figure 5.34(b).

Rate decrease The decrease of the count rate of the 15 keV monitor points during fill 3 has been fit with an exponential function (see equation (5.25)). The function parameters' correlated uncertainties are obtained from the fit. Random values for each parameter are drawn from the corresponding multivariate distribution of $1\,\sigma$ uncertainties. The rate correction is then performed for each set of parameters. As the rate correction depends on all monitor points in each of the three blocks (see equation (5.26)), the correlation expands over several sets, resulting in comparably large covariance matrices, e.g. $(M_{\mathrm{rate}})_{\mathrm{b1}}$ for the first block. Correctly accounting for all correlations in each block requires a simultaneous fit of all related sets according to the χ^2-function in matrix notation (see equation (5.32)). Both the measured points of all sets and the corresponding models are thus concatenated to large vectors, e.g.

$$y_{\mathrm{b1}} = \begin{pmatrix} y_{\mathrm{s3}} \\ y_{\mathrm{s4}} \\ \vdots \\ y_{\mathrm{s10}} \end{pmatrix} \qquad \text{and} \qquad f_{\mathrm{b1}} = \begin{pmatrix} f_{\mathrm{s3}} \\ f_{\mathrm{s4}} \\ \vdots \\ f_{\mathrm{s10}} \end{pmatrix} . \tag{5.38}$$

All other covariance matrices than M_{rate} are concatenated on the diagonal of an accordingly large matrix. Off-diagonal elements are filled with zero matrices $\mathbf{0}$ in the dimension of for instance $(M_{\mathrm{bump}})_{\mathrm{s}}$. In the case of the first block, this results in

$$(M_{\mathrm{bump}})_{\mathrm{b1}} = \begin{pmatrix} (M_{\mathrm{bump}})_{\mathrm{s3}} & \mathbf{0} & \dots & \mathbf{0} \\ \mathbf{0} & (M_{\mathrm{bump}})_{\mathrm{s4}} & & \vdots \\ \vdots & & \ddots & \mathbf{0} \\ \mathbf{0} & \dots & \mathbf{0} & (M_{\mathrm{bump}})_{\mathrm{s10}} \end{pmatrix} . \tag{5.39}$$

The resulting block-wise covariance matrices of all systematic uncertainties can then be added in the same manner as their small set-wise equivalents:

$$(M_{\mathrm{tot}})_{\mathrm{b1}} = (M_{\mathrm{rate}})_{\mathrm{b1}} + (M_{\mathrm{bump}})_{\mathrm{b1}} + \dots \tag{5.40}$$

As mentioned above, the sterile neutrino search focuses on the data of fill 3 set 3. A rate decrease covariance matrix $(M_{\mathrm{rate}})_{\mathrm{s3}}$ is thus generated using exclusively the data of this set. It thereby maintains the dimension of the other covariance matrices and is shown in figure 5.36(a). Figure 5.36(b) shows the corresponding fractional covariance matrix. The relative uncertainty is larger at low and high retarding energies, compared to intermediate eU. This is a feature of the linear function, which is more constrained in the middle of the data points.

Uncertainty budget All systematic uncertainty contributions, treated with the covariance matrix method, are shown in figure 5.37 for the data of set 3. The plot shows the diagonal of the respective covariance matrix, i.e. its uncorrelated uncertainties.

As in the standard Troitsk ν-mass sterile neutrino search, the largest contribution seems to emerge from the correction of events below detection threshold. A lower detection threshold or an improved modeling of events below detection threshold would decrease this uncertainty contribution. The contribution of the rate decrease correction exceeds the statistical uncertainty at $eU < 13\,\mathrm{keV}$. The uncertainty of the trapping correction reaches at most 0.3 % of the statistical uncertainty. As

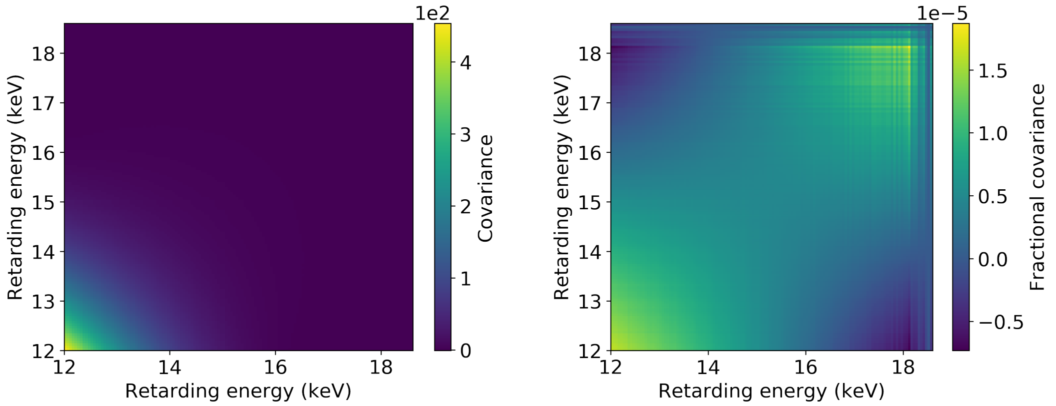

(a) Rate decrease covariance matrix.

(b) Fractional equivalent.

Figure 5.36: **Systematic uncertainty of the rate decrease correction.** (a) The rate decrease covariance matrix is produced by 10^4 varying the parameters of the exponential function, which is used to correct for the rate decease over time. (b) The relative covariance is largest at low and high retarding energies, respectively. A wide spread bin-to-bin correlation is apparent.

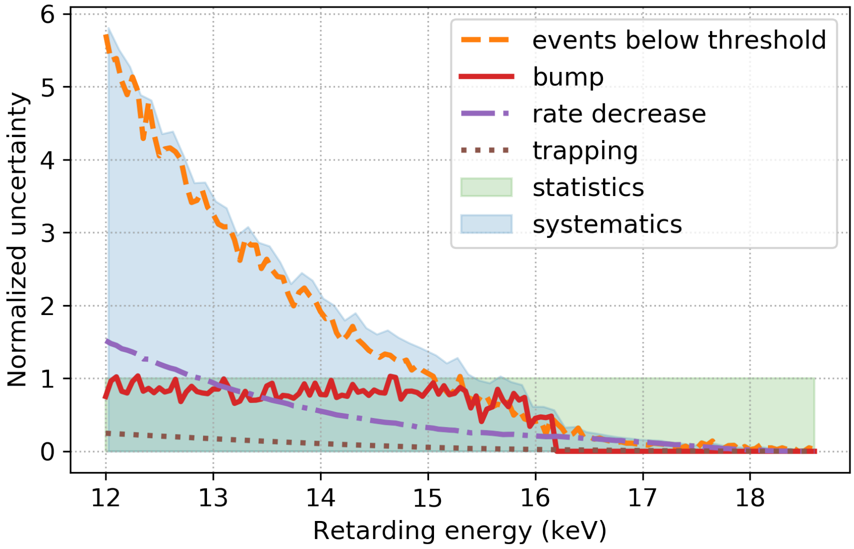

Figure 5.37: **Uncertainty budget in the integral campaign.** The plot refers to the data of fill 3 set 3. All contributions are normalized to the statistical uncertainty (green). Only the diagonal element of the respective covariance matrix are shown, i.e. bin-to-bin correlations are not visualized. Adapted from [Bru19].

uncertainties are added in squares, it is almost negligible compared to the other uncertainties. The uncertainty induced by the subtraction of the bump does not significantly exceed the statistical uncertainty at any retarding energy. However, the bump is the only uncertainty, which is fully bin-to-bin uncorrelated (see figure 5.32). As such, it actually makes up the largest uncertainty contribution.[16] As the bump appears only at retarding energies below around 16 keV, the corresponding systematic uncertainty drops to zero for higher eU.[17] All contributions increase with decreasing retarding energy and dominate over the statistical uncertainty at $eU < 15\,\text{keV}$. With a sophisticated measurement time distribution (MTD), the statistical uncertainty at high retarding energies can be decreased, to obtain an equilibrium of systematic and statistical uncertainty over the entire retarding energy range.

5.3.4.3 Bias method

Not all systematic uncertainty contributions are treated with the covariance matrix method. For some, it is not possible to generate the large amount of $\mathcal{O}(10^4)$ sample spectra, either because not enough data is available or due to unattainably high computational effort in the corresponding simulation. The bias method was thus used to still estimate the influence of these uncertainties. This is done as follows:

1. The analysis is performed including the corrections of all systematic effects, e.g. the multiplication with a linear function depending on parameters $\vec{\omega}$. The obtained result is the final result of the investigation. It is referred to as *result A*.

2. The analysis is repeated under the same conditions as before but assuming extremal uncertainty on the parameters of a certain correction, e.g. $\vec{\omega} + \sigma_{\vec{\omega}}$, yielding *result B*.

3. The absolute difference $D = |A - B|$ is calculated and enters the final uncertainty budget as *result* $A \pm D$.

This method has to be used with caution: It does not account for correlations, which may enhance or mitigate the influence of systematic uncertainty. Furthermore, uncertainties are quickly overestimated, as extremal parameter values of a certain correction are assumed.

---

[16] The dependence of systematic uncertainties on correlations is subject of chapter 6.

[17] It actually drops to the level of numerical precision of the computation: 10^{-14}.

Bump subtraction During fill 3, background measurements were performed, which have been used to subtract the bump from the tritium spectra. In these measurements, the bump amplitude is not stable over time. Hence, the effect of subtracting a bump, which emerged under different conditions, is investigated. To this end, the subtraction of the bump is performed using different combinations of background sets, which were performed at the end of the campaign (see table 5.7). The deviation between the obtained integral tritium spectra is on the level of statistical fluctuations and thus not further considered.

Background subtraction The same argument as for the bump subtraction holds also for the background subtraction: The same background measurements, which were used to subtract the bump, have been used to subtract the residual tritium background. Hence, the subtraction of the background is performed using a different background measurement, the one which was performed at the end of the campaign (see table 5.7). The deviation between the obtained integral background spectra is on the level of statistical fluctuation and is thus not further considered.

Column density SSC-sterile is not capable of propagating uncertainties into the response matrix R_{SSC}. The uncertainty of the magnetic field input values is negligible compared to the uncertainty on the column density determination. Extremal values of the column density determined for set 3 are fed into SSC-sterile. The obtained response matrix is used in a sterile neutrino search as presented in section 5.3.4.4. Compared to the result obtained with the original R_{SSC}, no deviation is obtained. To cross check this result, the column density of the nominal KATRIN source $\rho d = 5 \cdot 10^{17}\,\mathrm{cm}^{-2}$ [Ang05] was fed into SSC-sterile. A clear deviation in the result of the sterile neutrino search is observed. The uncertainty of the column density determination for Troitsk ν-mass is thus not further considered.

5.3.4.4 Fit & exclusion limit

As in the differential campaign, the sterile neutrino search is performed via a $\Delta\chi^2$-test with $Q = 5.991$ (95 % C.L.). The combination of many sets, however, leads to a residual pattern in the fit of the null-hypothesis. This is due to an incomplete subtraction of the bump, which is not resolved after many iterations of improving the procedure. There are two ways to deal with this issue:

1. **Increase systematic uncertainty.** Uncertainty can arbitrarily be enlarged to conceal the residual bump pattern.

2. **Decrease amount of data.** Analyzing only a fraction of the acquired data leads to enhanced statistical uncertainty, also concealing the pattern.

In both approaches, the sensitivity for a sterile neutrino search is decreased similarly. The second approach has the advantage, that the systematic uncertainty budget does not have to be reevaluated. Furthermore, the complexity of a simultaneous fit to account for correlations between sets is avoided. The second approach is thus pursued and the sterile neutrino search is performed solely on the data of fill 3 set 3. The following abbreviation is used:

$$y(eU)_{\mathrm{set}\,3} = y\ . \tag{5.41}$$

The model of the null-hypothesis $H_0(m_4 = 0, |U_{e4}|^2 = 0)$ is given in equation (5.29). It is abbreviated as follows:

$$f_{\mathrm{int.model}}(eU; N, E_0, B)_{\mathrm{s3}} = f(N, E_0, B)\ . \tag{5.42}$$

Fit of the null-hypothesis Applying the covariance matrix method, the χ^2-function takes the form

$$\chi^2(N,E_0,B) = \Big[y - f\,(N, E_0, B)\Big]^T M_{\mathrm{tot}}^{-1} \Big[y - f\,(N, E_0, B)\Big] \tag{5.43}$$

with the total covariance matrix

$$M_{\mathrm{tot}} = M_{\mathrm{bump}} + M_{\mathrm{thres}} + M_{\mathrm{trap}} + M_{\mathrm{crsec}} + M_{\mathrm{rate}}. \tag{5.44}$$

The same Gaussian pull term on the endpoint as in the differential campaign is added (see equation (5.17)). The 15 keV monitor points are excluded from the fit, as they are used for the rate decrease correction. The three free fit parameters are

N, the overall normalization,

E_0, the tritium spectral endpoint, and

B, a constant background.

The result of the fit is shown in figure 5.38. The pull term leads to a fitted endpoint value of $E_0 = 18\,572.2(33)\,\mathrm{eV}$. Neither normalization $N = 1.001(4)$ nor background $B = 0.20(17)$ show an unexpected behavior. The residuals are all normalized to the total uncertainty. In the retarding energy range of 12 − 13 keV, most of the residuals are negative. This pattern is, however, not significant considering the uncertainty. The contribution of statistical uncertainty increases with retarding

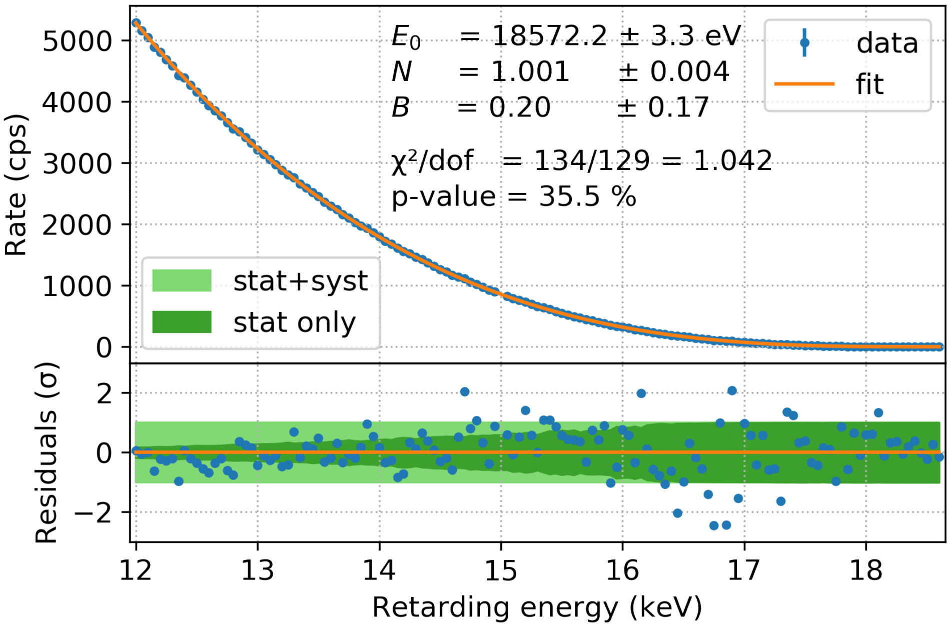

Figure 5.38: **Fit to the data of the integral campaign.** The data (blue) consists of the acquisitions during fill 3 set 3. Monitor points at 15 keV are not included in the fit, as they were used to correct for the rate decrease. The statistical error bars are too small to be visible. The model (orange) comprises a theoretical β-decay spectrum including corrections, and the response of source and transport section. The residuals are normalized to the total uncertainty (light green). The statistical uncertainty contribution is superimposed in dark green. Adapted from [Bru19].

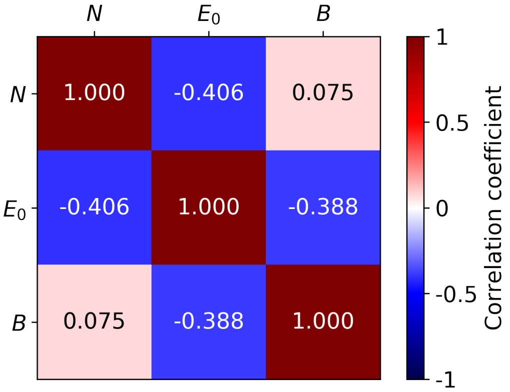

Figure 5.39: **Correlations of the fit parameters in the integral campaign.** Normalization N and background B are hardly correlated (light red). The spectral endpoint E_0 is anti-correlated to both of them (blue).

energy and dominates over the systematic uncertainty above 15 keV, as already apparent in figure 5.37. However, one has to keep in mind that also here only the uncorrelated part of the systematic uncertainty is displayed.

The correlation between the parameters is illustrated by the matrix in figure 5.39. The normalization N is anti-correlated ($r = -0.41$) to the spectral endpoint E_0, as one compensates for a change of the other. Normalization N and background B are hardly correlated ($r = 0.08$). The spectral endpoint E_0 is anti-correlated ($r = -0.39$) to the background B. The correlations are hence exactly as expected. The χ^2-value of the fit is 134. With 132 energy bins and 3 free parameters, this results in $132 - 3 = 129$ DOF and a reduced χ^2 of

$$\chi^2_{\text{red}} = \frac{\chi^2}{\text{DOF}} = 1.042 \ . \tag{5.45}$$

The corresponding p-value is 35.5 %, indicating a good fit of the model to the data. The null-hypothesis can thus be used as the baseline for the sterile neutrino search.

Sensitivity and exclusion The sensitivity curve of the integral campaign is shown in figure 5.40 as dashed blue line. The explored mass range is determined by the minimal retarding energy of the scans:

$$E_0 - 12\,\text{keV} = 6.6\,\text{keV} \ . \tag{5.46}$$

As in the differential campaign, the best sensitivity is reached at the intermediate mass range $m_4 = 3-4\,\text{keV}$. The sensitivity calculation is repeated 50 times with statistically fluctuated MC data sets. For some of these sets, the sensitivity is

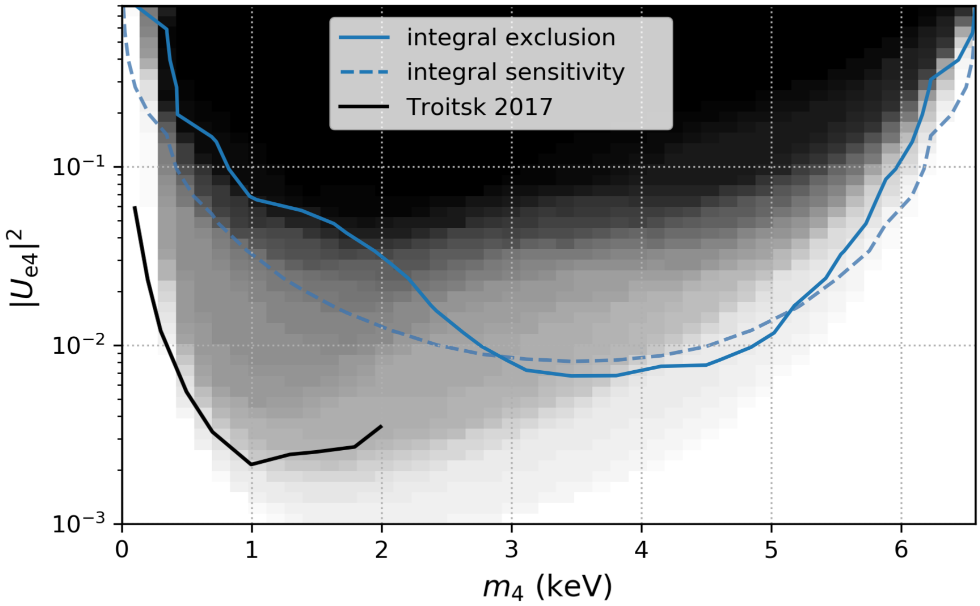

Figure 5.40: **Integral sensitivity and exclusion.** The dashed blue line indicates the combined statistical and systematic sensitivity, based on a non-fluctuated MC data set. The black parameter space is excluded by all 50 sensitivity curves with fluctuated MC data. The lighter the point, the less often it is excluded. The white area is never excluded. The straight blue line is the exclusion, based on the data of fill 3 set 3 and the corresponding systematic uncertainty. The black curve shows the latest result of the Troitsk ν-mass collaboration [Abd17]. The confidence level is 95 % for all curves.

increased at low masses in the range of 0.5 − 3 keV, where the statistical uncertainty dominates. This behavior is enhanced by the logarithmic y-axis of the plot: The sensitivity curve of the unfluctuated data (dashed blue line) is actually well surrounded by the grey area.

In the calculation of the exclusion curve, a better goodness of fit than for the null-hypothesis is obtained for 157 out of 20 × 20 points in the $(m_4, |U_{e4}|^2)$-parameter space. Most of them correspond to $m_4 < 2.5$ keV. However, even the difference to the best goodness $\chi^2 = 130$ ($|U_{e4}|^2 = 3.4 \cdot 10^{-2}$, $m_4 = 1.4$ keV) is not statistically significant, such that the null-hypothesis remains the baseline for the sterile neutrino exclusion. The exclusion curve is shown in figure 5.40 as solid blue line, with the best exclusion

$$|U_{e4}|^2 < 7 \cdot 10^{-3} \quad \text{at} \quad m_4 = 3.4\,\text{keV} . \tag{5.47}$$

At $m_4 < 2.5\,\mathrm{keV}$, the exclusion curve does not quite reach the expected sensitivity. This corresponds to the region, in which many points are found with a better goodness of fit than the null-hypothesis. Moreover, it corresponds to the retarding energy range, in which the bump did not appear. The decrease of the exclusion is due to the residual pattern of the incomplete bump subtraction: It is mitigated but not removed by limiting the amount of data to set 3. Nevertheless, the exclusion curve is generally well aligned with the expected sensitivity.

5.4 Comparison of differential & integral mode

The largest uncertainty in differential mode is induced by modeling the detector response. The model is based on the spectral shape of electrons from the spectrometer electrode, which have a different response than β-electrons. This uncertainty could be mitigated by using a calibration source like gaseous krypton, which also includes the response of the source section.

The largest systematic uncertainty in integral mode (apart from the bump) is induced by rate dependent effects, in particular the effects of events below threshold and the decreasing activity of the tritium source. This could be mitigated by an optimized setup with respect to noise and with a rate stabilized source. The retarding energy range above 15 keV is dominated by statistical uncertainty. This could be mitigated by distributing more measurement time to points above 15 keV. This means relatively less measurement time at points below 15 keV, where an increase of statistical uncertainty is tolerable due to the larger systematic uncertainties.

Directly comparing both modes, they are prone to complementary sources of systematic uncertainty. This is discussed on the example of events below threshold: This effect originates from the detector and is apparent in both modes but the resulting systematic uncertainty is largely different. In differential mode, events below threshold are not included in the tritium fit (ROI $> 2\,\mathrm{keV}$). These undetected events affect the measured spectral shape indirectly, as some charge sharing events remain unidentified. Applying the same threshold setting in both calibration and tritium measurements, however, this effect is included in the detector response. In integral mode, events below threshold lead to a large systematic uncertainty, as their number depends on the retarding energy setting of the respective measurement point. This can be interpreted as a rate dependent detector efficiency, which cannot be mitigated by a precise determination of the detector response.

The exclusion curves of both campaigns are displayed in figure 5.41, together with already existing limits in the investigated sterile neutrino mass range. Neither of the analyses depicts a world-leading sterile neutrino exclusion limit. However,

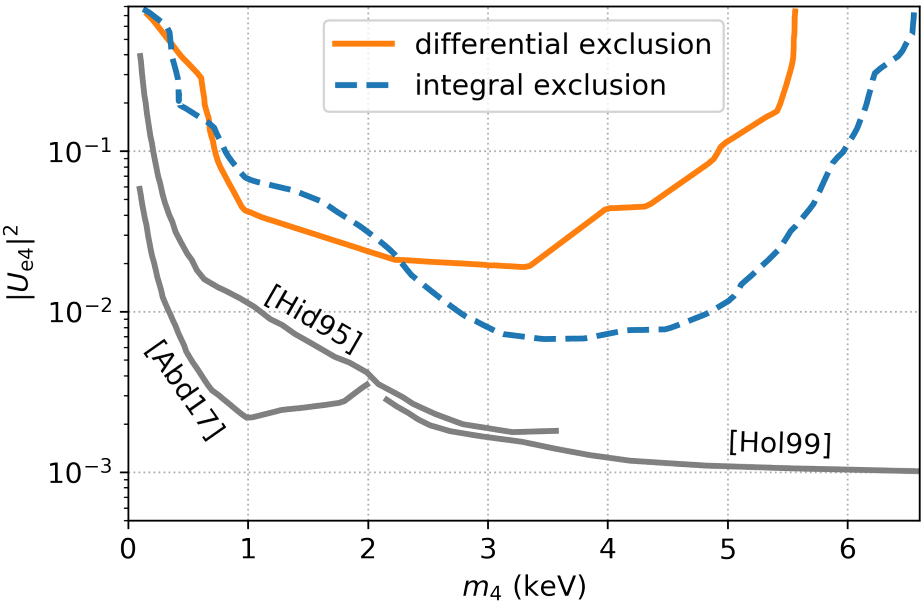

Figure 5.41: **Comparison of exclusion curves with existing limits.** The exclusion curves of both the differential (solid orange) and integral (dashed blue) campaign lie within a parameter space, which is excluded by other experiments [Hid95, Hol99, Abd17]. The confidence level of all limits is 95 %.

both modes are prone to largely different sources of systematic uncertainty. The combination of the two thus supports the reliability of the results and enables to exclude possible false-positive signals also in future sterile neutrino searches with more data.

5.5 Conclusion

In this chapter, the installation of the TRISTAN P-0 system at the Troitsk ν-mass experiment was presented. As a technological predecessor of KATRIN, Troitsk ν-mass offers a very similar experimental environment and hence an ideal test bench for a sterile neutrino search with the TRISTAN prototypes. The applied detector performed reliably with an energy resolution of around 300 eV (FWHM) for photons and 300 – 400 eV (FWHM) for electrons in the energy range of 12 – 19 keV. Data was taken in two campaigns in differential and integral mode, respectively. A detailed model was developed for both modes, including a full experimental response function, obtained via dedicated calibration measurements and extensive MC simulations. Two strategies were developed to analyze the respective data, resulting in the exclusion of a certain sterile neutrino parameter space for each campaign.

In differential mode, the retarding energy is set to a fixed value and the differential spectrum is measured by the detector. A sophisticated model of the detector response was developed, including energy dependent parameters of the empirical model for mono-energetic electrons. Its parameters are treated as nuisance parameters in the χ^2-fit to account for systematic uncertainty. The analysis resulted in the first publication of a sterile neutrino exclusion curve from a measurement in differential mode [Bru19]: It excludes the existence of a sterile neutrino with a mixing amplitude $|U_{e4}|^2 < 2 \cdot 10^{-2}$ at $m_4 = 3.3\,\mathrm{keV}$.

In integral mode, a range of retarding energies is scanned using the MAC-E spectrometer and the respective count rate is determined by the detector. The good performance of the TRISTAN detector at high rates enabled to measure at lower retarding energies than with the standard Troitsk ν-mass detector and to perform systematic corrections also on the differential spectrum. Systematic uncertainty was included with the covariance matrix method and a detailed uncertainty budget was established. The retarding energy range below 15 keV is dominated by systematic uncertainty, in particular by events below detection threshold, whereas the retarding energy range below 15 keV is dominated by statistical uncertainty. The analysis excludes the existence of a sterile neutrino with a mixing amplitude $|U_{e4}|^2 < 7 \cdot 10^{-3}$ at $m_4 = 3.4\,\mathrm{keV}$. The previously analyzed mass range of the Troitsk ν-mass experiment was enlarged by a factor of 3.3.

Directly comparing integral and differential measurement mode, they are prone to systematic uncertainty of largely different origins. Hence, the combination of the two is a key requirement to exclude possible false-positive signals in future sterile neutrino searches with more data. Neither of the analyses presented in this chapter leads to a world-leading sterile neutrino exclusion limit. However, the developed analysis methods depict a major milestone in the TRISTAN project and will serve as the basis for future sterile neutrino searches with the TRISTAN detector integrated at the KATRIN experiment.

6 Sensitivity studies

In this section, the impact of detector-related systematic uncertainty on the final sterile neutrino sensitivity of TRISTAN is investigated. For these studies, a total of 10^8 electrons is assumed, corresponding to the full amount of data acquired after three years of measurement with KATRIN. The studies focus on the differential measurement mode (see section 5.1.2) and make use of the experimentally determined electron detector response (see sections 4.3.2 and 5.2.3.1). As for the differential Troitsk ν-mass analysis, a search window $m_4 = 0 - 5.6\,\mathrm{keV}$ was assumed.

The chapter is divided into two sections: The subject of section 6.1 is the empirical model for mono-energetic electrons and the impact of uncertainty on its parameters on the sterile neutrino sensitivity. In section 6.2, the impact of uncertainty on actual detector effects is investigated, namely entrance window, backscattering, charge sharing and energy resolution.

6.1 Uncertainty in the empirical model

A first analysis strategy for the differential mode was developed within the campaign at the Troitsk ν-mass experiment (see section 5.2). A main ingredient to this strategy is the detector response matrix, which is convolved with the theoretical β-decay model to yield the spectrum measured at the detector. The response matrix is based on the empirical model for mono-energetic electrons (see section 4.3.2). The process of determining the model's parameter values and their respective energy dependence entails systematic uncertainties. Consequently, the following questions arise:

- How does an uncertainty on its parameters affect the sterile neutrino sensitivity?
- Are there more or less important parameters and if yes, which are they?

These questions shall be answered in this section by a sensitivity study. The approach is to simulate a sterile neutrino search including all steps of an analysis in differential mode under well defined conditions: Mono-energetic spectra are produced with KESS and used to determine a detector response based on the empirical model. The simulated tritium data are Asimov data, generated by the convolution of a tritium decay model with the empirical detector response model and normalized to the equivalent of 10^{18} measured electrons. With this, perfect modeling of the measured spectrum is assumed, such that a fit of the model to the simulated data results in $\chi^2 = 0$. Uncertainty is introduced via the covariance matrix method: Covariance matrices are generated by randomly varying one parameter of the empirical model at a time. With this, the impact on the sterile neutrino sensitivity can be studied for each parameter individually.

6.1.1 Determination of initial parameter values

In a first step, a detector response matrix is produced using KESS. To this end, simulations are performed with initial energies $E_{\text{in}} = 1 - 20\,\text{keV}$. Each simulated spectrum is fit with the empirical model given in equations (4.13) to (4.15). An example fit at 18 keV is shown in figure 4.21. Thereby, only one dead layer tail is used, as better fit results are achieved compared to a fit with two tails, as in section 5.2.3.1. For this sensitivity study, it is of minor importance, whether or not the simulated and measured electron responses agree, as here only the uncertainty on the empirical model parameters is of interest.

To achieve a good agreement of the MC simulated data with the empirical model, a detection threshold is added:

$$E_{\text{thres}} = a = 2\,\text{keV} \ . \tag{6.1}$$

Moreover, the energy range is restrained to $E_{\text{in}} = 13 - 20\,\text{keV}$, where the agreement of MC simulation and empirical model is most applicable.

Based on MC simulations of the electron response for mono-energetic electrons in the energy range of $13 - 20\,\text{keV}$, the energy dependence of the parameters of the empirical model ψ is obtained. For simplicity, a linear dependence is assumed, as shown in figure 6.1. This procedure is equivalent to the one described in section 5.2 on the Troitsk ν-mass analysis. Resulting slope m_ψ and offset m_ψ of all empirical model parameters are given in table 6.1. Considering only statistical uncertainty of 10^{18} measured events, corresponding to three years of measurement with KATRIN, a sensitivity study is performed, reproducing the expected sensitivity of an earlier investigation $|U_{e4}|^2 \approx 10^{-8}$ (90 % C.L.) at $m_4 = 4\,\text{keV}$ [Mer15a]. This supports the applicability of the model.

The performance of the model is cross checked in a second way: A sterile neutrino admixture with $m_4 = 2.1\,\text{keV}$ and $|U_{e4}|^2 = 10^{-4}$ is added in the simulated data. According to the statistical sensitivity study, these are values, to which the search

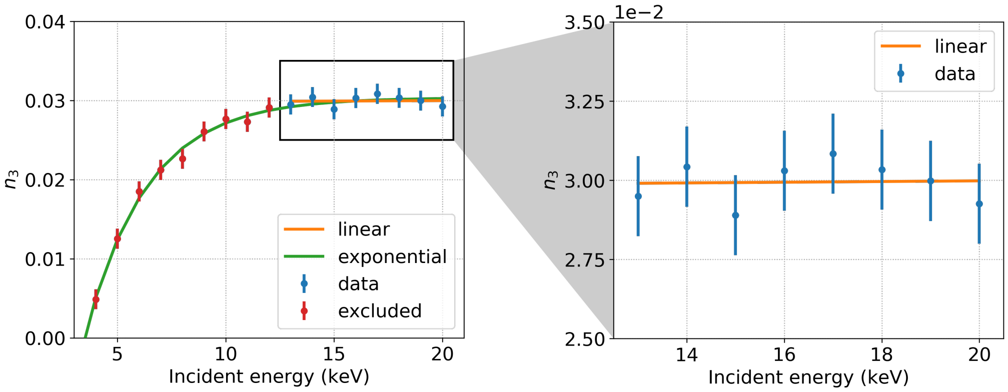

Figure 6.1: **Non-linear energy dependence of n_3.** The energy dependence of the shown parameter n_3 cannot be approximated by a linear function for incident energies $E_{\text{in}} < 13\,\text{keV}$ (red points). For simplicity, a linear dependence is assumed in the energy range $E_{\text{in}} = 13 - 20\,\text{keV}$.

Table 6.1: **Linear dependence of the empirical model parameters.** These values are extracted from KESS simulations of mono-energetic electrons with incident energies in the range $E_{\text{in}} = 13 - 20\,\text{keV}$. This dependence is used to interpolate the response for all energies and to generate a response matrix.

Parameter	Slope m	Offset c'
σ	$5.56(3) \cdot 10^{-3}$	$5.29(5) \cdot 10^{-1}$ eV
n_1	$-6(2) \cdot 10^{-7}$ eV^{-1}	$2.1(3) \cdot 10^{-3}$
n_3	$-1(1) \cdot 10^{-7}$ eV^{-1}	$2.6(2) \cdot 10^{-3}$
β	$2(2) \cdot 10^{-3}$	$2.6(3) \cdot 10^{1}$ eV
b	$1.7(3) \cdot 10^{-5}$ eV^{-1}	$3(4) \cdot 10^{-2}$
c	$1.5(3) \cdot 10^{-5}$ eV^{-1}	$1.36(5) \cdot 10^{-2}$

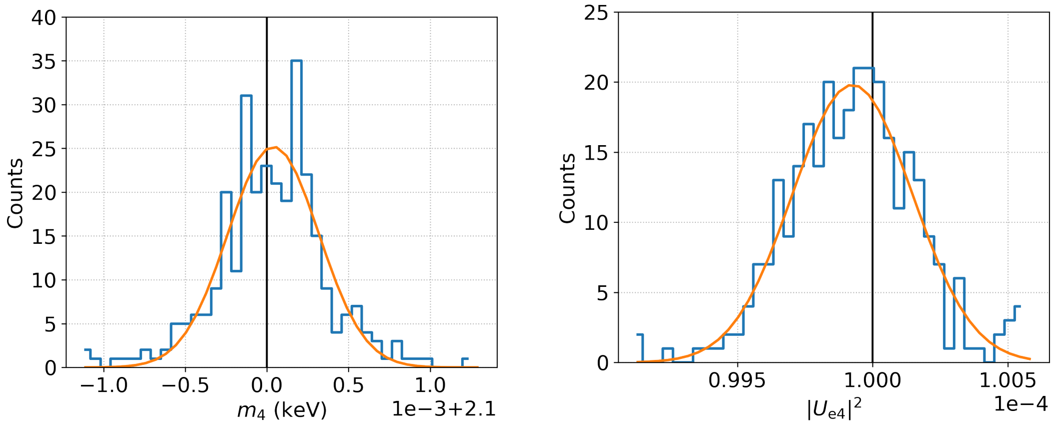

(a) MC distribution of m_4.

(b) MC distribution of $|U_{e4}|^2$.

Figure 6.2: **Cross check of the model obtained from simulation.** A sterile neutrino admixture is added in the simulated data and the model is extended by the two corresponding free parameters m_4 and $|U_{e4}|^2$. The fit to the differential spectrum is able to find back the input (vertical black lines) of (a) $m_4 = 2.1\,\text{keV}$ and (b) $|U_{e4}|^2 = 10^{-4}$.

should be sensitive. The fit function is extended by two free parameters: sterile neutrino mass m_4 and mixing element $|U_{e4}|^2$. A total of 300 fits is performed with statistically randomized simulated data. The results of these fits is shown in figure 6.2. The input is exactly found back with the expected variance and no bias.

6.1.2 Generation of uncertainty

The goal of the following investigation is to determine how an uncertainty on the empirical model, i.e. on the energy dependence of its parameters, affects the sensitivity to a sterile neutrino. Thereby, two aspects are investigated:

- **Correlation width** The energy dependence of the parameters is assumed to be linear, which implies a strong bin-to-bin correlation. Figure 6.1 shows, that the energy dependence is not necessarily linear. The deviation from this dependence is therefore investigated by allowing for a correlation width of a given energy range ΔE.

- **Uncertainty size** To identify the parameter ψ with the largest impact on the sensitivity, a relative uncertainty $\delta = 0 - 100\,\%$ is introduced on each parameter individually.

The covariance matrix method enables to cover both aspects at once. A covariance matrix Ω is generated for a parameter ψ (i.e. σ, n_1, ...) as follows:

1. An identity matrix is initialized with the dimensions $(n \times n)$, where n is the number of bins in the initial energy range $E_{\text{in}} = 13-20\,\text{keV}$. It will be referred to as the correlation width matrix ω.
2. The off-diagonal elements of ω are weighted according to a Gaussian distribution. Its width ΔE defines the correlation width of the matrix. This is illustrated in figures 6.4(a) and 6.4(b).
3. The matrix ω is "normalized" with a given fraction $\delta = 0-100\,\%$ of the value of a parameter ψ, such that a matrix element of Ω is expressed as

   $$\Omega_{jk} = \omega_{jk} \cdot \psi_j \cdot \delta \cdot \psi_k \cdot \delta \ . \tag{6.2}$$

   The diagonal of Ω represents the variance of parameter ψ in each energy bin for a defined uncertainty size δ. The off-diagonal elements represent the allowed bin-to-bin correlation of ψ over a defined energy range ΔE.

6.1.3 Impact on sensitivity

Impact of different correlation widths To determine a value for the manually introduced correlation width ΔE, the correlation width of the linear energy dependencies in table 6.1 is quantified. For each empirical model parameter ψ, 10^4 random linear function parameters ϕ are generated according to the corresponding multivariate distribution of slope m_ψ and offset c'_ψ. For each sample, the linear function is evaluated in the energy range of $12-20\,\text{keV}$. The correlation coefficients of the resulting MC data points are calculated. The correlation matrix and the obtained correlation width is exemplary shown in figure 6.3 for parameter β, the slope of the low energetic half of the dead layer tail.

Covariance matrices Ω are generated with several correlation widths $\Delta E = 0.5$, 2, and $5\,\text{keV}$, as well as fully uncorrelated ($\Delta E = 0$) and fully correlated ($\Delta E = \infty$). Figures 6.4(a) and 6.4(b) show ω exemplary for $\Delta E = 0.5$ and $2.0\,\text{keV}$. The smaller ΔE, the smaller the correlation coefficients at large distances from the diagonal. The covariance matrices are used to generate multivariate distributions, from which random values of a parameter ψ are drawn. Figure 6.4 shows, how the introduced correlation width is reflected in the random values at different energies on the example of the resolution parameter σ. For this investigation, an uncertainty size $\delta = 0.1$ is chosen for all correlation widths ΔE.

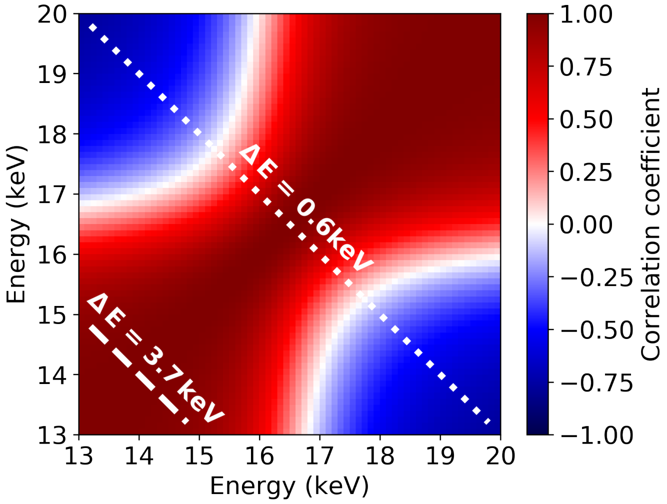

Figure 6.3: **Correlation width of parameter β.** The correlation width ΔE is determined as the standard deviation of a Gaussian fit to the correlation coefficients along the shown axes (dashed, dotted).

The random values for one parameter are then applied in the empirical model, together with the original values of all other parameters, according to table 6.1. This is done 10^4 times and each time, a response matrix is generated. These are translated into 10^4 tritium spectra, from which a covariance matrix $M_\psi(\Delta E)$ is calculated. The matrices are used to introduce uncertainty in a $\Delta\chi^2$-test (see section 5.3.4).

The results are discussed on the example of the resolution parameter σ. Figure 6.5 shows that correlations do have a strong impact on the sensitivity: While fully correlated uncertainty leaves the sensitivity almost unchanged, the latter is decreased by almost five orders of magnitude for fully uncorrelated uncertainty. The same trend is observed for all parameters ψ. The reason is, that uncorrelated parameters allow for steps of parameter values from one energy to another. A step like this leads to a kink in the tritium spectrum, which mimics a sterile neutrino signature and decreases the sensitivity for a sterile neutrino exclusion.

Impact of uncertainty sizes Covariance matrices Ω are generated with several uncertainty fractions $\delta = 0.1$, 1, 10, and 100 %. Figure 6.4 shows, how the introduced uncertainty size is reflected in the random values at different energies on the example of the resolution parameter σ. For this investigation, a constant correlation width $\Delta E = \infty$ is assumed. The covariance matrices are again used to generate multivariate distributions, from which random values of a parameter ψ are drawn. With these, 10^4 response matrices and tritium spectra are generated. The effect of a 10 %

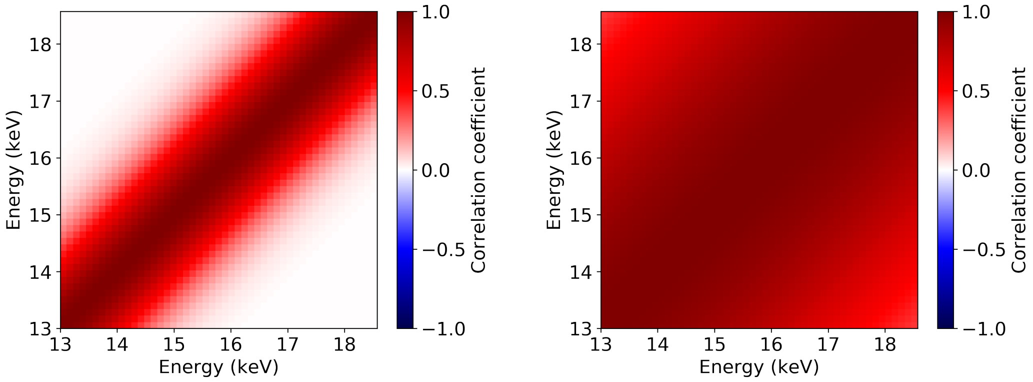

(a) ω with $\Delta E = 0.5\,\text{keV}$.   (b) ω with $\Delta E = 2\,\text{keV}$.

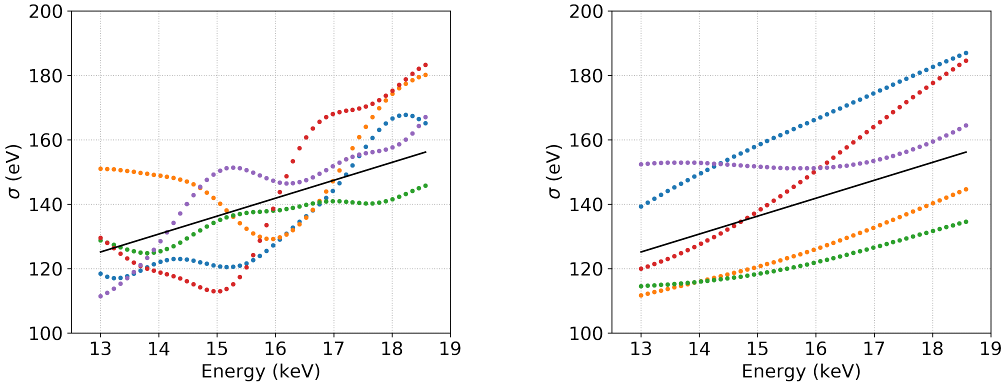

(c) $\Delta E = 0.5\,\text{keV}$, $\delta = 10\,\%$.   (d) $\Delta E = 2\,\text{keV}$, $\delta = 10\,\%$.

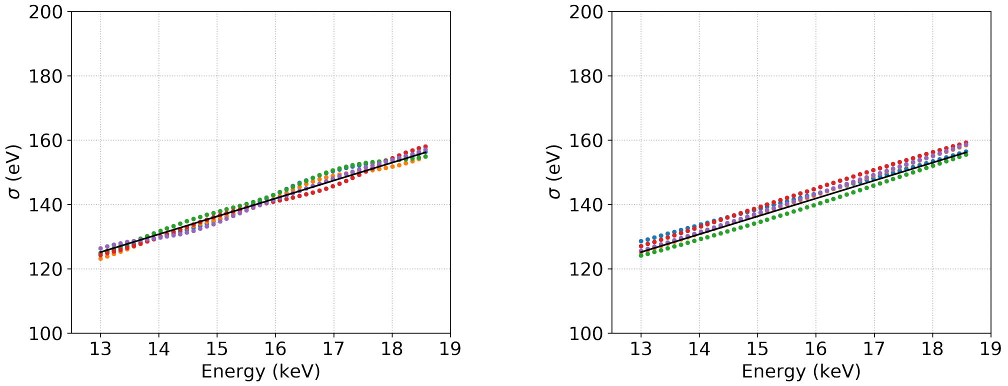

(e) $\Delta E = 0.5\,\text{keV}$, $\delta = 1\,\%$.   (f) $\Delta E = 2\,\text{keV}$, $\delta = 1\,\%$.

Figure 6.4: **Effect of correlation width $\boldsymbol{\Delta E}$ and uncertainty size $\boldsymbol{\delta}$.** Correlation between energy bins is introduced via a matrix ω with a certain correlation width ΔE, e.g. for (a) $0.5\,\text{keV}$ and (b) $2\,\text{keV}$. The correlation width gives more or less freedom to the energy dependence of the parameters of the empirical model to diverge from a strictly linear behavior, as shown (c) for $\Delta E = 0.5\,\text{keV}$ and (d) for $2\,\text{keV}$. Both of these plots are created with $\delta = 10\,\%$, whereas (e) and (f) are created with $\delta = 1\,\%$. The different colors represent different random realizations of the energy dependence of σ.

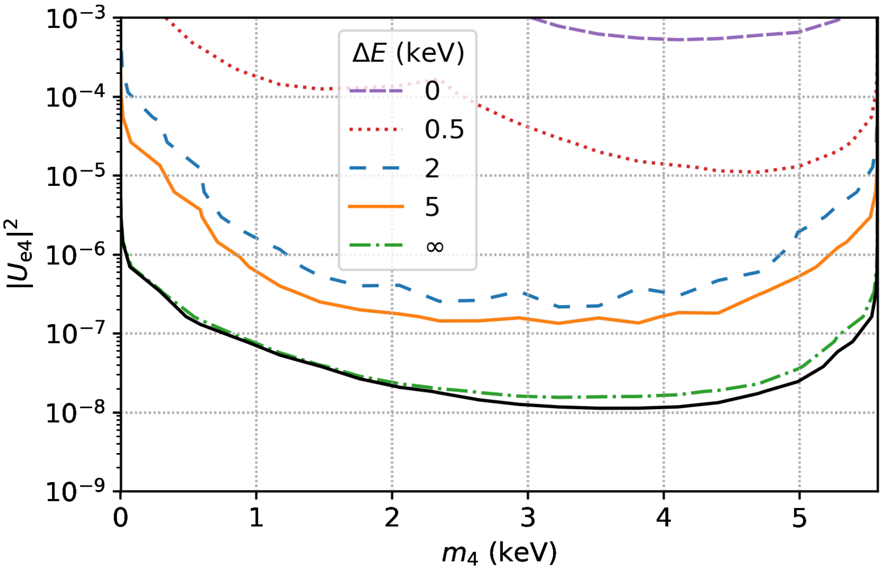

Figure 6.5: **Sensitivity for several correlation widths.** The curves are generated for several correlation widths and a constant uncertainty size $\delta = 10\,\%$ on the resolution parameter σ. The solid black line indicates the statistical sensitivity. The larger the correlation width ΔE, the better the sensitivity. Fully correlated uncertainty (dash dotted green) barely degrades the sensitivity. Fully uncorrelated uncertainty (densely dashed purple) leads to a degradation of almost five orders of magnitude.

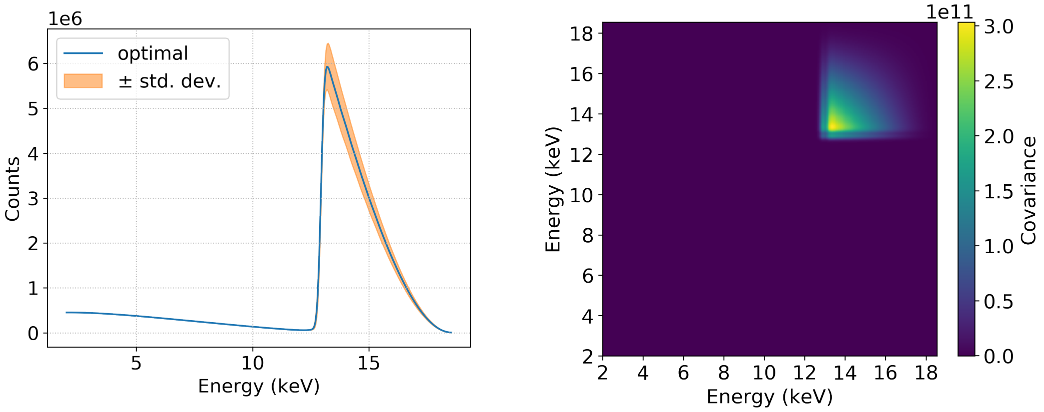

(a) Uncertainty band for $\delta = 10\,\%$.

(b) Covariance matrix for $\delta = 10\,\%$.

Figure 6.6: **Uncertainty on the resolution parameter.** A total of 10^4 differential tritium spectra are produced, each with a different random resolution within $10\,\%$ of the optimal value obtained from the fit to the simulated spectra. (a) The optimal tritium spectrum is shown in blue. The orange region indicates how the spectrum may change given the introduced uncertainty on the resolution parameter σ. (b) A covariance matrix is generated from the 10^4 model spectra. The covariance is large where the spectrum is affected the strongest.

uncertainty on σ on the tritium spectrum is shown in figure 6.6(a). It is strongest in the energy region above the HV cut, i.e. $E > 13\,\mathrm{keV}$. The spectrum largely changes its normalization in this region, while the backscattering background remains mostly unchanged. This behavior is also reflected in the corresponding covariance matrix, displayed in figure 6.6(b).

Figure 6.7 shows the impact of the above mentioned uncertainty sizes δ on the resolution parameter σ on the expected sensitivity. An uncertainty of $100\,\%$ degrades the sensitivity by about two orders of magnitude. An uncertainty size $\delta = 10\,\%$ degrades the sensitivity by a factor of almost two in the most sensitive region. This is the same curve as the fully correlated one ($\Delta E = \infty$) in figure 6.5. For $\delta < 10\,\%$, the sensitivity is not noticeably affected. The same trend is observed for all parameters ψ. This means, that a large uncertainty sizes on all parameters are allowed without decreasing the sensitivity to a sterile neutrino, as long as they are correlated over a large energy width and the functional dependence of the parameter on energy is known.

Examples for other parameters are displayed in figure 6.8. The impact of the dead layer tail parts (amplitude n_1 and slope β_1) is strongest around the HV cut but generally small. The corresponding uncertainty bands are too small to be

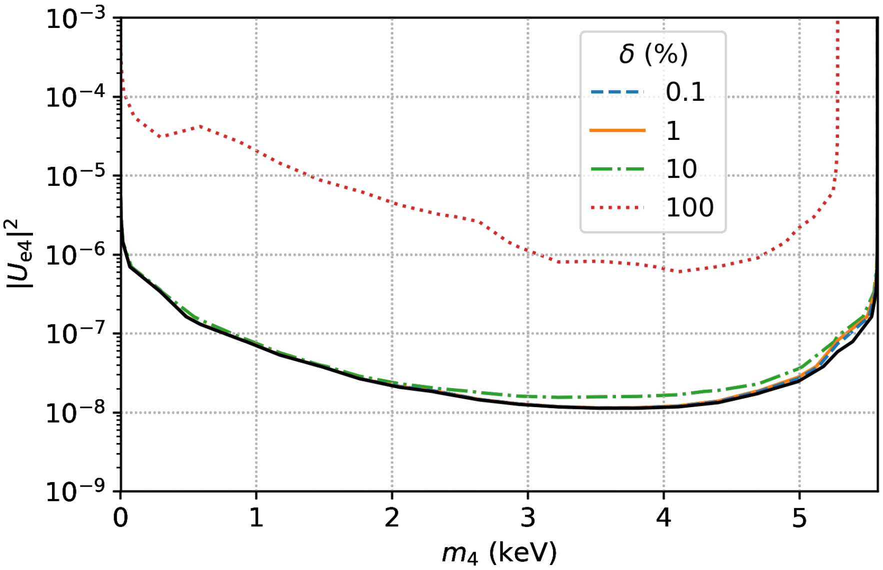

Figure 6.7: **Sensitivity for several uncertainty sizes.** The curves are generated for several uncertainty sizes and a constant correlation width $\Delta E = \infty$ on the resolution parameter σ. The sensitivity curves with uncertainty sizes $\delta = 0.1\,\%$ (dashed blue) and $1\,\%$ (solid orange) are largely concealed by the solid black curve, indicating the statistical sensitivity. For $\delta = 10\,\%$ (dashdotted green), a degradation of almost a factor two in the energy region $E \approx 2-5.5\,\mathrm{keV}$ is apparent. Only for $\delta = 100\,\%$ (dotted red), the sensitivity is strongly degraded by about two orders of magnitude.

visible. The backscattering background parts (amplitude n_3, and curvatures at low and high energy ends b and c) affect the backscattering background the strongest.

Comparison of the impact of an uncertainty for different parameters The sensitivity study is repeated for all empirical model parameters with $\delta = 10\,\%$ and $\Delta E = 2\,\text{keV}$. The resulting sensitivity curves are displayed in figure 6.9. The parameters are ranked according to the minimal reached mixing amplitude $|U_{\text{e4}}|^2$. The impact on the sensitivity is larger for parameters, which affect the tritium spectral shape above the HV cut, namely σ, β and n_1. The impact of the parameters of the backscattering background (c, n_3, and b) is smaller.

6.2 Uncertainty on the entrance window thickness

In the previous section, arbitrary uncertainty on the parameters of the empirical model was assumed and each parameter was investigated individually. In this section, the empirical model parameters are connected to realistic detector effects on the example of the entrance window thickness. This way, the influence of an uncertainty in determining the entrance window thickness on the sterile neutrino sensitivity is investigated. The study is conducted in the following three steps, which are also illustrated in figure 6.10:

1. Mono-energetic spectra are simulated with input parameters in a grid of incident energy E_{in} and entrance window thickness d_{DL}, assuming a dead layer model (see section 4.3.2).
2. Each simulated spectrum is fit with the empirical model to determine the energy dependence of all parameters ψ for different dead layer thicknesses d_{DL}.
3. For a given uncertainty on the dead layer thickness δ_{DL}, 10^4 sample spectra are created to generate a covariance matrix and to calculate the sensitivity curve for the corresponding δ_{DL}.

6.2.1 Modeling of detector effects

The first step of the study is the simulation of mono-energetic spectra at many points in a (E_{in}, d_{DL})-grid. In order to do so efficiently, a MC method is developed, which includes the most dominant detector effects — entrance window, backscattering, charge sharing, and detector resolution — but reduces the computation time compared

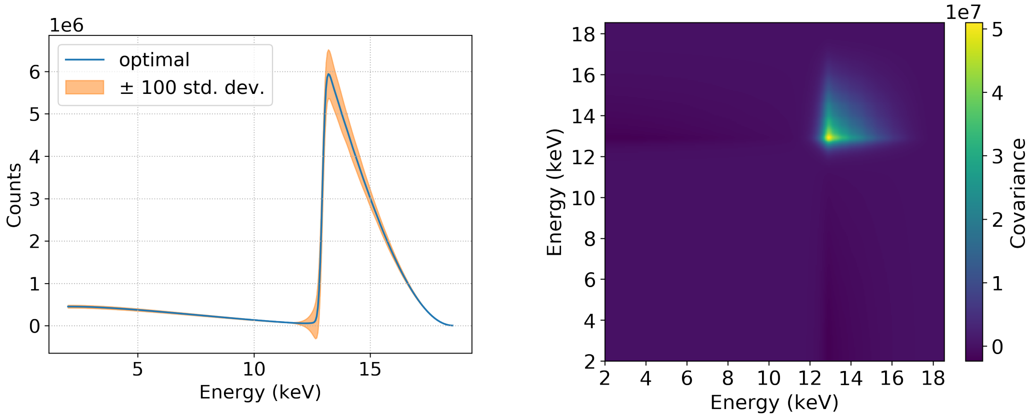

(a) Uncertainty band of n_1. (b) Covariance matrix of n_1.

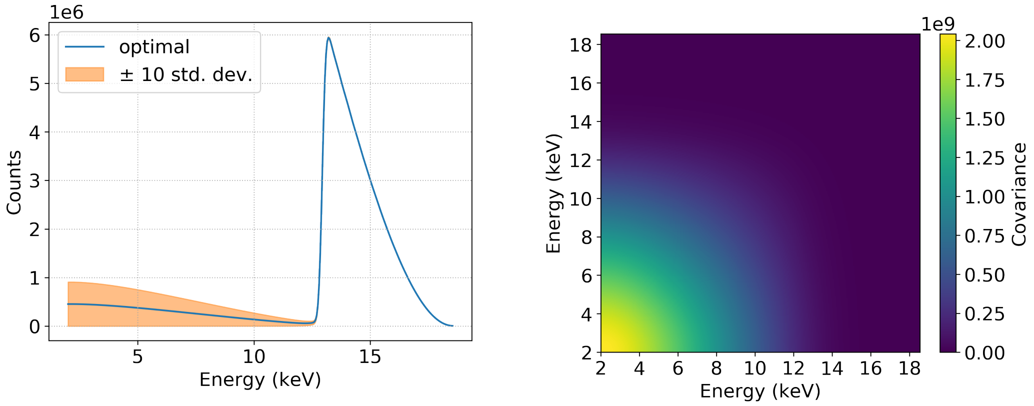

(c) Uncertainty band of n_3. (d) Covariance matrix of n_3.

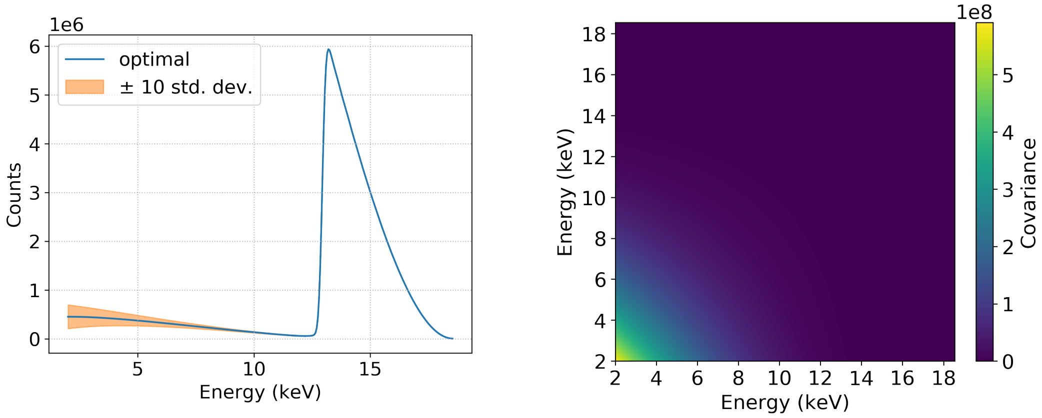

(e) Uncertainty band of b. (f) Covariance matrix of b.

Figure 6.8: **Uncertainty on other parameters of the empirical model.** All figures refer to 10 % uncertainty on the respective parameter. The 1 σ uncertainty bands are amplified as stated in the legends. An uncertainty on the dead layer tail parameters ((a) n_1 and β_1) has its largest effect around the HV cut. The effect of (c) n_3, (e) b, and c is strongest in the region of the backscattering background. This behavior is reflected by the size of entries in the covariance matrices (b), (d), and (f).

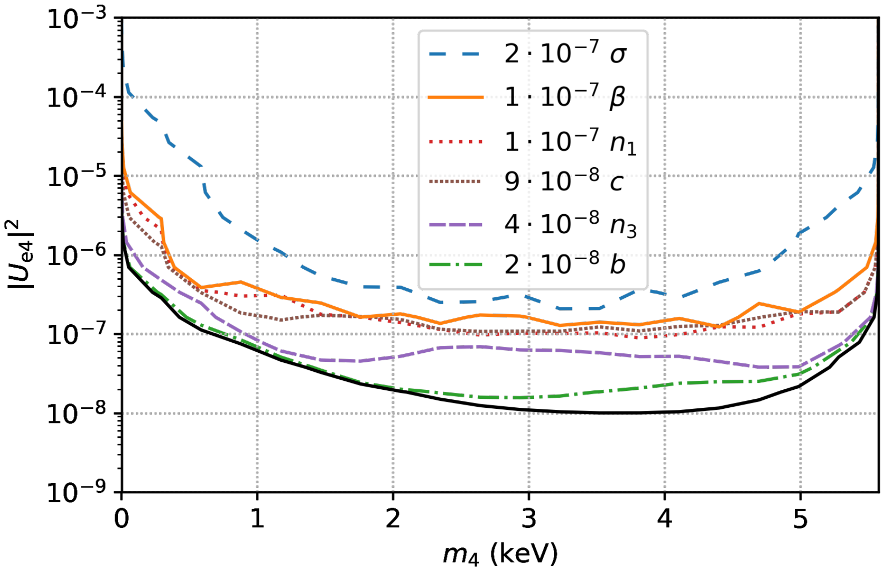

Figure 6.9: **Sensitivity for all empirical model parameters.** Each curve is generated with $\delta = 10\,\%$ and $\Delta E = 2\,\text{keV}$. The number in the legend states the minimal reached mixing amplitude $|U_{\text{e4}}|^2$ of the respective curve. The statistical curve (solid black) reaches $|U_{\text{e4}}|^2 = 10^{-8}$. The sensitivity is affected the strongest by an uncertainty on the resolution parameter σ and the least by an uncertainty on the curvature of the backscattering background at its low energy end b.

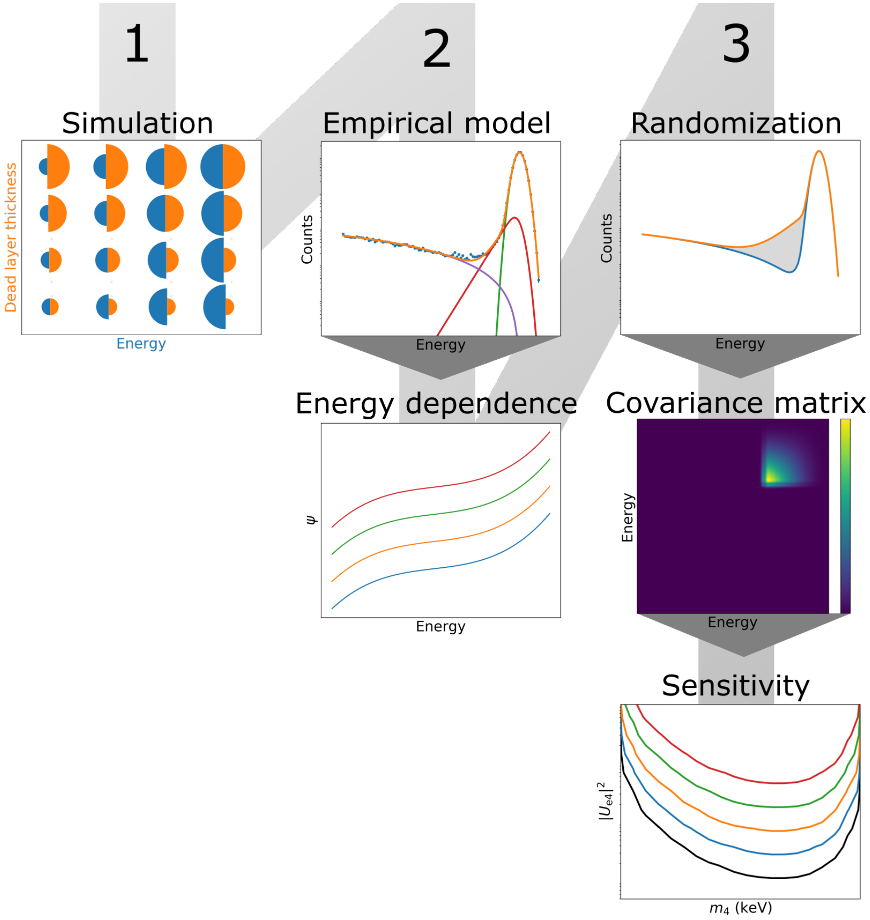

Figure 6.10: **Procedure of the dead layer thickness sensitivity study.** In step 1, mono-energetic spectra are simulated. In step 2, the spectra are fit to determine the energy dependence of the empirical model parameters. In step 3, the dead layer thickness is varied to generate a covariance matrix and to calculate its impact on the sterile neutrino sensitivity.

to KESS by a factor of about 90. This significant improvement furthermore enables the simulation of 10^9 electrons in each grid point, reducing the statistical uncertainty on the fitted parameters. For each considered detector effect, the MC method requires two ingredients:

1. The probability for electrons to undergo the effect.
2. The impact of the effect on the electrons' energy.

Both ingredients are modeled based on KESS simulations or actual measurements. Their behavior is parameterized using analytic functions. Generating random numbers according to the obtained functions, the influence of the respective effect is propagated on the energies of a large number N of mono-energetic events with initial energy E_{in}. In the following, the expression

$$\mathrm{rand}\left[f\left(E\right)\right] \tag{6.3}$$

refers to drawing a random number from a given energy distribution $f(E)$.

Entrance window The probability for electrons to be affected by the entrance window is obtained from KESS, where a dead layer model is assumed. Electrons, which have deposited energy in the dead layer, are accordingly tagged. The corresponding probability $P_{\mathrm{DL}}(E_{\mathrm{in}})$ is calculated as a function of incident energy E_{in}. The observed behavior is exponential, as shown in figure 6.11(a).

The distribution of energy loss in the dead layer per electron $f_{\mathrm{DL}}(E_{\mathrm{loss}})$ is also obtained from KESS. The simulated distributions are parameterized with six Cauchy functions for multiple plasmon excitations [Pen62, Ren11] and one exponential for large energy losses. Both simulated energy loss and fit are exemplary shown in figure 6.11(b) for a dead layer thickness $d_{\mathrm{DL}} = 80\,\mathrm{nm}$. The deviation of the fit from the data is up to $10\,\sigma$ in the energy loss range $E_{\mathrm{loss}} = 10-100\,\mathrm{eV}$. Although the number of events per bin in this range is much larger, it is the large energy losses, where a precise description of the distribution is crucial: Considering a differential spectrum, events with a large energy loss significantly contribute to the impact of the entrance window effect on the spectral shape at the low energy tail of the main peak.

The shape of the distribution in figure 6.11(b) is the same for different dead layer thicknesses d_{DL} but its normalization changes linearly with d_{DL}. In order to describe the energy loss for different dead layer thicknesses, a linear factor L is multiplied to P_{DL}. The number of affected events n_{DL} is hence described as

$$n_{\mathrm{DL}} = N \cdot P_{\mathrm{DL}}\left(E_{\mathrm{in}}\right) \cdot L\left(d\right) \ . \tag{6.4}$$

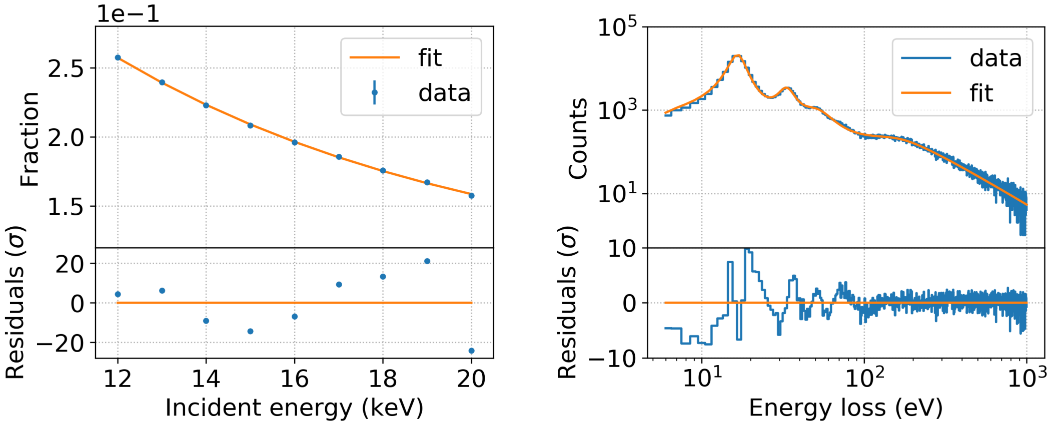

(a) Energy dependent probability.

(b) Energy loss distribution.

Figure 6.11: **Modeling the entrance window effect.** In the KESS simulation, a dead layer model is assumed. (a) The probability of depositing energy in the entrance window decreases exponentially with energy. (b) The parameterization of the energy loss distribution comprises six Cauchy functions and one exponential. Note the logarithmic axes.

An uncertainty on the dead layer thickness d_{DL} will be investigated in the sensitivity study. The energy loss of the affected events is simulated as

$$E_i = E_{\mathrm{in}} - \mathrm{rand}\Big[f_{\mathrm{DL}}\left(E_{\mathrm{loss}}\right)\Big] \qquad \text{for } i \in n_{\mathrm{DL}}\ . \tag{6.5}$$

Backscattering Analogously to the entrance window effect, backscattered electrons are tagged as such in KESS. The corresponding probability is fit linearly over E_{in}, as shown in figure 6.12(a). An uncertainty on the probability of being backscattered P_{bs} will be investigated in the sensitivity study. The number of backscattered events n_{BS} is described as

$$n_{\mathrm{BS}} = N \cdot P_{\mathrm{BS}}\left(E_{\mathrm{in}}\right)\ . \tag{6.6}$$

The backscattering background of the empirical model (see equation (4.15)) is used to parameterize the energy loss distribution of backscattered events. The fit to a KESS simulation with $E_{\mathrm{in}} = 19\,\mathrm{keV}$ is exemplary shown in figure 6.12(b). The energy loss of the backscattered events is simulated as

$$E_i = E_i' - \mathrm{rand}\Big[f_{\mathrm{BS}}\left(E\right)\Big] \qquad \text{for } i \in n_{\mathrm{BS}}\ , \tag{6.7}$$

where E_i' is the energy of an event after the simulation of the entrance window effect, i.e E_i' does not equal E_{in} for all events i.

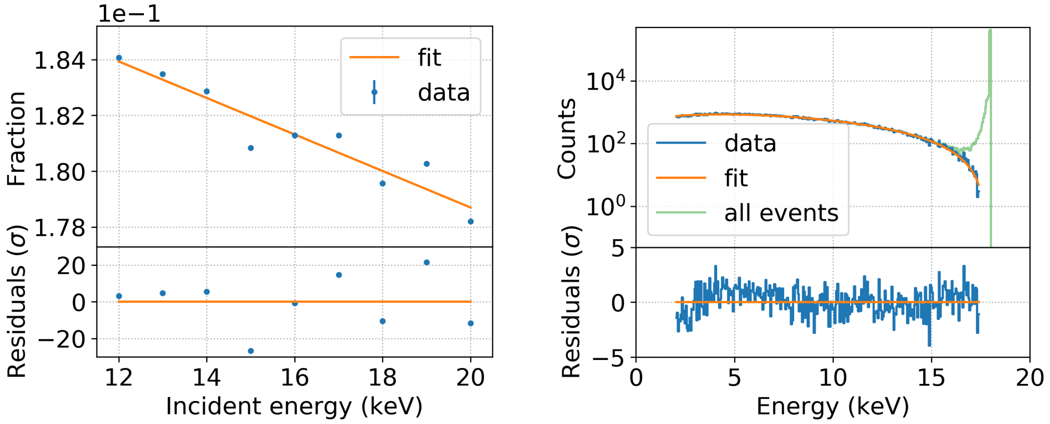

(a) Energy dependent probability.

(b) Energy loss distribution.

Figure 6.12: **Modeling the backscattering background.** (a) The probability for electrons to backscatter decreases linearly with energy. (b) The energy loss distribution of backscattered events is fit with the backscattering background part of the empirical model. All events of the simulation (i.e. including non-backscattered) are shown in light green.

Charge sharing The charge sharing probability P_{CS} is extracted from meaurements of an ^{241}Am spectrum and the investigations of charge sharing in its peaks in the energy range $E_{\mathrm{in}} = 14-26\,\mathrm{keV}$ [Alt19]. In this region, the charge sharing probability is approximately linear, illustrated by a linear fit in figure 6.13(a). However, this behavior cannot be extrapolated for much smaller energies, as P_{CS} gets negative before the incident energy reaches zero. This behavior is considered nonphysical and reveals an inaccuracy of this approximation. Nevertheless, the number of charge sharing events n_{CS} is described as

$$n_{\mathrm{CS}} = N \cdot P_{\mathrm{CS}}\left(E_{\mathrm{in}}\right) \; . \tag{6.8}$$

The energy loss distribution f_{CS} is the probability density function (PDF) of the fraction of shared charges η in one pixel. This PDF is calculated by a change of variables, assuming homogeneous detector illumination and a Gaussian shape $\mathcal{N}$ of the charge cloud [Kor20]:

$$f_{\mathrm{CS}}\left(\eta\right) = \tilde{c} \cdot \frac{\mathrm{d}}{\mathrm{d}\eta} \left[\eta^{-1}\left(x'\right)\right] \; , \tag{6.9}$$

where $\tilde{c}$ is a constant factor, x' denotes the distance of incidence from the pixel border, and the shared energy fraction

$$\eta\left(x'\right) = \int_{x'}^{\infty} \mathcal{N}\left(x\right) \mathrm{d}x \; . \tag{6.10}$$

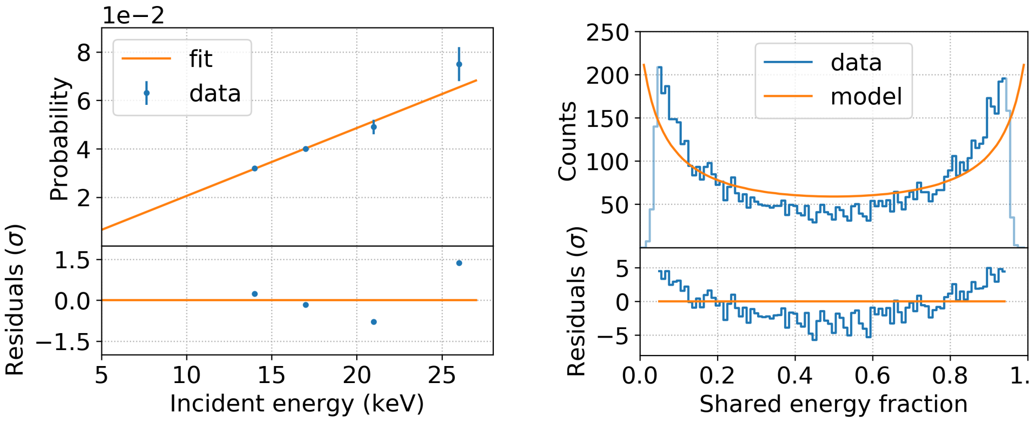

(a) Energy dependent probability.

(b) Energy loss distribution.

Figure 6.13: **Modeling charge sharing.** (a) The charge sharing probability in the energy range $E_{\text{in}} = 14-26\,\text{keV}$ is approximated with a linear function and extrapolated to lower incident energies. The fit is dominated by the measurement points at 13.9 and 17.8 keV and their small error bars. (b) The measured distribution of shared energy is described by a model assuming a Gaussian shape of the charge cloud.

is the integral of the Gaussian charge cloud over its fraction in one pixel. The model is shown in figure 6.13(b) together with data, measured with a TRISTAN prototype with 0.25 mm pixel diameter [Urb19]. The counts rapidly decrease close to shared energy fractions of zero and one. This is due to events below the detection threshold, i.e. due to undetected charge sharing. The model, however, includes these events but can also account for an arbitrary charge sharing detection efficiency $\epsilon_{\text{cs}} \in [0,1]$. An uncertainty on this efficiency will be investigated in the sensitivity study. The shape of the data does not exactly correspond to a Gaussian charge cloud, as indicated by the structure in the residuals. A more sophisticated model has to be developed for future investigations. The general shape of the distribution is considered to be at least similar for different pixel sizes, while only the amplitude decreases with increasing pixel diameter [Urb19]. The energy loss of the charge sharing events is simulated as

$$E_i = E_i' \cdot \text{rand}\Big[f_{\text{CS}}(\epsilon_{\text{cs}})\Big] \qquad \text{for } i \in n_{\text{CS}} \ . \tag{6.11}$$

Resolution The energy dependence of the energy resolution $\Delta E(E_i)$ (FWHM) is derived from the electrode measurements of the differential campaign at the Troitsk ν-mass experiment (see section 5.2.2). The energy E_i of each simulated event $i \in N$ is redistributed according to a Gaussian distribution with mean $\mu = E_i$ and standard deviation $\sigma = \Delta E(E_i)/2.355$, corresponding to the energy resolution at the respective

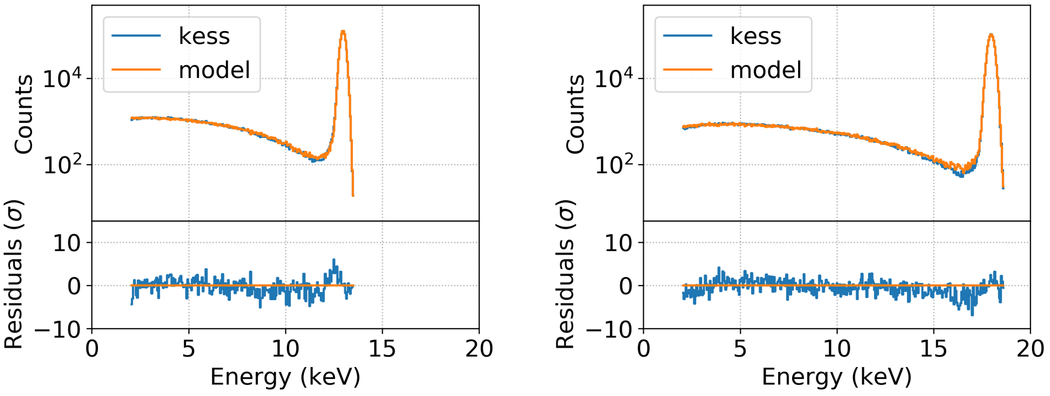

(a) Incident energy $E_{\text{in}} = 13\,\text{keV}$.

(b) Incident energy $E_{\text{in}} = 18\,\text{keV}$.

Figure 6.14: **Comparison of the detector effect model with KESS.** The model including all detector effects is compared to a KESS simulation of 10^6 events (a) for $E_{\text{in}} = 13\,\text{keV}$ and (b) for $18\,\text{keV}$. The same energy resolution as for the model has been applied to the simulated data.

energy E_i.[1] This is equivalent to a convolution of the spectrum with a Gaussian distribution of energy-dependent width. An uncertainty on the resolution ΔE will be investigated in the sensitivity study.

Comparison with simulation Figure 6.14 shows the model comprising all above mentioned effects. It is compared to a simulation with KESS. A slight deviation in the region of the dead layer tail is apparent but model and simulation are generally in good agreement. A good match is expected, as KESS has partly been used to model the individual effects. Nevertheless, the fact that the model is able to reproduce the underlying spectrum supports its applicability.

6.2.2 Energy dependence & impact on sensitivity

The second step of the study is the determination of the energy dependence of the empirical model parameters ψ. This is done for constant input parameters of backscattering, charge sharing, and energy resolution but for different dead layer thicknesses. The dead layer thickness of the P-0 detectors, obtained from the measurements in section 4.4, lie in the range $d_{\text{DL}} = 46-94\,\text{nm}$ with uncertainties $\delta_{\text{DL}} = 6$ and $7\,\text{nm}$. In this study, a dead layer thickness $d_{\text{DL}} = 80\,\text{nm}$ with uncertainties in the range $\delta_{\text{DL}} = 2-10\,\text{nm}$ in steps of $2\,\text{nm}$ is investigated. A spectrum

---

[1] The factor 2.355 translates a FWHM ΔE into a Gaussian standard deviation σ.

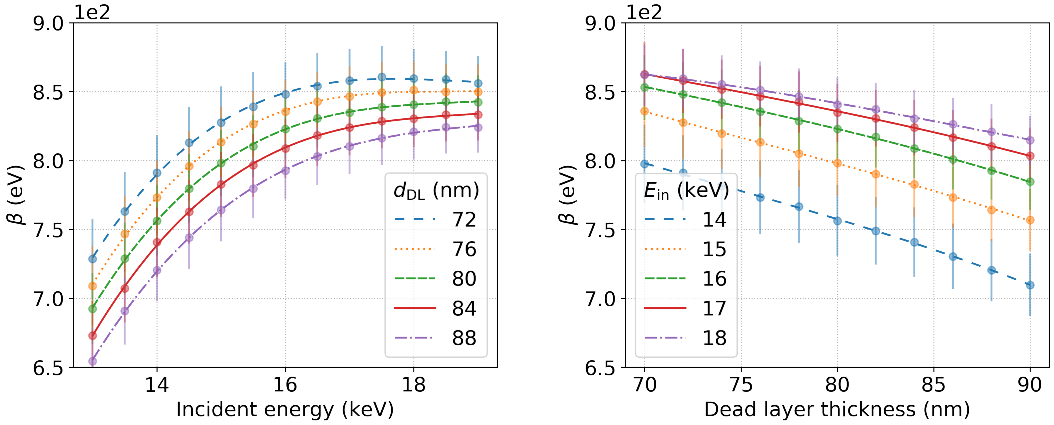

(a) Incident energy dependence of β.

(b) Dead layer thickness dependence of β.

Figure 6.15: **Parameter β over incident energy and dead layer thickness.** The plots illustrate the dependence of parameter β (a) on the incident energy E_{in} and (b) on the dead layer thickness d_{DL}. The points are interpolated with a one-dimensional cubic spline.

including 10^9 events is simulated for each (E_{in}, d_{DL})-grid point of incident energies in the range $E_{\mathrm{in}} = 13-19\,\mathrm{keV}$ in $0.5\,\mathrm{keV}$ steps and dead layer thicknesses in the range $d_{\mathrm{DL}} = 70-90\,\mathrm{nm}$ in $2\,\mathrm{nm}$ steps. With the grid having 13×11 points, this results in a total of 143 spectra. Each spectrum is fit with the empirical model (see section 4.3.2).

In figure 6.15, the parameter evolution is shown as a function of incident energy and dead layer thickness on the example of parameter β, the slope of the low energetic half of the dead layer tail. This parameter increases with energy and decreases with the dead layer thickness. Large values of β represent a strong influence of the dead layer effect. The conclusion is, that the influence of the entrance window is small for high energies and thin dead layers, which matches the expectation.

For each δ_{DL}, the respective energy dependencies of the parameters ψ are used to generate a response matrix and subsequently a tritium sample spectrum. This is done 10^4 times and a covariance matrix for the respective δ_{DL} is calculated. Fractional covariance and correlation matrices are exemplary show for $\delta_{\mathrm{DL}} = 2\,\mathrm{nm}$ in figure 6.16. The influence on the tritium spectrum is largest in the energy region around the HV cut and the uncertainty is highly correlated over the entire energy range.

Sensitivity curves are generated via the usual $\Delta\chi^2$-test and are shown in figure 6.17. The curves for $\delta_{\mathrm{DL}} = 2$ and $4\,\mathrm{nm}$ are indistinguishable from the statistical sensitivity, whereas the curve for $\delta_{\mathrm{DL}} = 10\,\mathrm{nm}$ shows a degradation of the sensitivity by a factor

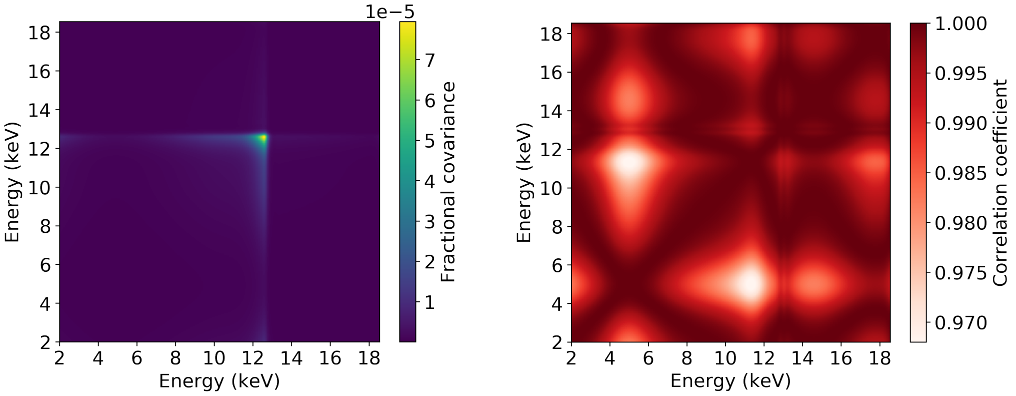

(a) Fractional covariance matrix.

(b) Correlation matrix.

Figure 6.16: **Covariance and correlation matrices for uncertainty on d_{DL}.** Both matrices are shown for $\delta_{\mathrm{DL}} = 2\,\mathrm{nm}$. (a) The fractional covariance matrix shows, that the influence on the tritium spectrum is largest in the energy region around the HV cut. (b) Uncertainty on the dead layer thickness is highly correlated over the entire energy range of the tritium spectrum. Note that the color scale starts at a correlation coefficient $r = 0.968$ (white).

of about three. Considering the curve of $\delta_{\mathrm{DL}} = 8\,\mathrm{nm}$, corresponding to an uncertainty size of $10\,\%$ for $d_{\mathrm{DL}} = 80\,\mathrm{nm}$, the measured uncertainties in section 4.4 would lead to an increase of the minimal reachable mixing amplitude $|U_{\mathrm{e4}}|^2$ relative to the statistical sensitivity by about $98\,\%$ in the most sensitive mass region $m_4 \approx 3.5\,\mathrm{keV}$.

As the smallest measured effective dead layer thickness in section 4.4 is $d_{\mathrm{DL}} \approx 50\,\mathrm{nm}$, the study is repeated based on this value. Relative to the statistical sensitivity in the most sensitive mass region $m_4 \approx 3.5\,\mathrm{keV}$, a $10\,\%$ uncertainty on a dead layer thickness of $50\,\mathrm{nm}$ leads to an increased reachable mixing amplitude $|U_{\mathrm{e4}}|^2$ by about $7\,\%$.

6.3 Conclusion

In this chapter, the impact of detector-related systematic uncertainties on the final sensitivity of a sterile neutrino search using KATRIN equipped with a TRISTAN detector was investigated. In section 6.1, the focus was put on the uncertainty of the parameters of the empirical detector response model. It was shown that the

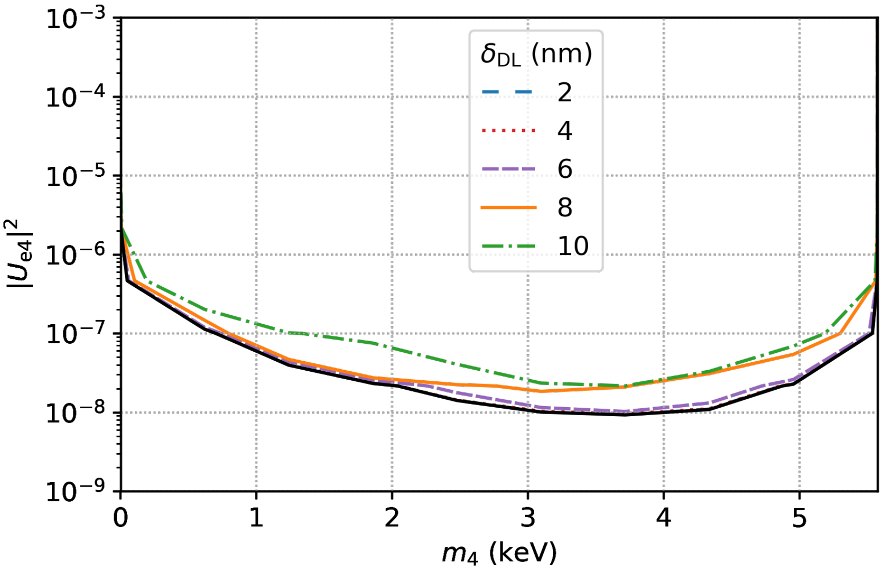

Figure 6.17: **Sensitivity for uncertainty on the dead layer thickness.** The curves for $\delta_{\mathrm{DL}} = 2\,\mathrm{nm}$ (loosely dashed blue) and $4\,\mathrm{nm}$ (dotted red) are concealed by the statistical sensitivity. An uncertainty $\delta_{\mathrm{DL}} = 10\,\mathrm{nm}$ (dashdotted green) leads to a degradation of the sensitivity by a factor of about three.

model allows for large uncertainties of its parameters, as long as the parameter values are correlated over large energy ranges. The weaker the bin-to-bin correlation, the stronger the impact on the sensitivity.

In section 6.2, the focus was put on uncertainty related to the entrance window thickness, assuming a dead layer model. It was shown that the measured uncertainty $\delta_{\mathrm{DL}} = 7\,\mathrm{nm}$ leads to a degradation of the sterile neutrino sensitivity by a factor of less than two. However, a relative uncertainty of for instance 10 % has a much stronger impact on the sterile neutrino sensitivity for thicker dead layers. The impact is expected to be stronger for lower E_{in}, as energy loss of electrons in the entrance window increases with decreasing incident energy. For the TRISTAN project, this means that both a thin entrance window and a precise determination of its thickness are important.

7 Summary & outlook

The goal of the TRISTAN project is to upgrade the KATRIN experimental setup in order to search for a keV-scale sterile neutrino signature in tritium β-decay. Sterile neutrinos with a mass in the keV-range could contribute to the abundance of DM in the universe. Their discovery would be a breakthrough in science with far reaching consequences for particle physics, cosmology, and astrophysics. Sterile neutrinos would mix with the active neutrino states, generating an imprint on the spectrum of weak decays. As the KATRIN experiment features a strong tritium source, it can be utilized to search for this imprint. The main goal of the experiment is to determine the effective mass of the electron anti-neutrino with a precision of 200 meV (90 % C.L.). The difference to a sterile neutrino search is the observed electron energy range: While a neutrino mass measurement focuses on the kinetic endpoint, a sterile neutrino imprint could occur at any point in the spectrum. By investigating a wide energy range — i.e. a large sterile neutrino mass range — the count rate on the detector increases by several orders of magnitude. This requires a novel detector system, which is being developed within the TRISTAN project. Its requirements are mainly the ability to manage these high rates and an excellent energy resolution of a few hundred eV. First prototypes have been produced, featuring seven pixels in SDD technology.

Within this work, the prototypes were characterized with regard to their general performance using standard photon sources. Excellent energy resolution, calibration linearity as well as pixel homogeneity were demonstrated, validating that the detectors are suited for the application in the frame of the TRISTAN project. The prototypes were moreover characterized with regard to their performance using mono-energetic electron sources. A model of the detector response to mono-energetic electrons was developed. As the detectors' entrance window has a strong effect on the measured response, several entrance window technologies were produced by HLL and strategies to determine their thicknesses were tested. For this purpose, two mono-energetic electron sources — namely an electron microscope and $^{83\mathrm{m}}$Kr — were utilized and the results were compared to dedicated MC simulations. The analyses yield small entrance window thicknesses in the range of 46 – 94 nm. The detailed characterization set the basis for the design of the next-generation prototype detector, whose production was completed in the beginning of 2020. The methods developed to characterize the detectors both with photons and electrons are now being applied for the next-generation prototypes. The careful optimization of measurement procedures and analysis techniques facilitates the ongoing characterization campaigns significantly.

The second focus in this thesis was a sterile neutrino search with a TRISTAN detector at the Troitsk ν-mass experiment. This includes the instrumentation of the Troitsk ν-mass experiment with a TRISTAN detector, measurements in two complementary measurement modes — differential and integral mode — and the analyses of the thereby acquired data. The analyses comprise the development of detailed detector response models and strategies to include systematic uncertainty. Diverse sources of uncertainty were identified and evaluated, such that an extensive budget of systematic uncertainty was established. It could be demonstrated that the two modes are prone to largely different systematic effects. This led to the first publication of sterile neutrino exclusion limits produced with a TRISTAN detector [Bru19], increasing the search window of the Troitsk ν-mass experiment by a factor of three: Best limits on the sterile neutrino mixing amplitude of $|U_{\mathrm{e}4}|^2 < 2 \cdot 10^{-2}$ could be set in a mass range $m_4 = 0-5.6\,\mathrm{keV}$ in differential mode and of $|U_{\mathrm{e}4}|^2 < 7 \cdot 10^{-3}$ in a mass range $m_4 = 0-6.6\,\mathrm{keV}$ in integral mode. These successful sterile neutrino searches at the Troitsk ν-mass experiment depict a major milestone of the TRISTAN project. The campaigns demonstrated the feasibility of a sterile neutrino search with the conventional integral and the novel differential mode, the combination of which is a key ingredient of the TRISTAN strategy. The analysis strategy, developed for both types of data sets, will be the essential basis for the sterile neutrino searches with TRISTAN. The possibilities of a next measurement campaign at the Troitsk ν-mass experiment with a 166 pixel TRISTAN detector module is currently being evaluated.

The third part of this thesis was to investigate the impact of detector-related systematic uncertainties on the final TRISTAN sensitivity. A special focus was put on the investigation of an uncertainty on the parameters of the empirical model for mono-energetic electrons and on the dead layer thickness. The framework of the Troitsk ν-mass analysis provided the basis for this studies. Following main results were obtained:

- Systematic uncertainties, which are uncorrelated over a wide energy range, impact the sterile neutrino sensitivity more than correlated uncertainties.
- Uncertainties affecting the region above the HV cut in a differential spectrum have a stronger impact on the sensitivity than uncertainties on the backscattering background.

- The sensitivity is stronger degraded for thick dead layers than for thin ones: Assuming the same relative uncertainty of 10 % on the dead layer thickness d_{DL}, the minimal reachable mixing amplitude $|U_{\mathrm{e4}}|^2$ is increased by about 98 % for $d_{\mathrm{DL}} = 80\,\mathrm{nm}$ and by about 7 % for $d_{\mathrm{DL}} = 50\,\mathrm{nm}$.

- The uncertainty on the effective dead layer thickness of 7 nm, determined in the characterization campaign, leads to a degradation of the sterile neutrino sensitivity by a factor of less than two.

The work of this thesis led to great advances of the TRISTAN project and will serve as a basis for future developments of the project. The final TRISTAN detector system with around 3500 pixels, composed of 21 modules, is planned to be ready in 2024. Only the combination of the strong KATRIN tritium source with the TRISTAN detector enables to reach a parameter space of cosmological interest in a reasonable time. Moreover, this will be a unique experiment, as an even larger setup in the kind of KATRIN is not foreseen to date.

A Proton grid

The subject of section 4.4 was to model the properties of the detector chip entrance window and to determine its thickness. Electrons were accelerated onto the chip, as the effect of the entrance window is stronger for massive particles. An even stronger effect could be observed for heavier particles like protons or ions. At MPP, a proton accelerator was constructed with the intention of investigating the properties of frictional cooling for the use in a muon collider scheme [Gre07]. This device serves as a model for a new proton accelerator test stand for the TRISTAN project, called “proton grid”.

The basic concept of the grid works as follows: To produce protons, an open ^{241}Am source is placed below a Mylar ($C_{10}H_8O_4$) foil. The α-radiation penetrates the foil and breaks bonds of hydrogen atoms just below its outlet surface. Protons, i.e. ionized hydrogen atoms, with almost no kinetic energy are set free. They are accelerated through a grid of conductive discs with holes in their centers and each set on a slightly more negative potential. The detector is located at the end of the grid, facing towards the proton beam. A magnetic coil around the grid confines the protons to defined trajectories, leading from the source to the detector.

Despite a great effort of trouble shooting, it has not been possible to operate the proton grid as intended to date. The reason is assumed to be electrical flashovers, which prohibit the simultaneous operation of high voltage, magnetic field and vacuum. This appendix is intended to document the legacy of the proton grid with respect to its requirements and construction. The results of the commissioning and trouble shooting attempts are summarized in reference [Leb19].

Requirements and construction

Simulations were performed to determine the optimal geometry and electromagnetic configuration of the grid.[1] The dimensions of the grid are summarized in table A.1. The grid is displayed in figure A.1. The proton source has to be movable in the direction of the symmetry axis of the grid in order to find the optimal acceleration

---

[1] The simulation is based on C++ code by F. Glück, private communication.

Table A.1: **Proton grid dimensions and parameters.** These values are the result of an optimization process using simulations. 1 — The maximal achieved stable voltage is 15 kV at a pressure of $5 \cdot 10^4$ mbar. 2 — The magnetic field actually reaches only about 86 mT.

Name	Symbol	Value	Unit	Comment
Maximal voltage	V_{max}	30	kV	1
Source position	z_{source}	20	mm	
Inner disc diameter	D_{in}	14	mm	
Outer disc diameter	D_{out}	100	mm	
Outer diameter of last disc	D_{last}	66	mm	
Disc distance	δz_{disc}	8	mm	
Distance of last disc	δz_{last}	15.3	mm	
Disc thickness	d_{disc}	1	mm	
Number of discs	n_{disc}	52		
Grid length	L_{grid}	457.3	mm	
Electrical resistance	R	1	GΩ	
Vessel length	L_{vessel}	657	mm	
Inner vessel diameter	Δ_{in}	200	mm	
Outer vessel diameter	Δ_{out}	210	mm	
Magnetic field	B	204.5	mT	2
Coil length	L_{coil}	537	mm	
Inner coil diameter	$Д_{\text{in}}$	210	mm	
Outer coil diameter	$Д_{\text{out}}$	230	mm	
Ampere windings	$N \cdot I$	32 000		

field. The proton energy shall adjustable in the range of 0 – 30 keV. To enable non-perpendicular particle incidence at the detector, the latter needs to be mounted in a tiltable way. Everything is enclosed by an air-tight vessel to operate the grid in vacuum. To simplify the signal feedthrough, the detector should sit on ground potential.

Grid As the protons are not generated on the first acceleration disc itself but with a certain distance, the electric potential is not fully exploited to obtain kinetic energy. For instance, applying a voltage of 30 kV to the first acceleration disc, the protons obtain a kinetic energy of only 28.4 keV. This loss is minimized by a small inner diameter of the holes in the acceleration discs. However, the hole diameter is not smaller than 14 mm, due to the diameter of the ^{241}Am source, which is 12 mm. The

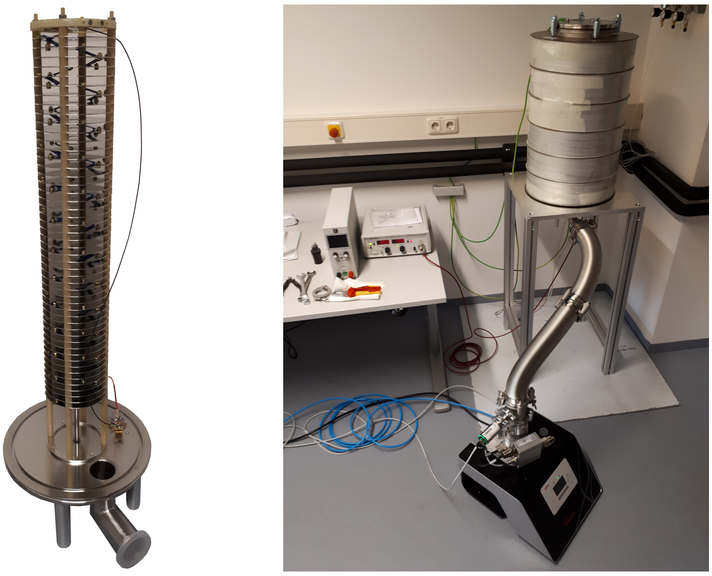

(a) Proton grid. (b) Ambient devices.

Figure A.1: **Proton grid setup.** (a) The proton grid consists of 51 acceleration discs. (b) The grid is installed inside the vacuum vessel. Ambient devices are a voltage supply for the grid, a current supply for the magnetic coil and a vacuum pump. The detector system is not installed on this picture.

potential minimum of the electric field is about 20 mm inside the grid, where the source has to be moved to. To avoid inhomogeneities in the field lines, the distance between two neighboring discs is not larger than 8 mm, the electric field is not stronger than 70 kV m^{-1}, and the outer diameter of the discs is not smaller than 100 mm. This results in 51 discs to reach a maximal potential of 30 kV.

The last acceleration disc carries the detector. Its diameter is 66 mm to provide enough space to screw the detector board. To tilt the detector by 20° and to avoid electric flashovers under this angle, the distance to the second last disc is 14.3 mm. The total length of the grid adds up to 457.3 mm with the voltage difference of 600 V between two discs. Electrical resistors serve as voltage dividers. With a resistance of 1 GΩ, they create a power of 3.6 mW, which is sufficiently small for operation in vacuum without the need of cooling. The discs are made of stainless steel (magnetic permeability $\mu_r = 2$).

Vessel The vacuum vessel is made of a tube with a flange on each end. The inner surface is electrically polished to not contain any sharp edges. The grid is attached to the lower flange on its vacuum side, while the air side carries supporting feet. To easily mount and dismount the source, the distance between flange and first acceleration disc is 100 mm. Three feedthroughs are installed at this flange: an electrical one for the high voltage of the discs, a mechanical one for the movable source holder, and a socket for a vacuum pump (ISO-KF 40). The vacuum must provide a mean free path of the protons, which is longer than the distance of the grid.

The distance of the last disc (carrying the detector) to the upper flange is also 100 mm. This flange carries a feedthrough for the detector signal chain (D-Sub-25) and one for high voltage diagnostics. The total length of the vacuum vessel adds up to 657 mm. The distance between the discs and the tube walls is 50 mm. In the KATRIN spectrometers, there are no flashovers in electric fields smaller than $1\,\mathrm{MV\,m^{-1}}$. Given the 30 keV of the proton grid, this would correspond to a distance of 30 mm but as the vacuum is worse than in KATRIN, 50 mm are assumed to be appropriate. For security reasons, the vessel and both flanges are grounded over a connection to a power plug.

Magnet Assuming a maximal proton kinetic energy of 2 eV perpendicular to the magnetic field lines, a magnetic field of 204.5 mT is required, to achieve a gyro radius of 1 mm. This way, an increased count rate on the detector is simulated (40 Hz with, and 5 Hz without B-field). As the protons are not adiabatically transported but accelerated, the magnetic field covers the entire distance from the source to the detector. Therefore, the magnetic coil has a length of 537 mm, an inner and outer diameter of 210 mm and 230 mm, respectively, and 32 000 ampere windings. In order to reduce the number of ampere windings, the coil is wrapped directly onto the vacuum vessel.

B Projected covariance & residuals

In section 5.3, the covariance matrix method was applied to account for systematic uncertainty in the integral campaign at the Troitsk ν-mass experiment. Figure 5.37 shows the budget of all considered uncertainty contributions as a function of retarding energy. Figure 5.38 shows the fit of the integral model to the measured data and its residuals, superimposed by the statistical and systematic uncertainty contributions. In both of these plots, however, the contributions of systematic uncertainty are represented by the diagonals of the respective covariance matrix, which contain uncorrelated uncertainty only. Omitting correlations, one gets an incomplete picture of the actual size and impact of the uncertainties. Thus, an attempt was made to also account for correlations in illustrations like these.

General idea The basic idea is to transform both the residuals and the covariance matrix into a basis, in which the matrix is diagonal.[1] This is done by means of an eigendecomposition of the covariance matrix M, as described in the following. The general form of a χ^2-fit function is

$$\begin{aligned}\chi^2 &= \left[y - f\left(x\right)\right]^T M^{-1} \left[y - f\left(x\right)\right] \\ &= r^T M^{-1} r \ , \end{aligned} \tag{B.1}$$

where $r = y - f\left(x\right)$ refers to the residuals. Performing an eigendecomposition of M, an orthogonal matrix Q ($Q^T Q = \mathbb{1}$) is determined, such that

$$\Lambda = Q^T M Q \tag{B.2}$$

is diagonal. With this, the χ^2-function in equation (B.1) becomes

$$\begin{aligned}\chi^2 &= r^T \left(Q Q^T\right) M^{-1} \left(Q Q^T\right) r \\ &= r^T Q \left(Q^T M Q\right)^{-1} Q^T r \\ &= \left(r^T Q\right) \Lambda^{-1} \left(Q^T r\right) \ . \end{aligned} \tag{B.3}$$

---

[1] M. Slezák, private communication.

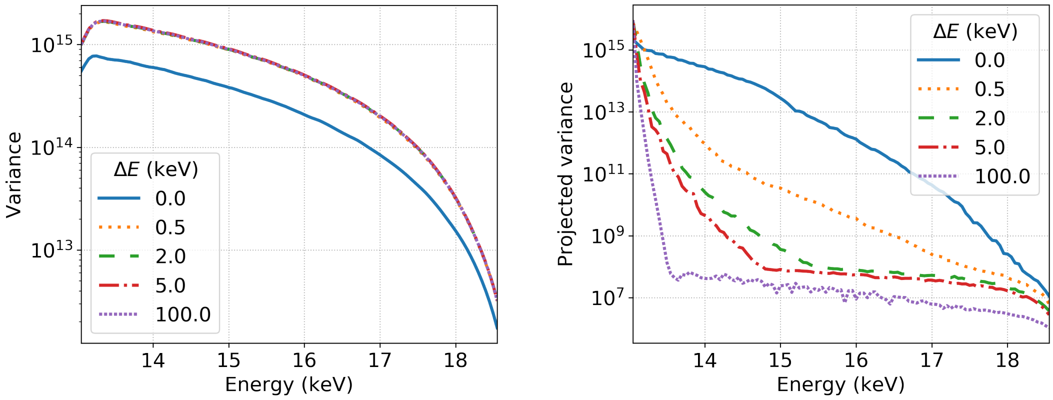

(a) Variance.

(b) Projected covariance.

Figure B.1: **Comparison of variance and projected covariance.** (a) The variance does not show the impact of the correlated uncertainty. (b) The projected covariance clearly shows the hierarchy of correlated uncertainty.

This appears like a usual χ^2-function with residuals of the form $Q^T r$, multiplied by the inverse eigenvalues of Λ. Interpreting these eigenvalues as “projected variance”, the normalized residuals are given as

$$\frac{Q^T r}{\sqrt{\Lambda}} \, . \tag{B.4}$$

Uncertainty budget The approach is tested on a well-defined example: In section section 6.1, the impact of uncertainty on parameters of the empirical model was studied. To also investigate the influence of correlations, a defined correlation width ΔE was added in the generation of covariance matrices for the resolution parameter σ. Figure B.1(a) shows the variance, i.e. the diagonals of these covariance matrices, for several correlation widths ΔE. Except for the case of uncorrelated uncertainty ($\Delta E = 0\,\mathrm{keV}$), all curves are identical. The deviation $\Delta E = 0\,\mathrm{keV}$ is a result of the transformation of the covariance matrix for σ into the tritium spectrum via the response matrix: The input correlation width matrices ω are identical on the diagonal for all correlation widths. In contrast to that, figure B.1(b) shows the situation after the eigendecomposition. The hierarchy of correlation widths is in the correct order: Uncorrelated uncertainty has the largest projected variance, while fully correlated uncertainty the smallest.

However, it is unclear how the kinks in the spectra are generated and why the the eigenvalues increase extreme so rapidly towards the lower end of the x-axis. Furthermore, a decomposition over the entire energy range $E = 2-18.6\,\mathrm{keV}$ shows the same trend but different eigenvalues and even more unaccountable features. It

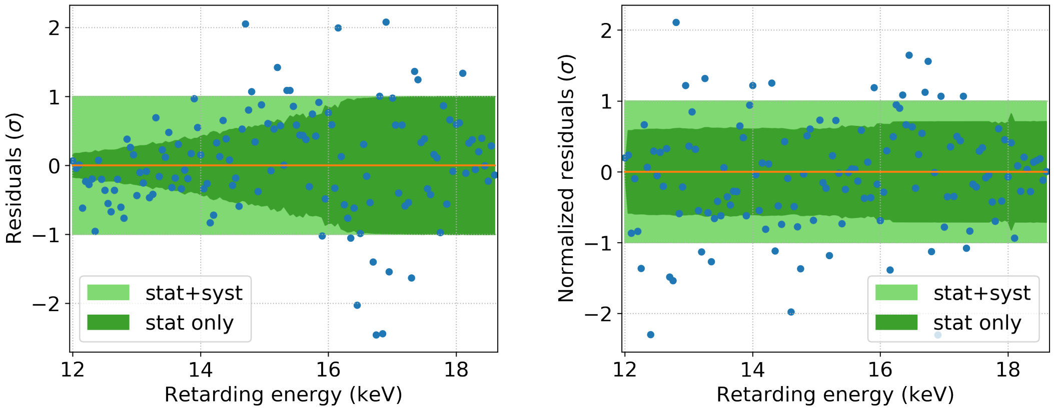

(a) Diagonal residuals.

(b) Projected residuals.

Figure B.2: **Comparison of diagonal and projected residuals.** (a) The plots shows the residuals of the fit to the spectrum of the integral campaign at the Troitsk ν-mass experiment (see figure 5.38). The residuals are normalized to the total uncertainty (light green). The statistical uncertainty contribution is superimposed in dark green. (b) The projected residuals.

is assumed to be related to the HV cut at 13 keV, which strongly affects the shape of the covariance matrix and distorts it from a smooth behavior. The covariance matrix is heavily ill-defined, such that the corresponding eigenvalues turn out to be spread over many orders of magnitude.

Residual plot Figure B.2(a) shows the residual plot of the fit to the tritium spectrum of the integral at the Troitsk ν-mass experiment (see figure 5.38). The systematic uncertainty dominates over the statistical uncertainty at retarding energies $eU < 15\,\text{keV}$. The residuals show a slight pattern at small eU and larger increasing fluctuations at large eU. In contrast, no pattern is apparent in the normalized residuals in figure B.2(b). Also the systematic contribution of the uncertainty stays at a constant over the entire retarding energy range $eU = 12-18.6\,\text{keV}$.

Conclusion The eigendecomposition approach presented in section is intended to illustrate not only uncorrelated uncertainty but also account for their bin-to-bin correlations. So far, it is not clear how to exactly interpret the result and some features cannot be explained. The approach requires further investigation but bears the potential to improve the illustration of correlations and thus the assessment of uncertainty. This holds for any analysis making use of the covariance matrix method.

C Covariance matrix convergence

The covariance matrix method was applied in section 5.3 to account for systematic uncertainty in the integral campaign at the Troitsk ν-mass experiment and in chapter 6 to introduce uncertainty in sterile neutrino sensitivity studies. These covariance matrices are estimators of the covariance, which converge to their true values for $N \to \infty$, according to the law of large numbers. One approach to determine the minimal number of samples N, which are needed to obtain reliable estimates of the covariance matrices, is the Cauchy convergence test [Bul00]

$$\forall \epsilon > 0, \quad \exists N \in \mathbb{N}, \quad \forall j > 0 : \quad ||M_{N+j} - M_N|| < \epsilon \; , \tag{C.1}$$

where

$$||M|| = \sqrt{\mathrm{Tr}\,(M \cdot M)} \; . \tag{C.2}$$

is the Frobenius norm. This means that a sample covariance matrix converges, if it does not change within a given precision ϵ, when j additional samples are used for its calculation.

In practice, however, the convergence test is limited by the finite number of samples. To make a qualitative statement on the convergence of the covariance matrices, in this thesis the norm $||M||$ is plot as a function of the number of samples, which was used to calculate the covariance matrix. This is shown in figure C.1 on the example of the cross section covariance matrix M_{crsec} (see section 5.3.4.2). A strong fluctuation of its norm $||M_{\mathrm{crsec}}||$ is apparent for less than 2000 used samples. However, the behavior can be described as approximately flat only for more than 8000 used samples. Conservatively, all covariance matrices in this thesis were generated on the basis of 10^4 samples.

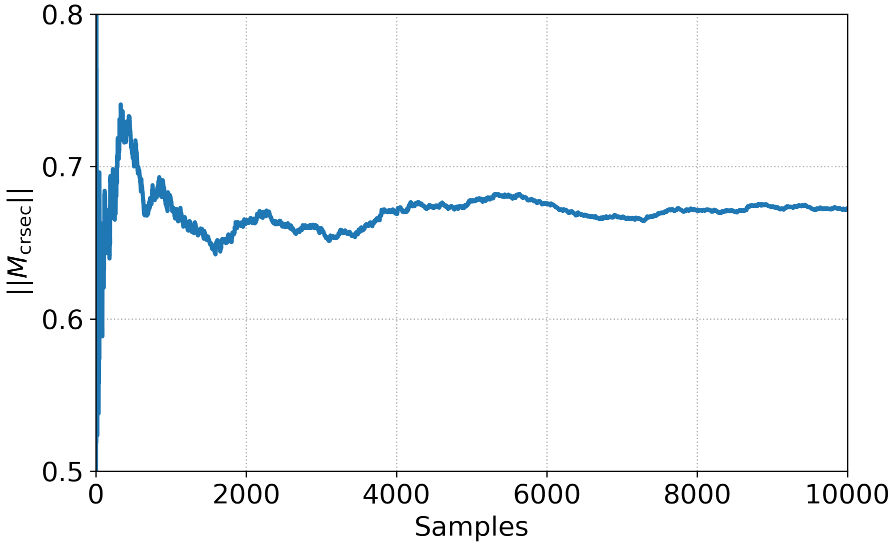

Figure C.1: **Covariance matrix convergence test.** The plot shows the Frobenius norm of the cross section covariance matrix M_{crsec} as a function of samples, which were used to generate the covariance matrix. The more samples are used, the more stable the norm and thus the more reliable the covariance estimates.

D List of publications

The following gives an overview of papers and proceedings published in the context of this work by the author and others.

Corresponding author peer reviewed

T. Brunst et al., *Development of a silicon drift detector system for the TRISTAN project — Future search for sterile neutrinos*, Nucl. Instrum. Meth. A 936 (2019), 235-6, DOI: 10.1016/j.nima.2018.09.116.

T. Brunst et al., *Measurements with a TRISTAN prototype detector system at the "Troitsk nu-mass" experiment in integral and differential mode*, J. Instrum. 14 (2019), DOI: 10.1088/1748-0221/14/11/p11013.

T. Brunst, *TRISTAN measurements at the Troitsk nu-mass experiment*, J. Phys. Conf. Ser. 1468, (2020), DOI: 10.1088/1742-6596/1468/1/012195.

Co-author peer reviewed

L. J. Broussard, R. Alarcon, S. Baeßler, L. Barrón Palos, N. Birge, T. Bode, J. D. Bowman, T. Brunst et al., *Neutron decay correlations in the Nab experiment*, J. Phys. Conf. Ser. 876 (2017) 012005, DOI: 10.1088/1742-6596/876/1/012005.

K. Altenmüller, T. Bode, T. Brunst et al., *Silicon drift detector prototypes for the keV-scale sterile neutrino search with TRISTAN*, Nucl. Instrum. Meth. A 912 (2018), 333-7, DOI: 10.1016/j.nima.2017.12.026.

M. Carminati, R. Bisognin, P. King, M. Gugiatti, P. Trigilio, L. Bombelli, P. Lechner, T. Brunst et al., *A Scalable Detection and Readout Platform for Large SDD Arrays for the TRISTAN Project*, in: *IEEE Nucl. Sci. Med. Imag. Conf. Proc.* 2018, 1-3, DOI: 10.1109/NSSMIC.2018.8824532.

P. Trigilio, L. Bombelli, M. Carminati, R. Bisognin, A. Grande, M. Gugiatti, C. Fiorini, P. Lechner, T. Brunst et al., *ETTORE: a 12-Channel Front-End ASIC for SDDs with Integrated JFET*, in: *IEEE Nucl. Sci. Med. Imag. Conf. Proc.* 2018, 1-4, DOI: 10.1109/NSSMIC.2018.8824675.

S. Mertens, A. Alborini, K. Altenmüller, T. Bode, L. Bombelli, T. Brunst et al., *A novel detector system for KATRIN to search for keV-scale sterile neutrinos*, J. Phys. G Nucl. Partic. 46:6 (2019), DOI: 10.1088/1361-6471/ab12fe.

A. Alborini, K. Altenmüller, M. Biassoni, L. Bombelli, T. Brunst et al., *Characterization of the TRISTAN SDDs with Monoenergetic Electrons*, Manuscript in preparation.

Non-peer reviewed

T. Brunst et al., *Detector Development for a Sterile Neutrino Search with the KATRIN Experiment*, 2018, arXiv: 1801.08182v1.

References

[Aba12] K. N. Abazajian et al., *Light Sterile Neutrinos: A White Paper*, 2012, arXiv: 1204.5379 [hep-ph].

[Abd15] D. Abdurashitov et al., *The current status of "Troitsk nu-mass" experiment in search for sterile neutrino*, J. Instrum. 10:10 (2015), T10005, DOI: 10.1088/1748-0221/10/10/t10005.

[Abd17] J. N. Abdurashitov et al., *First measurements in search for keV sterile neutrino in tritium beta-decay in the Troitsk nu-mass experiment*, JETP Lett. 105:12 (2017), 753–7, DOI: 10.1134/S0021364017120013.

[Abd96] J. N. Abdurashitov et al., *The Russian-American Gallium Experiment (SAGE) Cr Neutrino Source Measurement*, Phys. Rev. Lett. 77:23 (1996), 4708–11, DOI: 10.1103/PhysRevLett.77.4708.

[Ade16] P. A. R. Ade et al. (Planck Collaboration), *Planck 2015 results. XIII. Cosmological parameters*, Astron. Astrophys. 594 (2016), A13, DOI: 10.1051/0004-6361/201525830.

[Adh17] R. Adhikari et al., *A White Paper on keV sterile neutrino Dark Matter*, J. Cosmol. Astropart. P. 1 (2017), 025, DOI: 10.1088/1475-7516/2017/01/025.

[Ago19] M. Agostini et al., *Probing Majorana neutrinos with double-β decay*, Science 365:6460 (2019), 1445–8, DOI: 10.1126/science.aav8613.

[Agu01] A. Aguilar et al. (LSND Collaboration), *Evidence for neutrino oscillations from the observation of $\overline{\nu}_e$ appearance in a $\overline{\nu}_\mu$ beam*, Phys. Rev. D 64:11 (2001), 112007, DOI: 10.1103/PhysRevD.64.112007.

[Agu18] A. A. Aguilar-Arevalo et al. (MiniBooNE Collaboration), *Significant Excess of Electronlike Events in the MiniBooNE Short-Baseline Neutrino Experiment*, Phys. Rev. Lett. 121:22 (2018), 221801, DOI: 10.1103/PhysRevLett.121.221801.

[Ahm01] Q. R. Ahmad et al. (SNO Collaboration), *Measurement of the Rate of $\nu_e + d \to p + p + e^-$ Interactions Produced by ^8B Solar Neutrinos at the Sudbury Neutrino Observatory*, Phys. Rev. Lett. 87:7 (2001), 071301, DOI: 10.1103/PhysRevLett.87.071301.

[Ake19] M. Aker et al. (KATRIN Collaboration), *Improved Upper Limit on the Neutrino Mass from a Direct Kinematic Method by KATRIN*, Phys. Rev. Lett. 123:22 (2019), 221802, DOI: 10.1103/PhysRevLett.123.221802.

[Ake20] M. Aker et al. (KATRIN Collaboration), *First operation of the KATRIN experiment with tritium*, Eur. Phys. J. C 80:264 (2020), DOI: 10.1140/epjc/s10052-020-7718-z.

[Ali80] R. C. Alig, S. Bloom, and C. W. Struck, *Scattering by ionization and phonon emission in semiconductors*, Phys. Rev. B 22:12 (1980), 5565–82, DOI: 10.1103/PhysRevB.22.5565.

[Alt19] K. Altenmüller, *Search for sterile neutrinos in β-decays*, PhD thesis, Technical University of Munich, 2019, URL: http://nbn-resolving.de/urn/resolver.pl?urn:nbn:de:bvb:91-diss-20191010-1506307-1-4.

[Ams15] J. Amsbaugh et al., *Focal-plane detector system for the KATRIN experiment*, Nucl. Instrum. Meth. A 778 (2015), 40–60, DOI: 10.1016/j.nima.2014.12.116.

[Ana19] Analog Devices, 2019, URL: www.analog.com/media/en/technical-documentation/data-sheets/AD9265.pdf (visited on 12/06/2019).

[Ang05] J. Angrik et al. (KATRIN Collaboration), *KATRIN design report 2004*, Wissenschaftliche Berichte: FZKA 7090 (2005) Tech. Report, DOI: 10.5445/IR/270060419.

[Are18] M. Arenz et al., *First transmission of electrons and ions through the KATRIN beamline*, J. Instrum. 13:04 (2018), P04020, DOI: 10.1088/1748-0221/13/04/p04020.

[Arm04] T. Armbrust, *Messung der Eigenschaften eines Silizium Drift Detektors mit Elektronen im keV-Bereich*, Master's thesis, University of Karlsruhe, 2004.

[Asa05] T. Asaka and M. Shaposhnikov, *The νMSM, dark matter and baryon asymmetry of the universe*, Phys. Lett. B 620:1 (2005), 17–26, DOI: 10.1016/j.physletb.2005.06.020.

[Ase00] V. Aseev et al., *Energy loss of 18 keV electrons in gaseous T and quench condensed D films*, Eur. Phys. J. D 10:1 (2000), 39–52, DOI: 10.1007/s100530050525.

[Ase11] V. N. Aseev et al., *Upper limit on the electron antineutrino mass from the Troitsk experiment*, Phys. Rev. D 84:11 (2011), 112003, DOI: 10.1103/PhysRevD.84.112003.

[Bau16] J. Baur et al., *Lyman-alpha forests cool warm dark matter*, J. Cosmol. Astropart. P. 2016:08 (2016), 012, DOI: `10.1088/1475-7516/2016/08/012`.

[Bau19] M. Bauer and T. Plehn, *Yet Another Introduction To Dark Matter*, vol. 959, Lecture Notes in Physics, Springer, 2019, DOI: `10.1007/978-3-030-16234-4`.

[Bel13] A. I. Belesev et al., *Upper limit on additional neutrino mass eigenstate in 2 to 100 eV region from "Troitsk nu-Mass" data*, JETP Lett. 97:2 (2013), 67–9, DOI: `10.1134/S0021364013020033`.

[Bel14] A. I. Belesev et al., *The search for an additional neutrino masseigenstate in the 2–100 eV region from "Troitsk numass" data: a detailed analysis*, J. Phys. G Nucl. Partic. 41 (2014), 015001, DOI: `10.1088/0954-3899/41/1/015001`.

[Bet53] H. A. Bethe and J. Ashkin, *Experimental Nuclear Physics. Volume III*, ed. by E. Segrè, John Wiley & Sons, 1953, URL: `http://113.161.190.196:8080/thuvienso/handle/123456789/81`.

[Bez08] F. Bezrukov, *νMSM and its experimental tests*, J. Phys. Conf. Ser. 110:8 (2008), 082002, DOI: `10.1088/1742-6596/110/8/082002`.

[Bom11] L. Bombelli et al., *"CUBE", A low-noise CMOS preamplifier as alternative to JFET front-end for high-count rate spectroscopy*, in: *IEEE Nucl. Sci. Conf. R.* 2011, 1972–5, DOI: `10.1109/NSSMIC.2011.6154396`.

[Bow95] M. G. Bowler and N. A. Jelley, *Investigations into the origin of the spurious 17 keV neutrino signal observed in ^{35}S beta decay*, Z. Phys. C Part. Fields 68:3 (1995), 391–413, DOI: `10.1007/BF01620714`.

[Boy14] A. Boyarsky et al., *Unidentified Line in X-Ray Spectra of the Andromeda Galaxy and Perseus Galaxy Cluster*, Phys. Rev. Lett. 113:25 (2014), 251301, DOI: `10.1103/PhysRevLett.113.251301`.

[Boy19] A. Boyarsky et al., *Sterile neutrino Dark Matter*, Prog. Part. Nucl. Phys. 104 (2019), 1–45, DOI: `10.1016/j.ppnp.2018.07.004`.

[Bro70] C. G. Broyden, *The Convergence of a Class of Double-rank Minimization Algorithms 1. General Considerations*, IMA J. Appl. Math. 6:1 (1970), 76–90, DOI: `10.1093/imamat/6.1.76`.

[Bro71] J. Bromberg, *The Impact of the Neutron: Bohr and Heisenberg*, Historical Studies in the Physical Sciences 3 (1971), 307–41, DOI: `10.2307/27757321`.

[Bru19] T. Brunst et al., *Measurements with a TRISTAN prototype detector system at the "Troitsk nu-mass" experiment in integral and differential mode*, J. Instrum. 14:11 (2019), P11013, DOI: 10.1088/1748-0221/14/11/p11013.

[Bul00] V. V. Buldygin and Y. V. Kozachenko, *Metric characterization of random variables and random processes*, Providence, R.I.: American Mathematical Society, 2000, ISBN: 0821805339 (alk. paper), URL: https://trove.nla.gov.au/work/6547512.

[Bul14] E. Bulbul et al., *Detection of an Unidentified Emission Line in the Stacked X-ray Spectrum of Galaxy Clusters*, Astrophys. J. 789:1 (2014), 13, DOI: 10.1088/0004-637x/789/1/13.

[CER20] CERN, 2020, URL: home.cern/science/physics/standard-model (visited on 03/19/2020).

[Cha14] J. Chadwick, *Intensitätsverteilung im magnetischen Spectrum der β-Strahlen von radium B + C*, Verhandl. Dtsc. Phys. Ges. 16 (1914), 383, URL: http://cds.cern.ch/record/262756.

[Chu99] S. Chu, L. Ekström, and R. Firestone, *The Lund/LBNL Nuclear Data Search*, version 2, 1999, URL: nucleardata.nuclear.lu.se/toi (visited on 11/14/2019).

[Cow11] G. Cowan et al., *Asymptotic formulae for likelihood-based tests of new physics*, Eur. Phys. J. C 71:2 (2011) [Erratum ibid. C 73 (2013) 2501], 1554, DOI: 10.1140/epjc/s10052-011-1554-0.

[Cow56] C. L. Cowan et al., *Detection of the Free Neutrino: a Confirmation*, Science 124:3212 (1956), 103–4, DOI: 10.1126/science.124.3212.103.

[Cow98] G. Cowan, *Statistical Data Analysis*, Oxford science publications, Clarendon Press, 1998, ISBN: 9780198501558, URL: http://www.sherrytowers.com/cowan_statistical_data_analysis.pdf.

[Dan62] G. Danby et al., *Observation of High-Energy Neutrino Reactions and the Existence of Two Kinds of Neutrinos*, Phys. Rev. Lett. 9:1 (1962), 36–44, DOI: 10.1103/PhysRevLett.9.36.

[Dav64] R. Davis, *Solar Neutrinos. II. Experimental*, Phys. Rev. Lett. 12:11 (1964), 303–5, DOI: 10.1103/PhysRevLett.12.303.

[Dav68] R. Davis, D. S. Harmer, and K. C. Hoffman, *Search for Neutrinos from the Sun*, Phys. Rev. Lett. 20:21 (1968), 1205–9, DOI: 10.1103/PhysRevLett.20.1205.

[Des19] M. Descher, *High rate systematic effects for keV sterile neutrino searches at KATRIN*, Master's thesis, Karlsruhe Institute of Technology, 2019, URL: https://www.katrin.kit.edu/publikationen/mth-descher.pdf.

[Deu90] J. Deutsch, M. Lebrun, and R. Prieels, *Searches for admixture of massive neutrinos into the electron flavour*, Nucl. Phys. A 518:1 (1990), 149–55, DOI: 10.1016/0375-9474(90)90541-S.

[Dol17] K. Dolde et al., *Impact of ADC non-linearities on the sensitivity to sterile keV neutrinos with a KATRIN-like experiment*, Nucl. Instrum. Meth. A 848 (2017), 127–36, DOI: 10.1016/j.nima.2016.12.015.

[Dra15] O. Dragoun and D. Vénos, *Constraints on the Active and Sterile Neutrino Masses from Beta-Ray Spectra: Past, Present and Future*, 2015, arXiv: 1504.07496 [hep-ex].

[Egg04] T. Eggert, *Die spektrale Antwort von Silizium-Röntgendetektoren*, PhD thesis, München: Technical University of Munich, 2004, URL: http://nbn-resolving.de/urn/resolver.pl?urn:nbn:de:bvb:91-diss2004101114551.

[Eit01] K. Eitel, *Latest results of the KARMEN-2 experiment*, Nucl. Phys. B Proc. Sup. 91:1 (2001) Neutrino 2000, 191–7, DOI: 10.1016/S0920-5632(00)00940-3.

[Ell17] E. Ellinger et al., *Monitoring the KATRIN source properties within the beamline*, J. Phys. Conf. Ser. 888 (2017), 012229, DOI: 10.1088/1742-6596/888/1/012229.

[Erh14] M. Erhard et al., *High-voltage monitoring with a solenoid retarding spectrometer at the KATRIN experiment*, J. Instrum. 9:06 (2014), P06022, DOI: 10.1088/1748-0221/9/06/p06022.

[Est19] I. Esteban et al., *Global analysis of three-flavour neutrino oscillations: synergies and tensions in the determination of θ_{23}, δ_{CP}, and the mass ordering*, J. High Energy Phys. 2019:1 (2019), 106, DOI: 10.1007/JHEP01(2019)106.

[Fan47] U. Fano, *Ionization Yield of Radiations. II. The Fluctuations of the Number of Ions*, Phys. Rev. 72:1 (1947), 26–9, DOI: 10.1103/PhysRev.72.26.

[Fer34] E. Fermi, *Versuch einer Theorie der β-Strahlen. I*, Z. Phys. 88:3 (1934), 161–77, DOI: 10.1007/BF01351864.

[Fer71] H. Ferdinande et al., *Numerical calculation of absolute forward thick-target bremsstrahlung spectra*, Nucl. Instrum. Methods 91:1 (1971), 135–40, DOI: 10.1016/0029-554X(71)90649-5.

[Fle70] R. Fletcher, *A new approach to variable metric algorithms*, Comput. J. 13:3 (1970), 317–22, DOI: 10.1093/comjnl/13.3.317.

[Fra13] A. Franke, *Searching for Reactor Antineutrino Flavor Oscillations with the Double Chooz Far Detector*, PhD thesis, Columbia University in the City of New York, 2013, DOI: 10.7916/D8GH9R1H.

[Fuk98] Y. Fukuda et al. (Super-Kamiokande Collaboration), *Evidence for Oscillation of Atmospheric Neutrinos*, Phys. Rev. Lett. 81:8 (1998), 1562–7, DOI: 10.1103/PhysRevLett.81.1562.

[Fur17] D. Furse et al., *Kassiopeia: a modern, extensible C++ particle tracking package*, New J. Phys. 19:5 (2017), 053012, DOI: 10.1088/1367-2630/aa6950.

[Gat84] E. Gatti and P. Rehak, *Semiconductor drift chamber — An application of a novel charge transport scheme*, Nucl. Instrum. Methods 225:3 (1984), 608–14, DOI: 10.1016/0167-5087(84)90113-3.

[Gol58] M. Goldhaber, L. Grodzins, and A. W. Sunyar, *Helicity of Neutrinos*, Phys. Rev. 109:3 (1958), 1015–7, DOI: 10.1103/PhysRev.109.1015.

[Gol70] D. Goldfarb, *A family of variable-metric methods derived by variational means*, Math. Comput. 24 (1970), 23–6, DOI: 10.1090/S0025-5718-1970-0258249-6.

[Goo06] A. Goobar et al., *The neutrino mass bound from WMAP-3, the baryon acoustic peak, the SNLS supernovae and the Lyman-alpha forest*, 2006, arXiv: astro-ph/0602155 [astro-ph].

[Gre07] D. Greenwald, *Characterization of the Proton Source in the Frictional Cooling Demonstration experiment*, Master's thesis, Technical University of Munich, 2007.

[Gri16] P. Grigorieva et al., *The role of electron scattering from registration detector in the "Troitsk nu-mass" MAC-E type spectrometer*, Nucl. Instrum. Meth. A 832 (2016), 15–20, DOI: 10.1016/j.nima.2016.06.058.

[Gro15] S. Groh, *Modeling of the response function and measurement of transmission properties of the KATRIN experiment*, PhD thesis, Karlsruhe Institute of Technology, 2015, URL: https://publikationen.bibliothek.kit.edu/1000046546/3459156.

[Ham98] W. Hampel et al., *Final results of the ^{51}Cr neutrino source experiments in GALLEX*, Phys. Lett. B 420:1 (1998), 114–26, DOI: 10.1016/S0370-2693(97)01562-1.

[Har97] R. Hartmann et al., *Ultrathin entrance windows for silicon drift detectors*, Nucl. Instrum. Meth. A 387:1 (1997) New Developments in Photodetection, 250–4, DOI: 10.1016/S0168-9002(96)01000-5.

[Hid95] K.-H. Hiddemann, H. Daniel, and O. Schwentker, *Limits on neutrino masses from the tritium beta spectrum*, J. Phys. G Nucl. Partic. 21:5 (1995), 639–50, DOI: 10.1088/0954-3899/21/5/008.

[Hin98] M. M. Hindi et al., *Search for the admixture of heavy neutrinos in the recoil spectra of ^{37}Ar decay*, Phys. Rev. C 58:4 (1998), 2512–25, DOI: 10.1103/PhysRevC.58.2512.

[Hir84] T. Hirabayashi and M. Saeki, *Sorption of gaseous tritium on the surface of type 316 stainless steel*, J. Nucl. Mater. 120:2 (1984), 309–15, ISSN: 0022-3115, DOI: 10.1016/0022-3115(84)90069-2.

[Hol00] E. Holzschuh et al., *The β-spectrum of ^{35}S and search for the admixture of heavy neutrinos*, Phys. Lett. B 482:1 (2000), 1–9, DOI: 10.1016/S0370-2693(00)00476-7.

[Hol99] E. Holzschuh et al., *Search for heavy neutrinos in the β-spectrum of ^{63}Ni*, Phys. Lett. B 451:1 (1999), 247–55, DOI: 10.1016/S0370-2693(99)00200-2.

[Jel15] T. Jeltema and S. Profumo, *Discovery of a 3.5 keV line in the Galactic Centre and a critical look at the origin of the line across astronomical targets*, Mon. Not. R. Astron. Soc. 450:2 (2015), 2143–52, DOI: 10.1093/mnras/stv768.

[Joh90] G. A. Johansen, *Development and analysis of silicon based detectors for low energy nuclear radiation*, PhD thesis, University of Bergen, 1990, URL: https://inis.iaea.org/collection/NCLCollectionStore/_Public/23/002/23002484.pdf.

[Kap22] J. C. Kapteyn, *First Attempt at a Theory of the Arrangement and Motion of the Sidereal System*, Astrophys. J. 55 (1922), 302, DOI: 10.1086/142670.

[Kin20] P. King, *Kerberos: a 48-Channel Analog Processing Platform for Scalable Readout of Large SDD Arrays*, in: *IEEE Nucl. Sci. Med. Imag. Conf. Proc.* (in press), 2020.

[Kno10] G. Knoll, *Radiation Detection and Measurement*, John Wiley & Sons, 2010, ISBN: 9780470131480, URL: https://books.google.de/books?id=4vTJ7UDel5IC.

[Kod01] K. Kodama et al., *Observation of tau neutrino interactions*, Phys. Lett. B 504:3 (2001), 218–24, DOI: 10.1016/S0370-2693(01)00307-0.

[Kor16] M. Korzeczek, *eV- & keV-sterile neutrino studies with KATRIN*, Master's thesis, Karlsruhe Institute of Technology, 2016, URL: https://www.katrin.kit.edu/publikationen/MKorz-MA-eV-keV%20sterile%20Neutrinos.pdf.

[Kor20] M. Korzeczek, *Sterile neutrino search with KATRIN — Design of a novel detector system and investigation of detector-related systematic uncertainties*, (in preparation), PhD thesis, Karlsruhe Institute of Technology, 2020.

[Kra05] C. Kraus et al., *Final results from phase II of the Mainz neutrino mass searchin tritium β-decay*, Eur. Phys. J. C 40:4 (2005), 447–68, DOI: 10.1140/epjc/s2005-02139-7.

[Krö02] M. Krödel et al., *Short carbon-fiber-reinforced ceramic — Cesic — for optomechanical applications*, in: *Optomechanical Design and Engineering*, 2002, 230–42, DOI: 10.1117/12.482164.

[Kru83] P. Kruit and F. H. Read, *Magnetic field paralleliser for 2π electron-spectrometer and electron-image magnifier*, J. Phys. E Sci. Instrum. 16:4 (1983), 313–24, DOI: 10.1088/0022-3735/16/4/016.

[Kur36] F. N. D. Kurie, J. R. Richardson, and H. C. Paxton, *The Radiations Emitted from Artificially Produced Radioactive Substances. I. The Upper Limits and Shapes of the β-Ray Spectra from Several Elements*, Phys. Rev. 49:5 (1936), 368–81, DOI: 10.1103/PhysRev.49.368.

[Leb19] M. Lebert, *Characterization of the Detector Response to Electrons and Test of a New Entrance Window Technology of Silicon Drift Detectors for the TRISTAN Project*, Master's thesis, Technical University of Munich, 2019.

[Lec01] P. Lechner et al., *Silicon drift detectors for high count rate X-ray spectroscopy at room temperature*, Nucl. Instrum. Meth. A 458:1 (2001), 281–7, DOI: 10.1016/S0168-9002(00)00872-X.

[Lec95] P. Lechner and L. Strüder, *Ionization statistics in silicon X-ray detectors — new experimental results*, Nucl. Instrum. Meth. A 354:2 (1995), 464–74, DOI: 10.1016/0168-9002(94)01317-9.

[Lec98] P. Lechner, *Zur Ionisationsstatistik in Silicium*, PhD thesis, Technical University of Munich, 1998.

[LEP06] LEP Collaborations, *Precision electroweak measurements on the Z resonance*, Phys. Rep. 427:5 (2006), 257–454, DOI: 10.1016/j.physrep.2005.12.006.

[Liu87] J. W. Liu, *Total cross sections for high-energy electron scattering by H_2 ($^1\Sigma_g^+$), N_2 ($^1\Sigma_g^+$), and O_2 ($^3\Sigma_g^-$)*, Phys. Rev. A 35:2 (1987), 591–7, DOI: 10.1103/PhysRevA.35.591.

[Lob02] V. Lobashev, *Study of the tritium beta-spectrum in experiment "Troitsk ν-mass"*, Prog. Part. Nucl. Phys. 48:1 (2002), 123–31, DOI: 10.1016/S0146-6410(02)00118-7.

[Lob85] V. Lobashev and P. Spivak, *A method for measuring the electron antineutrino rest mass*, Nucl. Instrum. Meth. A 240:2 (1985), 305–10, DOI: `10.1016/0168-9002(85)90640-0`.

[Lob99] V. Lobashev et al., *Direct search for mass of neutrino and anomaly in the tritium beta-spectrum*, Phys. Lett. B 460:1 (1999), 227–35, DOI: `10.1016/S0370-2693(99)00781-9`.

[Lok18] A. Lokhov, *A model for a keV-scale sterile neutrino search with KATRIN: SSC-sterile*, in: *XXVIII International Conference on Neutrino Physics and Astrophysics*, 2018, 247, DOI: `10.5281/zenodo.1300735`.

[Lov12] M. R. Lovell et al., *The haloes of bright satellite galaxies in a warm dark matter universe*, Mon. Not. R. Astron. Soc. 420:3 (2012), 2318–24, DOI: `10.1111/j.1365-2966.2011.20200.x`.

[Mak62] Z. Maki, M. Nakagawa, and S. Sakata, *Remarks on the Unified Model of Elementary Particles*, Prog. Theor. Phys. 28:5 (1962), 870–80, DOI: `10.1143/PTP.28.870`.

[Mat02] K. Mathieson et al., *Charge sharing in silicon pixel detectors*, Nucl. Instrum. Meth. A 487:1 (2002), 113–22, DOI: `10.1016/S0168-9002(02)00954-3`.

[McC15] E. McCutchan, *Nuclear Data Sheets for $A = 83$*, Nucl. Data Sheets 125 (2015), 201–394, DOI: `10.1016/j.nds.2015.02.002`.

[Mei19] M. Meier, *TRISTAN Fly High - Design Studies for a CubeSat Compton Telescope*, Master's thesis, Technical University of Munich, 2019.

[Men11] G. Mention et al., *Reactor antineutrino anomaly*, Phys. Rev. D 83:7 (2011), 073006, DOI: `10.1103/PhysRevD.83.073006`.

[Mer15a] S. Mertens et al., *Sensitivity of next-generation tritium beta-decay experiments for keV-scale sterile neutrinos*, J. Cosmol. Astropart. P. 2015:02 (2015), 020, DOI: `10.1088/1475-7516/2015/02/020`.

[Mer15b] S. Mertens et al., *Wavelet approach to search for sterile neutrinos in tritium β-decay spectra*, Phys. Rev. D 91:4 (2015), 042005, DOI: `10.1103/PhysRevD.91.042005`.

[Mer17] A. Merle, *Sterile Neutrino Dark Matter*, 2053-2571, Morgan & Claypool Publishers, 2017, ISBN: 978-1-6817-4481-0, DOI: `10.1088/978-1-6817-4481-0`.

[Mer19] S. Mertens et al., *A novel detector system for KATRIN to search for keV-scale sterile neutrinos*, J. Phys. G Nucl. Partic. 46:6 (2019), 065203, DOI: `10.1088/1361-6471/ab12fe`.

[Mik85] S. P. Mikheev and A. Y. Smirnov, *Resonance amplification of oscillations in matter and spectroscopy of solar neutrinos*, Yadernaya Fizika 42:6 (1985), 1441–8, URL: `https://inis.iaea.org/search/search.aspx?orig_q=RN:17085134`.

[Moh80] R. N. Mohapatra and G. Senjanovi ć, *Neutrino Mass and Spontaneous Parity Nonconservation*, Phys. Rev. Lett. 44:14 (1980), 912–5, DOI: `10.1103/PhysRevLett.44.912`.

[Mye15] E. G. Myers et al., *Atomic Masses of Tritium and Helium-3*, Phys. Rev. Lett. 114:1 (2015), 013003, DOI: `10.1103/PhysRevLett.114.013003`.

[NAS19] NASA/IPAC Extragalactic Database, 2019, URL: `ned.ipac.caltech.edu` (visited on 12/06/2019).

[Nel65] J. A. Nelder and R. Mead, *A Simplex Method for Function Minimization*, Comput. J. 7:4 (1965) [Erratum ibid. 8 (1965) 1, 27], 308–13, DOI: `10.1093/comjnl/7.4.308`.

[Nic06] A. Niculae et al., *Optimized readout methods of silicon drift detectors for high-resolution X-ray spectroscopy*, Nucl. Instrum. Meth. A 568:1 (2006), 336–42, DOI: `10.1016/j.nima.2006.06.025`.

[NuF18] NuFIT 4.0, 2018, URL: `www.nu-fit.org` (visited on 10/11/2019).

[Ott08] E. W. Otten and C. Weinheimer, *Neutrino mass limit from tritium β-decay*, Rep. Prog. Phys. 71:8 (2008), 086201, DOI: `10.1088/0034-4885/71/8/086201`.

[Pau30] W. Pauli, *Offener Brief an die Gruppe der Radioaktiven bei der Gauvereins-Tagung zu Tübingen*, 1930, URL: `http://www.neutrino.uni-hamburg.de/sites/site_neutrino/content/e45939/e48540/e48541/e48544/infoboxContent48545/material-vorlesung1-moessbauer-pauli.pdf`.

[Pec77] R. D. Peccei and H. R. Quinn, *CP Conservation in the Presence of Pseudoparticles*, Phys. Rev. Lett. 38:25 (1977), 1440–3, DOI: `10.1103/PhysRevLett.38.1440`.

[Pen62] D. R. Penn, *Wave-Number-Dependent Dielectric Function of Semiconductors*, Phys. Rev. 128:5 (1962), 2093–7, DOI: `10.1103/PhysRev.128.2093`.

[Per75] M. L. Perl et al., *Evidence for Anomalous Lepton Production in $e^+ - e^-$ Annihilation*, Phys. Rev. Lett. 35:22 (1975), 1489–92, DOI: `10.1103/PhysRevLett.35.1489`.

[Pic92] A. Picard et al., *A solenoid retarding spectrometer with high resolution and transmission for keV electrons*, Nucl. Instrum. Meth. B 63:3 (1992), 345–58, DOI: `10.1016/0168-583X(92)95119-C`.

[Pon58] B. Pontecorvo, *Mesonium and Antimesonium*, J. Exp. Theor. Phys. 6 (1958), 429, URL: http://www.jetp.ac.ru/cgi-bin/e/index/e/6/2/p429?a=list.

[Pon68] B. Pontecorvo, *Neutrino Experiments and the Problem of Conservation of Leptonic Charge*, J. Exp. Theor. Phys. 26:5 (1968), 984–8, URL: http://www.jetp.ac.ru/cgi-bin/dn/e_026_05_0984.pdf.

[Pop00] M. Popp, *Untersuchung und analytische Modellierung der Systemantwort von pn-CCD Detektoren*, PhD thesis, Ludwig Maximilian University of Munich, 2000, URL: http://nbn-resolving.de/urn:nbn:de:bvb:19-4087.

[Pri15] F. Priester, M. Sturm, and B. Bornschein, *Commissioning and detailed results of KATRIN inner loop tritium processing system at Tritium Laboratory Karlsruhe*, Vacuum 116 (2015), 42–7, DOI: 10.1016/j.vacuum.2015.02.030.

[Ren11] P. Renschler, *KESS - A new Monte Carlo simulation code for low-energy electron interactions in silicon detectors*, PhD thesis, Karlsruhe Institute of Technology, 2011, DOI: 10.5445/IR/1000024959.

[Rob91] R. G. H. Robertson et al., *Limit on $\bar{\nu}_e$ mass from observation of the β-decay of molecular tritium*, Phys. Rev. Lett. 67:8 (1991), 957–60, DOI: 10.1103/PhysRevLett.67.957.

[Sae00] A. Saenz, S. Jonsell, and P. Froelich, *Improved Molecular Final-State Distribution of HeT^+ for the β-Decay Process of T_2*, Phys. Rev. Lett. 84:2 (2000), 242–5, DOI: 10.1103/PhysRevLett.84.242.

[Sch13] M. Schlösser et al., *Accurate calibration of the laser Raman system for the Karlsruhe Tritium Neutrino Experiment*, J. Mol. Struct. 1044 (2013), 61–6, DOI: 10.1016/j.molstruc.2012.11.022.

[Sch14] J. Schwarz, *The Detector System of the KATRIN Experiment - Implementation and First Measurements with the Spectrometer*, PhD thesis, Karlsruhe Institute of Technology, 2014, DOI: 10.5445/IR/1000042772.

[Sch19a] C. Schätz, *Development of an energy dependent Final State Distribution for T_2*, Master's thesis, Technical University of Munich, 2019.

[Sch19b] L. Schlüter, *Development of New Methods to Include Systematic Effects in the First Tritium Data Analysis and Sensitivity Studies of the KATRIN Experiment*, Master's thesis, Technical University of Munich, 2019.

[Sch83] K. Schreckenbach, G. Colvin, and F. von Feilitzsch, *Search for mixing of heavy neutrinos in the β^+ and β^- spectra of the ^{64}Cu Decay*, Phys. Lett. B 129:3 (1983), 265–8, DOI: 10.1016/0370-2693(83)90858-4.

[Sem14] Y. K. Semertzidis et al., *Conceptual design of the International Axion Observatory (IAXO)*, J. Instrum. 9 (2014), DOI: 10.1088/1748-0221/9/05/T05002.

[Sen18] J. Sentkerestiová et al., *Gaseous* ^{83m}Kr *generator for KATRIN*, J. Instrum. 13:04 (2018), P04018, DOI: 10.1088/1748-0221/13/04/p04018.

[Sha70] D. F. Shanno, *Conditioning of quasi-Newton methods for function minimization*, Math. Comput. 24 (1970), 647–56, DOI: 10.1090/S0025-5718-1970-0274029-X.

[Shr80] R. Shrock, *New tests for and bounds on neutrino masses and lepton mixing*, Phys. Lett. B 96:1 (1980), 159–64, DOI: 10.1016/0370-2693(80)90235-X.

[Sie19] D. Siegmann, *Investigation of the Detector Response to Electrons of the TRISTAN Prototype Detectors*, Master's thesis, Technical University of Munich, 2019.

[Sim81] J. J. Simpson, *Measurement of the* β*-energy spectrum of* ^3H *to determine the antineutrino mass*, Phys. Rev. D 23:3 (1981), 649–62, DOI: 10.1103/PhysRevD.23.649.

[Sim85] J. J. Simpson, *Evidence of Heavy-Neutrino Emission in Beta Decay*, Phys. Rev. Lett. 54:17 (1985), 1891–3, DOI: 10.1103/PhysRevLett.54.1891.

[Sle15] M. Slezák, *Monitoring of the energy scale in the KATRIN neutrino experiment*, PhD thesis, Charles University, Prague, 2015, URL: https://www.katrin.kit.edu/publikationen/phd-Martin_Slezak.pdf.

[Spi05] H. Spieler, *Semiconductor Detector Systems. Series on Semiconductor*, Oxford University Press, 2005, ISBN: 9780198527848, DOI: 10.1093/acprof:oso/9780198527848.001.0001.

[Sto95] W. Stoeffl and D. J. Decman, *Anomalous Structure in the Beta Decay of Gaseous Molecular Tritium*, Phys. Rev. Lett. 75:18 (1995), 3237–40, DOI: 10.1103/PhysRevLett.75.3237.

[Tan18] M. Tanabashi et al., *Review of Particle Physics* English (US), Phys. Rev. D 98:3 (2018), DOI: 10.1103/PhysRevD.98.030001.

[Tho01] A. C. Thompson et al., *X-ray Data Booklet*, 2001, URL: https://xdb.lbl.gov/xdb.pdf (visited on 12/27/2019).

[Tra83] S. Trajmar, D. F. Register, and A. Chutjian, *Electron scattering by molecules II. Experimental methods and data*, Phys. Rep. 97:5 (1983), 219–356, DOI: 10.1016/0370-1573(83)90071-6.

[Tri03] M. Trinczek et al., *Novel Search for Heavy ν Mixing from the β^+ Decay of ^{38m}K Confined in an Atom Trap*, Phys. Rev. Lett. 90:1 (2003), 012501, DOI: 10.1103/PhysRevLett.90.012501.

[Tri18] P. Trigilio et al., *ETTORE: a 12-Channel Front-End ASIC for SDDs with Integrated JFET*, in: *IEEE Nucl. Sci. Med. Imag. Conf. Proc.* 2018, 1–4, DOI: 10.1109/NSSMIC.2018.8824675.

[Urb19] K. Urban, *Application of a TRISTAN Silicon Drift Detector as Forward Beam Monitor in KATRIN*, Master's thesis, Technical University of Munich, 2019.

[Var67] Y. Varshni, *Temperature Dependence of the Energy Gap in Semiconductors*, Physica 34:1 (1967), 149–54, DOI: 10.1016/0031-8914(67)90062-6.

[Vén18] D. Vénos et al., *Properties of ^{83m}Kr conversion electrons and their use in the KATRIN experiment*, J. Instrum. 13:02 (2018), T02012, DOI: 10.1088/1748-0221/13/02/t02012.

[Wal13] B. L. Wall, *Karlsruhe Tritium Experiment: Detector System Commissioning and In-Situ PIN-Diode Array Dead-Layer Measurement*, PhD thesis, University of Washington, 2013, URL: http://hdl.handle.net/1773/22845.

[Wan13] N. Wandkowsky, *Study of background and transmission properties of the KATRIN spectrometers*, PhD thesis, Karlsruhe Institute of Technology, 2013, DOI: 10.5445/IR/1000036631.

[Wat12] C. R. Watson, Z. Li, and N. K. Polley, *Constraining sterile neutrino warm dark matter with Chandra observations of the Andromeda galaxy*, J. Cosmol. Astropart. P. 2012:03 (2012), 018, DOI: 10.1088/1475-7516/2012/03/018.

[Wil91] D. Wilkinson, *Small terms in the beta-decay spectrum of tritium*, Nucl. Phys. A 526:1 (1991), 131–40, DOI: 10.1016/0375-9474(91)90301-L.

[Wol78] L. Wolfenstein, *Neutrino oscillations in matter*, Phys. Rev. D 17:9 (1978), 2369–74, DOI: 10.1103/PhysRevD.17.2369.

[Yan80] T. Yanagida, *Horizontal Symmetry and Masses of Neutrinos*, Prog. Theor. Phys. 64:3 (1980), 1103–5, DOI: 10.1143/PTP.64.1103.

[Zie04] J. F. Ziegler, *SRIM-2003*, Nucl. Instrum. Meth. B 219-220 (2004), 1027–36, DOI: 10.1016/j.nimb.2004.01.208.

[Zie19] J. F. Ziegler, 2019, URL: www.srim.org (visited on 12/16/2019).

[Zub12] K. Zuber, *Neutrino Physics*, Boca Raton: CRC Press, 2012, DOI: 10.1201/b11065.

Acknowledgments

At this point, I want to thank everyone who contributed in whatever way to the successful completion of this work, starting with my two supervising professors Susanne Mertens and Stefan Schönert. I also want to thank Norbert Kaiser for serving as a referee in my defense.

Susanne, it was a pleasure working with you throughout these three and a half years. I think, not every PhD student is as lucky to have such a supportive supervisor. I feel privileged to be among the first contributors in your group at MPP and have enjoyed seeing it grow. All the best for the rest of your tenure track and what comes after. Thank you also — and of course Thierry Lasserre — for the many invitations to barbecues and Christmas parties at your place.

Then, I want to thank all past and current members of the KATRISTAN group at MPP, namely Martin Slezák for his indispensable support in python coding and server related "stuff", Thibaut Houdy for his tireless contributions to the Troitsk analysis, as well as both of them, Frank Edzards, Anna Schaller (aka. Pollithy) and Daniel Siegmann for proof reading parts of this thesis. I also thank Daniel, who had to share the office by far the longest time with me, for his contributions with the SEM, as well as Manuel Lebert for his $^{83\mathrm{m}}$Kr investigations and efforts to the proton grid; I'm sorry we couldn't make Susanne bake waffles for the group. Last but by no means least, I'm thankful to Lisa Schlüter for her company in highs and lows of my PhD and beside that.

For what concerns the extended KATRISTAN group, a big thank you goes to Docteur Konrad Altenmüller, with whom I closely worked together in all three campaigns in Troitsk. I send my gratitude to Peter Lechner and David Fink for all the valuable discussions and explanations, and also for proof reading parts of this thesis, as well as to Tobias Bode and David Radford, who facilitated my way into the detector business. I am also very thankful for the support from Stefan Horn and Gennadiy Finenko, and from my fellow IMPRS PhD students at MPP. Special thanks go to Natascha Savić: If it wasn't for her, I would probably not have started at MPP in the first place.

In the group at KIT, I thank Anton Huber for a brilliant crash course in Kassiopeia and fun times in Russia, as well as Marc Korzeczek, Martin Descher, Joachim Wolf and Ferenc Glück for support and fruitful discussions.

Furthermore, I'd like to thank Marco Carminati, Matteo Gugiatti, and Pietro King from Politecnico di Milano, Paolo Trigilio and Luca Bombelli from XGLab, as well as Matteo Biassoni and Stefano Pozzi from Milano Bicocca for participating over years in the weekly detector call and their hospitality in Milan. Special thanks go to Antonio Alborini from XGLab for immediate availability to spend hours of DAQ consulting via Skype.

I wouldn't want to miss thanking Vladislav Pantuev and Aleksander Nozik for their guidance during the measurement campaigns in Troitsk and their endurance in the analyses. Vlad was even kind enough to let us stay in his son's apartment twice. My gratitude also goes to Alexey Lokhov for taking some of my night shifts at Troitsk ν-mass and calculating all the SSC-sterile responses, as well as to Djohn Abdurashitov and his wife for the delicious пельмени recipe. I also want to use the opportunity to dis-thank the Bump for all the headaches and complications it caused. At least it served for quite some gallows jokes.

Apart from all the work related stuff, I want to thank all of my friends, especially the Tiefenbronner Delegation in Munich and the extended Karlsruher Wolfpack, and of course my family, especially my parents and my sister. It's good to know that I can always count on you!